Numerical modelling of low temperature plasma

by

Craig Stewart MacLachlan, MSci.

Thesis
submitted to the
University of Glasgow
for the degree of
Ph.D.

Astronomy and Astrophysics Group
Department of Physics and Astronomy
University of Glasgow
Glasgow, G12 8QQ.

Submitted
July 2009

Contents

List of Figures

List of Tables

Abstract

The intention of this thesis is to gain a better understanding of basic physical processes occurring in low temperature plasmas. This is achieved by applying both analytic and numerical models. Low temperature plasmas are found in both technological and astrophysical contexts. Three different situations are investigated: an instability in electronegative plasmas; electron avalanches during plasma initiation; and a phenomenon called the Critical Ionisation Velocity interaction.

Industrial plasma discharges with electronegative gases are found to be unstable in certain conditions. Fluctuations in light emission, particle number densities and potential are observed. The instability has been reproduced in a variety of experiments. Reports from the experiments are discussed to characterise the key features of the instability. An, as yet un-considered, physical process that could explain the instability is introduced. The instability relies on the plasma's transparency to the electric field. This mechanism is investigated using simple zero-dimensional numerical and analytic models. The results from the models are compared to experimental results. The calculated frequencies are in good agreement with the experimental measurements. This shows that the instability mechanism described here is relevant.

For the remaining two problems a three-dimensional particle model is constructed. This model calculates the trajectories of each individual particle. The potential field is solved self-consistently on a computational mesh. Poisson's equation is solved using a Multigrid technique. This iterative solution method uses many grids, of different resolutions, to smooth the error on all spatial scales. The mathematical foundation and details of the components of the Multigrid method are presented. Several test cases where analytic solutions of Poisson's equation exist are used to determine the accuracy of the solver. The implemented solver is found to be both efficient and accurate.

Collisions are vitally important to the evolution of plasmas. The chemistry resulting from collisions is the reason why plasmas are so useful in technological applications. Electron collisions are included in the particle model using a Monte-Carlo technique. A basic method is given and several improvements are described. The most efficient combination of improvements is determined through a series of test cases. The error resulting from the collision selection process is characterised.

Technological plasmas are formed from the electrical breakdown of a neutral gas. At atmospheric pressure the breakdown occurs as an electron avalanche. The particle model is used to simulate the nanosecond evolution of the avalanche from a single electron-ion pair. Special attention is paid to the inelastic collisions and the creation of metastables. The inelastic losses are used to estimate the photon emission from the electron avalanche.

The Critical Ionisation Velocity phenomena is investigated using the particle model. When a neutral gas streams across a magnetised plasma the ionisation rate increases rapidly if the speed of the neutrals exceeds a critical value. Collisions between neutrals and positive ions create pockets of unbalanced negative charge. Electrons in these pockets are accelerated by their potential field and can reach energies capable of ionisation. The evolution of such an electron overdensity is simulated and their energy gain under different density and magnetic field conditions is calculated. The results from the simulation may explain the discrepancy between laboratory and space experiments.

Acknowledgements

I am very confident that my life as a PhD student was and will be one of the best periods of my life. It was the people surrounding me that are responsible for my fantastic experience. I am glad to have this opportunity to show my gratitude to these people.

Of all the people in my life, those who have had the greatest influence on my life are my family. My grandparents nurtured, at a young age, many of my current pleasures: travel, art, money counting and cookery. I thank my sister, for setting the bar high and giving me somebody to compete with.

I especially want to thank my parents, who I don't thank nearly enough, for all their love, support, kindness and guidance. They have supported all of the decisions I have made in my life and I know that the same would be true whatever those choices might have been. I want to thank them not just for their help and support but for the values, curiosity and enthusiasm they have instilled in me.

My supervisor Declan truly is a remarkable man. I am fairly convinced there is almost nothing he doesn't know and even less he couldn't work out. His amazing knowledge is supplemented by his enthusiasm for his subject and the ability to induce that enthusiasm in others. I found this skill crucial when deciding to begin my PhD and managing to finish it.

I would also like to thank Declan for putting me in the office with the best office-mates a PhD student could have asked for. There was very rarely a dull moment in that office with Craig and Hugh. These two incredibly intelligent chaps were an invaluable source of help and knowledge. I thank Craig for being my partner-in-crime and Hugh for being a good natured victim of our pranks.

There were other brilliant people in the physics departments: Fiona, Catherine, Gordon, Robert, Russell and Luis. To avoid writing a huge list of names: thanks to all the footballers, badmintoners, tutors, staff, PhD students and non-physicists friends from high school.

How do I thank Rachel, the girl I love? She was one of the people who checked my atrocious spelling and grammar but more than that, she was my sanctuary from physics when work was hard. I can't describe how much I've enjoyed the last four years that Rachel has been in my life and I can't imagine a single day without her.

To all of you named and hinted at above you have my complete gratitude and I wish you all the happiness life can bring!

Declaration

This thesis is my own composition except where indicated in the text and the work presented herein has not been submitted for any other qualication from any other institution.

Chapter 1

Introduction

> "Research is to see what everybody else has seen, and to think what nobody else has thought." - *Albert Szent-Györgi*

> "The truth is rarely pure and never simple." - *Oscar Wilde*

1.1 Introducing plasma

The term "plasma" was first used by Langmuir in 1928 [1] to describe the region in a discharge which contained roughly equal numbers of ions and electrons. He was investigating oscillations in ionised gas; these were oscillations at the plasma frequency. In popular culture, "plasma" has become a stereotypical science-fiction term but what is a "plasma"? A current dictionary uses the following definition:

> "**plasma**, *n.*, An ionized gas containing free electrons and positive ions, formed usually at very high temperatures (as in stars and in nuclear fusion experiments) or at low pressures (as in the upper atmosphere and in fluorescent lamps); esp. such a gas which is electrically neutral and exhibits certain phenomena due to the collective interaction of charges. Also: an analogous collection of charged particles in which one or both kinds are mobile, as the conduction electrons in a metal or the ions in a salt solution." - *Oxford English Dictionary* [2].

This definition is quite good but a couple of points should be noted. A complete definition of a plasma would not restrict the ionised gas to being made up of electrons and positive ions; a collection of charged particles, of any type, can be called a plasma. Plasmas are found over a large range in temperature and pressure not just the two extremes mentioned in the definition. One of the key features of a plasma are the collective effects caused by the charged particles. The charged particles result in the plasma being a good conductor and susceptible to various wave and instability phenomena. Collective effects are responsible for much of the interesting science found in plasmas.

1.1.1 Plasma regimes

Typically the first type of plasma people learn about are electron-proton plasma. The behaviour of this type of plasma is dominated by the electric and magnetic fields induced by and applied to the particles. Inelastic collisions play a secondary role to long range Coulomb interactions. The difference in mass of the electrons and protons results in wave phenomena at different frequencies. The lighter, more mobile electrons have a high frequency response, the protons respond at a lower frequency meaning they are often considered to be static. This type of plasma is not the most common due to its idealised nature. Very high energies and pressures are usually required to maintain a purely electron-proton plasma.

At extremely high temperatures and pressures plasmas can consist purely of electrons and positrons. This type of plasma is found in the magnetospheres of pulsars, active galactic nuclei, microquasars and gamma-ray bursters [3]. The behaviour of an electron-positron plasma, similar to an electron-proton plasma, is dominated by electromagnetic fields but annihilation of oppositely charged particles through collisions is also possible. In this case the mobility of the particles is the same and consequently the wave phenomena can be more complicated than the electron-proton case.

The most common type of plasma is an electron-ion plasmas. These types of plasma are found in space and in everyday Earth-bound life. They are used extensively in commercial and industrial processes: energy saving light bulbs and silicon chip manufacture are just two examples. At temperatures and pressures lower than in electron-proton plasmas more complex atomic and molecular structures are less readily broken up and survive in the plasma environment. In this case plasmas consist of electrons, positive and negative ions and neutral gas particles. The presence of molecular compounds increases the importance of collisions between all species: electron-ion, electron-neutral, ion-ion and ion-neutral. allowing complex chemistry to occur. It is the chemistry of a plasma that makes it invaluable for many applications.

The final plasma regime of note is the where the positive and negative charges of the plasma are agglomerations of many positive and negative ions. These plasmas are termed complex [4] or dusty plasmas [5]. Dust is formed when many atomic and molecular particles coalesce to form much larger, nanometre scale, particles. These macroscopic particles can form naturally in almost any plasma regime: planetary rings, inter-planetary medium, flames, low-temperature discharges and even tokamak fusion plasmas. The presence of dust in a discharge can be very important; dust particles present in fusion plasmas can contain radioactive isotopes. This presents a serious environmental safety problem and it may also affect the performance of the discharge [6]. Complex plasmas [4] are created in laboratories using charged silica beads. These plasmas currently do not have a specific application but do exhibit some interesting behaviour. They can show behaviour similar to liquid or crystalline states depending on the applied conditions.

1.1.2 Low temperature plasmas

Two main parameters are used to classify types of plasma: density and electron temperature. A plot showing where various plasmas lie in pressure-temperature space is shown in figure 1.1. Low temperature plasmas are characterised by electron temperatures $\lesssim 20$ eV however there is no official definition. In this energy range plasmas can be found in a wide range of pressures. They can be found in astrophysical situations: the solar wind,

the solar photosphere and low chromosphere can be described as low temperature plasmas. Laboratory plasmas exist at higher pressures: glow discharges, low pressure discharges and high pressure arcs for example.

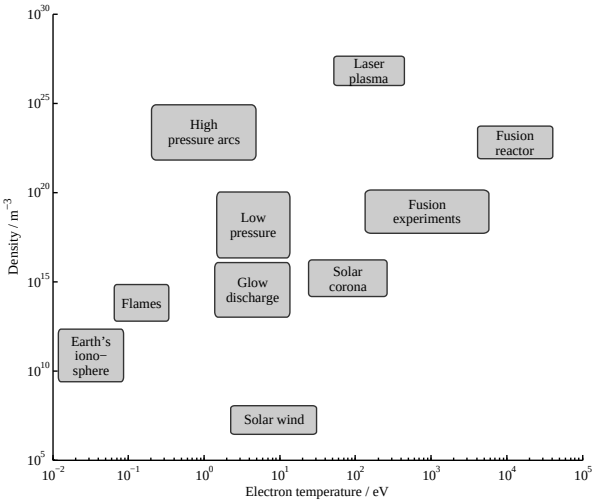

Figure 1.1: Diagram of plasma types across different electron temperature and pressure regimes [7].

Another method of classifying plasmas is whether or not they are in thermal equilibrium. A plasma is in thermal equilibrium when all the species have the same temperature and the distribution of velocities is a Maxwell-Boltzman distribution. Maxwell-Boltzman distributions are described in section 1.2. Plasma thermal equilibrium only occurs at high temperatures and pressures; for example in arc discharges and fusion plasmas. These conditions favour large numbers of collisions allowing efficient energy exchange between species equilibrating the plasma. If the plasma is in thermal equilibrium in some spatial locations then the plasma is described as being in local thermal equilibrium.

When a plasma is not in thermal equilibrium the idea of temperature is not strictly applicable as a temperature can only be assigned to a equilibrium distribution (*i.e.* a Maxwellian). In this non-equilibrium case we assume the temperature refers to the mean energy of the particles. Bearing this in mind, a plasma is described as being non-equillibrium when the species have different temperatures. Weakly ionised gases, *i.e.* when the plasma species are a minority in the gas, are usually non-equilibrium and different temperatures can be given to the neutral, ions and electrons.

1.1.3 Plasma applications

Plasmas exist in many different regimes: from pulsar pair-plasmas to household flames. Perhaps the best known application of plasma is fusion. However, low temperature plasmas are used extensively in a wide variety of technological processes. The aim here is to give a brief overview of some of these applications and the references contained provide an opportunity for further reading.

Low pressure discharges

Plasmas created in reactors at low pressure, typically 0.1 - 130 Pa (often expressed as $1 - 10^3$ mTorr), are used in the manufacture of microchips and the application of coatings.

The production of microchips involves many different stages and plasma processing is involved in many of these. The conducting channels in the silicon wafer are created in a process called etching [8; 9]. Deposition of specific chemicals is also required to tailor the conductive properties of the silicon wafer. These weakly ionised plasmas have conditions suitable for the existence of many different chemical species. Energetic ions bombard the substrate causing chemical reactions at the surface.

Deposition processes [10; 11] are also responsible for many coatings that are found in everyday life. Coatings that harden a surface, make it non-reflective, or absorb UV radiation can all be applied through plasma processes.

Lighting

Another major use of plasma in everyday life is in lighting. Fluorescent tubes and compact fluorescent lamps (CFL) are both plasma technologies [12]. These light bulbs have greater life spans and expend considerably less energy than "traditional" incandescent light bulbs. Noble gases such as Argon, Xenon, Neon or Krypton are excited in a glass tube producing ultraviolet (UV) radiation. The UV photons are converted into visible light by a phosphor coating on the inner surface of the tube. Plasmas used in lighting are created at low pressure, like those used in etching and deposition.

Atmospheric pressure

Dielectric Barrier Discharges (DBDs) [13] are devices where the electrodes are shielded from the plasma by dielectric barriers. These discharges are often operated at atmospheric pressure. In an atmospheric pressure discharge the conditions are favourable for 3-body reactions; the creation of Ozone is a 3-body interaction. Ozone is very good at destroying bacteria and has been used in water treatment since 1897 [13].

Plasmas at atmospheric pressure have also found use in medicine. Prototype hand-held plasma devices that are capable of wound [14] and dental [15] sterilisation have recently been created. Sterilisation is not the first application of plasmas in medicine: plasma scalpels [16] and coagulation devices are used in surgery [17]. A small plasma is created at the tip of a device and when it is pressed against tissue it makes an incision. The plasma scalpels cause less damage than conventional knife-like scalpels and consequently the wound heals faster. Other medical applications being investigated are plasma catalysed healing of wounds and cell detachment [17]. The activating effect is controversial since it is unknown if the key factor is the chemistry of the plasma or the electromagnetic fields created by the device.

It is worth mentioning that DBDs are also the devices forming the pixels in plasma televisions. These devices operate at pressures slightly below atmospheric pressure and work in a similar fashion to plasma lamps. UV radiation is produced through reactions in the plasma and stimulates a phosphor to give light emission in visible wavelengths.

Carbon nanotubes are often proposed as the solution to numerous future engineering problems. They are nanometer scale cylindrical structures with walls formed from hexagonally linked Carbon atoms. Their chemical bonding structure makes them very strong and they are also good conductors of electricity and heat. Carbon nanotubes can be created through a plasma process. The type of Carbon nanotube depends of the pressure of the discharge: at low pressure multi-walled nanotubes are produced; and at atmospheric pressure single walled nanotubes can be grown [18].

1.2 Mathematical description of a plasma

In order to properly describe the constituent particles of a plasma we must understand the motions of all the particles. For any given time a particle has 3 position and 3 velocity components so 7 co-ordinates are required to define the evolution of each particle through time. Obviously the number of particles in a plasma depends on its spatial size and density however it is unlikely there would be less than many billions of particles. Problems with such large numbers of particles are intractable without simplification. To tackle such a problem the idea of a distribution function can be introduced. A distribution function is a statistical description of the ensemble of particles in 7-dimensional space time.

The evolution of the distribution function, $f_s(x, y, z, u_x, u_y, u_z, t)$, for a given species s is given by Boltzmann's equation,

$$\frac{\partial f_s}{\partial t} + \boldsymbol{u} \cdot \frac{\partial f_s}{\partial \boldsymbol{r}} + \boldsymbol{a}_s \cdot \frac{\partial f_s}{\partial \boldsymbol{u}} = \left(\frac{\partial f_s}{\partial t}\right)_c, \tag{1.1}$$

where $\boldsymbol{r}$, $\boldsymbol{u}$ and $\boldsymbol{a}_s$ are the spatial co-ordinate, velocity co-ordinate and the acceleration respectively and the arguments of f_s have been dropped for notational convenience. The first term gives the evolution of the distribution function in time, the second term describes how the particles move in position space and the final term on the left hand side describes how the particles move in velocity space. The term on the right hand side of Boltzmann's equation (1.1) describes the change in the distribution function due to collisions. There is no canonical form for this term. It is often called the collision operator and the standard expressions used to represent this operator are discussed in section 1.3.3. Figure 1.2 shows an example of Boltzmann's equation operating on the particles in an area element of 1-d phase space.

If the particles of a gas or plasma are in thermal equilibrium and there are no external fields then there are no temporal, spatial or velocity gradients and Boltzmann's equation reduces to

$$\left.\frac{\partial f_s}{\partial t}\right|_c = 0. \tag{1.2}$$

When collisions occur between particles of the same species, the solution to (1.2) is a Maxwell-Boltzmann distribution:

$$f_M(\boldsymbol{u}) = n\left(\frac{m}{2\pi k_B T}\right)^{\frac{3}{2}} \exp\left(-\frac{m(\boldsymbol{u} - \langle \boldsymbol{u} \rangle)^2}{2k_B T}\right) \tag{1.3}$$

here n, m, $\boldsymbol{u}$ are the number density, mass and velocity of the particles respectively. The temperature of the distribution is given by T and k_B is Boltzmann's constant. The mean velocity is $\langle \boldsymbol{u} \rangle$.

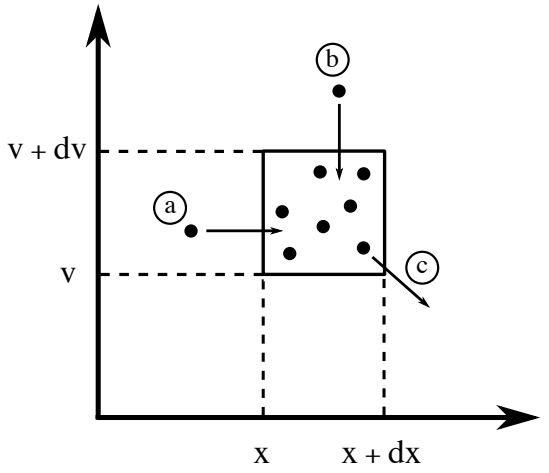

Figure 1.2: Diagram of a 1-d phase space element dxdv. Particle (a) has flows into the element dues to its speed; particle (b) is decelerated into the phase element due to some applied force or collisional scattering; particle (c) leaves the phase element due to its velocity and acceleration components.

The Maxwell-Boltzmann distribution is used widely in technological plasma physics but frequently in the wrong conditions. This type of energy distribution is often assumed in fluid and global models but when there are external forcing this is not appropriate. It requires the assumption that there are no external fields and the particles are in thermal equilibrium; this is rarely true, especially in laboratory plasmas which are electrically driven. There is a distribution function, called the generalised Margenau form [19], which describes the distribution of speeds for electrons in a neutral gas when there is an applied electric field of root-mean-squared amplitude $E_{\rm rms}$ and frequency ω:

$$f_G = Ae^{-W} \tag{1.4}$$

$$W = \int_0^u m_e u \left(k_B T_g + \frac{2e^2 E_{\rm rms}^2}{3m_e(\nu^2+\omega^2)\xi} \right)^{-1} du \tag{1.5}$$

where T_g is the gas temperature, ν is the electron-neutral collision frequency and ξ is the energy loss parameter for electron-neutral collisions.

When the thermal motion of the gas is dominant

$$W = \frac{mu^2}{2k_B T_g} \tag{1.6}$$

and the generalised distribution reduces to a Maxwellian.

Another well known distribution function, a Druyvesteyn distribution function [19], is achieved when the electric field is uniform ($\omega = 0$ and $E = E_{\rm rms}$) and the thermal energy of the gas is negligible compared to the electrons ($k_B T_g \ll 2e^2E^2/3m_e\nu^2\xi$). When the distribution functions are written in terms of kinetic energy, instead of speed, the distributions have the form

$$f(\varepsilon) = c_1 \varepsilon^{\frac{1}{2}} \exp(-c_2 \varepsilon^x) \tag{1.7}$$

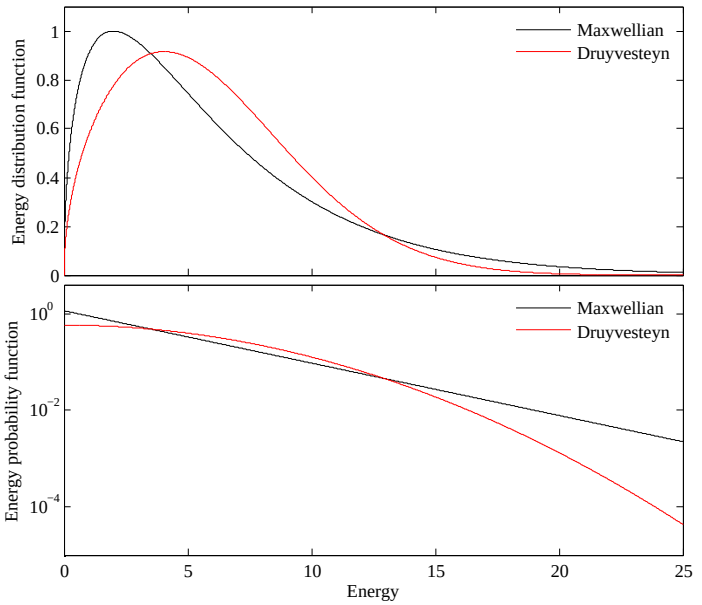

Figure 1.3: Example Maxwellian and Druyvesteyn energy distribution functions and energy probability functions. The top panel corresponds to (1.7). The bottom panel corresponds to (1.11).

where $x = 1$ gives a Maxwellian distribution and $x = 2$ gives a Druyvesteyn. The coefficients c_1 and c_2 can be given by [20]:

$$c_1(x) = \frac{x}{(\frac{3}{2}k_B T_e)^{3/2}} \frac{\Gamma(\zeta_5)^{3/2}}{\Gamma(\zeta_3)^{5/2}}, \tag{1.8}$$

$$c_2(x) = \frac{1}{(\frac{3}{2}k_B T_e)^{x}} \left(\frac{\Gamma(\zeta_5)}{\Gamma(\zeta_3)}\right)^{x}, \tag{1.9}$$

$$\zeta_\alpha = \frac{\alpha}{2x}. \tag{1.10}$$

Examples of the Maxwellian and Druyvesteyn distribution can be seen in the top panel of figure 1.3. An electron population with a Druyvesteyn distribution has fewer high energy electrons than the corresponding Maxwellian distribution and consequently high energy processes, such as ionisation, are less abundant.

The energy probability function is defined as

$$g_p(\varepsilon) = \varepsilon^{-\frac{1}{2}} f(\varepsilon). \tag{1.11}$$

This is defined such that the logarithm of g_p for a Maxwellian probability distribution is linear. The probability functions of a Maxwellian and a Druyvesteyn are plotted in the bottom panel of figure 1.3. Using the energy probability function it is easy, in theory, to deduce whether a plasma is non-equilibrium: if the probability function is not linear in logspace then it is not Maxwellian.

Integrating the distribution function over velocity space, to calculate its various moments, yields the following macroscopic quantities

$$n(\boldsymbol{r},t) = \int f(\boldsymbol{r},\boldsymbol{u},t)\mathrm{d}\boldsymbol{u} \tag{1.12}$$

$$\bar{\boldsymbol{u}}(\boldsymbol{r},t) = \frac{1}{n}\int \boldsymbol{u} f(\boldsymbol{r},\boldsymbol{u},t)\mathrm{d}\boldsymbol{u} \tag{1.13}$$

$$\bar{\epsilon}(\boldsymbol{r},t) = \frac{m}{2n}\int (\bar{\boldsymbol{u}}-\boldsymbol{u})^2 f(\boldsymbol{r},\boldsymbol{u},t)\mathrm{d}\boldsymbol{u} \tag{1.14}$$

$$\boldsymbol{P}(\boldsymbol{r},t) = \frac{1}{n}\int (\boldsymbol{u}-\bar{\boldsymbol{u}})(\boldsymbol{u}-\bar{\boldsymbol{u}}) f(\boldsymbol{r},\boldsymbol{u},t)\mathrm{d}\boldsymbol{u} \tag{1.15}$$

which are the plasma number density, bulk fluid velocity, mean kinetic energy and pressure tensor respectively.

1.3 Collisions

Particle-particle collisions are an important aspect of plasma evolution. The breakdown of a neutral gas to a plasma requires ionisation of the neutral species through collisions. Diffusion is caused by the random walks of particles which are characterised by collisions. The probability of any given collision governs the relative abundance of each species involved in the interaction. In this section the important collision parameters are defined and then the collision operators used to describe the evolution of a plasma are discussed.

1.3.1 Basic collision parameters

Consider a beam of incident particles moving, with speed v and mass m, through a gas of infinitely massive stationary target particles, as in figure 1.4. The flux of incident particles is

$$\Gamma = nv \tag{1.16}$$

where n is the number density of the beam. The number of particles scattered from the beam (dn) through some binary interaction is proportional to: the target density n_t, the distance travelled by the beam dx, the 'size' of the target particles σ and the incident particle number density n. The removal of particles from the beam is

$$dn = -\sigma n n_t dx. \tag{1.17}$$

The target size σ is called the cross-section for the interaction. If we consider the particles to be hard spheres with radii a_1 and a_2 then a simple interpretation of the cross-section is the sum of the hard sphere radii, $\sigma = \pi(a_1 + a_2)^2$. Different types of interactions will have different values of σ. Cross-sections also have a dependence on the relative speed of the interaction particles. The change in flux $d\Gamma$ is

$$d\Gamma = v dn = -\sigma \Gamma n_t dx, \tag{1.18}$$

integrating gives

$$\Gamma(x) = \Gamma_0 e^{-\sigma n_t x}. \tag{1.19}$$

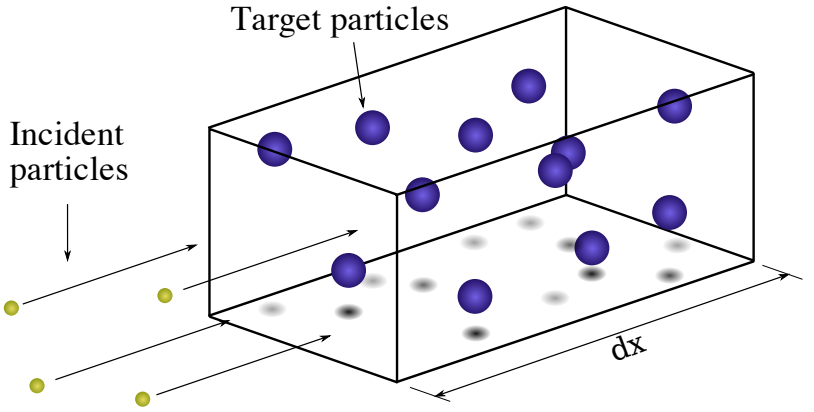

Figure 1.4: Diagram for collision frequency.

For fixed values of σ and n_t, (1.19) shows the beam flux decays exponentially with distance at the rate λ

$$\lambda = \frac{1}{\sigma n_t} \tag{1.20}$$

this decay rate is commonly known as the mean free path. The mean time between collisions τ is

$$\tau = \frac{\lambda}{v} \tag{1.21}$$

where v is the speed of the incident particles. We can now define the collision frequency ν as the number of interactions per unit time

$$\nu = \tau^{-1} = \sigma n_t v. \tag{1.22}$$

The number of collisions N_c occurring in time Δt is

$$N_c = \nu\tau = n_t \sigma v \Delta t. \tag{1.23}$$

For sufficiently small time ($\Delta t < \nu^{-1}$) the probability of a collision P_c can be written as

$$P_c = \nu \Delta t. \tag{1.24}$$

The collision frequency per unit density, or the rate constant K, is

$$K = \sigma v \tag{1.25}$$

1.3.2 Rate coefficients for distributions

The two most commonly used collision parameters are the collision cross-section and the rate coefficient. A reaction cross-section describes an interaction area surrounding the target particle which if intersected by the incident particle will result in a reaction. The cross-section usually has an energy dependence. When the particles involved in a collisional process have a distribution of energies the rate coefficient includes the information from the cross-section and the energy distribution. Often the rate coefficient is pre-determined by assuming an energy distribution, typically a Maxwellian. This makes the rate constant

a function of species temperature. For velocity distributions of the incident and target particles: $f_1(\boldsymbol{v}_1)$ and $f_2(\boldsymbol{v}_2)$, that have been normalised, the rate constant is defined as:

$$K = \int f_1(\boldsymbol{v}_1) f_2(\boldsymbol{v}_2) \sigma(|\boldsymbol{v}_1 - \boldsymbol{v}_2|) |\boldsymbol{v}_1 - \boldsymbol{v}_2| d^3 v_1 d^3 v_2. \tag{1.26}$$

If the incident particle velocities are much larger than the target particle velocities *i.e.* $v_1 - v_2 \approx v_1$ and an isotropic Maxwellian is used to represent the energy distribution of the incident particles

$$f_1 = 4\pi \left(\frac{m}{2\pi k_B T_1} \right)^{3/2} v_1^2 \exp\left(\frac{-m v_1^2}{2 k_B T_1} \right) \tag{1.27}$$

then the rate coefficient is

$$K(T_1) = \left(\frac{m}{2\pi k_B T_1} \right)^{3/2} \int_0^\infty \sigma(v_1) v_1 \exp\left(\frac{-m v_1^2}{2 k_B T_1} \right) 4\pi v_1^2 dv_1. \tag{1.28}$$

Typically measurements of rate constants are fitted to modified Arrhenius form [21]

$$K(T) = K_0 T^n \exp\left(\frac{-\varepsilon}{T} \right) \tag{1.29}$$

or simply Arrhenius form where $n = 0$ in (1.29).

1.3.3 Collision operators

The collision operator is the term in the Boltzmann equation (1.1) that represents the effect of collisions on the distribution function. There is no definitive form for the collision operator that is suitable for every situation. Several possible forms exist and are each suitable under particular conditions.

Boltzmann operator

The Boltzmann collision term is [22–24]

$$\left(\frac{\partial f_s}{\partial t} \right)_c = \sum_j \int \left[f_s(\boldsymbol{u}') f_j(\boldsymbol{u}_j') - f_s(\boldsymbol{u}) f_j(\boldsymbol{u}_j) \right] |\boldsymbol{u} - \boldsymbol{u}_j| \sigma_{sj} d\boldsymbol{u}_j \tag{1.30}$$

where f_j is the distribution function of the target particles, the $'$ denotes post-collision quantities and σ_{sj} is the collision cross section for the interaction between particle types s and j. The integral is summed over all target species to include all collision types. For simplicity $f(\boldsymbol{x}, \boldsymbol{v}, t)$ has been written as $f(\boldsymbol{v})$. The first term in the square brackets represents the particles scattered into the velocity range $\boldsymbol{u}$ to $\boldsymbol{u} + d\boldsymbol{u}$ and the second term gives the particles scattered out of the same velocity range.

The Boltzmann operator requires the assumptions that: all collisions are binary interactions; collisions are uncorrelated *i.e.* the collision does not depend on any previous collision; and each interaction must occur on time- and length-scales smaller than the variations in f_s. The Boltzmann operator fails to recover the physics of many simultaneous weak interactions, such as Coulomb forces, not represented by binary collisions. The Boltzmann operator is appropriate for weakly ionised plasmas where the electrons mostly interact with the neutral species.

Fokker-Planck operator

An operator which treats weak interactions more simply than the Boltzmann operator, is the Fokker-Planck operator. This operator uses a probability function $\psi(\boldsymbol{u}, \Delta\boldsymbol{u})$ to describe the probability that a particle with initial velocity $\boldsymbol{u}$ gains a velocity increment of $\Delta\boldsymbol{u}$ after many weak interactions in time Δt. The probability function depends on the time step Δt but must not depend on any other elapsed time. The distribution function f of the particles can be written as

$$f(\boldsymbol{r}, \boldsymbol{u}, t) = \int f(\boldsymbol{r}, \boldsymbol{u} - \Delta\boldsymbol{u}, t - \Delta t)\psi(\boldsymbol{u}, \Delta\boldsymbol{u}) d(\Delta\boldsymbol{u}). \tag{1.31}$$

This simply states that the distribution function f at time t is the sum of all the particles scattered into the phase space element $(\boldsymbol{r}, \boldsymbol{u})$ by the collisional process represented by ψ during a time Δt. If the velocity increment $\Delta\boldsymbol{u}$ is small then the initial distribution function, $f(\boldsymbol{r}, \boldsymbol{u} - \Delta\boldsymbol{u}, t - \Delta t)$, can be approximated using a Taylor series expansion. Writing only the first two terms we have:

$$f(\boldsymbol{r}, \boldsymbol{u}, t) \approx \int \left[f(\boldsymbol{r}, \boldsymbol{u}, t - \Delta t)\psi - \Delta\boldsymbol{u} \cdot \frac{\partial}{\partial \boldsymbol{u}}(f\psi) + \frac{1}{2}\Delta\boldsymbol{u}\Delta\boldsymbol{u} : \frac{\partial^2}{\partial \boldsymbol{u}\partial \boldsymbol{u}}(f\psi) \right] d(\Delta\boldsymbol{u}) \tag{1.32}$$

where ':' denotes the dyadic product. After integration the first term in the square brackets has no dependence on $\Delta\boldsymbol{u}$ since ψ is a probability and it integrates to one over the range of $\Delta\boldsymbol{u}$. Taking this term to the left hand side gives the difference between the distribution function at time $t - \Delta t$ and t. If this change in the distribution function is assumed to be due to the collisions then we can call it a collision operator, known as the Fokker-Planck equation:

$$\left(\frac{\partial f_s}{\partial t}\right)_c = -\frac{\partial}{\partial \boldsymbol{u}} \cdot (f\langle\Delta\boldsymbol{u}\rangle) + \frac{1}{2}\frac{\partial^2}{\partial \boldsymbol{u}\partial \boldsymbol{u}} : (f\langle\Delta\boldsymbol{u}\Delta\boldsymbol{u}\rangle) \tag{1.33}$$

where

$$\langle\Delta\boldsymbol{u}\rangle = \frac{1}{\Delta t}\int \psi\Delta\boldsymbol{u}\, d(\Delta u) \tag{1.34}$$

$$\langle\Delta\boldsymbol{u}\Delta\boldsymbol{u}\rangle = \frac{1}{\Delta t}\int \psi\Delta\boldsymbol{u}\Delta\boldsymbol{u}\, d(\Delta u). \tag{1.35}$$

The first term on the right hand side of (1.33) is called the coefficient of dynamical friction, this gives the deceleration of the particle velocities due to collisions. The second term, called the coefficient of diffusion, describes the spreading of the particles in velocity space. The key parameter determining the physical effect of the Fokker-Planck operator is the probability function ψ. Rutherford scattering is often used as a physical model for determining the probability function.

The Fokker-Planck operator is only suitable in certain conditions, it requires that all collisions result in only small velocity changes. Any large velocity changes must be due to the accumulated effect of many small changes. This means the plasma density must be much higher than the neutral density as electron-neutral collisions can result in large angle scattering. For weakly ionised low temperature plasmas the Fokker-Planck formalism may not be suitable.

Krook operator

A simple collision operator is derived [19] from the assumption that the distribution function is not far from equilibrium. We can write

$$\left(\frac{\partial f_s}{\partial t}\right)_c = \frac{f - f_0}{\tau} \tag{1.36}$$

where f_0 is the equilibrium distribution function and τ is a characteristic time for collisions, such that the collision frequency can be written as $\nu = 1/\tau$. Equation (1.36) is called the Bhatnagar, Gross and Krook (BGK), or simply the Krook, collision model.

The Krook operator can be used to determine several useful transport properties such as: plasma conductivity, electron mobility, diffusion coefficient, thermal conductivity and coefficient of viscosity. However these are fairly general diagnostics and do not help in understanding the underlying physical processes at work in the plasma. The Krook collision model is not guaranteed to conserve particle number, momentum or energy. It is a good approximation for electron interacting with large stationary particles, neutral species for example.

1.4 Modelling

The subsequent chapters of this thesis will involve the application of modelling techniques used in plasma physics. In this introductory section the different computational methods used to model plasmas will be discussed: basic principles and the main equations will be presented; the validity of the assumptions will be discussed; and some comparisons of model to experiment will be surveyed.

1.4.1 Kinetic

The most thorough models of plasmas are kinetic models where the particle kinetics are calculated using the Boltzmann equation (1.1). Each species is represented by a distribution function. One method of evaluating the kinetic equations is referred to as the Convected Scheme [25–27]. Particles are moved across a mesh in phase space according to their initial position and velocity, electromagnetic fields, and collision probabilities. In some cases the governing equations are evaluated using propagator matrices [28]. These matrices represent the application of many finite difference iterations. The motion of particles is calculated in two parts: evaluation of the collisionless motion and the collisional effects.

The Boltzmann equation is often solved to determine transport coefficients and reaction rates for use in fluid simulations. BOLSIG+ [29] is one such Boltzmann solver. The solver is general enough to simulate different discharge conditions. Inputs include: reduced electric field, ionisation fraction, gas mixture and frequency of the applied field. Several key assumptions are made to make the solution of the Boltzmann equation fast and self-consistent within the chosen parameter range: the electric field and collision probabilities are assumed to be spatially uniform; the distribution function is approximated by a two-term Legendre polynomial; and an exponential growth model is used to model changes in the electron number density due to ionisation or attachment. The transport coefficients and reaction rates calculated in the Boltzmann solver are often used in fluid models.

Discussion

Boltzmann's equation (1.1) is too complex to solve numerically. Assumptions, such as those employed in BOLSIG+, must be made to reduce the complexity. Particle-in-Cell methods (see section 1.4.4) are often used to simulate effects only apparent in the kinetic regime.

1.4.2 Fluid

The fluid equations are constructed by taking moments of the Boltzmann Equation (1.1). The zeroth, first and second moments are

$$\frac{\partial n_s}{\partial t} + \nabla \cdot (n_s \bar{\boldsymbol{u}}_s) = S \tag{1.37}$$

$$n_s m_s \left(\frac{\partial}{\partial t} + \bar{\boldsymbol{u}}_s \cdot \nabla \right) \bar{\boldsymbol{u}}_s + \nabla p_s - n_s q_s (\boldsymbol{E} + \bar{\boldsymbol{u}}_s \times \boldsymbol{B}) = \pm \boldsymbol{K} \tag{1.38}$$

$$\frac{\partial}{\partial t} \left(n_s \frac{1}{2} m_s \bar{u}_s^2 \right) + \nabla \cdot \left(n_s \frac{1}{2} m_s \bar{u}_s^2 \boldsymbol{u}_s \right) - n_s e \boldsymbol{E} \cdot \bar{\boldsymbol{u}}_s = \pm \boldsymbol{H} \tag{1.39}$$

where $\boldsymbol{K}$ and $\boldsymbol{H}$ represent the momentum and energy exchange between species and S is a source term describing the creation and destruction of particles of a given species. The Lorentz equation has been substituted for the acceleration

$$\boldsymbol{a}_s = \frac{q_s}{m_s} (\boldsymbol{E} + \boldsymbol{u}_s \times \boldsymbol{B}). \tag{1.40}$$

The zeroth moment (1.37) describes the particle conservation, the first moment (1.38) gives the conservation of momentum and the second moment (1.39) describes the energy conservation.

Examining the fluid equations presented above, equations (1.37-1.38), it becomes clear that this system of equations is not closed. Each moment depends on a higher order moment, for example the zeroth moment (1.37) requires the mean speed which is calculated in the first moment (1.38).

There are two basic strategies for closing the system of fluid equations: truncation or asymptotic closure. Truncating the system of equations is achieved by assuming some higher order moment vanishes or that it can be expressed empirically in terms of some lower moments. For example, the heat tensor can be assumed to be zero and the pressure tensor to be isotropic, this is equivalent to neglecting viscosity. An asymptotic closure method attempts to make assumptions about a particular parameter, assuming the functional form of the distribution function for example. The different choices for closing the fluid equations means that all fluid models do not conform to the same basic system of physical equations.

One common assumption is made when the timescale for momentum transfer collisions is much shorter than the timescale for variation in the electric field, this is called the drift-diffusion approximation. This approximation means that the inertia of charged particles is neglected and consequently their mean velocities respond instantly to the electric field. The mean particle fluxes are determined by adding a diffusion term due to spatial density gradients and a drift term for the charged particles due to the electric field. Thus the expression for momentum conservation 1.38 can be replaced with:

$$n_s \bar{\boldsymbol{u}}_s = -\mu_s \boldsymbol{E} - \nabla (n_s D_s) \tag{1.41}$$

where

$$\mu_s = \frac{e}{m\nu} \tag{1.42}$$

$$D_s = \frac{k_B T}{m\nu} \tag{1.43}$$

are the mobility and diffusion coefficients. These coefficients can be assigned from tabulated data, calculated using a Boltzmann solver or the Krook operator, as discussed previously.

Discussion

The mathematical framework of fluid modelling is not fixed since there are a variety of strategies for closing the fluid equations. For example the number of moments of the Boltzmann equation to be solved varies between models. Often the underlying distribution function is assumed to be Maxwellian. Assuming the velocity distribution means that fluid models cannot reproduce the full kinetic behaviour of the particles. Fluid models are best applied to situations where there are many collisions between particles. Despite their inability to reproduce certain physics fluid models can still achieve comparable results to particle models [30] and are often used because they are less computationally demanding and provide quantitative results.

Comparison to experiment

Fluid models are used widely in the simulation of plasma, including: plasma display cells [31; 32], lighting [33] and low pressure systems [34–36].

When compared to experiment, fluid models often manage to recreate trends but they are not able to make qualitative predictions, as seen in [32; 34–36]. The disagreement between simulation and experiment could be related to the assumptions made. Electron energy distributions are often assumed to be Maxwellian but in low temperature plasmas this rarely the case and may be a source of discrepancy [34]. In other cases it has been shown that removing some common assumptions, such as the drift-diffusion approximation, can result in better predictions of experiment [35].

1.4.3 Global models

Plasma models where the spatial variation is assumed are called global models [20; 37–40]. This does not necessarily mean that the plasma is spatially uniform; often analytically determined functions are used to define the spatial variation [41; 42]. Global or zero-dimensional models are typically used to simulate situations where the gas chemistry is complicated. Models where many chemical reactions are included are sometimes, confusingly, called kinetic models but they should not be confused with models that calculate the evolution of distribution functions as described previously.

Basic algorithm

When the spatial dependence is removed the number of governing equations is, in general, reduced to two: a particle balance and a power balance equation. Each species included in the simulation will require its own particle balance equation which describes the rate of change of any particular species due to various reactions and system losses. Particle balance equations generally take the form,

$$\frac{dn_k}{dt} = S_k - W_k + \sum_{i=1}^{N_k} a_i K_i \prod_{j}^{M_i} n_j \tag{1.44}$$

where n_k is the particle density, S_k is the mass flow rate in and out of the vessel, W_k represents the loses to the walls, N_k is the number of reactions, a_i is the number of particles lost/gained per collision, K_i is the rate constant, M_i is the number of reactants, n_j is the number density of the j^{th} reactant, this includes the incident species.

Each species, at least the electrons, is also subject to a power balance equation; this describes the energy a species gains or loses due to external forcing or collisions. The external forcing term can be used to describe the effects of different driving systems.

Discussion

Global models are much less computationally intensive than fluid or particle models, this makes them quick to execute and a good choice for a first approximation of a plasma system.

The distribution function of the particles is generally assumed and in most cases it is chosen to be Maxwellian. With a fixed distribution it is often the variation in temperature that is calculated and subsequently used to determine the rate coefficients from temperature dependent functions. Changing the underlying distribution function can make an important difference [20].

The spatial structure of the plasma can be inferred when a density profile is available. These profiles are usually calculated analytically and are subject to their own assumptions. The profiles are scaled using the densities resulting from the global model. Alternatively the temporal evolution of a point in the plasma can be simulated [43]. Density profiles are based on equilibrium and are not suitable for use with temporal evolution.

Comparison to experiment

Due to their relative simplicity, global models are often used as a first attempt at describing plasma systems. They are able to give information on volume-averaged densities and the temperatures of species. Comparing the results of global models with experimental results shows that global models are capable of predicting trends [38–40; 42] in parameter space but can easily be an order of magnitude out [44].

1.4.4 Particle-in-Cell

Ideally a plasma simulation would calculate the trajectories and collisions of every particle. However, the densities of species in almost all systems mean this is computationally impossible. Agglomerating many particles into "super-particles" is a technique used to simulate large numbers of particles. Super-particles are often used to represent $10^3 - 10^6$ real particles. These super-particles are governed by the Lorentz equation and the fields are solved self-consistently with Maxwell's equations. This simulation strategy is called Particle-in-Cell (PiC). Collisions are simulated using Monte-Carlo schemes.

History

The history of Particle-in-Cell modelling is outlined by Birdsall [45]. One of the very first one-dimensional calculations of self-consistent fields and particle trajectories was carried out by hand in the 1940's by Hartree and Nicolson. They were investigating charge flow in vacuum tubes.

Digital computers were introduced in the 1950's and the existing methodologies were applied to computer simulations. One of the first computer based models was written by Tien and Moshman [46] in 1956. They modelled a high-frequency diode in one-dimension using 360 sheets of electrons over approximately 3000 time steps. The simulation solved the trajectories, fields and even calculated some emission statistics using a Monte-Carlo method. They were successful in reproducing experimental observations.

Perhaps one of the most important steps was taken by Dawson [47] in 1962. A one-dimensional model of warm electrons in a static ion background was used to investigate the thermalisation and statistical properties of a plasma. The important conclusion of the work was that theoretically-determined kinetic behaviour could be reproduced with small numbers of particle sheets.

The next decade saw the introduction of particle weighting and mesh-based Poisson solvers. This reduced the computational load required by the solution of the electric fields and eventually led to two- and three-dimensional models. In the 1980's the PiC (also called cloud-in-cell) strategy was formalised in the texts by Birdsall & Langdon [48] and Hockney & Eastwood [49] [1]. These remain two of the most comprehensive treatments of PiC theory. To the present day PiC models have become more sophisticated by including aspects such as external circuits, realistic collision cross-sections and parallelisation to run on large numbers of computers.

Basic algorithm

In this type of model the particle positions are allowed to be continuous inside the computational domain. Electric and magnetic fields are typically calculated on rectangular or triangular grids as mesh-based solvers are generally less computationally demanding compared to other N-body methods. Particles are weighted to the grid to give charge and current densities and the electric and magnetic fields are calculated from these properties.

[1] The two texts ([48; 49]) cited here are not the first editions of the relevant books.

The choice of weighting scheme is important; different methods offer different computational efficiency and numerical accuracy. Linear interpolation is the most common weighting technique. The force at any given particle position is interpolated from the grid values. The particles can then be moved and collisions calculated, returning to the start of the computational cycle. This cycle is shown in figure 1.5.

Monte-Carlo schemes [24] compare the collision probabilities (see (1.24)) and random numbers to decide what collisions, if any, occur in in a given time step. The details of one such Monte-Carlo scheme are given in chapter 5.

Discussion

Large numbers of particles are required to effectively sample the distributions [50]: *e.g.* a Mawellian distribution of 2eV has ten thousand less particles at 20eV than at 2eV but it is important to represent these high energy electrons because the ionisation occurring due to the high energy tail of a low energy distribution could play a significant role. This demand for large numbers of particles tends to make PiC simulations more computationally intensive than fluid models.

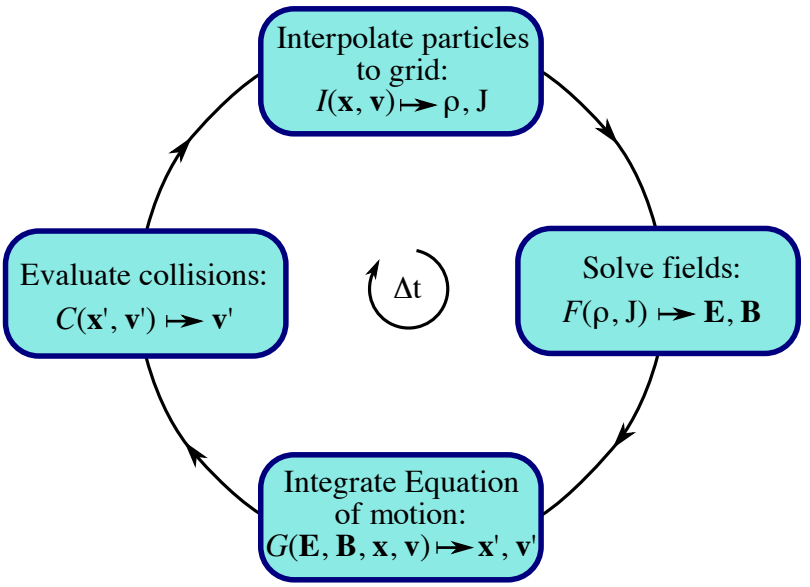

Figure 1.5: Diagram showing a typical particle-in-cell time step. Interpolation (I) is typically the first step of the cycle, particle positions ($\boldsymbol{x}$) and velocities ($\boldsymbol{v}$) are weighted to the grid to give the charge (ρ) and current ($\boldsymbol{J}$) densities. These mesh properties are used in the next step to calculate the electric ($\boldsymbol{E}$) and magnetic fields ($\boldsymbol{B}$), denoted here by the function F. These fields are then used to integrate the equations of motion (G), giving updated particle positions and velocities. The final operation in the cycle involves calculating the effects of any collisions, represented here by the function C.

Representing the plasma as particles and using the Lorentz equation to describe their motions raises the problem of time scales. It is obvious that the electrons respond to applied fields and collisions on a much shorter time scale than the heavier ions and neutral species. It is inefficient to update the trajectories of the heavier species at the same rate as the electrons. A technique called time-cycling, or subcycling, [48] is common where the ions are updated on a different, longer timestep than the electrons.

Statistical noise [50] associated with PiC models can result in the non-physical heating, or cooling, of particles. For N particles the noise is proportional to $1/\sqrt{N}$. The number of particles in a given cell must be large enough to ensure that the statistical noise is negligible compared to any applied fields.

Even though PiC models tend to be more expensive computationally than fluid models they are frequently used to model plasmas as they can recreate kinetic effects that are inaccessible in the fluid regime. For example, striations in plasma display cells can be recovered in particle models but are smoothed out in fluid models [51].

Comparison to experiment

The configuration of any individual PiC model varies between implementation; some include representations of the external circuitry, surface processes, extensive chemistry sets or a mixture of aspects, mostly depending on the physical situation of interest. Particle-in-cell models have proved to be a useful tool and have recreated experimental behaviour. The formation of bi-Maxwellian electron energy distributions at low pressure through stochastic heating was experimentally reported [52] and reproduced numerically through PiC simulation [53].

Often it is difficult to compare data from experimental diagnostics with simulation results. O'Connell *et al.* [54] compared simulated and experimentally measured ion energy distributions. The aperture, transmission efficiency and signal attenuation of the diagnostic probe was considered before comparing the energy distributions. Qualitative agreement between experiment and simulation was achieved, the initial conditions were thought to be responsible for the discrepancy.

Plasma modelling is often able to recreate trends and qualitatively agree with experiment [55–58] but exact agreement with experimental results is rare.

1.4.5 Hybrid

A hybrid model is a model constructed using elements of different computational methods. Usually fluid and particle models [59–64] are combined but other combinations exist such as coupling global and fluid models [65]. The aim of combining different methods is to take the best aspects of each method. Combining the kinetic effects recovered by particle models and the execution speed of fluid models is a desirable prospect. The models are combined by selecting some particles to be modelled as a fluid and others as particles. There are many different choices for separating the particles, strategies include: particular ions and fluid electrons [64]; fluid ions and electrons, except the high energy electrons which are treated as particles [61]; or a fluid model with transport coefficients calculated by a particle model [59; 62].

History

The first hybrid model was constructed by Lee and Birdsall [66] in 1979 to investigate instabilities of ring shaped distributions in velocity space. A particle code was used to simulate particles from the ring and a fluid was used to represent the background plasma. The model was motivated by previous results from a noisy particle model where the instability was obscured by the background plasma.

The hybrid technique went mostly unused for more than a decade and it was the early 90's when hybrid models were investigated further [59; 62; 64]. This renaissance stemmed from multi-beam models [61; 67] where fluid species were split into separate energies which led quickly to hybrid models.

Basic algorithm

Obviously the nature of hybrid models means that a canonical algorithm cannot be given. Any hybrid method borrows from the techniques which have been discussed previously and they can be cannibalised accordingly. Care must be taken when combining the two methodologies especially with regard to the time steps; particle and fluid models have very different time step requirements.

The most common hybrid method is when the transport coefficients for a fluid model are calculated using a particle model. This technique is discussed by Sommerer and Kushner [59] and is outlined here. There are three parts to this particular model: a fluid model; a Monte-Carlo simulation; and a neutral chemistry and transport model. The fluid model calculates the spatial dependence of the density and electromagnetic fields. It is the fluid model which calculates the time-dependent behaviour of the system. The other parts provide data for the fluid model. The Monte-Carlo model simulates the evolution of the electrons with regard to the conditions, such as density and fields strengths, calculated by the fluid model. From this calculation the current excitation rates and transport coefficients are determined and used in the other parts of the model. The final part, the neutral chemistry and transport module updates the neutral density depending on diffusion, gas phase chemistry and surface chemistry.

Comparison to experiment

The quality of results from hybrid models can vary due to the different methods used. Hybrid models can suffer from poor assumptions about transport coefficients [68]. Hybrid models have been used in a wide range of situations and comparison to experiment has resulted in qualitative agreement, similar to PiC models [60; 63; 65; 69; 70].

1.4.6 Summary

Each modelling methodology has its own merits and disadvantages. Techniques predicting averaged parameters, such as global and fluid models, have short execution times but may smooth out important physical processes. Particle-in-cell models tend to capture the essential kinetic effects but at the cost of computational loads.

For some parameters, fluid models can produce very similar results to their kinetic counterparts [30], the discrepancy an acceptable cost of the reduced computation time. Global models can only provide volume-averaged properties, which may be sufficient for the case in hand. They are mostly used in systems where there are complicated gas mixtures and chemistries. If kinetic effects are not important in the physical system then fluid and global models are effective techniques.

Particle-in-cell models are the closest computational models to a full kinetic solution. These models require large numbers of particles to remain statistically sound, making them computationally expensive. Convected Scheme models have not been used extensively. When kinetic effects are important PiC models have been favoured over Convected Schemes.

Incorporating a kinetic aspect to a fluid model means that hybrid models can predict effects that are not recovered by standard fluid models. Results from hybrid models can be qualitatively similar to those of PiC model [50; 68] but computation time can be an order of magnitude less, making hybrid modelling an attractive option.

In an effort to compare the different models discussed here several groups applied their models to a standard problem [71]: a 1-d capacitively coupled RF system. There was good agreement between the particle and hybrid models. Comparing these models to a Convected Scheme showed discrepancies in the electron density and mean energy but other parameters compared well. Separate implementations of fluid models showed greater disparity than the kinetic-like models, particularly at low pressure. Variations of around 50-60% were seen in some parameters while others compared well to their kinetic counterparts.

In an ideal world there would be a single plasma model which given the physical and electromagnetic field boundary conditions of the system would calculate the trajectories of every particle, characterising the system completely. Obviously this is not currently possible. This is actually a blessing in disguise for the plasma modeller as their role in science would be made redundant!

Not only is the exact solution not available, there is no single modelling technique with the 'best' approximations. In modelling a plasma questions must be asked about the plasma: are the assumptions of the modelling technique valid? What level of accuracy is required? What computational resources are available?

With the increase in computational power and the development of modelling techniques, it may be pertinent to ask the question: Will plasma modelling become a precision science, and if not, why not? This is not a question this thesis aims to answer; the modelling carried out in the subsequent chapters aims to isolate the essential physics and develop understanding of these aspects. With all the simulations studies discussed here there are few quantitative predictions. This may be due to the type of model used or the assumptions made but perhaps not all the blame can be laid at the feet of the modeller.

The output of a simulation is only as good as its input. Cross-sections are an important input but they can be subject to large uncertainties and are unknown for many reaction types. Uncertainties in the values of cross-sections are not always given and when they are they can be estimated to be as much as 20-30% [72].

Another source of error may be in the experimental measurements themselves. Typically diagnostic probes do not directly measure useful plasma properties, such as number

densities or temperature. The physics of the interaction between the plasma and the probe must be assumed. Langmuir probe uncertainties can be around 20% [73].

1.5 Outline of thesis

The aim of this thesis is to investigate basic physical processes occurring in various low temperature plasmas. Isolating and modelling the essential features will lead to a better understanding of the plasmas. This introductory chapter gives a brief overview of low temperature plasmas and the physical, mathematical and computational techniques used to describe them. The subsequent chapters of this thesis contain more detailed discussion and examples of the the physical and technical aspects covered in relative brevity in the introduction.

Chapter 2 investigates a plasma instability found in industrial plasma discharges. Details of the experimental observations are summarised and the existing models are discussed. The stability of the competing chemical reactions is explored using equilibrium analysis. Then an un-considered physical process that could explain the instability is offered. The instability relies on the plasmas transparency to the electric field. When the plasma frequency is less than the driving frequency the electric field can penetrate deeper into the plasma and energise the electrons. If the plasma frequency is greater than the driving frequency, the electric field is excluded from the plasma. The plasma frequency is dominated by the electron density, which evolves under the competition of attaching and detaching reactions. To test this physical model a zero-dimensional model is constructed. The results of the simulation are compared those of an experiment in molecular Oxygen gas. Further simplification of the numerical scheme results in an analytic expression for the instability period. This expression is used to calculate the instability period for a molecular Oxygen discharge and the results are compared to experiment.

In the following chapters two- and three-dimensional particle models are used to investigate two different plasmas. The particle model is introduced in chapter 3. The construction of the particle model is given and the required numerical techniques are presented. The two most important components: the potential field solver and the Monte-Carlo collision routine are discussed in detail in chapter 4 and chapter 5 respectively.

In the particle model Poisson's equation is solved to find the electric potential resulting from the charged species in the domain. Chapter 4 shows how the finite difference approximation can be used to solve Poisson's equation on a mesh. A fast solution algorithm, called Multigrid, is introduced. This iterative solution method uses many grids, of different resolutions, to smooth the error on all spatial scales. The main components: grid transfer and smoothing operators are described. A series of tests are carried out to determine the most efficient configuration of the Multigrid solver. Then the accuracy of the solver is investigated.

The occurrence of collisions in the particle model is calculated using a Monte-Carlo technique. The method used in the particle model is detailed in chapter 5. A basic process for the selection of collisions is described. Several techniques to increase the efficiency of the process are described. The most efficient implementation is determined by comparing different combinations of the techniques. The validity of the methods is also examined.

In chapter 6 the particle model is used to simulate the initial stages of breakdown in an atmospheric pressure gas. The evolution of the plasma species from a single electron-ion pair in a uniform electric field is calculated. The effect on the metastable production due to the reversal of the electric field is investigated. Results from calculations in two and three dimensions are presented.

The particle model is then used, in chapter 7, to investigate the Critical Ionisation Velocity phenomena. When a neutral gas streams across a magnetised plasma the ionisation rate increases rapidly if the speed of the neutrals exceeds a critical value. The phenomena is reproducible for different gas species and experimental systems. Collisions between neutrals and positive ions create pockets of unbalanced negative charge. The electrons in these pockets are accelerated by the potential field and can reach energies capable of ionisation. The evolution of one such electron overdensity is simulated under different magnetic field and density conditions.

Finally, chapter 8 gives an overview of the work presented in this thesis and proposes how it can be extended.

Chapter 2

Electronegative Instability

2.1 Introduction

Low pressure discharges are used in many technological plasma processes, such as etching and deposition. Gases with high electron affinities, termed electronegative gases, such as Chlorine and Sulfur Hexafluoride (SF_6) are often used as working gases in these industrial processes. The homogeneity of the plasma in these applications is very important for yield and quality. Periodic variations in plasma species number densities, plasma potential, light emission and plasma size have been reported in the literature [43; 74–83]. Reports of the instability in the literature are summarised in section 2.1.1 and table 2.1. Section 2.1.2 contains a summary of the existing explanations of the instability and numerical models of the instability. Unstable behaviour resulting from the competition of chemical reactions is investigated in section 2.2 using equilibrium analysis. In section 2.3 a new physical mechanism responsible for driving the oscillations is discussed. The validity of the mechanism is investigated by constructing numerical and analytic models of the system in section 2.4 and 2.5. Comparison between experimental results and simulation are made.

2.1.1 Reports of the instability

Tuszewski 1996

Instabilities in electronegative discharges were first reported in 1996 by Tuszewski [78]. Experiments were carried out with a cylindrical inductive plasma source driven at 0.46MHz. Figure 2.1(a) shows a diagram of the plasma source which is attached to a vacuum vessel 1.2m in length. Periodic variations in the ion current were measured, by a Langmuir probe, in the vacuum vessel away from the plasma source. The oscillations occured when electronegative gas mixtures (Ar/SF_6, O_2) were used in the discharge; electropositive gases (N_2, Ar) did not produce similar phenomena in the power and pressure regimes investigated. For 300W of power and a pressure of 1mTorr instability frequecies of 10kHz and 4kHz were reported for Oxygen and Ar/SF_6 mixtures respectively. The Oxygen discharge

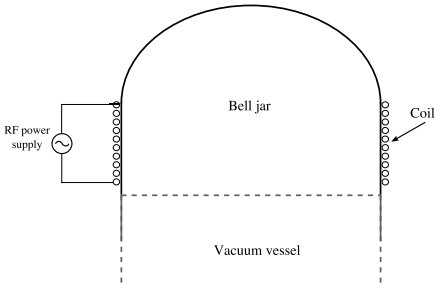

(a) Diagram of cylindrical ICP set-up. The plasma is created inside the bell jar between in the coil region. The plasma is allowed to propagate into the vacuum vessel. The size of the vacuum vessel may vary between discharge configurations. Measurements of the plasma are typically made in the vacuum vessel region.

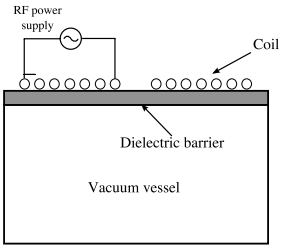

(b) Diagram of planar ICP set-up.

Figure 2.1: Diagrams of cylindrical and planar configurations for inductively coupled discharge systems.

exhibited the instability between pressures of 0.3–2.5mTorr and the frequency decreased with pressure. Ar/SF_6 was unstable between 0.5 and 3mTorr and exhibited the same pressure dependence.

The frequency and amplitude of the oscillation showed no dependence on the power, except in the capacitive to inductive transition region. Modulations in the probe current of 10–50% were reported. The author suggested that the instability measured in the vacuum vessel was driven by an instability near the plasma source. It was later revealed that there are two instabilities occurring in this type of discharge system: a source instability and a downstream instability [84]. The downstream instability occurs in a different power-pressure regime and has frequencies which are typically an order of magnitude less than the source instabilities. The downstream instability is discussed further in the following articles [80; 81; 85]. The source instability is the focus of the work in this chapter.

Lieberman, Lichtenberg and Marakhtanov 1999

Lieberman *et al.* investigated the instability, reported in [78], in a discharge system with a planar coil (a schematic diagram of the system can be found in figure 2.1(b)) driven by a 100–1000W power source at 13.56MHz. The discharge could be driven in two different modes: capacitively, where the power and the plasma density are low; and inductively, where the power and the plasma density are high. As with the experiment of Tuszewski [78] electronegative gases exhibited an instability. Langmuir probe and optical emission measurements were used to measure variations in the charged particle densities, electron temperature and plasma potential. The instability was confined to a well-defined power and pressure regime (320–600W and 4–8mTorr for SF_6). A range of frequencies between

1 Hz and 900kHz were recorded with modulations of up to 100% in the current to an unbiased probe.

Chabert, Lichtenberg, Lieberman and Marakhtanov 2001

Chabert *et al.* [43] used a similar discharge system to Lieberman *et al.* [82] with a power range of 0–900W and a pressure range of 1–100mTorr. SF_6 and Ar/SF_6 gas mixtures were investigated with Langmuir probe measurements and optical spectroscopy of Argon and Fluorine. The matching system of the discharge was set to minimise the average reflected power. Varying the matching conditions was found to alter the instability frequency, substantially in certain situations: pure SF_6 discharges showed variations of $\sim$20% in the instability frequency; and Ar/SF_6 mixtures showed $\sim$800% variation in the frequency when the tuning of the matching network was varied between inductive and capacitive modes. A well defined power-pressure range was found and the addition of Argon in the gas mixture reduces the maximum power capable of producing the instability. The frequency of the instability showed a clear dependence on pressure; the frequency increased with increasing pressure. There was not a strong dependence on the applied power. The low frequency oscillations were observed to have large amplitude modulations, while at high frequency modulations of the light intensity were smaller. The periodic variations of the electron, positive ion and negative ion were in phase, *i.e.* the electron and ion number densities were at a maximum at the same time.

Corr, Steen and Graham 2003

Corr *et al.* [75] investigated the instability in a GEC reactor (planar coil) driven at 13.56MHz with Oxygen gas. A pressure range of 1-100mTorr was investigated with optical emission and Langmuir probe measurements. At a pressure of 11mTorr and power 238W an instability frequency frequency of 10kHz was measured.

The frequency showed a clear pressure dependence of increasing frequency with increasing pressure but little dependence on the applied power. The amplitude of the oscillations varied with the pressure and decreased with increasing power; variations of up to 40% were measured. As with previous experiments there was a well defined power-pressure regime.

Time delayed measurements of the particle species density were made at 10μs intervals spaced to sample the instability cycle. The time resolved measurements of the particle number densities showed that the periodic variations in the negative ion density were anti-correlated with the electron and positive ion number densities.

Marakhtnov et al. 2003

Stable and unstable discharges in SF_6 and Ar/SF_6 were investigated to provide plasma parameters for a numerical model. A planar coil ICP with a 2kW power supply at 13.56MHz was used. As with previous work the instability frequency increased as the pressure increased. A dependence on the gas flow rate was found; increasing the flow rate increased the instability frequency.

Goodman and Benjamin 2003

Goodman and Benjamin investigated the use of a feedback mechanism to remove the unstable behaviour. A variety of RF driving frequencies were used to drive a planar coil. Instabilities were found in pure SF_6, CF_4 and O_2 and mixtures of these gases with Argon. Two instability types were identified: a bursting relaxation mode ('B-mode') and a quasi-steady oscillatory mode ('O-mode'). The B-mode exhibited as a rapid ($< 1\mu s$) brightening of the optical emission which decayed to the previous brightness after $1\mu s$. The period was varied by adjusting the power or pressure but was typically in the range 10 to 50kHz. The O-mode in a lower frequency range of 200Hz to 1kHz. Both instability modes could be stabilised or reduced under some conditions by increasing the RF power when the ion saturation current increased. The authors suggested that if the instability was controllable the variations in electron temperature and ion energy could be advantageous in certain plasma processes; the instability would cause an environment similar to a pulsed discharge.

Descoeudres, Sansonnens and Hollenstein 2003

Instabilities in electronegative discharges have also been found in purely capacitively coupled plasmas [74]. A RF power source applying up to 100W at 13.56MHz was used to investigate discharges of O_2, CF_4 and SF_6 in the pressure range 70-300mTorr. Instabilities in O_2 and CF_4 were observed but SF_6 remained stable in all investigated conditions. As with previous reports the instability was confined to a well defined power range and was present above a threshold for pressure: 146mTorr for O_2 and 75mTorr for CF_4. The frequency of the variations in O_2 at 188mTorr was ~ 3.5kHz; in CF_4 at 188mTorr the frequency was ~ 80kHz. The oscillations in voltage, light emission and ion flux were synchronised. When Argon was added to each discharge (O_2, CF_4), increasing the Argon concentration resulted in a decrease in the amplitude of oscillations.

Corr 2003 (Thesis)

The instability is also observed as a spatial movement of the edge plasma emission (figure 2.2): the plasma is observed to be alternately expanding and contracting on a timescale of 100μs, for an Oxygen plasma at 13mTorr.

Corr, Steen and Graham 2005

Corr *et al.* carried out experiments in a planar ICP filled with various Ar/Cl concentrations. The system was driven at 13.56MHz. Two phenomenologically different instabilities were reported. When fully matched, the instabilities were similar to those reported in Corr 2003 [75]. Periodic bursts were also found to exist under certain matching conditions. When the system was fully matched the authors were not able to produce unstable behaviour in pure Ar or pure Cl mixtures. Chlorine concentrations of 30–60% produced unstable behaviour. The instability was found to exist in a specific power (70–300W) and pressure range (4–24mTorr) with frequencies between 20 and 520Hz. The variations in light emission; electron density; and negative and positive ion densities were observed to be in phase.

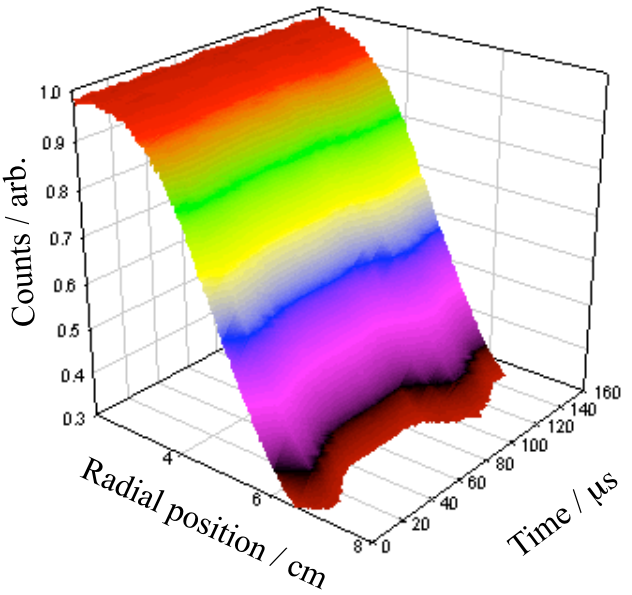

Figure 2.2: Spatial and temporal variation of emission at 844nm through one oscillation period in molecular Oxygen at 13mTorr and 275W. [86]

Soberon et al. 2006

A detailed study of the matching network operating on a Cl/Ar discharge identified several different instabilities: an instability as discussed previously in the kilohertz range where the incident and reflected powers do not affect the frequency; a larger amplitude modulation with frequencies around 10–100Hz, which occurs alongside modulations in the reflected power; a relaxation modulation of the RF generator, the reflected power increases to a preset maximum the generator then reduces its power output, reducing the reflected power, the generator power drops to a value where it will attempt to deliver the set power; and a self-pulsing sub-hertz instability where the discharge drops into a low density, cool state and then returns to the previous state. The mechanism responsible for the sub-hertz pulsing remains unknown.

Summary of experimental observations

The experimental evidence discussed above is summarised in table 2.1. Instabilities in electronegative plasma are found in a wide variety of situations. They are clearly reproducible and consequently, they are not the result of a fluke choice of parameters. The observations are linked mostly by their electronegativity and instability frequencies in the kilohertz range. They also have similar power and pressure ranges. All the unstable systems are driven with radio frequency (RF) power sources.

Unstable behaviour is not found in electropositive gases, at least not for the wide parameter ranges investigated. This suggests that the formation or destruction of negative ions plays an important role in the instability.

Gas	Power / W	Pressure / mTorr	Discharge system	Driving freq. / MHz	Instability freq. / kHz	Ref.
O_2	300	1	Cylindrical ICP	0.46	1	[78]
O_2	230 - 340	5 - 23	Planar (GEC) ICP	13.56	3 - 21	[75]
O_2	100	188	CCP	13.56	3.5	[74]
Ar / SF_6	300	1	Cylindrical ICP	0.46	4	[78]
Ar / SF_6	320 - 600	4 - 8	Planar ICP	13.56	10^{-3} - 900	[82]
Ar / SF_6	200 - 600	1 - 100	Planar ICP	13.56	-	[43]
Ar / SF_6	100 - 500	3 - 100	Planar ICP	13.56	-	[83]
SF_6	300 - 900	1 - 100	Planar ICP	13.56	1 - 90	[43]
SF_6	100 - 600	5 - 100	Planar ICP	13.56	1 - 100	[83]
Ar / Cl	70 - 300	4 - 24	Planar (GEC) ICP	13.56	(20 - 520) $\times 10^{-3}$	[76]
CF_4	100	188	CCP	13.56	80	[74]

Table 2.1: Table of experimental observations of instabilities in electronegative gases.

The experiments discussed above were carried out in a variety of discharge systems with different power coupling and reactor shapes. For the instability to exist in a wide range of experimental set-ups it is unlikely to be driven due a quirk of the system. An intrinsic physical process must be responsible; such as the one described in section 2.3.

2.1.2 Existing models of the instability

Lieberman *et al.* [82] proposed that the instability is driven by the transition between capacitive and inductive modes. A coil attached to a RF power generator can deliver power to the discharge either capacitively or inductively. For lower powers the electric field couples directly into the plasma, this is called capacitive coupling. During the power cycle the magnetic field generated by the current in the coil collapses and an electric field is induced in the discharge vessel. This inductive coupling occurs at high powers.

The different modes of power coupling deliver different amounts of power to the plasma. The amount of power absorbed by the plasma affects the energy distribution function of the plasma species, which in turn alters the rate coefficients of the reactions. Varying the rate coefficients causes variations in the number densities of the species, resulting in the observed instability.

The geometry of the discharge vessel is important as wall losses are identified as an important loss mechanism for the plasma species. The following instability cycle is proposed:

1. The cycle begins in inductive mode where the electron density grows until a quasi-equilibrium is reached. The negative ion density is also increasing during this period

but continues to grow after the electron population reaches the quasi-equilibrium.

2. The continuing growth of the negative ion density disturbs the quasi-equilibrium.

3. Electrons are lost rapidly in the creation of negative ions and to the walls. The power coupling switches to capacitive coupling.

4. Negative ions are lost slowly through ion-ion recombination and wall collisions. The discharge eventually returns to the inductive mode: the start of the instability cycle.

A global model was constructed to numerically model this process [82]. The particle balance equations for the electron and negative ion densities; and the energy balance equation were solved to produce the dynamical behaviour of the discharge. The particle balance equations for the electron and negative ion were dependent on collisions: ionisation, electron attachment and ion-ion recombination; along with wall losses. The energy balance equation described the effect on the electron temperature of the power absorbed by the electrons from the capacitive and inductive modes and the power lost from the electrons, this was dependent on the inelastic losses of the included reactions and the wall losses. The positive and negative ions were assumed to be cold. Simulated and experimentally measured results were not compared. For certain parameters the model was able to produce instability frequencies similar to the experimental measurements.

An improved version of the global model described in [82] was used to simulate the instability in Ar/SF_6 and pure SF_6 by Chabert *et al.* [43]. Several alterations to the model were made: the negative ions were given a fixed non-zero temperature; the neutral gas was assumed to be weakly dissociated; electron detachment from negative ions through impact of excited neutrals was included as a destruction method for the negative ions; and the effect of the matching conditions on the power absorption was included.

The dynamical behaviour produced by the simulation agreed qualitatively with the experimental results; the simulation produced the same correlated oscillation of election and ion number densities. The frequency of the simulated instability agreed with experiment for particular matching conditions for an Ar/SF_6 mixture. The electron densities were lower than those measured in the experiment. Simulations of pure SF_6 over a series of pressures produced simulated frequencies that were typically a factor $\sim 5 - 10$ smaller than those measured experimentally but did show a similar trend. The simulation did not recover the pressure range observed experimentally.

Corr *et al.* [75] adapted the model by changing the reaction set to represent molecular Oxygen and their discharge vessel geometry. The model did not predict the significant pressure dependence of the frequency as seen in the experimental results. The simulation only produced unstable behaviour in the range 6 - 14mTorr while the experiment observed the instability in the range 5 - 23mTorr.

Descoeudres, Sansonnens and Hollenstein 2003

The E-H transition proposed for the instability in inductively coupled plasma is not possible in the capacitively coupled plasma of [74]. The unstable behaviour is described in terms of a feedback loop [74]. The process begins with a small increase in electron number density. In an isolated system where the the total energy is shared between the electrons, increasing

the electron density causes a decrease in electron temperature. The response to this event depends on the temperature dependence of the attachment and ionisation rate coefficients.

- If the attachment rate decreases more quickly than the ionisation rate, as the electron temperature drops, the electron number density will increase. This positive feedback causes the discharge to become unstable.
- If the attachment rate decreases less strongly than the ionisation rate then the electron population will decrease, resulting in an increase in electron temperature, and stabilising the discharge.

A numerical model of the unstable plasma evolution is not investigated. The authors define a parameter which predicts the onset of unstable behaviour in a discharge. The stability parameter, R, is,

$$R = \frac{\partial\alpha/\partial T_e}{\partial\beta/\partial T_e}. \tag{2.1}$$

If $R > 1$, *i.e.* the attachment rate drops more rapidly than the ionisation rate, then the discharge is unstable. It is found that O_2 and CF_4 are unstable when the electron temperatures are below 3.9eV and 5.05eV; for SF_6 the ratio R does not reach the unstable regime. This finding is complemented by the experimental results where SF_6 was found to be stable in a capacitive discharge.

SF_6 is found to be unstable in inductively coupled plasmas thus the temperature dependence of the attachment and ionisation rates cannot be completely responsible for the instability observed in inductively coupled plasmas.

2.2 Equilibrium analysis of competing chemical reactions

The instability is found only in discharges with electronegative gases; under the same operating conditions electropositive gases do not exhibit similar oscillations. This evidence suggests that the electron affinity of the gas, its ability to create negative ions, is responsible for the periodic variations in the particle number densities, potential and light emission.

To determine if the unstable behaviour is due to the competing reactions, the equations describing the particle balance are linearised and perturbed. The main plasma species: electrons (n_e), negative ions (n_-), positive ions (n_+) and neutral gas (n_g) are considered with the reactions: electron impact ionisation of neutral species; electron detachment from negative ions; electron attachment to neutral species; and electron-ion recombination. These species and reactions can be represented by the equations:

$$\dot{n}_e = \beta n_g n_e + \delta n_- n_e - \alpha n_g n_e - \gamma n_+ n_e, \tag{2.2}$$
$$\dot{n}_g = -\beta n_g n_e + \delta n_- n_e - \alpha n_g n_e + \gamma n_+ n_e, \tag{2.3}$$
$$\dot{n}_- = -\delta n_- n_e + \alpha n_g n_e, \tag{2.4}$$
$$\dot{n}_+ = \beta n_g n_e - \gamma n_+ n_e, \tag{2.5}$$

where $\dot{n}_s$ denotes the time derivative of species s, the coefficients β, δ, α and γ are the rate coefficients of ionisation, detachment, attachment and recombination respectively. Suppose that there is some equilibrium point for each of the particle species. Adding a

small perturbation to each species may cause an oscillation in the number densities of the species. The perturbed number densities can be written:

$$\begin{aligned} n_e &\mapsto n_{e_0} + n_{e_1}, && (2.6)\\ n_+ &\mapsto n_{+_0} + n_{+_1}, && (2.7)\\ n_- &\mapsto n_{-_0} + n_{-_1}, && (2.8)\\ n_g &\mapsto n_{g_0} + n_{g_1}, && (2.9) \end{aligned}$$

where n_{s_0} are values of the equilibrium and n_{s_1} are small perturbations from the equilibrium value. We note that at the equilibrium point values are constant, *i.e.* $\dot{n}_{s_0} = 0$ thus evaluating $\dot{n}_s(t=0)$ for all species s gives

$$\begin{aligned} \beta n_{g_0} &= \gamma n_{+_0}, && (2.10)\\ \delta n_{-_0} &= \alpha n_{g_0}. && (2.11) \end{aligned}$$

Substituting the perturbations (2.6–2.9) into the particle balance equations (2.2–2.5) gives

$$\begin{aligned} \dot{n}_{e_1} &= n_{e_0}(\beta n_{g_1} + \delta n_{-_1} - \alpha n_{g_1} - \gamma n_{+_1}), && (2.12)\\ \dot{n}_{+_1} &= n_{e_0}(\beta n_{g_1} - \gamma n_{+_1}), && (2.13)\\ \dot{n}_{-_1} &= n_{e_0}(-\delta n_{-_1} + \alpha n_{g_1}), && (2.14)\\ \dot{n}_{g_1} &= n_{e_0}(-\beta n_{g_1} + \delta n_{-_1} - \alpha n_{g_1} + \gamma n_{+_1}). && (2.15) \end{aligned}$$

We can write the differential equations (2.12–2.15) in the form of a linear system

$$\begin{aligned} \begin{bmatrix} \dot{n}_{e_1} \\ \dot{n}_{+_1} \\ \dot{n}_{-_1} \\ \dot{n}_{g_1} \end{bmatrix} &= n_{e_0} \begin{bmatrix} 0 & -\gamma & \delta & \beta-\alpha \\ 0 & -\gamma & 0 & \beta \\ 0 & 0 & -\delta & \alpha \\ 0 & \gamma & \delta & -\beta-\alpha \end{bmatrix} \begin{bmatrix} n_{e_1} \\ n_{+_1} \\ n_{-_1} \\ n_{g_1} \end{bmatrix}, && (2.16)\\ \dot{n}_{s_1} &= n_{e_0} \boldsymbol{A} n_{s_1}. && (2.17) \end{aligned}$$

The eigenvalues of the matrix $\boldsymbol{A}$ determine the behaviour of this system of differential equations: complex eigenvalues will give an oscillatory system. The eigenvalues (λ) are the roots of the characteristic polynomial and are found by solving

$$\det(\boldsymbol{A} - \lambda \boldsymbol{I}) = 0, \tag{2.18}$$

where $\boldsymbol{I}$ is the identity matrix. After some simple row reduction of $\boldsymbol{A}$,

$$\begin{aligned} \det(\boldsymbol{A} - \lambda \boldsymbol{I}) &= \begin{vmatrix} \lambda & 0 & 0 & 0 \\ 0 & -\gamma-\lambda & 0 & \beta \\ 0 & 0 & -\delta-\lambda & \alpha \\ 0 & 0 & \delta & -\alpha-\lambda \end{vmatrix}, && (2.19)\\ 0 &= (\lambda^2 + \lambda\gamma)\Big[\alpha\delta - (\lambda+\delta)(\lambda+\alpha)\Big]. && (2.20) \end{aligned}$$

The eigenvalues are

$$\lambda = 0,\ -\gamma,\ -(\alpha+\delta). \tag{2.21}$$

An eigenvalue of zero gives an equilibrium solution and a negative eigenvalue gives a solution that converges to the equilibrium point. This shows that there is no oscillation caused solely by the competing rate coefficients and that there must be some additional factor which drives the observed electronegative instability.

2.3 Proposed Mechanism: Attachment-detachment instability cycle

Here another possible explanation for the instability in electronegative plasmas, independent of the reactor geometry and electrical circuit of the plasma, is proposed. This method relies on the transparency of the plasma to the driving electric field: if the plasma frequency (ω_p) is greater than the driving frequency (ω_E) then the electric field is confined to the sheath region.

This process does not occur simultaneously across the whole plasma; the source of the instability is confined to the boundary between the sheath and the plasma. The idea is that the position of the sheath edge, the region shielding the bulk plasma from the electric field, fluctuates. This point is defined as the position where the plasma frequency equals the driving frequency. The movement of the sheath will result in a periodic change of the bulk plasma volume, this is consistent with experimental observations (see figure 2.2).

Electrons lose energy through collisions with neutrals and eventually this loss of energy allows the electrons to undergo attachment to neutrals or recombination with positive ions, causing a drop in the free electron population. In a real plasma, the electron population is distributed in energy, and so processes such as attachment and ionization are always present, to some extent.

If the electron number density drops sufficiently the plasma frequency will cease to be dominated by the electrons and will be dominated by the ions. If the plasma frequency falls below the driving frequency of the electric field then the plasma's dielectric coefficient ϵ becomes positive:

$$\epsilon = 1 - \frac{\omega_p^2}{\omega_E^2} \tag{2.22}$$

allowing the electric field to penetrate into the plasma.

The electric field now energises the remaining free electrons that were previously shielded from it. The increase in energy will increase the occurrence of detachment and ionising collisions and so liberate more electrons. The increase in free electron population will eventually expel the electric field.

In this way a cycle of attachment and detachment can be set up, leading to the periodic optical emission observed experimentally.

2.4 Numerical zero-dimensional simulation

To test the proposed physical model a simple zero-dimensional numerical simulation is employed. The point in the discharge to be simulated is chosen to be just outside the bulk plasma where the electron density is sufficiently low that the plasma frequency is close to the driving frequency. This point will be directly affected by the change in electric field penetration. There are six governing equations: four particle species balance equations, an equation of motion for the electrons and the expression for the plasma frequency.

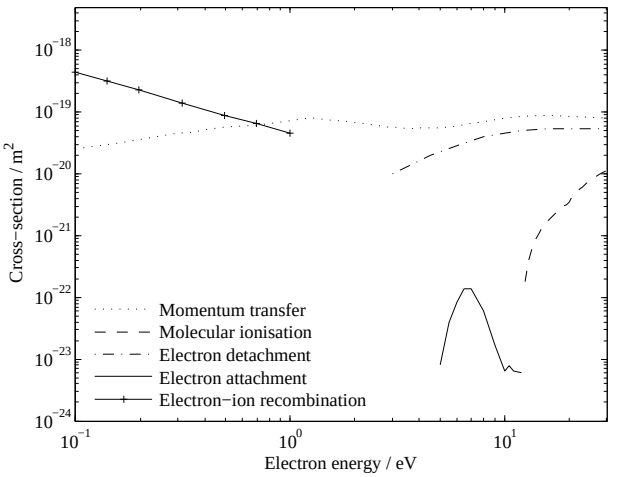

Figure 2.3: The energy dependence of the momentum-transfer [87], ionisation [88], detachment [89], dissociative attachment [90] and electron-ion recombination [91] reactions for molecular Oxygen.

2.4.1 Numerical model construction

The equations (2.2–2.5) are used to describe the evolution of each of the species.

In this simple model the rate coefficients have only two possible values: zero or a defined constant. The rate coefficients are switched on and off according to the kinetic energy of the electrons, as given by their average speed v. For example, processes liberating electrons can only turn on above some threshold speed and processes reducing the number of free electrons can only turn on below some threshold speed, *i.e.* $\alpha = \alpha_0 \times H(v_\alpha - v)$, where H is the Heaviside Step Function

$$H(x) = \begin{cases} 0 & \text{if } x \leqslant 0, \\ 1 & \text{if } x > 0. \end{cases} \tag{2.23}$$

All other processes are treated in a similar way.

These threshold speeds and reaction rates will be determined by the reaction cross sections and rate coefficients for the relevant processes; figure 2.3 and table 2.2 show the relevant data for an Oxygen discharge which will be used later to asses the physical mechanism. The energy dependence of the cross sections can be seen in figure 2.3, from this data the reaction thresholds can be chosen and converted to speeds. The values of the rate coefficients are calculated from the expressions in table 2.2 given an experimentally measured electron temperature.

The equation of motion dictating the average speed of the electrons, v, takes the form

$$\dot{v} = \frac{e}{m} E - \nu v, \tag{2.24}$$

where $\frac{e}{m}$, E, ν are the electron charge to mass ratio, the electric field strength and electron-

Reaction	Rate coeff. / $m^3\ s^{-1}$
Ionisation	$2.34 \times 10^{-15} T_e^{1.03} \exp(-12.29/T_e)$
Detachment	$5.47 \times 10^{-14} T_e^{0.324} \exp(-2.98/T_e)$
Attachment	$1.07 \times 10^{-15} T_e^{-1.391} \exp(-6.26/T_e)$
Recombination	$2.2 \times 10^{-14} T_e^{-0.5}$

Table 2.2: Table of Rate Coefficient expressions for molecular Oxygen[92].

neutral collision frequency, respectively. The plasma frequency can be written as,

$$\omega_p^2 = \sum_s \frac{q_s^2 n_s}{\varepsilon_0 m_s}, \tag{2.25}$$

where s is an index over all charged species.

The collision frequency ν is taken to be:

$$\nu = n_g \sigma_m v \tag{2.26}$$

where n_g is the neutral gas density and $\sigma_m v$ is taken to be a constant derived from the momentum-transfer cross-section [87]. This product is chosen to be a constant to maintain simplicity. The $\sigma_m v$ constant is the product of the the mean of the cross section (over an energy range relating to the range of mean speeds) and the mean speed given by a kinetic energy equivalent to the temperature T_e. The temperature, an experimental measurement, is used to characterised the speed in an attempt to be consistent.

The plasma frequency controls the electric field: when ω_p drops below ω_E the electric field in the plasma switches on to a constant value; when $\omega_p > \omega_E$ the field decays. The electric field must have a fixed decay timescale. If the electric field is allowed to turn on and off instantaneously then the amplitude of the oscillation is dependent on the timestep; smaller timesteps will produces smaller amplitude oscillations resulting in higher frequencies.

Electric field decay

The general form for an oscillation is

$$E = |E| \exp(i\omega\tau) \tag{2.27}$$

where τ is the time since the plasma frequency increased above the driving frequency and ω is complex. To determine the field decay rate, consider the evolution of a plasma oscillation in a plasma in which the background number density (n_0) is slowly decreasing. This decay rate is derived by considering a cold plasma oscillation. Beginning with the continuity equation, momentum equation and Gauss's Law:

$$\frac{\partial n_e}{\partial t} + \nabla.(n_e v) = 0 \tag{2.28}$$

$$m_e \Big[\frac{\partial v}{\partial t} + (v.\nabla)v\Big] = -eE \tag{2.29}$$

$$\nabla \cdot E = \frac{e}{\varepsilon_0}(n_i - n_e) \tag{2.30}$$

The variables are perturbed:

$$n_e \mapsto n_0(t) + n_1(t) \tag{2.31}$$
$$n_i \mapsto n_0(t) \tag{2.32}$$
$$v \mapsto v_1(x,t) \tag{2.33}$$
$$E \mapsto E_1(x,t) \tag{2.34}$$

note that both n_0 and n_1 are time varying. However, it is assumed that n_0 varies on a much longer timescale than n_1 such that $\dot{n}_0 = S_0 \ll \dot{n}_1$, where S_0 is some source term. The decay of n_0 represents the reduction of the electron population due to electron attachment and recombination. Thus for the shorter timescale (2.28)–(2.30) become,

$$\dot{v}_1 = -\frac{eE_1}{m_e} \tag{2.35}$$
$$\dot{n}_1 + n_0 \nabla.v_1 = 0 \tag{2.36}$$
$$\nabla \cdot E_1 = \frac{e}{\varepsilon_0} n_1 \tag{2.37}$$

Taking the time derivative of (2.36),

$$\ddot{n}_1 + \dot{n}_0 \nabla.v_1 + n_0 \nabla.\dot{v}_1 = 0 \tag{2.38}$$

substituting $\dot{v}_1$ from (2.35), $\nabla.v_1$ from (2.36) and $\nabla.E_1$ from (2.37) results in:

$$\ddot{n}_1 - \frac{\dot{n}_0}{n_0}\dot{n}_1 + \frac{n_0 e^2}{m_e \varepsilon_0} n_1 = 0 \tag{2.39}$$

Due to the slow varying nature of n_0, $\Omega = \dot{n}_0/n_0$ and also note that $\omega_p^2 = n_0 e^2/m_e\varepsilon_0$. Fourier transforming ($\partial/\partial t \to -i\omega$) gives:

$$-\omega^2 n_1 + i\omega\Omega n_1 + \omega_p^2 n_1 = 0 \tag{2.40}$$

Solving (2.40) for ω gives,

$$2\omega = i\Omega \pm \sqrt{4\omega_p^2 - \Omega^2} \tag{2.41}$$

For critical damping of the field, set $\Omega = 2\omega_p$, thus (2.27) becomes,

$$E = |E| \exp(-\omega_p \tau) \tag{2.42}$$

2.4.2 Application to Oxygen discharge

Figures (2.4-2.8) show results from the zero-dimensional simulation of a pure molecular Oxygen discharge. The parameters of the simulation are shown in table 2.3.

The neutral number density is an independent parameter in the simulation, varying the number density shows the pressure dependence of the instability frequency. In figure 2.4 the basic dependencies of the simulation and experiment are compared. However, the results from the simulation are a function of number density and the experimental results are a function of pressure. Figure 2.4 shows the dependence of the instability frequency

Parameter	Value
ω_E	13.56MHz
T_e	4eV
E_0	$518\mathrm{Vm}^{-1}$
mean speed	$1.19 \times 10^6 \mathrm{ms}^{-1}$
mean σ_m	$6.63 \times 10^{-20} \mathrm{m}^2$
Ionisation threshold energy	13eV
Detachment threshold energy	3.5eV
Attachment threshold energy	8eV
Recombination threshold energy	1eV

Table 2.3: Table of data used in numerical simulation.

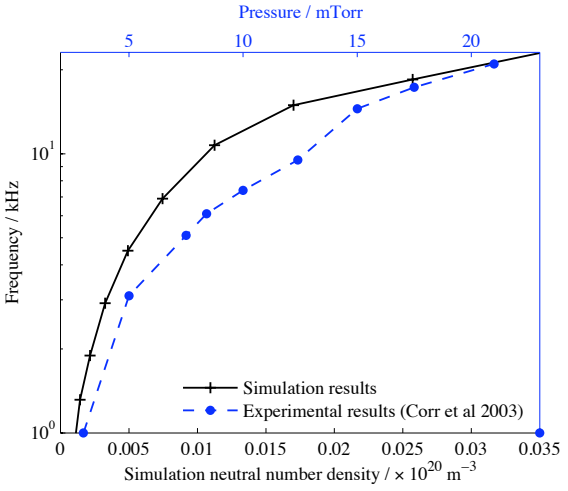

Figure 2.4: Results from the numerical simulation showing the instability frequency dependency on neutral number density. The experimental frequency-pressure dependance results from [75] are plotted with the variation in pressure plotted on the top x-axis.

Pressure / mTorr	Gas Temp. / K	Atom Temp. / K	Dissociation fraction	O_2 Density / m^{-3}	O Density / m^{-3}
11	~ 600	~ 3000	0.45	6×10^{19}	5×10^{19}
25	~ 600	~ 3000	0.2	32×10^{19}	8×10^{19}

Table 2.4: Table of experimental data for Oxygen (at ~ 250 W) [93] used to calculate the O_2 number densities for various pressures.

on the neutral gas number density with the pressure dependence of the frequency from experiment[75] plotted on the top x-axis.

To compare the frequency dependencies clearly the number density corresponding to the experimentally measured pressure must be calculated. Table 2.4 shows experimental calibration data for the Oxygen discharge. The total pressure p is the sum of partial pressures from the neutral molecular and atomic species,

$$p = p_{O_2} + p_O. \tag{2.43}$$

Assuming an ideal gas the neutral molecular number density can be writtin as

$$n_{O_2}(p) = \frac{p}{k_B T_g + \frac{D}{1-D} k_B T_a} \tag{2.44}$$

where T_g is the gas temperature, T_a is the atom temperature, k_B is the Boltzmann constant and D is the dissociation fraction

$$D = \frac{n_O}{n_{O_2} + n_O}. \tag{2.45}$$

To calculate intermediate values of the molecular neutral number density it is assumed that the dissociation fraction is a linear function of the experimentally measured total pressure (p),

$$D(p) = a_1 p + a_2 \tag{2.46}$$

where $a_1 = -0.018\text{mTorr}^{-1}$, $a_2 = 0.646$. The number density dependence of the numerical results and the experimental dependence are compared in figure 2.5.

The number densities of the simulation and experiment are not in agreement; the numerically derived number density is systematically a factor ~ 36 lower. As stated earlier the instability is driven by a region at the plasma-sheath boundary where the electron number density is sufficiently low to allow the penetration of the electric field. It is most likely that this will occur towards the edge of the vacuum vessel, far from the point at which the original neutral pressure was measured. The results of Shimada *et al.* [94] indicate that neutral number densities are significantly depressed near the vessel edges as a result of local heating. This will contribute to lowering the O_2 number density consistent with our model but may not explain the whole effect. Moreover, Franklin [95] has shown that electronegative plasmas in equilibrium are highly spatially structured, suggesting that measurements taken at the centre of the plasma may not be representative of the plasma properties at the edge.

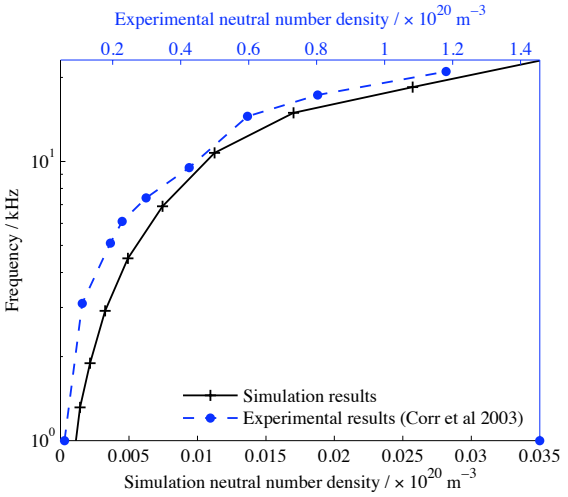

Figure 2.5: Comparison between the frequency dependence on the neutral number density of the numerical simulation and experimental results of [75]. Numerical number density is on the bottom axis and extrapolated experimental number density is on the top x-axis.

Experimental results [75] show a well-defined pressure regime between 3 and 23mTorr where the instability occurs. The numerical simulation does not show any defined pressure range of operation. At these regime boundaries there must be a change in the system not accounted for in the simulation. This could be a change in relative particle abundances resulting in a change of the dominant reaction.

There are three central parameters in the simulation: the neutral number density, the electron temperature(T_e) and the electric field strength.

Variation in the neutral number density shows the pressure dependence of the instability. The electron temperature is a constant during the simulation and fixes the values of the rate coefficients. The frequency of the instability is mostly insensitive to changes in the electron temperature. Variations of 25% in T_e produced no significant change in simulation output compared with sensitivity to the neutral number density. The variation of the rate coefficients over the temperature range 3 to 4eV is shown in figure 2.6. The numerical simulation of the attachment-detachment cycle shows the cycle is dominated by the attachment timescale. Over the temperature range the attachment and recombination rate coefficients vary by less than 15%. However, across the range of experimental pressures the neutral number density varies by a factor ~ 25 to produce the instability frequency; marginal variations in the rate coefficients, resulting from temperature fluctuations, are not significant in deciding the instability frequency. The rate coefficients (k_i) are used in the simulation to evaluate equations (2.2-2.5); it is the product $k_i n_g$ which affects the period of the instability. The variation in number density dominates this product.

The electric field strength can also be varied. This parameter also changes the frequency of the instability: increasing the electric field strength decreases the frequency of the instability. An increased electric field strength results in a higher electron speed and more free electrons in the detachment phase, the time required to attach the electrons increases.

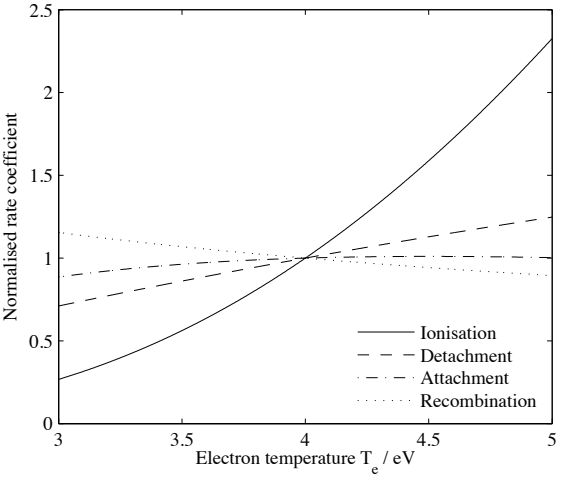

Figure 2.6: Rate coefficients as a function of electron temperature normalised to their values at 4eV.

Consequently this parameter can change the number density at which the simulated instability frequency matches the experimental frequency. Under the simple approximations in this model the electric field required to achieve the correct frequency at the experimental number density causes the system to become relativistic violating the initial assumptions. For consistency with the experimental setup the electric field should be no greater than 1 kVm^{-1}.

Figure 2.7 shows the time variations of each of the species and the electric field, and the detail of the electric field penetration can be seen in figure 2.8. We note that the variation in the electron and negative ion number densities are anti-correlated as reported in Corr *et al.* [75]. The number densities calculated here cannot be compared to the experimentally measured values because the point simulated here is not in the plasma bulk where the experimental measurements are made.

2.4.3 Discussion of zero-dimensional model results

The numerical model shows that a simple physical process can explain the unstable behaviour found in electronegative discharges. With the exception of the neutral gas, which is inferred to be significantly different from the experimentally measured one, the number densities are consistent with the values measured experimentally. The neutral gas number density enters the simulation in two key areas: the requirement for electron cooling via neutral interactions (bottom graph of figure 2.8), and the electron attachment process that forms negative ions (rising phases in the second from top plot of figure 2.7). If the neutral density implied by the experimental measurement is used in the simulations, the simulated instability frequencies in the pressure range are considerably different.

There may be several underlying causes for this discrepancy:

- the reliance on a total momentum transfer cross-section to remove energy from the electrons may be too simplistic - in fact there may be additional mechanisms asso-

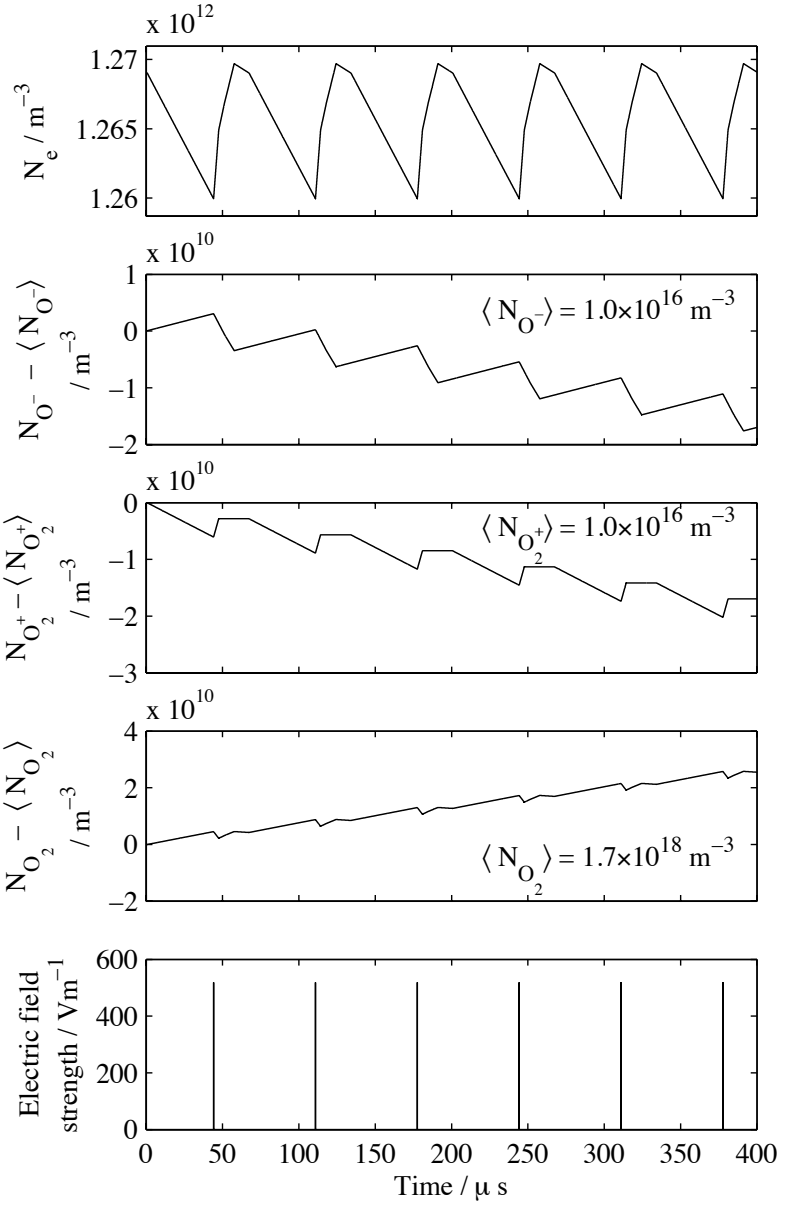

Figure 2.7: This set of plots shows from the top down the evolution of the electron, negative ion, positive ion and neutral gas number densities and the electric field. The plots of the negative ion, positive ion and neutral gas number densities show the variation from their mean values. The simulation was run with an electron temperature of 4eV and an electric field of 518 Vm^{-1}.

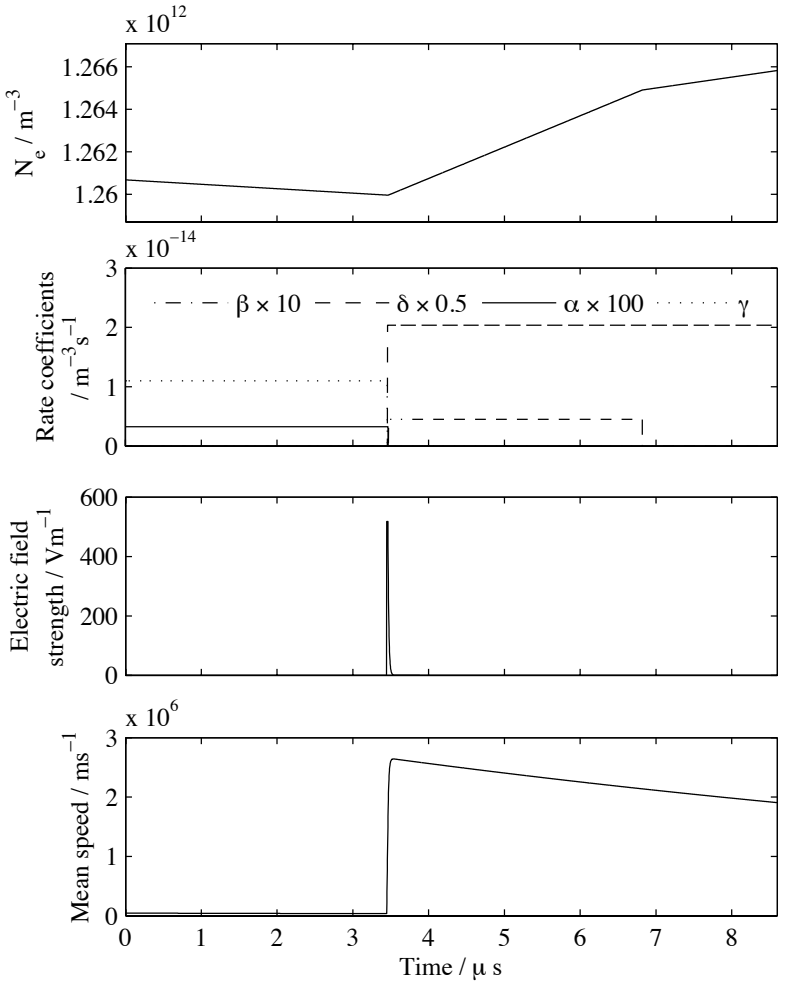

Figure 2.8: Shown here, from top to bottom, is the evolution of the electron number density, the rate coefficients, electric field and mean speed of the electrons as the electric field penetrates the plasma. The rate coefficients in the second plot are not to scale, this only shows when each of the constants is 'switched on'.

ciated with the experiment that impact on electron energy loss rates which are not included in this simple model;

- there may be more than one simultaneous underlying cause of the instability, where our model addresses only the effect at the plasma edge where the electron density is low;
- the step-function approximation of cross-sections may be too unsophisticated;
- the pressure measurements may not be reflecting the true situation near the plasma edge, where our model is valid.

The plasma pressure measurements [75] and the experimental data [93] (table 2.4) may not reflect the ambient conditions near the plasma edge, especially if the electronegative plasma is strongly structured, with higher negative ion density in the plasma interior. The fact that the simulations recover the observed phenomena in aspects other than the neutral number density at the edge suggests that there is merit in the simple plasma physics which the model seeks to represent, but that additional insight into related neutral edge effects may be required in a more complete description.

2.5 Analytic model

The numerical model presented in section 2.4 makes a number of assumptions about the discharge to allow the system to be reduced to a small number of differential equations which can numerically evaluated. Making a few more assumptions reduces the system such that an analytic solution of the instability period can be determined.

2.5.1 Analytic model construction

The proposed mechanism is driven by the changing electron number density. Clearly the other species, the ions and neutrals, play an important role in determining the rate of change of the electron density. Assuming that only the electron number density varies and the number densities of the negative ion, positive ion and neutral gas are fixed we can find an expression for the instability period. This assumption is motivated by the results from the simulation where the variations in the ion and neutral densities are very small compared to their actual values, *i.e.*

$$\frac{\dot{n}_s}{n_s} \approx 0, \qquad \text{where } s = -, +, g. \tag{2.47}$$

This assumption reduces equations (2.2–2.5) to:

$$\dot{n}_e = \beta n_g n_e + \delta n_- n_e - \alpha n_g n_e - \gamma n_+ n_e \tag{2.48}$$
$$\dot{n}_g = 0 \tag{2.49}$$
$$\dot{n}_- = 0 \tag{2.50}$$
$$\dot{n}_+ = 0 \tag{2.51}$$

where as before n_e, n_g, n_-, n_+ are the electron, neutral gas, negative ion and positive (molecular) ion number densities and their time derivatives denoted by $\dot{n}_s$. β, δ, α, γ are rate coefficients for impact ionisation, electron detachment from negative ions, electron attachment to neutral species and recombination of electrons and positive ions respectively. It is further assumed that the electric field is 'switched' on and off instantaneously.

As before, the rate coefficients are expressed as Heaviside Step functions (2.23) where the values are determined by the rate coefficients and the step are defined by the threshold speeds. Re-arranging (2.48)

$$\dot{n}_e = n_e(\beta n_g + \delta n_- - \alpha n_g - \gamma n_+) \tag{2.52}$$
$$\dot{n}_e = n_e R(v) \tag{2.53}$$

where $R(v)$ is piecewise constant

$$R(v) = \begin{cases} -\alpha n_g - \gamma n_+ & \text{if } v \leqslant v_\gamma, \\ -\alpha n_g & \text{if } v_\gamma < v \leqslant v_\delta, \\ \delta n_- - \alpha n_g & \text{if } v_\delta < v \leqslant v_\alpha, \\ \delta n_- & \text{if } v_\alpha < v \leqslant v_\beta, \\ \beta n_g + \delta n_- & \text{if } v_\beta < v. \end{cases} \tag{2.54}$$

Here the order of the speed thresholds corresponds to the Oxygen reaction set. This ordering may be different for another type of gas. Equation (2.53) can be easily solved in each of the speed intervals

$$\dot{n}_e = n_e R(v) \tag{2.55}$$
$$\int dt = \frac{1}{R(v)} \int \frac{dn_e}{n_e} \tag{2.56}$$
$$t_i - t_{i-1} = \frac{1}{R(v)} \log\left(\frac{n_{e_i}}{n_{e_{i-1}}}\right). \tag{2.57}$$

For ease of notation from now on the five different vales of $R(v)$ will be defined as:

$$R_1 = -\alpha n_g - \gamma n_+ \tag{2.58}$$
$$R_2 = -\alpha n_g \tag{2.59}$$
$$R_3 = \delta n_- - \alpha n_g \tag{2.60}$$
$$R_4 = \delta n_- \tag{2.61}$$
$$R_5 = \beta n_g + \delta n_-. \tag{2.62}$$

The equation of motion for the speed of the electrons (2.24) can be defined when the electric field is impinging and when it is excluded

$$\dot{v} = \tfrac{e}{m}E - \nu v \quad \textit{(Field impinging)} \tag{2.63}$$
$$\dot{v} = -\nu v \quad \textit{(Field excluded).} \tag{2.64}$$

In subsequent expressions $E_0 = \frac{e}{m}E$ for notational ease.

The solution to equation (2.63) when the electric field is on is

$$\int dt = \int \frac{dv}{E_0 - \nu v} \tag{2.65}$$
$$t_i - t_{i-1} = \frac{1}{\nu} \log\left(\frac{E_0 - \nu v_{i-1}}{E_0 - \nu v_i}\right) \tag{2.66}$$

t_i	t_0	t_1	t_2	t_3	t_4	t_5	t_6	t_7	t_8	t_9	t_{10}
$n_e(t)$	n_e^*	n_{e_1}	n_{e_2}	$n_{e_{min}}$	n_{e_4}	n_e^*	n_{e_6}	$n_{e_{max}}$	n_{e_8}	n_{e_9}	n_e^*
$v(t)$	$v_{\min}$	v_γ	v_δ	v_α	v_β	$v_{\max}$	v_β	v_α	v_δ	v_γ	$v_{\min}$

Table 2.5: Table of boundary conditions for the instability cycle when R_3 is attachment dominated.

and when the electric field is zero the solution to equation (2.64) is

$$\int dt = \int \frac{dv}{-\nu v} \tag{2.67}$$

$$t_i - t_{i-1} = \frac{1}{\nu} \log\left(\frac{v_{i-1}}{v_i}\right) \tag{2.68}$$

The expressions (2.57), (2.66) and (2.68) completely describe the evolution of the electron density and speed. To be able to write down an expression for the instability period the boundary conditions of each speed interval are required. Firstly, there are three different cases for the number density evolution: one where R_3 is attachment dominated *i.e.* $R_3 < 0$; another when R_3 is detachment dominated *i.e.* $R_3 > 0$ and finally where both processes are balanced equally *i.e.* $R_3 = 0$. The final case is not considered here because it is very unlikely. The cases are treated differently as the sign of R_3 determines when the maximum and minimum values of the electron number density occur.

$R_3 < 0$ case

Table 2.5 shows the boundary conditions at each time, figure 2.9 shows the evolution of electron speed and number density schematically.

Substituting the appropriate boundary conditions to the equations (2.63) or (2.64) and

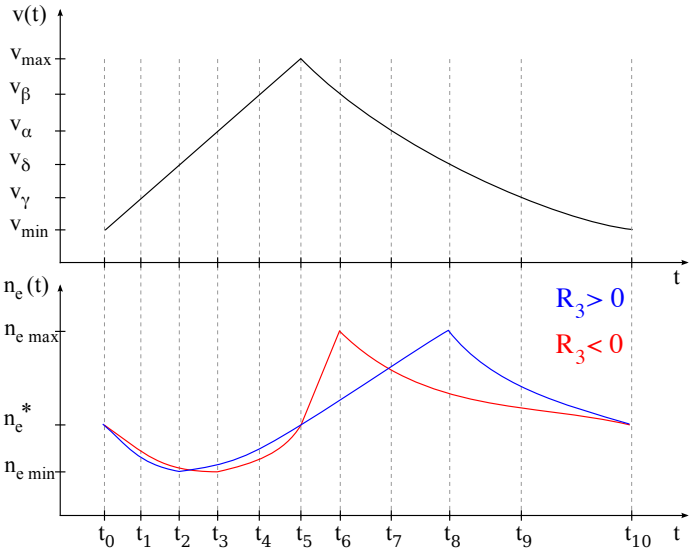

Figure 2.9: Diagram showing the evolution of the electron speed and number density during the instability cycle. The diagram is not to scale. The different evolutions of the electron number density for the cases of $R_3 > 0$ and $R_3 < 0$ are shown by the blue and red lines respectively.

(2.48), giving expressions for the time of each interval:

$$t_1 - t_0 = \frac{1}{\nu}\log\left(\frac{E_0 - \nu v_{\min}}{E_0 - \nu v_\gamma}\right) = \frac{1}{R_1}\log\left(\frac{n_{e_1}}{n_e^*}\right) \tag{2.69}$$

$$t_2 - t_1 = \frac{1}{\nu}\log\left(\frac{E_0 - \nu v_\gamma}{E_0 - \nu v_\delta}\right) = \frac{1}{R_2}\log\left(\frac{n_{e_2}}{n_{e_1}}\right) \tag{2.70}$$

$$t_3 - t_2 = \frac{1}{\nu}\log\left(\frac{E_0 - \nu v_\delta}{E_0 - \nu v_\alpha}\right) = \frac{1}{R_3}\log\left(\frac{n_{e_{\min}}}{n_{e_2}}\right) \tag{2.71}$$

$$t_4 - t_3 = \frac{1}{\nu}\log\left(\frac{E_0 - \nu v_\alpha}{E_0 - \nu v_\beta}\right) = \frac{1}{R_4}\log\left(\frac{n_{e_4}}{n_{e_{\min}}}\right) \tag{2.72}$$

$$t_5 - t_4 = \frac{1}{\nu}\log\left(\frac{E_0 - \nu v_\beta}{E_0 - \nu v_{\max}}\right) = \frac{1}{R_5}\log\left(\frac{n_e^*}{n_{e_4}}\right) \tag{2.73}$$

$$t_6 - t_5 = \frac{1}{\nu}\log\left(\frac{v_{\max}}{v_\beta}\right) = \frac{1}{R_5}\log\left(\frac{n_{e_6}}{n_e^*}\right) \tag{2.74}$$

$$t_7 - t_6 = \frac{1}{\nu}\log\left(\frac{v_\beta}{v_\alpha}\right) = \frac{1}{R_4}\log\left(\frac{n_{e_{\max}}}{n_{e_6}}\right) \tag{2.75}$$

$$t_8 - t_7 = \frac{1}{\nu}\log\left(\frac{v_\alpha}{v_\delta}\right) = \frac{1}{R_3}\log\left(\frac{n_{e_8}}{n_{e_{\max}}}\right) \tag{2.76}$$

$$t_9 - t_8 = \frac{1}{\nu}\log\left(\frac{v_\delta}{v_\gamma}\right) = \frac{1}{R_2}\log\left(\frac{n_{e_9}}{n_{e_8}}\right) \tag{2.77}$$

$$t_{10} - t_9 = \frac{1}{\nu}\log\left(\frac{v_\gamma}{v_{\min}}\right) = \frac{1}{R_1}\log\left(\frac{n_e^*}{n_{e_9}}\right). \tag{2.78}$$

The time intervals $t_1 \rightarrow t_4$ and $t_6 \rightarrow t_9$ can be easy evaluated using the expressions

involving the collision frequency and threshold speeds as these are known quantities

$$t_4 - t_1 = \frac{1}{\nu}\log\left(\frac{E_0 - \nu v_\gamma}{E_0 - \nu v_\beta}\right) \tag{2.79}$$

$$t_9 - t_6 = \frac{1}{\nu}\log\left(\frac{v_\beta}{v_\gamma}\right). \tag{2.80}$$

Expressions for the remaining times can be found by considering the times as a function of number density. Note that the instability cycle is periodic so $t_0 = t_{10}$ and then

$$(t_1 - t_0) + (t_{10} - t_9) = t_1 - t_9 = \frac{1}{R_1}\log\left(\frac{n_{e_1}}{n_{e_9}}\right). \tag{2.81}$$

Both n_{e_1} and n_{e_9} are unknowns. Using the middle and RHS equations of (2.70) and (2.71) an expression for n_{e_1} can be written:

$$\frac{1}{\nu}\log\left(\frac{E_0 - \nu v_\delta}{E_0 - \nu v_\alpha}\right) = \frac{1}{R_3}\log\left(\frac{n_{e_{\min}}}{n_{e_2}}\right) \tag{2.82}$$

$$n_{e_2} = n_{e_{\min}}\left(\frac{E_0 - \nu v_\alpha}{E_0 - \nu v_\delta}\right)^{\frac{R_2}{\nu}} \tag{2.83}$$

$$\frac{1}{\nu}\log\left(\frac{E_0 - \nu v_\gamma}{E_0 - \nu v_\delta}\right) = \frac{1}{R_2}\log\left(\frac{n_{e_2}}{n_{e_1}}\right) \tag{2.84}$$

$$n_{e_1} = n_{e_2}\left(\frac{E_0 - \nu v_\delta}{E_0 - \nu v_\gamma}\right)^{\frac{R_2}{\nu}} \tag{2.85}$$

$$= n_{e_{\min}}\left(\frac{E_0 - \nu v_\alpha}{E_0 - \nu v_\delta}\right)^{\frac{R_2}{\nu}}\left(\frac{E_0 - \nu v_\delta}{E_0 - \nu v_\gamma}\right)^{\frac{R_2}{\nu}} \tag{2.86}$$

Similarly for n_{e_9} with and equations (2.77) and (2.76)

$$\frac{1}{\nu}\log\left(\frac{v_\alpha}{v_\delta}\right) = \frac{1}{R_3}\log\left(\frac{n_{e_8}}{n_{e_{\max}}}\right) \tag{2.87}$$

$$n_{e_8} = n_{e_{\max}}\left(\frac{v_\alpha}{v_\delta}\right)^{\frac{R_3}{\nu}} \tag{2.88}$$

$$\frac{1}{\nu}\log\left(\frac{v_\delta}{v_\gamma}\right) = \frac{1}{R_2}\log\left(\frac{n_{e_9}}{n_{e_8}}\right) \tag{2.89}$$

$$n_{e_9} = n_{e_8}\left(\frac{v_\delta}{v_\gamma}\right)^{\frac{R_2}{\nu}} \tag{2.90}$$

$$= n_{e_{\max}}\left(\frac{v_\alpha}{v_\delta}\right)^{\frac{R_3}{\nu}}\left(\frac{v_\delta}{v_\gamma}\right)^{\frac{R_2}{\nu}}. \tag{2.91}$$

Thus,

$$t_1 - t_9 = \frac{1}{R_1}\log\left(\frac{n_{e_1}}{n_{e_9}}\right) \tag{2.92}$$

$$= \frac{1}{R_1}\log\left\{\frac{n_{e_{\min}}}{n_{e_{\max}}}\left(\frac{v_\delta}{v_\alpha}.\frac{E_0-\nu v_\delta}{E_0-\nu v_\gamma}\right)^{\frac{R_2}{\nu}}\left(\frac{v_\gamma}{v_\delta}.\frac{E_0-\nu v_\alpha}{E_0-\nu v_\delta}\right)^{\frac{R_3}{\nu}}\right\}. \tag{2.93}$$

The final expression for the remaining time, $t_4 \to t_6$, is

$$t_6 - t_4 = (t_6 - t_5) + (t_5 - t_4) = \frac{1}{R_5}\log\left(\frac{n_{e_6}}{n_{e_4}}\right) \tag{2.94}$$

both n_{e_6} and n_{e_4} are unknown. The middle and RHS of (2.75) can be used to write an expression for n_{e_6}

$$\frac{1}{\nu}\log\left(\frac{v_\beta}{v_\alpha}\right) = \frac{1}{R_4}\log\left(\frac{n_{e_{\max}}}{n_{e_6}}\right) \tag{2.95}$$

$$n_{e_6} = n_{e_{\max}}\left(\frac{v_\beta}{v_\alpha}\right)^{\frac{R_4}{\nu}}. \tag{2.96}$$

Using the middle and RHS of (2.72) n_{e_4} can be expressed as

$$\frac{1}{\nu}\log\left(\frac{E_0-\nu v_\alpha}{E_0-\nu v_\beta}\right) = \frac{1}{R_4}\log\left(\frac{n_{e_4}}{n_{e_{\min}}}\right) \tag{2.97}$$

$$n_{e_4} = n_{e_{\min}}\left(\frac{E_0-\nu v_\alpha}{E_0-\nu v_\beta}\right)^{\frac{R_4}{\nu}}. \tag{2.98}$$

Thus the expression for time $t_4 \to t_6$ is

$$t_6 - t_4 = \frac{1}{R_5}\log\left\{\frac{n_{e_{\max}}}{n_{e_{\min}}}\left(\frac{v_\beta}{v_\alpha}.\frac{E_0-\nu v_\beta}{E_0-\nu v_\alpha}\right)^{\frac{R_4}{\nu}}\right\}. \tag{2.99}$$

Finally, the expression for the period of the instability in the attachment dominated ($R_3 < 0$) case is given by:

$$T = \frac{1}{R_1}\log\left\{\frac{n_{e_{\min}}}{n_{e_{\max}}}\left(\frac{v_\delta}{v_\alpha}.\frac{E_0-\nu v_\delta}{E_0-\nu v_\gamma}\right)^{\frac{R_2}{\nu}}\left(\frac{v_\gamma}{v_\delta}.\frac{E_0-\nu v_\alpha}{E_0-\nu v_\delta}\right)^{\frac{R_3}{\nu}}\right\} \tag{2.100}$$

$$+\frac{1}{\nu}\log\left(\frac{E_0-\nu v_\gamma}{E_0-\nu v_\beta}\right) \tag{2.101}$$

$$+\frac{1}{R_5}\log\left\{\frac{n_{e_{\max}}}{n_{e_{\min}}}\left(\frac{v_\beta}{v_\alpha}.\frac{E_0-\nu v_\beta}{E_0-\nu v_\alpha}\right)^{\frac{R_4}{\nu}}\right\} \tag{2.102}$$

$$+\frac{1}{\nu}\log\left(\frac{v_\beta}{v_\gamma}\right). \tag{2.103}$$

t_i	t_0	t_1	t_2	t_3	t_4	t_5	t_6	t_7	t_8	t_9	t_{10}
$n_e(t)$	n_e^*	n_{e_1}	$n_{e_{min}}$	n_{e_3}	n_{e_4}	n_e^*	n_{e_6}	n_{e_7}	$n_{e_{max}}$	n_{e_9}	n_e^*
$v(t)$	$v_{\min}$	v_γ	v_δ	v_α	v_β	$v_{\max}$	v_β	v_α	v_δ	v_γ	$v_{\min}$

Table 2.6: Table of boundary conditions for the instability cycle when R_3 is detachment dominated.

$R_3 > 0$ **case**

Table 2.6 shows the boundary conditions at each time, 2.9 shows the evolution of electron speed and number density schematically.

Substituting the appropriate boundary conditions into the equations (2.63) or (2.64) and (2.48), resulting in expressions for the time of each interval:

$$t_1 - t_0 = \frac{1}{\nu}\log\left(\frac{E_0 - \nu v_{\min}}{E_0 - \nu v_\gamma}\right) = \frac{1}{R_1}\log\left(\frac{n_{e_1}}{n_e^*}\right) \tag{2.104}$$

$$t_2 - t_1 = \frac{1}{\nu}\log\left(\frac{E_0 - \nu v_\gamma}{E_0 - \nu v_\delta}\right) = \frac{1}{R_2}\log\left(\frac{n_{e_{\min}}}{n_{e_1}}\right) \tag{2.105}$$

$$t_3 - t_2 = \frac{1}{\nu}\log\left(\frac{E_0 - \nu v_\delta}{E_0 - \nu v_\alpha}\right) = \frac{1}{R_3}\log\left(\frac{n_{e_3}}{n_{e_{\min}}}\right) \tag{2.106}$$

$$t_4 - t_3 = \frac{1}{\nu}\log\left(\frac{E_0 - \nu v_\alpha}{E_0 - \nu v_\beta}\right) = \frac{1}{R_4}\log\left(\frac{n_{e_4}}{n_{e_3}}\right) \tag{2.107}$$

$$t_5 - t_4 = \frac{1}{\nu}\log\left(\frac{E_0 - \nu v_\beta}{E_0 - \nu v_{\max}}\right) = \frac{1}{R_5}\log\left(\frac{n_e^*}{n_{e_4}}\right) \tag{2.108}$$

$$t_6 - t_5 = \frac{1}{\nu}\log\left(\frac{v_{\max}}{v_\beta}\right) = \frac{1}{R_5}\log\left(\frac{n_{e_6}}{n_e^*}\right) \tag{2.109}$$

$$t_7 - t_6 = \frac{1}{\nu}\log\left(\frac{v_\beta}{v_\alpha}\right) = \frac{1}{R_4}\log\left(\frac{n_{e_7}}{n_{e_6}}\right) \tag{2.110}$$

$$t_8 - t_7 = \frac{1}{\nu}\log\left(\frac{v_\alpha}{v_\delta}\right) = \frac{1}{R_3}\log\left(\frac{n_{e_{\max}}}{n_{e_7}}\right) \tag{2.111}$$

$$t_9 - t_8 = \frac{1}{\nu}\log\left(\frac{v_\delta}{v_\gamma}\right) = \frac{1}{R_2}\log\left(\frac{n_{e_9}}{n_{e_{\max}}}\right) \tag{2.112}$$

$$t_{10} - t_9 = \frac{1}{\nu}\log\left(\frac{v_\gamma}{v_{\min}}\right) = \frac{1}{R_1}\log\left(\frac{n_e^*}{n_{e_9}}\right). \tag{2.113}$$

A similar process to that in section 2.5.1 must be carried out to determine the expression for the instability period in the detachment dominated regime, the details of this are

omitted for this case. The period of the instability when $R_3 > 0$ is given by

$$T = \frac{1}{R_1}\log\left\{\frac{n_{e_{\min}}}{n_{e_{\max}}}\left(\frac{v_\gamma}{v_\delta}.\frac{E_0-\nu v_\delta}{E_0-\nu v_\gamma}\right)^{\frac{R_2}{\nu}}\right\} \tag{2.114}$$

$$+\frac{1}{\nu}\log\left(\frac{E_0-\nu v_\gamma}{E_0-\nu v_\beta}\right) \tag{2.115}$$

$$+\frac{1}{R_5}\log\left\{\frac{n_{e_{\max}}}{n_{e_{\min}}}\left(\frac{v_\delta}{v_\alpha}.\frac{E_0-\nu v_\alpha}{E_0-\nu v_\delta}\right)^{\frac{R_3}{\nu}}\left(\frac{v_\alpha}{v_\beta}.\frac{E_0-\nu v_\beta}{E_0-\nu v_\alpha}\right)^{\frac{R_4}{\nu}}\right\} \tag{2.116}$$

$$+\frac{1}{\nu}\log\left(\frac{v_\beta}{v_\gamma}\right). \tag{2.117}$$

2.5.2 Application of analytic expression to Oxygen discharge

Table 2.7 shows the data used to evaluate the analytic expression. Most of the values used in the calculation of the instability period are the same as those used or derived in the numerical model. The ratio of maximum to minimum electron number density is taken from Corr [75]. Figure 2.10 compares the analytic solution to the experimentally measured frequency. The dominant term in the period is the first term representing the time $t_9 \rightarrow t_1$ where the recombination reaction occurs.

Parameter	Value
T_e	4eV
E_0	518 Vm^{-1}
mean speed	$1.19 \times 10^6 \mathrm{ms}^{-1}$
mean σ_m	$6.63 \times 10^{-20} \mathrm{m}^2$
Ionisation threshold energy	13eV
Detachment threshold energy	3.5eV
Attachment threshold energy	8eV
Recombination threshold energy	1eV
n_-	$1 \times 10^{-16} \mathrm{m}^{-3}$
n_+	$1 \times 10^{-16} \mathrm{m}^{-3}$
$\frac{n_{e_{\min}}}{n_{e_{\max}}}$	0.92

Table 2.7: Table of data for the analytic expression.

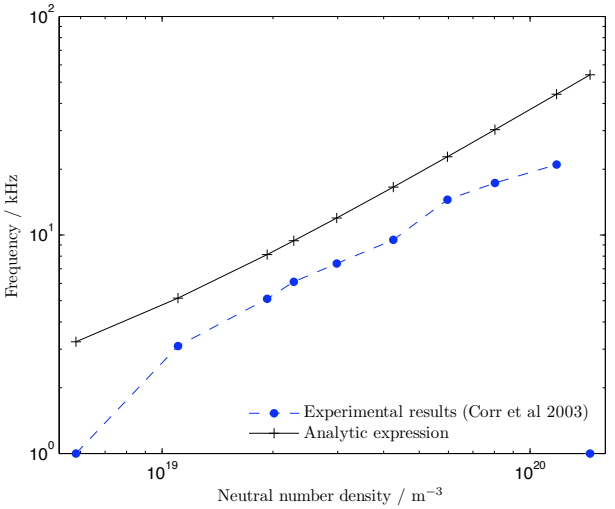

Figure 2.10: Comparison of experimentally measured and analytically calculated instability frequency.

2.5.3 Discussion of results from analytic model

The results from the analytically derived period are in good agreement with the experimental results from Corr [75]. The analytic and experimental frequencies disagree by a factor of approximately 2 for across the pressure range. The analytic expression does not predict the range of pressures the instability exists in. This is clearly a effect that has not been taken into account in the model equation or the input data as the range is not produced by the numerical work either.

2.6 Conclusion

The numerical and analytic simulations have shown that a simple physics model can correctly predict the essential aspects of the electronegative instability, without reference to the reactor geometry or the electrical circuit for the case of a pure oxygen discharge.

This model of the electronegative instability relies on the transparency of the plasma to the driving electric field: as the local electron number density drops (via the formation of negative ions) the electric field is able to penetrate further into the boundary layer, energising the remaining free electrons and leading to the break-up of the negative ions and an increase in the electron number density. The electric field is then expelled and the cycle repeats. This is clearly an edge plasma effect, and is corroborated by direct experimental measurements of emission at the plasma boundary which shows that the plasma contracts and expands on the same timescale as the pulsed emission. This strongly suggests that the mechanism described here is at least contributing to the overall behaviour; there may be other unrelated effects occurring in the plasma volume that are not addressed here.

2.6.1 Comparison of numerical and analytic results

The discrepancy in the number density found in the numerical work is not found in the analytic work. This is due to the initial values used in the analytic model. The analytic expression requires the ratio of minimum to maximum electron number density and this is calculated from experimental data. The instability period is very sensitive to this value. It describes the amplitude of the oscillation in the electron number density. The numerical model calculates the amplitude self-consistantly and cannot support a large enough amplitude at the desired pressure (*cf.* numerical ratio ≈ 0.99 and experimental ratio ≈ 0.92.)

The numerical model has the benefit of being able to predict where the instability may exist, the analytic expression requires information about the amplitude of the instability from experimental data to calculate the frequency of the oscillations. The analytic model cannot predict unstable regimes but it does show that the physical model presented here is relevant.

2.6.2 Comparison to previous results

Our model shows that a very simple physical concept can reproduce the basic aspects of the electronegative instability of the inductive discharge of Corr *et al.* [75], assuming that edge effects are important.

There are existing models that might explain this electronegative instability, as discussed in section 2.1.2, which raises the question why another would be required? The model originally proposed by Lieberman *et al.* [82] depends on the transition between E and H power coupling modes however, instabilities have been reported when the power is coupled entirely inductively [75] and entirely capacitively [74]. The model described here is not intended to replace existing descriptions. In fact, the E-to-H transition concept is similar to the model presented here; the strength of the electric field changes depending on the value of the electron number density. In the Lieberman model the electric field changes between capacitive and inductive modes whereas in the model described here it is simply 'on' and 'off'.

Electronegative instabilities are also found in purely capacitively coupled discharges, these have been investigated by Descoeudres *et al.* [74]. In their model the instability is caused by the temperature dependence of the rate coefficients. This instability has the potential to be active throughout the plasma volume in a capacitive set-up, so long as the electron temperature fulfils the given criteria in (2.1). Our model depends on decreasing the electron number density so that the penetration of the electric field increases, corresponding to the experimental results shown in 2.2.

Although the onset of the instability is triggered by a positive feedback mechanism acting due to the temperature drift, there is no end-process identified, *i.e.* how do you stop the plasma quenching? The stability ratio for Oxygen gives a threshold of 3.9eV; below this threshold the positive feedback mechanism is active. While the positive feedback occurs the temperature continues to drop and there seems no way for the process to enter the stable region again. Presumably the process is halted by the influx of energy from the RF driving system, which heats the electrons above the instability threshold. In this respect, the mechanism in [74] is not unlike the attachment-detachment cycle discussed in this

chapter, in that the power injected into the plasma plays a critical role in 'resetting' the conditions.

As a final observation, it may be possible to reverse engineer the physical processes here to infer new cross-section data for gas species. The energy dependence of many cross-sections is disputed or unknown; however competing reaction cross-sections play a critical role in the electronegative instability described in this paper. An experimental measurement of the instability frequency could be used as input to a numerical model. Selecting a particular cross-section to be an independent variable and requiring the simulation to produce the measured instability frequency would allow the energy dependence of the reaction cross-section to be investigated. This technique could be used as verification of other cross-section measurement techniques or as an independent method to measure reaction cross-sections.

Chapter 3

Particle model

3.1 Introduction

The aim of this chapter is to introduce a particle model which will be used to simulate two different plasmas. This particle model is similar to the Particle-in-Cell method (see section 1.4.4), with one exception: in this particle model each simulation particle represents one real particle [96]. There are no super-particles in this model.

The structure of the particle model will be outlined here and the basic components will be presented. Two of the most important elements: the potential field solver and the Monte-Carlo collision routine are discussed in chapters 4 and 5 respectively.

3.2 To mesh or not to mesh?

One of the first decisions when implementing a plasma model is whether to use a mesh or not. Particle models can be divided into three categories [49]: particle-particle, particle-mesh and particle-particle–particle-mesh. In a particle-particle model the force on a particle is calculated by evaluating Coulomb's law for every other particle. The calculation of the force, for all particles, requires approximately $O(N_p^2)$ calculations where N_p is the number of particles. For large numbers of particles this method takes a long time to compute. There are efficient algorithms which evaluate the force on a particle by particle basis. Tree codes [97] are used in cosmological simulations. In this method groups of particles at a distance are considered as a single mass. This method is discussed in slightly more detail in the final chapter.

In the particle-mesh method the potential is calculated on a mesh and the force on a particle is calculated from the mesh values. The continuous differential in Poisson's equation is approximated on a grid, which allows the potential to be solved. The calculation of the force on a particle becomes a three step process:

- Calculate the charge density by assigning the charged particles to the mesh (see section 3.4).
- Calculate the electric potential by solving Poisson's equation on the mesh (see chapter 4)
- Calculate the force on each particle from the electric potential (see section 3.4)

The number of operations to calculate the force on the particles using a mesh depends on both the number of particles and the number of grid points (N_g). The number of operations required to solve Poisson's equation varies between methods; an operation count of $O(N_g \log_2 N_g)$ is a reasonable estimation. The whole process of calculating the force requires approximately $O(N_p + N_g \log_2 N_g)$ operations. For a 100^3 grid containing one million particles the mesh based method requires approximately a factor of 10^6 less operations than a particle-particle model. Introducing a mesh smoothes the potential over a grid spacing and consequently features smaller than a grid spacing cannot be represented.

The particle-particle–particle-mesh (P^3M) method is a combination of the previous two methods. The force on a particle is split into short and long range components. Short range forces are calculated on a particle-particle basis and the long range forces from a mesh. The number of operations for the P^3M method is approximately $O\Big(N_p(1+\gamma N_p) + N_g \log_2 N_g\Big)$ where the γN_p term is the number of neighbours. This is the number of particles evaluated using the particle-particle method.

A particle-mesh method is chosen for the particle model. This method provides a significant speed advantage over the particle-particle method. It also requires less operations than the P^3M method and is easier to implement. Solving the potential on a mesh requires boundary conditions which can be used to describe the applied field easily and self-consistently.

3.3 Densities in two-dimensions

Two versions of the particle model have been constructed: the first is a purely two-dimensional, and the second is a full three-dimensional model. In the two-dimensional model the particle positions and velocities are restricted to a single plane. This means that the charge distributions calculated in the two-dimensional model represent an infinite column density. This density distribution will result in a electric potential proportional to $\log_e(r)$, where r is the distance from a particle. In the three-dimensional situation the potential will be proportional to $1/r$. No such assumptions are made in the three-dimensional model.

3.4 Interpolation to and from a mesh

In the particle model the particle positions are allowed to be continuous across the computational domain. The fields are defined at the nodes of the mesh. Mathematical functions are required to transfer information from a discrete mesh to continuous positions and vice-versa. These processes can be achieved using interpolation.

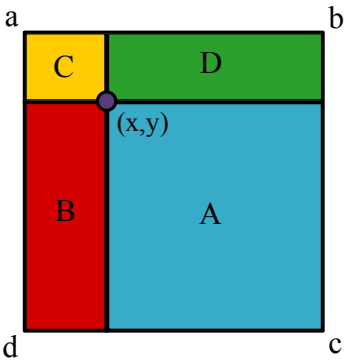

Figure 3.1: Interpolation diagram

The most basic method is called nearest neighbour interpolation; the value is weighted to, or taken to be, the nearest grid point. A better approximation is linear interpolation where the distance between points is used in the calculation. Linear interpolation assumes the data between two points can be represented by a straight line. In two- and three-dimensions these methods are called bilinear and trilinear interpolation.

An intuitive example of how bilinear interpolation works is shown in figure 3.1. When weighting the particle to the grid points, the largest weight is attributed to the nearest grid point. In the example, the area "A" corresponds to corner "a", similarly each of the other areas corresponds to its opposite corner. This intuitive scheme can be expressed mathematically. Suppose corner "a" has co-ordinates (x_a, y_a) and the remaining corners follow the same pattern, then the value of the mesh function M at point (x, y) is

$$\begin{aligned} M(x,y) &= (x_c - x)(y - y_c)M(x_a, y_a) + (x - x_a)(y - y_c)M(x_b, y_b) && (3.1)\\ &\quad +(x - x_a)(y_b - y)M(x_c, y_c) + (x_b - x)(y_a - y)M(x_d, y_d). && (3.2) \end{aligned}$$

If the particle is to be weighted to the mesh then

$$\begin{aligned} M(x_a, y_a) &= (x_c - x)(y - y_c)W(x,y) && (3.3)\\ M(x_b, y_b) &= (x - x_a)(y - y_c)W(x,y) && (3.4)\\ M(x_c, y_c) &= (x - x_a)(y_b - y)W(x,y) && (3.5)\\ M(x_d, y_d) &= (x_b - x)(y_a - y)W(x,y) && (3.6) \end{aligned}$$

where $W(x, y)$ is the value at position (x, y). The method can easily be extended to three-dimensions.

Using the same interpolation function for the calculation of the charge density and the force on the particle ensures that the force of a particle on itself is zero [49].

Higher order interpolation techniques do exist: polynomial, spline or gaussian. These higher order techniques incur an extra computational cost.

3.5 Integration of particle motion

The motion of the individual particles is described by the Lorentz equation,

$$\frac{d\boldsymbol{v}}{dt} = \frac{q}{m}(\boldsymbol{E} + \boldsymbol{v} \times \boldsymbol{B}), \tag{3.7}$$

and

$$\frac{d\boldsymbol{x}}{dt} = \boldsymbol{v} \tag{3.8}$$

where $\boldsymbol{v}$ is the velocity of the particle, $d\boldsymbol{v}/dt$ is the rate of change of velocity, q is the particle charge, m is the particle mass, $\boldsymbol{E}$ and $\boldsymbol{B}$ are the electric and magnetic fields at the particle position. The Lorentz equation is an ordinary differential equation and can be numerically integrated using the Runge-Kutta method.

For an ordinary differential equation of the form

$$\frac{dy}{dt} = f(t, y) \tag{3.9}$$

the simplest numerical integration scheme is the Euler method and it is given by

$$y(t + h) = y(t) + hf(t, y(t)) \tag{3.10}$$

where h is one step of the Euler method. The Euler method is used to solve (3.8). The Runge-Kutta method improves on the Euler method by adding a "trial" step. The derivative is evaluated at the midpoint of the interval. The fourth-order Runge-Kutta formula [98] is

$$\begin{aligned}
k_1 &= h\, f(t, y) && (3.11)\\
k_2 &= h\, f\left(t + \frac{1}{2}h, y + \frac{1}{2}k_1\right) && (3.12)\\
k_3 &= h\, f\left(t + \frac{1}{2}h, y + \frac{1}{2}k_2\right) && (3.13)\\
k_4 &= h\, f\left(t + \frac{1}{2}h, y + k_3\right) && (3.14)\\
y(t + h) &= y(t) + \frac{1}{6}\left(k_1 + 2k_2 + 2k_3 + k_4\right) && (3.15)
\end{aligned}$$

The fourth-order Runge-Kutta method is constructed such that several error terms cancel, leaving a error of $O(h^5)$. Higher order versions of the Runge-Kutta method exist but ratio of the number of calculations to the order of the error increase *i.e.* more work is required to achieve the desired accuracy.

3.6 Algorithm for the particle model

The algorithm for the particle model is

- Set the initial conditions: fix initial spatial and velocity distributions of particles, set time step, number of steps and configure the potential field solver.

- Repeat the following steps to calculate the trajectories of the particles.
  - Calculate the charge density, ρ, on the computational grid:

$$\rho = e(n_+ - n_e) \tag{3.16}$$

    where e is the electron charge, n_+ is the positive ion density and n_e is the electron density. The particle densities are calculated by weighting each particle to its surrounding grid points, this is achieved through interpolation.
  - The electric potential, ϕ, is calculated by solving Poisson's equation,

$$\nabla^2\phi = \frac{\rho}{\varepsilon_0}, \tag{3.17}$$

    where ∇^2 is the Laplace operator and ε_0 is the permittivity of free space. See chapter 4 for further details.
  - Take the gradient of the potential to get the electric field

$$\boldsymbol{E} = -\nabla\phi \tag{3.18}$$

  - Determine the new velocity of each particle. Evaluate (3.7) using the fourth-order Runge-Kutta method.
  - Calculate the effects of collisions on the velocities of the particles and the number of each species. See chapter 5 for further details.
  - Update the particle positions using (3.8).
- Periodically write diagnostic data to file: particle densities, energy distributions, potential field.
- Return to start of loop.

Only the current particle positions and velocities are stored. When the new properties are calculated the initial position and velocities are replaced.

3.7 Electron subcycling

The different masses of the electron and ion mean that the timescales relevant for their motions are different. The lighter electrons move on a much shorter timescale than the ions can. Ions do not travel far on the electron timescale. One way to reduce the computation load is to have a different time step for the electrons and ions. This technique is called electron subcycling or time cycling [48]. For every ion time cycle the electron motion is updated many times. These subcycles have a shorter time step. In this particle model there are twenty electron subcycles per ion timestep.

Chapter 4

Poisson solver

4.1 Finite difference representation

The differential form of Gauss's Law is

$$\nabla \cdot \boldsymbol{E} = \frac{\rho}{\varepsilon_0} \tag{4.1}$$

where ∇ is the gradient operator, ε_0 is the permittivity of free space, $\boldsymbol{E}$ is the electric field vector and ρ is the free charge density. The electric field is the negative gradient of the electric potential, ϕ:

$$E = -\nabla\phi. \tag{4.2}$$

Substituting (4.2) into (4.1) gives

$$\nabla^2\phi = -\frac{\rho}{\varepsilon_0}, \tag{4.3}$$

this is Poisson's equation. The differential operator, sometimes called the Laplace operator, in Cartesian coordinates is

$$\nabla^2 = \frac{\partial^2}{\partial x^2} + \frac{\partial^2}{\partial y^2} + \frac{\partial^2}{\partial z^2}. \tag{4.4}$$

Poisson's equation is a second order partial differential equation. There are some situations where it can be solved analytically. However, these mostly require the use of symmetry to reduce the difficulty. To evaluate this function numerically the partial derivatives can be approximated with finite differences. For a second order differential the centred finite difference approximation is

$$\frac{\partial^2}{\partial x^2} f \approx \frac{f(x+\Delta x) - 2f(x) + f(x-\Delta x)}{(\Delta x)^2} \tag{4.5}$$

thus (4.4) can be approximated by

$$\begin{aligned}\nabla^2 f \approx & \frac{f(x+\Delta x,y,z)+f(x-\Delta x,y,z)-2f(x,y,z)}{(\Delta x)^2} \\ & + \frac{f(x,y+\Delta y,z)+f(x,y-\Delta y,z)-2f(x,y,z)}{(\Delta y)^2} \\ & + \frac{f(x,y,z+\Delta z)+f(x,y,z-\Delta z)-2f(x,y,z)}{(\Delta z)^2}. \end{aligned} \tag{4.6}$$

If the coordinates are changed to array indices such that $f(x,y,z) = f_{ijk}$ and the mesh spacing is set to be equal in all directions($h = \Delta x = \Delta y = \Delta z$), then the operator is

$$\nabla^2 f = \frac{f_{i+1jk} + f_{i-1jk} + f_{ij+1k} + f_{ij-1k} + f_{ijk+1} + f_{ijk-1} - 6f_{ijk}}{h^2}. \tag{4.7}$$

Thus the finite difference approximation of Poisson's equation is

$$\frac{\phi_{i+1jk} + \phi_{i-1jk} + \phi_{ij+1k} + \phi_{ij-1k} + \phi_{ijk+1} + \phi_{ijk-1} - 6\phi_{ijk}}{h^2} = \frac{\rho_{ijk}}{\varepsilon_0} \tag{4.8}$$

4.2 Boundary conditions

There several boundary conditions which are relevant for plasma physics. Laboratory plasmas are typically produced inside a discharge vessel which will include conducting walls, electrodes and/or dielectric barriers. Also the vessel may be open to the atmosphere or be part of an array of devices. All of these boundary types must be represented numerically for the field to be solved on the computational domain.

4.2.1 Dirichlet boundaries

Conducting boundaries, internal electrodes and boundary electrodes require a fixed potential this can be achieved by using Dirichlet boundary conditions. They can be simply expressed as

$$\phi_{ijk} = V_{ijk} \tag{4.9}$$

where V is a prescribed constant and (i,j,k) is the index of a point on the boundary.

4.2.2 von Neumann boundaries

If the physical boundary can be considered far away from the computational edge von Neumann boundary conditions can be used. The von Neumann boundary prescribes the value of the gradient of the function normal to the boundary. Prescribing the gradient g at the boundary is given by

$$\nabla\phi \cdot \boldsymbol{n} = g \tag{4.10}$$

where $\boldsymbol{n}$ is the normal vector to the boundary. The most common method of representing a Neumann boundary condition is to introduce ghost points. A one dimensional system is

considered to illustrate the process. Consider a computational domain extending from 1 to N. Setting both boundaries as Neumann boundaries and adding ghost points at 0 and $N+1$ the system of equations is

$$\frac{\phi_2 - \phi_0}{2h} = g_0 \qquad \text{if } i = 0, \tag{4.11}$$

$$\frac{\phi_{i+1} + \phi_{i-1} - 2\phi_i}{h^2} = \frac{\rho_i}{\varepsilon_0} \qquad \text{if } i \in [1, N] \tag{4.12}$$

$$\frac{\phi_{N-1} - \phi_{N+1}}{2h} = g_N \qquad \text{if } i = N+1 \tag{4.13}$$

The ghost points can be eliminated by altering the finite difference equation at the boundary points. Equation (4.11) can be rearranged to give an expression for ϕ_0

$$\phi_0 = \phi_2 - 2hg_0 \tag{4.14}$$

this expression can be substituted into (4.12) where $i = 1$

$$\frac{2\phi_2 - 2hg_0 - 2\phi_1}{h^2} = \frac{\rho_1}{\varepsilon_0} \tag{4.15}$$

A similar treatment for the second boundary gives the following system of equations

$$\frac{2\phi_2 - 2\phi_1}{h^2} = \frac{\rho_1}{\varepsilon_0} + \frac{2g_0}{h} \qquad \text{for } i = 1, \tag{4.16}$$

$$\frac{\phi_{i+1} + \phi_{i-1} - 2\phi_i}{h^2} = \frac{\rho_i}{\varepsilon_0} \qquad \text{for } i \in [2, N-1] \tag{4.17}$$

$$\frac{2\phi_{N-1} - 2\phi_N}{h^2} = \frac{\rho_N}{\varepsilon_0} + \frac{2g_N}{h} \qquad \text{for } i = N \tag{4.18}$$

4.2.3 Periodic boundaries

If a small volume of the overall plasma is to be simulated and the surrounding plasma can be considered to have the same properties or the device is part of an array of many devices periodic boundaries may be required. Using the one dimensional example from above a periodic boundary condition can be satisfied by setting $\phi_0 = \phi_N$ and $\phi_{N+1} = \phi_1$ this gives the equations

$$\frac{\phi_2 + \phi_N - 2\phi_1}{h^2} = \frac{\rho_1}{\varepsilon_0} \qquad \text{if } i = 1, \tag{4.19}$$

$$\frac{\phi_{i+1} + \phi_{i-1} - 2\phi_i}{h^2} = \frac{\rho_i}{\varepsilon_0} \qquad \text{if } i \in [2, N-1] \tag{4.20}$$

$$\frac{\phi_1 + \phi_{N-1} - 2\phi_N}{h^2} = \frac{\rho_N}{\varepsilon_0} \qquad \text{if } i = N+1 \tag{4.21}$$

4.2.4 Dielectric interfaces

The inclusion of dielectric walls in the computational domain can be achieved by altering the finite difference equation (4.8) to include spatially varying values of the dielectric constant ε. Figure 4.1 shows the intersection of four different dielectrics on a two dimensional

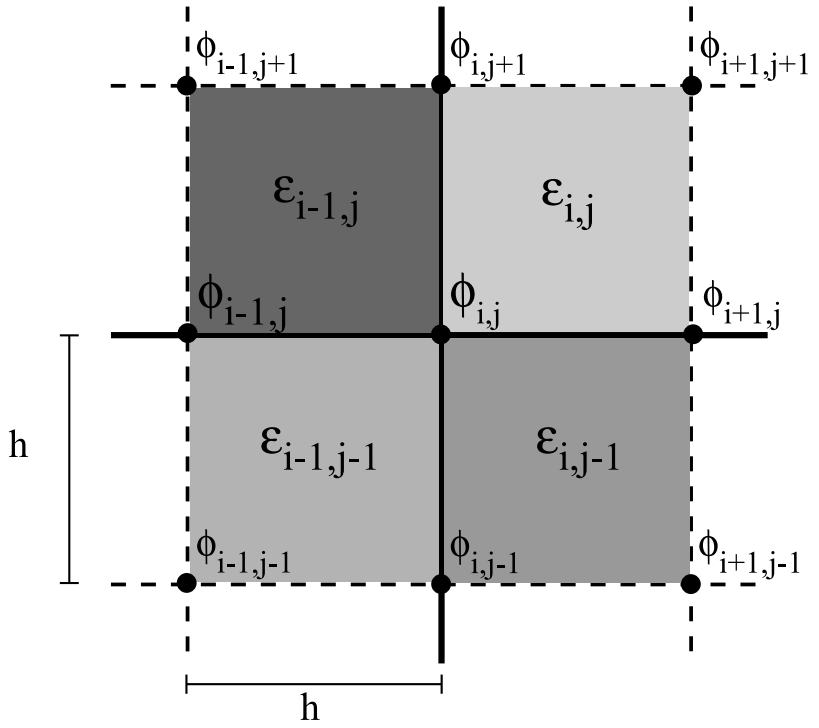

Figure 4.1: Diagram showing labelling of points for potential and dielectrics.

mesh. The dielectrics are defined at the cell centres and the values of the potential (and charge density) are defined on the vertices. The mean values of the permittivity along each mesh line are used. Thus the two dimensional Poisson's equation with a varying dielectric constant is [99]

$$\frac{(\varepsilon_{ij}+\varepsilon_{ij-1})(\phi_{i+1j}-\phi_{ij})}{2h^2}+\frac{(\varepsilon_{i-1j}+\varepsilon_{i-1j-1})(\phi_{i-1j}-\phi_{ij})}{2h^2}$$
$$+\frac{(\varepsilon_{i-1j}+\varepsilon_{ij})(\phi_{ij+1}-\phi_{ij})}{2h^2}+\frac{(\varepsilon_{ij-1}+\varepsilon_{i-1j-1})(\phi_{ij-1}-\phi_{ij})}{2h^2}=\rho_{ij}. \quad (4.22)$$

Re-expressing gives

$$(\varepsilon_{ij}+\varepsilon_{ij-1})\phi_{i+1j}+(\varepsilon_{i-1j}+\varepsilon_{i-1j-1})\phi_{i-1j}+(\varepsilon_{i-1j}+\varepsilon_{ij})\phi_{ij+1}$$
$$+(\varepsilon_{ij-1}+\varepsilon_{i-1j-1})\phi_{ij-1}-2(\varepsilon_{ij}+\varepsilon_{ij-1}+\varepsilon_{i-1j}+\varepsilon_{i-1j-1})\phi_{ij}=2h^2\rho_{ij} \quad (4.23)$$

4.3 Numerical methods

There are many different methods that can be used to solve the finite difference formulation of Poisson's equation. The methods can be split into two categories: iterative and direct. Iterative solvers continually refine an approximate solution until the approximation converges to the solution. Direct methods solve the field in a single step. A good overview of various solution techniques can be found in Hockney and Eastwood [49]. The Multigrid technique that follows is not included in that discussion.

4.4 Iterative methods

4.4.1 Linear systems

The finite difference equations describing Poisson's equation on a computational mesh can be written as a linear system of equations. To illustrate, consider the one dimensional case with N grid points and Dirichlet boundary conditions at both ends. The problem is fully described by

$$\phi_1 = V_1 \qquad \text{if } i = 1, \tag{4.24}$$

$$\frac{\phi_{i+1} + \phi_{i-1} - 2\phi_i}{h^2} = \frac{\rho_i}{\varepsilon_0} \qquad \text{if } i \in [2, N-1] \tag{4.25}$$

$$\phi_N = V_N \qquad \text{if } i = N \tag{4.26}$$

This set of equations can be written as a linear system

$$\frac{1}{h^2}\begin{bmatrix} h^2 & & & & & & & \\ 1 & -2 & 1 & & & & & \\ & 1 & -2 & 1 & & & & \\ & & & \ddots & & & & \\ & & & 1 & -2 & 1 & & \\ & & & & 1 & -2 & 1 & \\ & & & & & & h^2 \end{bmatrix} \cdot \begin{bmatrix} \phi_1 \\ \phi_2 \\ \phi_3 \\ \vdots \\ \phi_{N-2} \\ \phi_{N-1} \\ \phi_N \end{bmatrix} = \frac{1}{\varepsilon_0}\begin{bmatrix} \varepsilon_0 V_1 \\ \rho_2 \\ \rho_3 \\ \vdots \\ \rho_{N-2} \\ \rho_{N-1} \\ \varepsilon_0 V_N \end{bmatrix}.$$

The matrix of finite difference coeficients in the one-dimensional case is tridiagonal, *i.e.* the only non-zero elements are those on the main diagonal and the first diagonals above and below. The linear system can be written in matrix notation as

$$L \cdot \bar{\phi} = \bar{\rho} \tag{4.27}$$

where $\bar{\phi}$, $\bar{\rho}$ and L are the electric potential vector, charge density vector and an $N \times N$ matrix of finite difference coefficients respectively. The constants h^2 and ε_0 have been absorbed in the matrix and the charge density for notational convenience. Two and three dimensional problems can also be cast as linear systems, for example a two dimensional system (of size N_x, N_y) with Dirichlet boundaries would have the form

$$L_{2d} \cdot \bar{\phi} = \bar{\rho} \tag{4.28}$$

explicitly this is

$$\frac{1}{h^2}\begin{bmatrix} h^2 I & & & & & & & \\ I & L-2I & I & & & & & \\ & I & L-2I & I & & & & \\ & & & \ddots & & & & \\ & & & I & L-2I & I & & \\ & & & & I & L-2I & I & \\ & & & & & & h^2 I \end{bmatrix} \cdot \begin{bmatrix} \phi_{1,y} \\ \phi_{2,y} \\ \phi_{3,y} \\ \vdots \\ \phi_{N_x-2,y} \\ \phi_{N_x-1,y} \\ \phi_{N_x,y} \end{bmatrix} = \frac{1}{\varepsilon_0}\begin{bmatrix} \varepsilon_0 V_{1,y} \\ \rho_{2,y} \\ \rho_{3,y} \\ \vdots \\ \rho_{N_x-2,y} \\ \rho_{N_x-1,y} \\ \varepsilon_0 V_{N_x,y} \end{bmatrix}$$

where I is the $N_y \times N_y$ identity matrix, L_{2d} is a $N_x N_y \times N_x N_y$ block matrix, L has a similar form as above and the potential and charge density variables take the form

$$\beta_{i,y} = \begin{bmatrix} \beta_{i,1} \\ \beta_{i,2} \\ \vdots \\ \beta_{i,N_y-1} \\ \beta_{i,N_y} \end{bmatrix}$$

At first glance, calculating the solution of the linear systems in (4.27) and (4.37) appears trivial. Pre-multiplying through by the inverse of the matrix gives the solution

$$L^{-1} \cdot L \cdot \bar{\phi} = L^{-1} \cdot \bar{\rho} \tag{4.29}$$

$$\bar{\phi} = L^{-1} \cdot \bar{\rho}. \tag{4.30}$$

To evaluate the solution $\bar{\phi}$ numerically the inverse of the matrix L must be calculated. Determining the inverse of a matrix is the difficult part. There are an number of algorithms that can be used to calculate a matrix's inverse, such as: Gauss-Jordan elimination or LU decomposition. For large values of $N_x \times N_y$ the calculation of the inverse matrix is very slow.

Large linear systems are often solved iteratively. An approximation of the solution is made and the finite difference equations are used to update each value in the solution. For the interior points (4.8) the new approximation ϕ'_{ijk} is

$$\phi'_{ijk} = \frac{1}{6}\Big(\phi_{i+1jk} + \phi_{i-1jk} + \phi_{ij+1k} + \phi_{ij-1k} + \phi_{ijk+1} + \phi_{ijk-1} - h^2\rho_{ijk}\Big) \tag{4.31}$$

where ϕ_{xyz} is the current approximation. The application of (4.31) is called a Jacobi iteration.

Returning to the linear system, the matrix of finite difference coefficients can be split into

$$L = A - B. \tag{4.32}$$

This allows the linear system to be written as

$$A\phi - B\phi = \rho \tag{4.33}$$

$$A\phi' = B\phi + \rho \tag{4.34}$$

where ϕ' is the new approximation and the vector notation $\bar{\theta}$ has been left out for notational ease. We now have a new linear system with matrix A; solution ϕ' and right hand side $B\phi + \rho$. This linear system (4.34) can be made much easier to solve by splitting L such that A is easily invertible. For the Jacobi iteration A is the diagonal of L.

The inverse of a triangular matrix is relatively easy to calculate. If A is set to be the full lower triangular portion of L, i.e.

$$A = \begin{cases} L_{ij}, & \text{when } i \leqslant j, \\ 0, & \text{when } i > j \end{cases} \tag{4.35}$$

then B is the the strictly upper triangular portion of L. Figure 4.2 shows the entries in the lower triangular, upper triangular and diagonal portions. This matrix splitting results in a Gauss-Seidel iteration.

$$\begin{bmatrix} D & U & U & U & U \\ L & D & U & U & U \\ L & L & D & U & U \\ L & L & L & D & U \\ L & L & L & L & D \end{bmatrix}$$

Figure 4.2: An example showing the entries in the strictly lower (L), diagonal (D) and strictly upper (U) parts of a square matrix.

A useful variation of Gauss-Seidel is Successive-Over-Relaxation (SOR). The expression for the updated approximation using SOR is

$$(D + \omega L)\phi' = \Big(D(1-\omega) - \omega U\Big)\phi + \omega\rho \tag{4.36}$$

where ω is a single value constant, D, L and U are the diagonal, strictly lower and strictly upper parts of L. The choice of ω determines the convergence rate: the convergence rate can be increased or decreased depending on the value of ω. The optimal value of ω is dependent on the the matrix of finite difference coefficients L and the value of ρ.

There are more iterative methods [49] for the numerical solution of equations of the form (4.27) but they will not be discussed here.

4.5 The Multigrid method

The problem with most iterative methods is that they converge slowly. They are good at smoothing errors on small spatial scales but often fail at reducing large scale errors. This can be seen by examining the expression of an iteration. The Jacobi iteration for an interior grid point (4.31) shows that the new approximation of the solution of the grid point depends only on the neighbouring points. The approximate solution at a point does not explicitly depend on the boundary conditions or even on a point more than one grid cell away. This means that the effects of boundary conditions and distant features of the solution require many iterations to 'propagate' through the solution. The high spatial frequency smoothing property of iterative methods will turn out to be very important. Some iterative methods, such as conjugate gradients, reduce the error on multiple scales but are still computationally intensive.

The next important idea is the approximation of smooth functions. A smoothly varying quantity can be represented on a coarser scale with little loss in accuracy. Iterations carried out on a coarse grid are less expensive in computational terms. These two ideas: smoothing and coarse grid approximation form the basis of a fast and efficient numerical technique called Multigrid. This method utilises smoothing on multiple scales to quickly reduce the error in the approximation. The following description of the Multigrid method is based on the books by Trottenberg *et al.* [100] and Briggs *et al.* [101].

The Multigrid method is a framework for the application of the iterative methods discussed earlier. It should not be confused with adaptive mesh refinement [102] where the

computational domain contains meshes with different resolutions. Adaptive meshes can be included a Multigrid implementation [100] but this is not a standard part of the Multigrid method and will not be discussed here.

4.5.1 Mathematical primer

Before describing the details of the Multigrid method some mathematical definitions must be made. Let

$$L \cdot u = f \tag{4.37}$$

be a linear system, where u and f are vectors of length n and L is an invertible $n \times n$ matrix. The approximate solution of the linear system is defined to be

$$\tilde{u} = u + v, \tag{4.38}$$

where v is called the correction and is simply the difference between the true solution u and the approximate solution $\tilde{u}$. Another measurement of the error is the defect

$$d = f - L \cdot \tilde{u}. \tag{4.39}$$

Substituting the defect (4.39) into the expression for the linear system (4.37) gives

$$\begin{aligned} L \cdot u &= d + L \cdot \tilde{u} && (4.40)\\ L \cdot (u - \tilde{u}) &= d && (4.41)\\ L \cdot v &= d. && (4.42) \end{aligned}$$

This re-expression of the original linear system is called the defect equation. It is no easier to solve than the original linear system as it still requires the calculation of the inverse matrix.

Stencil notation is often used when defining grid operators. It is an array representation of the coefficients that are applied to the arguments. A general two dimensional stencil, $\mathcal{S}$, would be written as

$$\mathcal{S} = \begin{bmatrix} s_{i-1,j-1} & s_{i,j-1} & s_{i+1,j-1} \\ s_{i-1,j} & s_{i,j} & s_{i+1,j} \\ s_{i-1,j+1} & s_{i,j+1} & s_{i+1,j+1} \end{bmatrix}. \tag{4.43}$$

For example, the two-dimensional finite difference Poisson equation operator can be written in stencil notation,

$$\begin{aligned} \nabla^2 u &= -\frac{1}{h^2}(u_{i-1,j} + u_{i+1,j} + u_{i,j-1} + u_{i,j+1} - 4u_{i,j}), && (4.44)\\ &= \frac{1}{h^2}\begin{bmatrix} 0 & -1 & 0 \\ -1 & 4 & -1 \\ 0 & -1 & 0 \end{bmatrix} u_{i,j}, && (4.45) \end{aligned}$$

the array in (4.45) is the stencil of the operator. The centre point of the stencil gives the coefficient of the point $u_{i,j}$. The outside points of the stencil relate to the points surrounding the point $u_{i.j}$.

There are three main components of the Multigrid method: smoothing, restriction and interpolation. The smoothing step has already been discussed in terms of iterative solvers (*e.g.* jacobi (4.31) and Gauss-Seidel iterations). The smoothing of the errors is simply a single iterative step. The process of transferring information from a fine mesh to a coarse mesh is called restriction and interpolation is the inverse process.

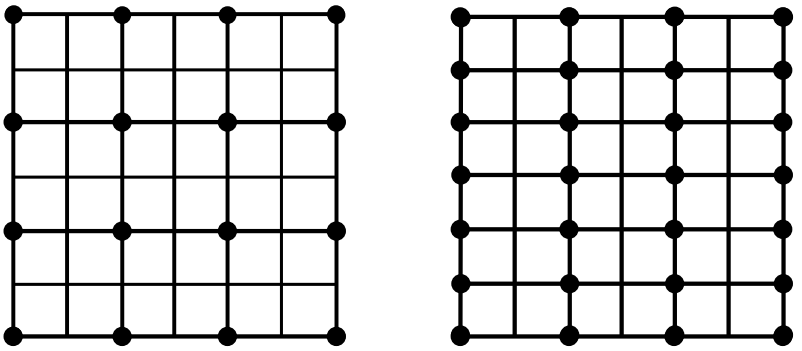

(a) Standard Coarsening **(b)** Semi-coarsening

Figure 4.3: The diagrams show examples of: a) standard coarsening, where the mesh spacing is doubled in both directions; and b) semi-coarsening where the mesh spacing has been doubled in only the x-direction, on a two-dimensional grid. The black dots (•) represent the coarse grid points and the intersections of each line are points on the fine mesh.

4.5.2 Grid coarsening

Before the restriction and interpolation operators van be defined the refinement between grids must be chosen. The most basic strategy is standard coarsening; the grid spacing is doubled in each direction, an example of standard coarsening is shown in figure 4.3(a). Other types of coarsening are possible such as semi-coarsening which involves increasing the grid spacing differently in at least one direction, see 4.3(b). Certain coarsening strategies may be suited to particular problems, for example if the differential equation contains an anisotropic term then semicoarsening along the preferred direction can aid the solution process. In the following discussion and implementation of the Multigrid process standard coarsening will be used.

4.5.3 The restriction operator

The restriction function maps information on a fine grid to a coarse grid. If x_h and x_{2h} are some property on the fine and coarse mesh respectively then the restriction function, $\mathcal{R}$, is

$$x_{2h} = \mathcal{R}(x_h). \tag{4.46}$$

The simplest restriction operator is an injection operator where the values at the coarse grid points are taken as the values at the coincident fine grid points. One of the most common restriction operators is the Full Weighting operator which samples the fine points surrounding the coarse grid point.

The one dimensional Full Weighting restriction stencil is

$$\mathcal{R}_{1d} = \frac{1}{4}[1 \quad 2 \quad 1]. \tag{4.47}$$

The restriction stencil is applied to each fine grid point that coincides with a coarse grid point, e.g.

$$x_{2i} = \mathcal{R}_{1d} x_i = (x_{i-1} + 2x_i + x_{i+1})/4. \tag{4.48}$$

The restriction stencil in an arbitrary number of dimensions can be constructed from the tensor products of the one dimensional operator. Thus the two- and three-dimensional restriction stencils are

$$\mathcal{R}_{2d} = \frac{1}{16} \begin{bmatrix} 1 & 2 & 1 \\ 2 & 4 & 2 \\ 1 & 2 & 1 \end{bmatrix}, \tag{4.49}$$

and

$$\mathcal{R}_{3d} = \frac{1}{64} \left\{ \begin{bmatrix} 1 & 2 & 1 \\ 2 & 4 & 2 \\ 1 & 2 & 1 \end{bmatrix}, \begin{bmatrix} 2 & 4 & 2 \\ 4 & 8 & 4 \\ 2 & 4 & 2 \end{bmatrix}, \begin{bmatrix} 1 & 2 & 1 \\ 2 & 4 & 2 \\ 1 & 2 & 1 \end{bmatrix} \right\}. \tag{4.50}$$

A similar strategy of using tensor products can be used for points next to a boundary. The one dimensional restriction operator at a boundary is

$$\mathcal{R}^b_{1d} = \frac{1}{4}[2 \quad 2]. \tag{4.51}$$

The restriction operator at a corner is the tensor product of one-dimensional boundary operators, for example the operator at a two-dimensional corner is

$$\mathcal{R}^c_{2d} = \frac{1}{16} \begin{bmatrix} 4 & 4 \\ 4 & 4 \end{bmatrix}, \tag{4.52}$$

and at a two-dimensional boundary

$$r^b_{2d} = \frac{1}{16} \begin{bmatrix} 2 & 2 \\ 4 & 4 \\ 2 & 2 \end{bmatrix}. \tag{4.53}$$

4.5.4 The interpolation operator

The interpolation function maps information on a coarse grid to a fine grid. For most cases linear interpolation is a suitable choice for the transfer operator. For more complicated systems of equation higher order interpolations may be desirable. Interpolation has already been discussed in section 3.4. The same linear interpolation technique is used in the Multigrid method. For completeness the interpolation function is explicitly stated again. The interpolation function, $\mathcal{I}$, is defined as follows

$$x_h = \mathcal{I}(x_{2h}), \tag{4.54}$$

where x_h and x_{2h} are the same variable defined on the fine and coarse grids respectively.

Consider the point $x_h(i, j, k)$ on the fine mesh. The subscript h denotes the mesh spacing and i, j and k are the mesh indices. If the fine mesh point is coincident with a coarse mesh point, *i.e.* $i, j, k \in G_{2h}$, then the fine grid point takes the same value as the coarse grid point. When the indices of the fine point are not coincident with any of the coarse mesh indices then the value on the fine mesh is the mean of the surrounding eight coarse values. Figure 4.4 shows a coarse mesh cell with the fine grid refinements. Equation (4.55) shows

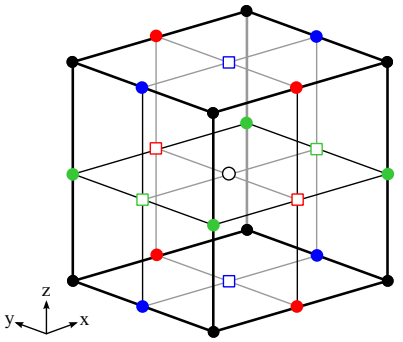

Figure 4.4: The black dots (•) represent the coarse grid points and all the other markers on the cube are points on the fine mesh. The markers at the fine grid points correspond to the expression for the interpolated value given in (4.55).

how trilinear interpolation is applied when transferring from a coarse (G_{2h}) to a fine mesh in three-dimensions

$$
x_h(i,j,k) = \begin{cases}
x_{2h}(i,j,k), & \text{if } i,j,k \in G_{2h} \ (\bullet) \\
\frac{1}{2}\Big(x_{2h}(i-h,j,k) + x_{2h}(i-h,j,k)\Big), & \text{if } j,k \in G_{2h} \ (\bullet) \\
\frac{1}{2}\Big(x_{2h}(i,j-h,k) + x_{2h}(i,j+h,k)\Big), & \text{if } i,k \in G_{2h} \ (\bullet) \\
\frac{1}{2}\Big(x_{2h}(i,j,k-h) + x_{2h}(i,j,k+h)\Big), & \text{if } i,j \in G_{2h} \ (\bullet) \\
\frac{1}{4}\Big(x_{2h}(i-h,j-h,k) + x_{2h}(i+h,j-h,k) & \\
\quad + x_{2h}(i-h,j+h,k) + x_{2h}(i+h,j+h,k)\Big), & \text{if } k \in G_{2h} \ (\square) \\
\frac{1}{4}\Big(x_{2h}(i-h,j,k-h) + x_{2h}(i+h,j,k-h) & \\
\quad + x_{2h}(i-h,j,k+h) + x_{2h}(i+h,j,k+h)\Big), & \text{if } j \in G_{2h} \ (\square) \\
\frac{1}{4}\Big(x_{2h}(i,j-h,k-h) + x_{2h}(i,j+h,k-h) & \\
\quad + x_{2h}(i,j-h,k+h) + x_{2h}(i,j+h,j+h)\Big), & \text{if } i \in G_{2h} \ (\square) \\
\frac{1}{8}\Big(x_{2h}(i+h,j+h,k-h) + x_{2h}(i+h,j-h,k-h) & \\
\quad + x_{2h}(i-h,j+h,k-h) + x_{2h}(i-h,j-h,k-h) & \\
\quad + x_{2h}(i+h,j+h,k+h) + x_{2h}(i+h,j-h,k+h) & \\
\quad + x_{2h}(i-h,j+h,k+h) + x_{2h}(i-h,j-h,k+h)\Big), & \text{if } i,j,k \notin G_{2h} \ (\circ)
\end{cases} \tag{4.55}
$$

4.5.5 The Multigrid algorithm

Having defined the key components of the method, the Multigrid algorithm can be presented. The simplest Multigrid algorithm is the Two-grid correction scheme. This version has little practical use as the reduction in computation offered by a single coarse grid is not significant however, it is an instructive example to begin with. The steps are as follows:

- Smooth the solution on the finest grid by calculating a new approximation $\tilde{u}_h$ [see (4.34)].
- Compute the defect on the finest grid: $d_h = f_h - L_h \cdot \tilde{u}_h$.
- Restrict the defect to coarser grid: $d_{2h} = \mathcal{R}(d_h)$.
  - Calculate the correction (v_{2h}) on the coarse grid by solving the defect equation: $L_{2h} \cdot v_{2h} = d_{2h}$
  - Interpolate the correction from the coarse grid to the fine grid: $v_h = \mathcal{I}(v_{2h})$.
- Update the solution on the finest grid: $\tilde{u} = \tilde{u} + v_h$

- Smooth the solution.

The final step is another smoothing operation, this is to reduce the error introduced by the interpolation on to the fine grid. The Multigrid algorithm is still an iterative solution method, many iterations of the Two-grid correction scheme or any Multigrid process may be required to reach convergence.

The generalisation to a true many grid Multigrid process is achieved by recognising that the defect equation (4.42) has the same form as the original system of equations. This similarity means that the defect equation can also be solved using a Two-grid correction scheme, introducing a third grid. This recursion can be continued for many sets of defect equations until the grid is small enough that the defect equation can be solved exactly in a short amount of time.

The algorithm for a Multigrid cycle can now be written down. To simplify the naming of the variables, the grid spacing notation is replaced with numbering of the grids from coarsest (1) to finest (k). The existence of the grid transfer and the finite difference operator, for each grid level, is assumed. The algorithm is:

Multigrid function: $u_k = f_{mg}(k, \gamma, u_k, L_k, f_k, \nu_1, \nu_2)$

1. Smoothing: carry out ν_1 smoothing iterations.
2. Calculate the defect: $d_k = f_k - L_k \cdot \tilde{u}_k$
3. Restrict the defect to coarser grid: $d_{k-1} = \mathcal{R}(d_k)$.
4. Calculate the approximate correction, v_{k-1}, using the defect equation $L_{k-1} \cdot v_{k-1} = d_{k-1}$.
   - If $k = 1$: Solve the defect equation directly.
   - If $k > 1$: Use the Multigrid function γ times with a zero value approximation to solve for the correction:

     $$v_{k-1} = f_{mg}(k-1, \gamma, 0, L_{k-1}, d_{k-1}, \nu_1, \nu_2)$$

5. Interpolate the correction: $v_k = \mathcal{I}(v_{k-1})$.
6. Apply the correction: $u_k = u_k + v_k$.
7. Smooth the solution ν_2 times.

The structure of the Multigrid cycle is controlled by the parameter γ. If $\gamma = 1$ then the structure of the process is called a "V-cycle" and for $\gamma = 2$ the structure is called a "W-cycle". Figure 4.5 shows the structures of V- and W-cycles. The efficiency of the Multigrid algorithm can be strongly influenced by the parameters γ, ν_1 and ν_2. There are no single values of these parameters which provide the most efficient Multigrid algorithm. The vaules of the parameters resulting in the most efficient solution depend on the linear system being solved.

4.5.6 Finite difference operator

Section 4.4 showed how the system of finite difference equations representing the Poisson's equation on a grid could be written as a matrix. The interpolation and restriction operators

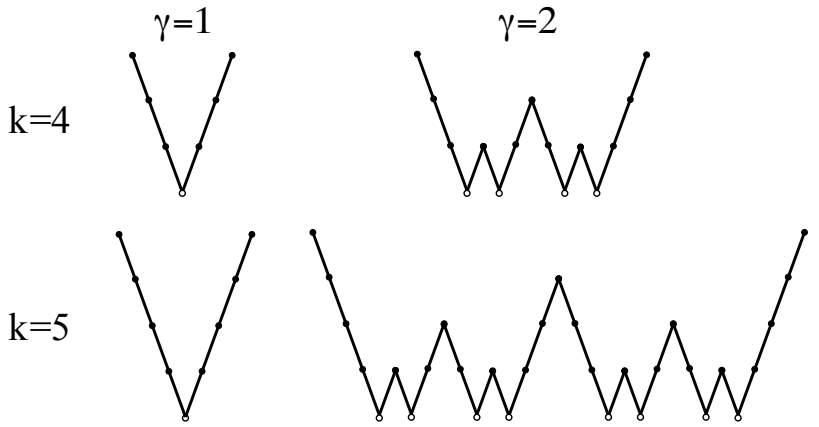

Figure 4.5: Diagrams showing V-cycles and W-cycles.

can also be written as matrices. The coefficients of theses matrices can be taken from the stencil notation. When the operators are written as matrices the functions are a single matrix multiplication.

If there are N grid points on the fine grid and M grid points on the coarse grid then the interpolation matrix will be a $M \times N$ matrix and the restriction matrix will be a $N \times M$ matrix.

From the description of the Multigrid cycle it is clear that the finite difference matrix for each grid level is required. The finite difference matrix for each grid level can be calculated using the interpolation (I) and restriction (R) matrices. If L_h is the operator on a grid with spacing h then the operator on the next coarsest grid is given by

$$L_{2h} = RL_hI. \tag{4.56}$$

4.5.7 Full Multigrid method

The number of steps required to converge a solution using a Multigrid method depends on the initial approximation. This is true for any iterative method. Obviously a good initial approximation will converge in less steps than a poor approximation.

One way to get a good initial approximation is to interpolate the exact, or converged, solution from a coarse grid. When combined with Multigrid cycles, this process is called Full Multigrid. The exact solution is approximated on the coarsest grid and it is then interpolated to a finer grid. The approximation on the finer grid is then smoothed using V- or W-cycles and then interpolated to the next finest grid. Figure 4.6 shows the structure of a Full Multigrid cycle. The diagram shows only one V-cycle for each new grid level but several may be required to converge the solution before the next interpolation.

The Full Multigrid algorithm is

For $k = 1$ solve $L_1 \cdot u_1 = f_1$.

For k =2,...,k:

$u_{k+1} = \mathcal{I}(u_k)$.
$u_{k+1} = f_{mg}(k+1, \gamma, u_{k+1}, L_k, f_k, \nu_1, \nu_2)$

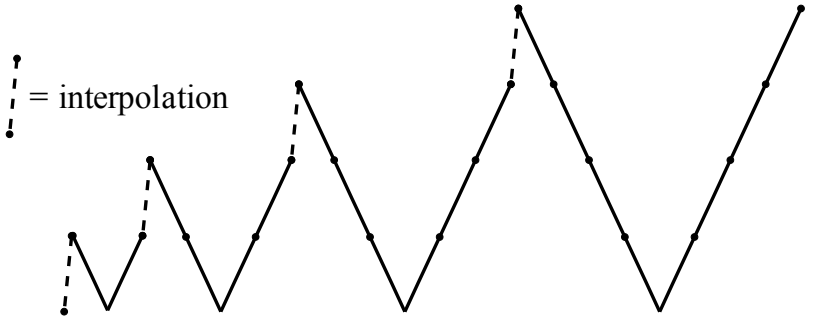

Figure 4.6: Diagram showing a Full Multigrid cycle. An exact solution is calculated on the coarsest grid and the interpolated to a finer grid. The solution of the second level is smoothed and then interpolated to the next finest grid level. The process continues until the finest grid is reached.

4.5.8 Comparison of standard iterative and multigrid methods

The advantge of the Multigrid method over a standard iterative method is best shown in an example. To compare the convergence of standard and Multigrid iterative methods the solution to the 1-dimensional Laplace equation,

$$\frac{d^2\phi}{dx^2} = 0, \tag{4.57}$$

is computed using each method. When the boundaries are fixed at zero, the solution is zero at all points.

The initial approximation is set to

$$\phi = \sin\left(\frac{2\pi x}{N_x}\right) + 0.01\sin\left(\frac{20\pi x}{N_x}\right) + 0.00005\sin\left(\frac{200\pi x}{N_x}\right), \tag{4.58}$$

where N_x is the number of grid points. This approximation is chosen to highlight the inadequacy of standard iterative solvers, it has errors on multiple length scales. Standard Gauss-Seidel iterations are compared to Gauss-Seidel iterations used in a Multigrid method. The top panel of figure 4.7 shows the defect of the initial approximation. The subsequent panels in the figure show the evolution of the defect over many iterations. The Gauss-Seidel iterations quickly smooth the very small scale errors but do not cope well with the mid- and long-scale errors. The Multigrid solver reduces the error substantially on all scales after a small number of cycles. The Multigrid cycles do have a greater computational cost, as seen in the time taken for a single iteration. Even when the computation time is considered the Multigrid still has a greater convergence rate.

The convergence rate can be seen in figure 4.8: the dependence of the root-mean-square (RMS) of the defect on the number of iterations and the elapsed computation time are

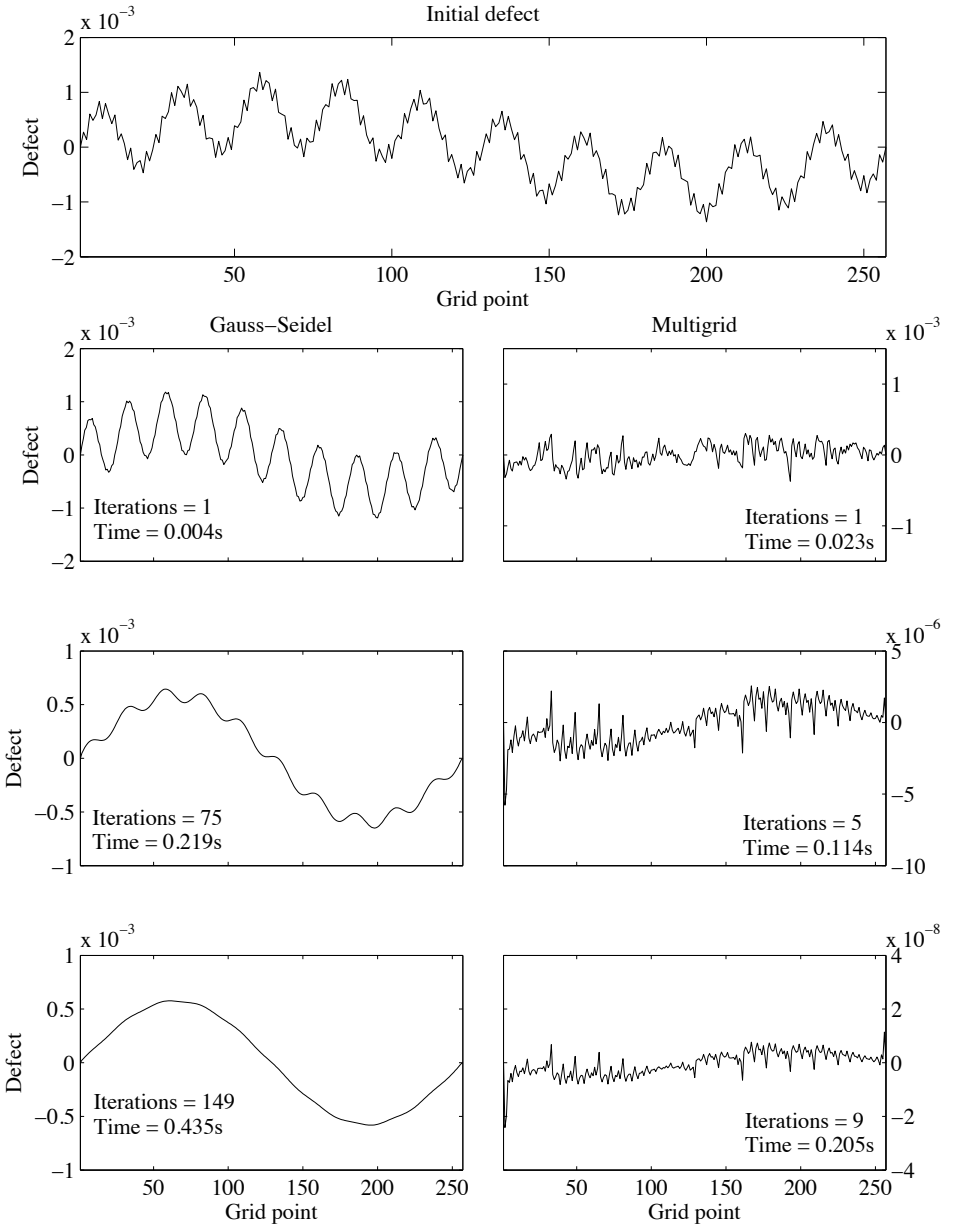

Figure 4.7: Plots showing the evolution of the defect for Gauss-Seidel and Multigrid iterations. Note that the scales for defect in the Multigrid method and the Gauss-Seidel defect are different.

plotted in figures 4.8(a) and 4.8(b) respectively. The several thousand Gauss-Seidel iterations are required to give an error equal to a handful of Multigrid cycles. In terms of computation time, the Multigrid method converges a factor 300 faster.

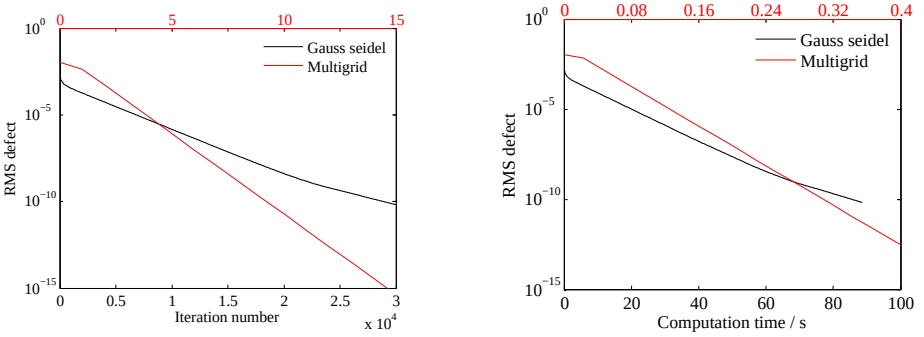

(a) The dependence of the RMS defect on the number of iterations.

(b) The dependence of the RMS defect on the elapsed computational time.

Figure 4.8: The convergence rates, in terms of number of iterations and computation time, for standard Gauss-Seidel and Mulitgrid Gauss-Seidel iterations. The convergence of the Multigrid method is denoted by the red line and is related to the top x-axis (also coloured red). The bottom x-axis relates to the Gauss-Seidel method (black line).

4.5.9 Tuning the Multigrid implimentation

There are many options for the actual implementation of a Multigrid solver: smoothing method, coarsening strategy, grid transfer operators and cycle type. Standard coarsening and full weighting transfer operators have already been chosen. Although basic, these choices are more than suitable for the solution of Poisson's equation.

The convergence of different smoothing techniques in a Multigrid framework is investigated by solving Poisson's equation for a random distribution of charge on a 2-dimensional domain. Figure 4.9 shows the convergence rate for different smoothing types in a V-cycle. The Gauss-Seidel and SOR iterations have similar convergence rates. The time dependence of the different smoothing methods is shown in figure 4.9(b). There is little difference between the time for the different iterations; Jacobi iterations taking the shortest time and SOR taking the longest.

For the same problem figure 4.10 shows the convergence rate for different cycle types using Gauss-Seidel smoothing. Figure 4.10(a) shows that increasing the number of smoothing steps per iteration increases the rate of convergence. The W(2,2) has the most smoothing operations of those shown in the plot and consequently it convergence in the fewest number of iterations. However, increasing the number of smoothing operations comes with a computational cost. Figure 4.10(b) shows the elapsed time for each iteration. The most efficient cycle is a V(1,2) cycle.

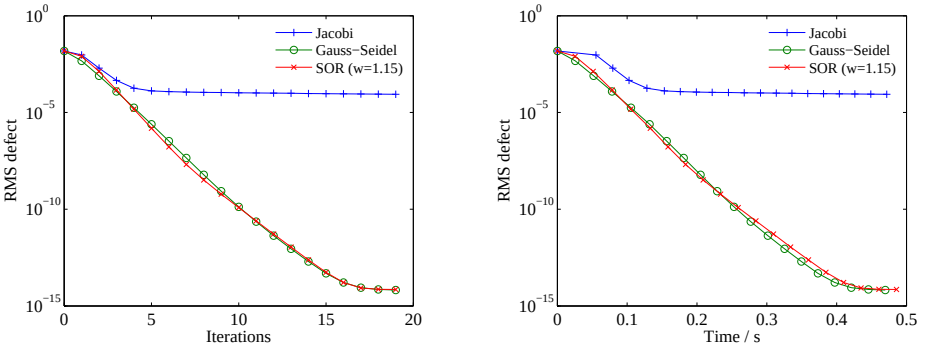

(a) The evolution of the defect for series of iterations.

(b) Time dependence of the defect for different smoothing techniques.

Figure 4.9: The evolution of the defect for different smoothing iterations.

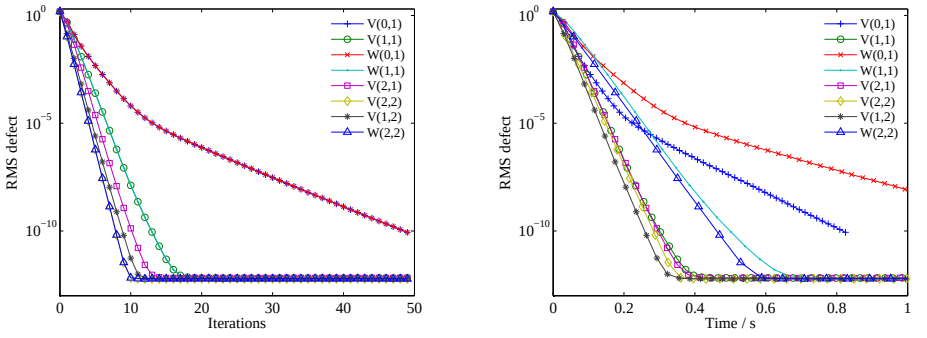

(a) Variation of root-mean-squared defect with number of iterations.

(b) Variation of root-mean-squared defect with time elapsed.

Figure 4.10: The diagrams show comparisons of V- and W-cycles.

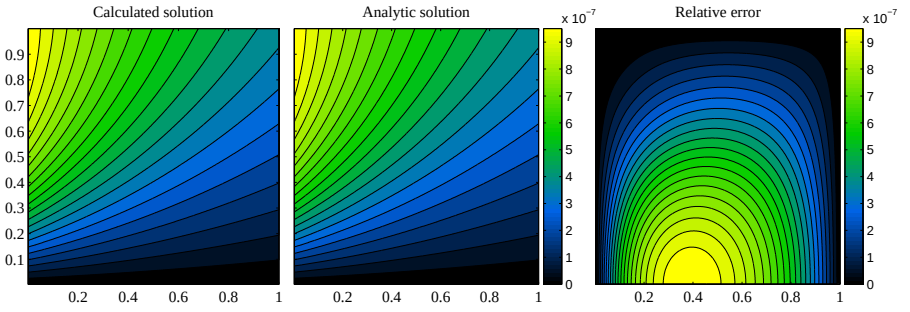

Figure 4.11: Calculated, simulated and residual for math test 1

4.6 Solver tests

The Multigrid Poisson solver is tested by computing the solution for several situations where an analytic solution is known. The following cases are used: two mathematical functions, an infinite cylinder of charge, a sphere of charge and a slab of dielectric in a uniform field. The root-mean-squared fractional error and maximum fractional error for each test case are shown in tables 4.1 and 4.2. The calculated and analytic solutions and the their residual for each of the 2-dimensional cases are shown in figures 4.11, 4.12, 4.15, and 4.13.

4.6.1 Mathematical functions

Math test 1

The Laplace equation

$$\nabla^2 \phi = 0 \tag{4.59}$$

with the boundary conditions

$$\phi(0, y) = \frac{y}{1 + y^2} \tag{4.60}$$

$$\phi(1, y) = \frac{y}{4 + y^2} \tag{4.61}$$

$$\phi(x, 0) = 0 \tag{4.62}$$

$$\phi(x, 1) = \frac{1}{(1 + x)^2 + 1} \tag{4.63}$$

has the solution

$$\phi = \frac{y}{(1 + x)^2 + y^2} \tag{4.64}$$

where $x \in [0, 1]$ and $y \in [0, 1]$. Figure 4.11 shows the simulated and calculated results and the residual.

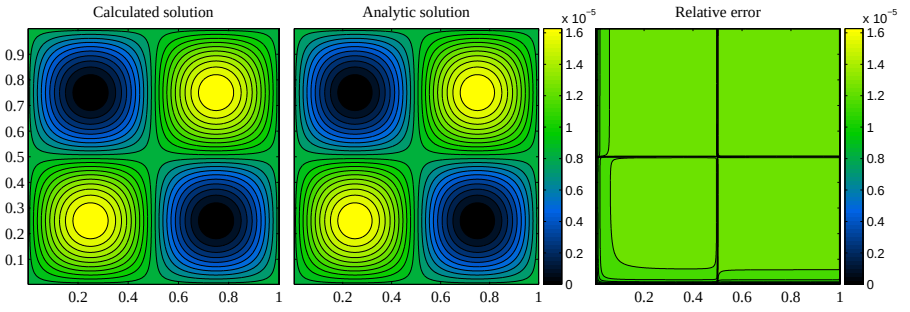

Figure 4.12: Calculated, simulated and residual for math test 2

Math test 2

In 2-dimensions

$$\phi = \sin\left(\frac{2\pi x}{n_x}\right)\sin\left(\frac{2\pi y}{n_y}\right) \tag{4.65}$$

is a solution of

$$\nabla^2\phi = \left(\left(\frac{2\pi}{n_x}\right)^2 + \left(\frac{2\pi}{n_y}\right)^2\right)\sin\left(\frac{2\pi x}{n_x}\right)\sin\left(\frac{2\pi y}{n_y}\right) \tag{4.66}$$

The simulated and calculated solutions are compared in 4.12.

In 3-dimensions

$$\phi = \sin\left(\frac{2\pi x}{n_x}\right)\sin\left(\frac{2\pi y}{n_y}\right)\sin\left(\frac{2\pi z}{n_z}\right) \tag{4.67}$$

is a solution of

$$\nabla^2\phi = \left(\left(\frac{2\pi}{n_x}\right)^2 + \left(\frac{2\pi}{n_y}\right)^2 + \left(\frac{2\pi}{n_z}\right)^2\right)\sin\left(\frac{2\pi x}{n_x}\right)\sin\left(\frac{2\pi y}{n_y}\right)\sin\left(\frac{2\pi z}{n_z}\right) \tag{4.68}$$

4.6.2 Charge cylinder

In this test, the potential of an infinite cylinder of charge is calculated. The charge density is defined, in cylindrical coordinates (r,θ,z), as

$$\rho = \begin{cases} \rho_0\left(1 - \dfrac{r^2}{a^2}\right), & \text{when } r \leqslant a, \\ 0, & \text{when } r > a \end{cases} \tag{4.69}$$

where a is the radius of the cylinder of charge. The charge density inside the cylinder is quadratic to prevent a discontinuity in the solution at $r = a$. The cylinder is considered to be infinite in the z direction and perfectly circular thus the potential is independent of θ and z. Poisson's equation in cylindrical polar coordinates with no θ or z dependence is

$$\nabla^2\phi = -\frac{\rho}{\varepsilon_0} \tag{4.70}$$

$$\frac{1}{r}\frac{\partial}{\partial r}\left(r\frac{\partial\phi}{\partial r}\right) = -\frac{\rho_0}{\varepsilon_0}\left(1 - \frac{r^2}{a^2}\right) \tag{4.71}$$

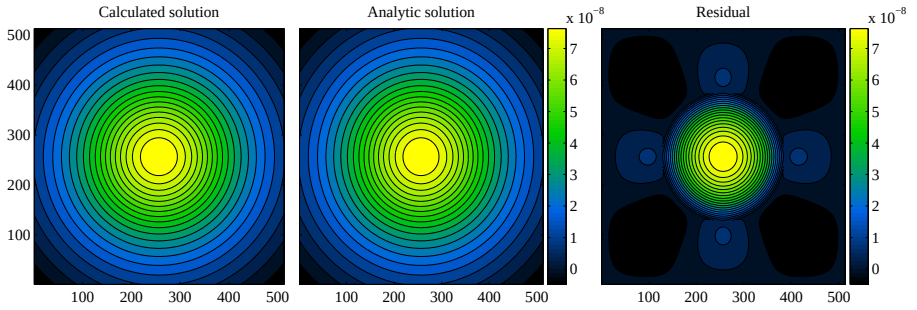

Figure 4.13: Calculated, simulated and residual for infinite cylinder of charge. The colourscale is in arbitrary units.

The solutions of (4.71) are

$$\phi = \begin{cases} -\dfrac{\rho_0 r^2}{4\varepsilon_0}\left(1 - \dfrac{r^2}{4a^2}\right) + C_1 \log r + C_2, & \text{when } r \leqslant a, \\ D_1 \log r + D_2, & \text{when } r > a \end{cases} \tag{4.72}$$

To prevent the solution tending to infinity as $r \to 0$, C_1 must be zero. The choice of the potential at the boundary of the cylinder is arbitrary, so it is set to zero, giving

$$\phi = \begin{cases} -\dfrac{\rho_0 r^2}{4\varepsilon_0}\left(1 - \dfrac{r^2}{4a^2}\right) + \dfrac{3\rho_0 a^2}{16\varepsilon_0}, & \text{when } r \leqslant a, \\ D_1 \log \dfrac{r}{a}, & \text{when } r > a \end{cases} \tag{4.73}$$

The electric field is continuous across the boundary of the cylinder, i.e.

$$\left.\frac{\partial \phi_{r\leqslant a}}{\partial r}\right|_a = \left.\frac{\partial \phi_{r>a}}{\partial r}\right|_a \tag{4.74}$$

this fixes the remaining constant

$$D_1 = -\frac{\rho_0 a^2}{4\varepsilon_0}. \tag{4.75}$$

Thus the potential is given by

$$\phi = \begin{cases} -\dfrac{\rho_0 r^2}{4\varepsilon_0}\left(1 - \dfrac{r^2}{4a^2}\right) + \dfrac{3\rho_0 a^2}{16\varepsilon_0}, & \text{when } r \leqslant a, \\ -\dfrac{\rho_0 a^2}{4\varepsilon_0} \log \dfrac{r}{a}, & \text{when } r > a. \end{cases} \tag{4.76}$$

The boundary conditions in the calculated solution are fixed at the value determined in the analytic solution. Figure 4.13 compares the simulated and analytic solutions where $a = 128.25$.

4.6.3 Charge sphere

In 3-dimensions, a spherical charge distribution is used to test the Poisson solver. In spherical coordinates (r, θ, Φ), the charge density is given by

$$\rho = \begin{cases} \rho_0 \left(1 - \dfrac{r^2}{a^2}\right), & \text{when } r \leqslant a, \\ 0, & \text{when } r > a \end{cases} \tag{4.77}$$

where a is the radius of the sphere of charge and ρ_0 is a scale factor for the charge density. Poisson's equation in spherical coordinates when there is only variation in the radial direction reduces to

$$\frac{1}{r^2}\frac{\partial}{\partial r}\left(r^2 \frac{\partial \phi}{\partial r}\right) = -\frac{\rho_0}{\varepsilon_0}\left(1 - \frac{r^2}{a^2}\right). \tag{4.78}$$

The solutions of (4.78) are

$$\phi = \begin{cases} \dfrac{\rho_0 r^2}{\varepsilon_0}\left(\dfrac{1}{6} - \dfrac{r^2}{20a^2}\right) - \dfrac{C_1}{r} + C_2, & \text{when } r \leqslant a, \\ -\dfrac{D_1}{r} + D_2, & \text{when } r > a. \end{cases} \tag{4.79}$$

To prevent the solution tending to infinity as $r \to 0$, C_1 must be zero. The choice of the potential at the boundary of the cylinder is arbitrary so it is set to zero and the electric field is continuous across the boundary of the sphere. These conditions result in the expression

$$\phi = \begin{cases} -\dfrac{\rho_0 r^2}{\varepsilon_0}\left(\dfrac{1}{6} - \dfrac{r^2}{20a^2}\right) - \dfrac{7\rho_0 a^2}{60\varepsilon_0}, & \text{when } r \leqslant a, \\ \dfrac{2\rho_0 a^3}{15\varepsilon_0}\left(\dfrac{1}{a} - \dfrac{1}{r}\right), & \text{when } r > a. \end{cases} \tag{4.80}$$

This test case is used to test the full three-dimensional solver. Details of the results are given in table 4.2. The boundary conditions in the calculated solution are fixed at the value determined in the analytic solution.

4.6.4 Capacitor

In the final test, the potential due to two infinite conducting parallel plates separated by vacuum and a slab of dielectric is calculated. The plates are separated by a distance $N-1$ and at a distance a between the plates there is a slab of dielectric with width $b-a$. The dielectric slab has a relative permittivity of ε_1. The charge density is zero throughout. This set up is shown in figure 4.14. When a dielectric is present Poisson's equation is (4.1) gives

$$-\nabla \cdot \varepsilon_r \varepsilon_0 \nabla \phi = \rho. \tag{4.81}$$

The symmetry of the infinite parallel plate capacitor means the solution of Poisson's equation is independent of the direction parallel to the capacitor plates and the problem reduces to a single dimension. In one dimension (x) Poisson's equation is

$$-\frac{d}{dx}\left(\varepsilon \frac{d}{dx}\phi\right) = 0. \tag{4.82}$$

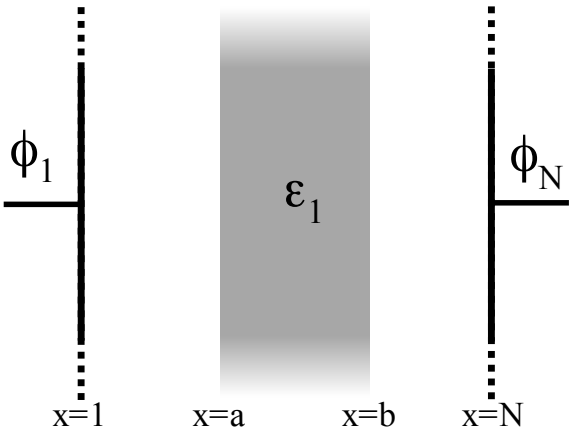

Figure 4.14: Sketch showing infinite parallel plates with a slab of dielectric in the middle.

The system into three separate parts, each with constant relative permittivities. Then the solutions are

$$\phi = \begin{cases} \dfrac{A_1}{\varepsilon_0}x + A_2, & 1 \le x \le a, \\ \dfrac{B_1}{\varepsilon_1\varepsilon_0}x + B_2, & a \le x \le b, \\ \dfrac{C_1}{\varepsilon_0}x + C_2, & b \le x \le N. \end{cases} \tag{4.83}$$

Fixing the boundary conditions gives:

$$A_2 = \phi(1) - \frac{A_1}{\varepsilon_0}, \tag{4.84}$$

$$B_2 = \phi(b) - \frac{B_1 b}{\varepsilon_0\varepsilon_1}, \tag{4.85}$$

$$C_2 = \phi(N) - \frac{C_1 N}{\varepsilon_0}, \tag{4.86}$$

$$A_1 = \varepsilon_0\frac{\phi(a) - \phi(1)}{a - 1}, \tag{4.87}$$

$$B_1 = \varepsilon_0\varepsilon_1\frac{\phi(b) - \phi(a)}{b - a}, \tag{4.88}$$

$$C_1 = \varepsilon_0\frac{\phi(N) - \phi(b)}{N - b}. \tag{4.89}$$

The electric flux density D is constant through dielectric interfaces then

$$D = \varepsilon E, \tag{4.90}$$

$$= -\varepsilon\nabla\phi, \tag{4.91}$$

and consequently

$$D = \varepsilon_0\frac{\phi(a) - \phi(1)}{a - 1} = \varepsilon_0\varepsilon_1\frac{\phi(b) - \phi(a)}{b - a} = \varepsilon_0\frac{\phi(N) - \phi(b)}{N - b}. \tag{4.92}$$

Substituting (4.84 - 4.89) and (4.92) into the solution gives

$$\phi = \begin{cases} \dfrac{D}{\varepsilon_0}(x-1) + \phi(1), & 1 \le x \le a, \\ \dfrac{D}{\varepsilon_0\varepsilon_1}(x-b) + \phi(b), & a \le x \le b, \\ \dfrac{D}{\varepsilon_0}(x-N) + \phi(N), & b \le x \le N. \end{cases} \tag{4.93}$$

Evaluating (4.93) at points $x = a$ and $x = b$:

$$\phi(a) = \frac{D}{\varepsilon_0}(a-1) + \phi(1), \tag{4.94}$$

$$\phi(b) = \frac{D}{\varepsilon_0}(b-N) + \phi(N). \tag{4.95}$$

To find an expression for D (4.94) in subtracted from (4.95):

$$\phi(b) - \phi(a) = \frac{D}{\varepsilon_0}(b-N+1-a) + \phi(N) - \phi(1), \tag{4.96}$$

$$(b-a)\frac{D}{\varepsilon_0\varepsilon_1} = \frac{D}{\varepsilon_0}(b-N+1-a) + \phi(N) - \phi(1), \tag{4.97}$$

$$(b-a)\frac{M}{\varepsilon_1} = M(b-N+1-a) + \phi(N) - \phi(1), \tag{4.98}$$

$$\frac{D}{\varepsilon_0} = \frac{\phi(N) - \phi(1)}{\left(b\left(\dfrac{1}{\varepsilon_1} - 1\right) - a\left(\dfrac{1}{\varepsilon_1} - 1\right) + N - 1\right)}. \tag{4.99}$$

Finally, the solution is

$$\phi = \begin{cases} \dfrac{D}{\varepsilon_0}(x-1) + \phi(1), & 1 \le x \le a \\ \dfrac{D}{\varepsilon_0\varepsilon_1}(x-b) + \dfrac{D}{\varepsilon_0}(b-N) + \phi(N), & a \le x \le b \\ \dfrac{D}{\varepsilon_0}(x-N) + \phi(N), & b \le x \le N \end{cases} \tag{4.100}$$

This situation is simulated and the results are shown in figure 4.15.

4.6.5 Summary

In each of the 2-dimensional tests the solution was calculated on a 513^2 grid. The solver works well on most test except the charge cylinder. In this case the RMS error is similar to that found in other tests however, it is much larger at the boundary between the charge and vacuum. This is partly because the potential is set to be zero at the boundary and because the circular boundary is not suited to the square mesh.

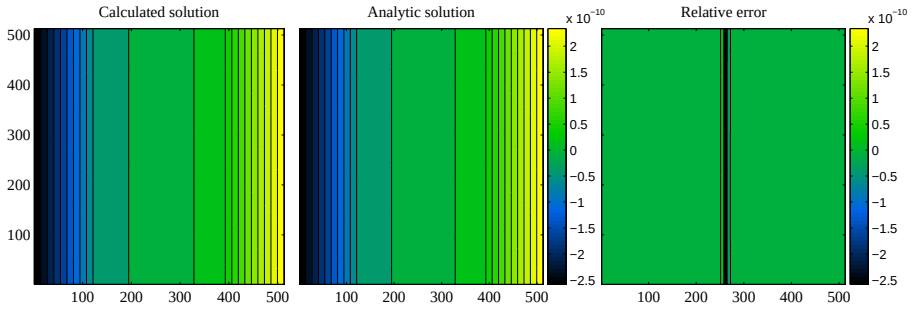

Figure 4.15: Calculated, simulated and residual for test of infinite parallel plate with dielectric slab. The colourscale is in arbitrary units.

Test	RMS fractional error	Maximum fractional error
Math test 1	3.77×10^{-7}	9.98×10^{-7}
Math test 2	1.22×10^{-5}	1.71×10^{-5}
Charge cylinder	6.85×10^{-6}	0.01
Dielectric test	2.36×10^{-12}	3.17×10^{-10}

Table 4.1: Table of errors resulting from test cases in 2d.

All of the 3-dimensional tests were calculated on a 129^3 grid. The charge sphere test has a similar problem to the 2-dimensional charge cylinder test; the RMS error is competitive with other tests but there are some large errors are the boundary of the sphere where the solution is zero. Generally the fractional errors for the 3-dimensional tests are larger than those found in the 2-dimensional tests, this is due to the number of grid points. Increasing the number of gridpoints reduces the truncation error associated with discretising the problem to a grid.

Test	RMS fractional error	Maximum fractional error
Math test 1	1.18×10^{-4}	6.68×10^{-3}
Math test 2	1.80×10^{-4}	2.28×10^{-4}
Charge sphere	2.87×10^{-5}	0.03
Dielectric test	1.68×10^{-8}	3.95×10^{-7}

Table 4.2: Table of errors resulting from test cases in 3d.

Chapter 5

Collisions

5.1 Simulating Collisions

A realistic model of a plasma requires treatment of particle collisions. In a model based on particles the effect of collisions must be calculated on a particle-by-particle basis. Before any particular type of collision can be carried out the type of collision must be determined. Testing the probability of each collision type for each incident particle is a time consuming process. In a numerical simulation an efficient algorithm for determining collisions is required. Here the method proposed by Nanbu [103] and the modifications described by Sugawara *et al.* [104] are discussed.

Some of the basic collision parameters have already been introduced in section 1.3 and they will be used here. As a first step a rudimentary Monte-Carlo scheme for determining a collision is examined. The expression for the probability of a collision can be written for each collision type

$$P_i = n_t \sigma_i(\varepsilon) v \Delta t \tag{5.1}$$

where P_i is the probability of the i^{th} collision type, n_t is the number density of the targets, v is the speed, Δt is the computational timestep and $\sigma_i(\varepsilon)$ is the value of the i^{th} cross-section at energy ε. The probability of the incident particle having any collision P is

$$P = n_t v \Delta t \sum_{i=1}^{M} \sigma_i(\varepsilon) \tag{5.2}$$

where each of the M different collisions are indexed by i. This expression assumes that the target species is the same for each collision type but it can easily be altered to include various target species.

A random number is used to determine if a collision occurs, hence the Monte-Carlo nomenclature. If a random number (R_1) selected from a uniform distribution is less than the calculated total probability (P) then the incident particle collides. Another random number (R_2) is used to choose between the collision types, using their relative probabilities (P_i/P). A schematic for this technique can be seen in figure 5.1.

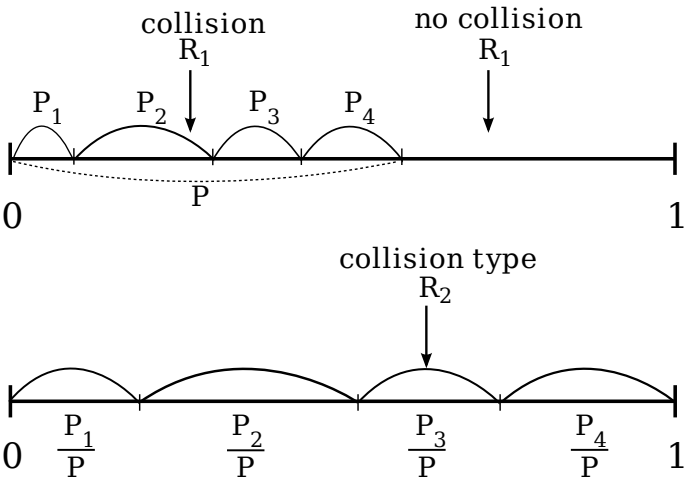

Figure 5.1: Diagram for straightforward Monte-Carlo collision selection method. The top line shows the choice between collision and no collision. A collision occurs if the random number R_1 is less than the total collision probability. The second line shows how the type of collision is chosen: a second random number is compared to the relative sizes of each collision probability.

This basic method requires the calculation of the probability for each collision type for every incident particle. Depending on the target gas or gas mixture the number of collision types can be very large (>70 for N_2[72], >90 O_2[105]). Minimising the number of evaluations of the collision probabilities reduces the computational load.

Nanbu's method [103] requires the calculation of only one collision probability per particle. In this method the random number domain ($R \in [0,1]$) is divided into M equal intervals. Each of these intervals relates to a different collision type. One random number (R_1) is selected and it is used to determine both the collision type and if the collision occurs. Firstly the collision type is selected by determining which of the M intervals the random number lies in by taking the integer part of MR_1. The collision occurs if the random number minus the starting value of the interval (i/M) is less than the calculated probability for that collision ($R - i/M < P_i$). Figure 5.2 shows Nanbu's method.

For Nanbu's method to be self-consistent the following condition must be satisfied

$$P_i < \frac{1}{M} \qquad \forall i, \varepsilon \tag{5.3}$$

this condition will be referred to as Nanbu's criterion. Examining expression (5.1), the above constraint puts an upper limit on the time step Δt as it is the only independent parameter in the expression. The upper limit for the time step is

$$\Delta t < \frac{1}{M n_t \sigma_i(\varepsilon) v} \qquad \forall\, i, \varepsilon \tag{5.4}$$

$$\Delta t < \frac{1}{M \nu_{\max}} \tag{5.5}$$

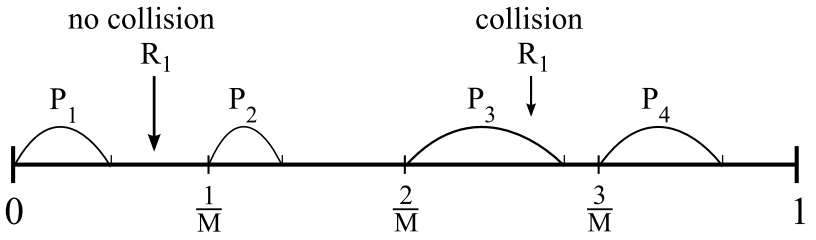

Figure 5.2: Diagram showing Nanbu's collision selection method. The interval $[0, 1]$ is divided into different collision types. Only the collision probability relating to the subinterval that the random number (R_1) lies in is calculated.

where $\nu_{\max}$ is the maximum value for the collision frequency for all energies and collision types.

Nanbu's criterion (5.3) is a technical limit on the time step but a physical constraint can also be derived. The time step should ensure that the probability of more than one collision occurring per time step is small. The Poisson distribution [106] expresses the probability of a certain number of events occurring in a given time where the event rate is known and the collisions are not dependent on the time since the last collision. The collision frequency gives an event rate. The second condition for the application of the Poisson distribution is not true for inelastic collisions which involve energy loss to internal atomic or molecular excitations. However, the elastic collision cross-section is the dominant collision and the energy loss from the incident electrons is small enough to consider the second statement valid. Thus the probability $\mathcal{P}$ of a number of collisions x is given by

$$\mathcal{P}(x) = \frac{(\nu\Delta t)^x e^{-\nu\Delta t}}{x!}. \tag{5.6}$$

The probability of two or more collision is

$$\begin{aligned} \mathcal{P}(x \geq 2) &= 1 - \mathcal{P}(0) - \mathcal{P}(1) && (5.7)\\ &= 1 - \exp(-\nu\Delta t) - \exp(-\nu\Delta t)\nu\Delta t. && (5.8) \end{aligned}$$

Expanding the exponential terms as infinite series gives

$$\begin{aligned} \mathcal{P}(x \geq 2) &= 1 - [1 - \nu\Delta t + \frac{(\nu\Delta t)^2}{2!} - \frac{(\nu\Delta t)^3}{3!} + \ldots] \\ &\quad - [\nu\Delta t - (\nu\Delta t)^2 + \frac{(\nu\Delta t)^3}{2!} + \ldots] && (5.9)\\ &= \frac{(\nu\Delta t)^2}{2} - \frac{(\nu\Delta t)^3}{3} + \ldots. && (5.10) \end{aligned}$$

Assuming the product $\nu\Delta t < 1$, which is what we want, then

$$\mathcal{P}(x \geq 2) > \frac{(\nu\Delta t)^2}{2}. \tag{5.11}$$

If the required accuracy is defined as

$$\mathcal{A} = 1 - \mathcal{P}(x \geq 2) \tag{5.12}$$

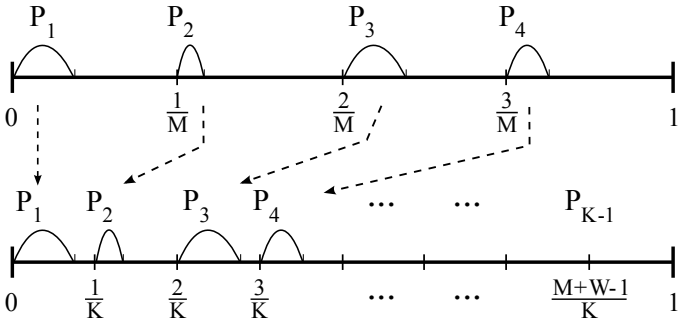

Figure 5.3: Diagram showing the addition of null collisions to Nanbu's method

then the limit for the timestep Δt is

$$\Delta t < \frac{\sqrt{2(1-\mathcal{A})}}{\nu_{\max}}. \tag{5.13}$$

The minimum of the limits (5.5) and (5.13) should be used to define the time step Δt. A time step less than the physical limit (5.13) is undesirable because it would require more timesteps than is necessary to reproduce the collisional effects. If Nanbu's criterion is violated because of a few dominant collision types then these collisions can be split; this aproach is discussed below.

Sugawara *et al.* [104] suggest several alterations to Nanbu's method [103] to reduce the computational costs. The aim of these techniques is to decrease the number of times that the probability is calculated. There are three enhancements: the introduction of 'null' collisions, the division of large probabilities and limits from the maximum probabilities.

The aim of the first alteration is to move the space in each interval ($[i/M + \max(P_i), i + 1/M]$) which results in no collision to the end of the random number domain. This puts an upper limit on the value of a random number which can possibly result in a collision. Consequently, for some random numbers no collision probability must be calculated. This can be achieved by adding 'null' collisions. Having fixed Δt using (5.13) the number of null collisions (W) that can be accommodated is

$$W < \frac{1}{\nu_{\max}\Delta t} - M \tag{5.14}$$

where M is the number of real collisions. With the addition of the null collisions there is now $K = M + W$ intervals. Figure 5.3 shows this process pictorially.

For collision sets with large numbers of collisions Nanbu's criterion can be violated despite the time step fulfilling condition (5.13). The obvious but costly solution to this violation is to use the condition (5.5) to determine Δt. This is an unnecessary refinement of the time step which requires an increase in the number of iterations increasing the total computation time. An alternative strategy is to split collision types, with large probabilities, into multiple collision selection intervals. A single collision type usually occupying one selection interval is converted into b collisions each with the same collision type, where integer $b \geq 2$. This procedure increases the number of intervals to $M + b - 1$ and Nanbu's criterion (5.3) must be satisfied using the total number of intervals. Figure 5.4 shows this procedure.

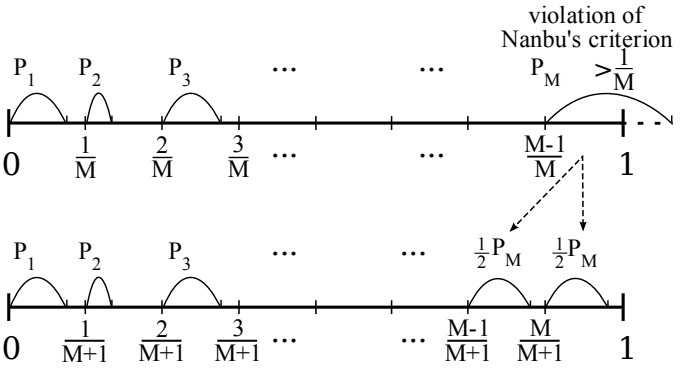

Figure 5.4: Diagram showing the splitting of a collision in Nanbu's method

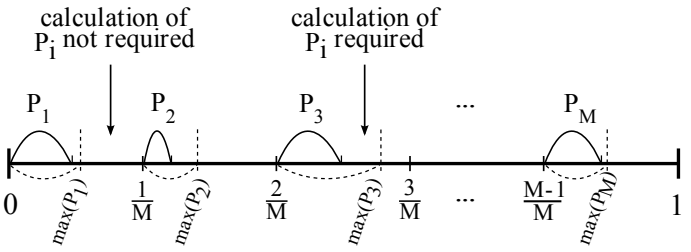

Figure 5.5: Diagram showing the use of maximum probabilities in Nanbu's method

The final modification further reduces the number of evaluations of P_i. In most cases when there is little (or no) fluctuation in the target number density, the maximum values for each P_i can be calculated before the simulation is started. The random number must be in the interval $(i/M, i/M + \max(P_i))$ for an evaluation of P_i to be carried out. Figure 5.5 shows how pre-calculated maximum probabilities can be used with Nanbu's method.

5.2 Testing Nanbu's method

To show the efficiency and veracity of the Nanbu method and the modifications some molecular Nitrogen cross-sections are used in an example. To determine the most efficient method for selecting collisions, several implementations of Nanbu's method are compared. Afterwards, the accuracy of the method is examined by considering the removal of particles from a mono-energetic beam.

5.2.1 Comparing efficiencies

The energy dependence of the molecular Nitrogen cross-sections for elastic and inelastic scattering, metastable excitation and ionisation [72] are shown in figure 5.6(a). The corresponding collision frequencies at atmospheric pressure are shown in figure 5.6(b).

The value of the time step is calculated using equation (5.13) and is found to be $\Delta t =$

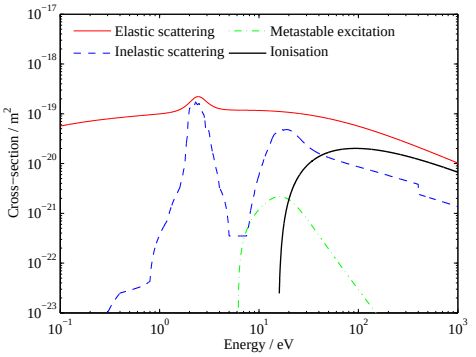

(a) Molecular Nitrogen cross-sections as a function of energy.

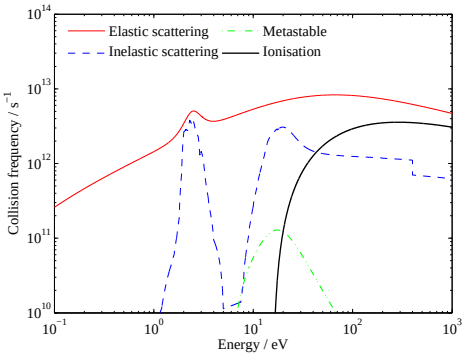

(b) Molecular Nitrogen collision frequency as a function of energy.

Figure 5.6: Molecular Nitrogen collision cross-sections and collision frequencies.

1.70×10^{-14} s giving the probabilities shown in figure 5.7(a). The probability of two or more collisions is shown in figure 5.7(b).

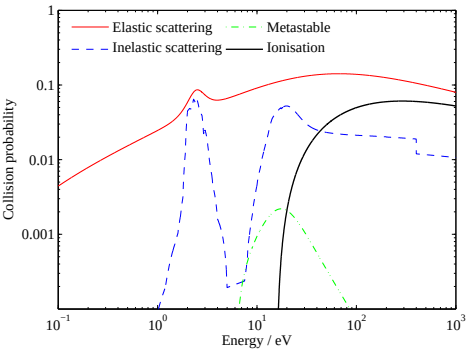

(a) The energy dependent probabilities for molecular Nitrogen reactions.

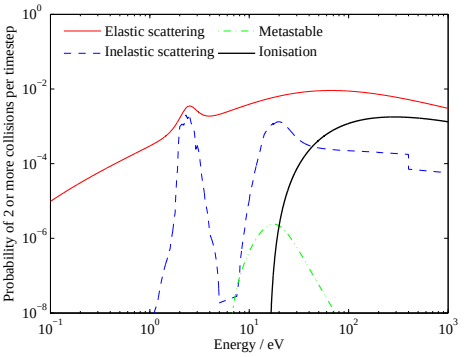

(b) Probabilities of two or more collisions per time step molecular Nitrogen reactions.

Figure 5.7: Collision probabilities for molecular Nitrogen.

The maximum probability of any collision is 0.141, this satisfies Nanbu's criterion (5.3) where there are four collision types ($0.141 < 1/M$).

The computational loads of the various collision methods are compared by recording the time they take to execute. Each collision method is applied to an ensemble of 10^5 electrons with random energies. An average execution time is found by running each method one hundred times. The time lapsed includes the selection process only, no evaluation of collision dynamics occurs. The results are shown in table 5.1. The first column in table 5.1 shows which alterations have been included in each test run.

The abbreviation MP denotes the inclusion of maximum probabilities. This reduces the number of times the collision probability is evaluated and reduces the execution time. This technique works well when the probability of the collision type is always much smaller than the selection interval. The addition of Null Collision (NC) reduces the execution time.

The maximum collision probabilities of elastic and inelastic scattering are much larger

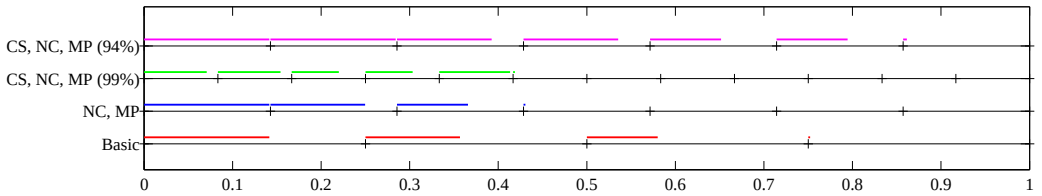

Figure 5.8: Diagram showing the probability intervals for the tests. The labels correspond to the Description in table 5.1. The 95% accuracy test has an additional splitting of the ionisation collision.

than the other collision types and consequently are the main limit for the selection intervals. Splitting large collisions can be carried out even if it is not required by Nanbu's criterion (5.3) allowing the addition of null collisions or an increase in time step (increasing the time step is achieved by reducing the prescribed accuracy). In the first test marked with CS, the elastic and inelastic collision types are each split into two equal parts. When the accuracy is reduced to 96 % the ionisation collision type is also split in two. Splitting a collision type into two parts increases the number of collisions by one.

Description	Accuracy	Time step / s	Number of collisions (null)	Nanbu criterion	Maximum Probability	Av. exec. time / s
Basic	99 %	1.70×10^{-14}	4(0)	0.250	0.141	0.1396
MP	99 %	1.70×10^{-14}	4(0)	0.250	0.141	0.0731
NC, MP	99 %	1.70×10^{-14}	7(3)	0.143	0.141	0.0575
CS, NC, MP	99 %	1.70×10^{-14}	12(6)	0.083	0.080	0.0581
CS, MP	96 %	3.41×10^{-14}	7(0)	0.143	0.141	0.0762

Table 5.1: Table of computational details of various combinations of Nanbu methods. MP ≡ Maximum Probabilities, NC ≡ Null Collisions and CS ≡ Collision Splitting. Tests were run using Matlab 2007b on a 2.4GHz Intel processor with 4GB of RAM.

The ratio of the time step to the computation time gives the length of simulation time that can be carried out per second of computation. A large value for this ratio means that the collision selection part of the simulation requires less computation time overall. The ratios are shown in table 5.2. The Nanbu method with the addition of null collisions and the inclusion of maximum probabilities gives the most efficient result. A longer time step (as in the final test) may be desirable if other parts of the simulation have large computational overheads each time step, this comes at the cost of accuracy.

Description	(Simulation time/computational time) / s s^{-1}
Basic	1.2197×10^{-13}
MP	2.3306×10^{-13}
NC, MP	2.9639×10^{-13}
CS, NC, MP (99%)	2.9336×10^{-13}
CS, MP (96%)	4.3167×10^{-13}

Table 5.2: Table showing the efficiency of each of the runs. Tests were run using Matlab 2007b on a 2.4GHz Intel processor with 4GB of RAM.

5.2.2 Verifying Nanbu's method

To verify Nanbu's collision method the example, introduced in section 1.3, of a beam of mono-energetic electrons is used. Equation (1.19) gives the flux of the beam as a function of the distance x as it passes through the slab of neutral gas, density n_t. Assuming that any interaction causes the electron to be scattered out of the beam, the number of electrons, N_e, in the beam is

$$N_e = N_{e_0} e^{-\sigma n_t x} \tag{5.15}$$

where σ is the cross-section for the interaction. The electron beam is mono-energetic and distance x can be expressed in terms of energy

$$x = \frac{1}{\tau}\sqrt{\frac{2\varepsilon}{m}} \tag{5.16}$$

where τ, ε and m are the time the beam has spent in the slab, the energy of the electrons and the mass of the electrons respectively. Thus,

$$N_e = N_{e_0} \exp\left(-\frac{\sigma n_t \sqrt{2\varepsilon}}{\tau\sqrt{m}}\right). \tag{5.17}$$

This equation will be used to verify the collision method.

The two examples discussed previously are considered and verified separately: the case MP, NC; and CS, MP with an accuracy of 96 %. Plots of the simulated number of electrons in the beam against the analytic solution versus time for the first example are shown in figure 5.9 and figure 5.10 shows the result from the second example.

Nanbu's method reproduces the predictions of (5.17) well (see figure 5.9). Errors are typically less than 12% over the 50 iterations. The change in accuracy to 96 % for the second example results in an increase in the error (see figure 5.10). Over the same number of iterations the error increases by approximately a factor four.

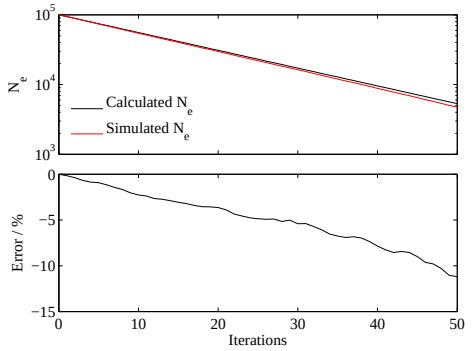

(a) Elastic scattering of electrons with neutrals.

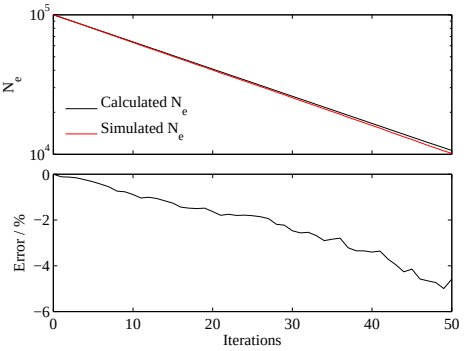

(b) Inelastic scattering of electrons with neutrals.

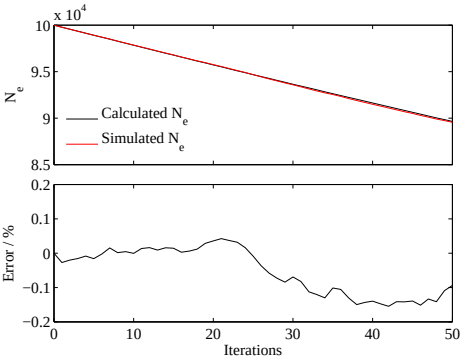

(c) Metastable excitation collisions.

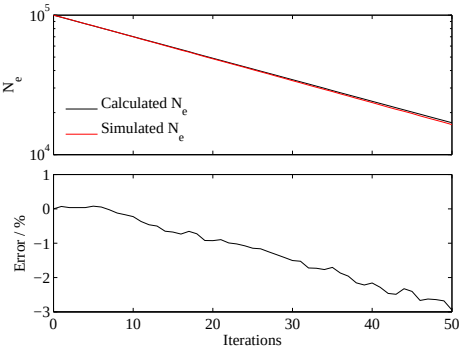

(d) Ionisation of neutrals.

Figure 5.9: Verification of Nanbu collision method with null collisions added and maximum probabilities used. The plots show the number of electrons in the beam (N_e) over 50 iterations and the percentage errors.

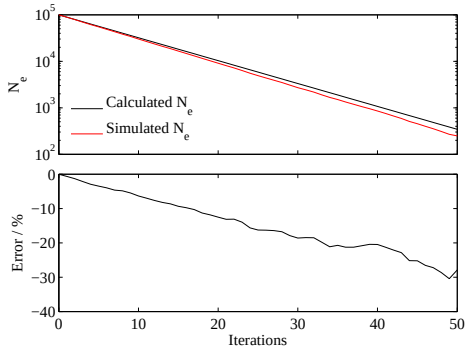

(a) Elastic scattering of electrons with neutrals.

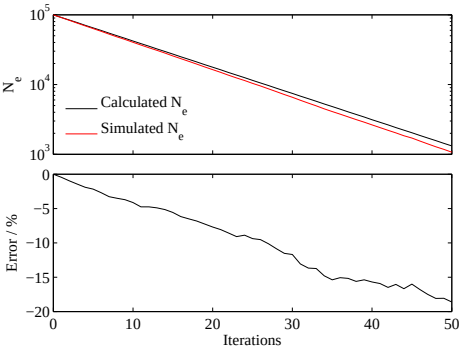

(b) Inelastic scattering of electrons with neutrals.

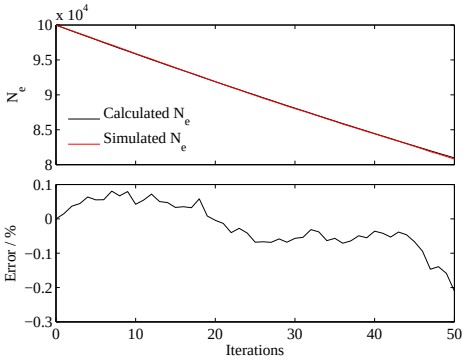

(c) Metastable excitation collisions.

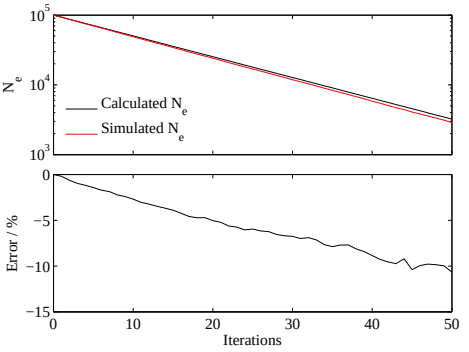

(d) Ionisation of neutrals.

Figure 5.10: Verification of Nanbu collision method with null collisions added and maximum probabilities used. The plots show the number of electrons in the beam (N_e) over 50 iterations and the percentage errors.

5.3 General inelastic cross-section

Molecular gases often have many species changing reactions, for example: dissociation, ionisation, attachment or charge exchange. There are also several types of possible excitations: rotational, vibrational, electronic. Although these excitations do not necessarily effect the chemical composition of the plasma, they do have a important affect on the energy distributions of the particles. These inelastic collisions act as an energy sink for the electrons. There can be many of these inelastic collisions and including them all in a computational model is time consuming.

One possible method of reducing the computational cost of including the inelastic collisions is by considering a general inelastic cross-section that is the sum of many inelastic processes. In this discussion of a general inelastic cross-section molecular Nitrogen will be used as an example but the method is equally valid for any set of inelastic cross-sections. Twenty-nine various excitation cross-section for molecular Nitrogen [72; 107] are plotted in figure 5.11.

It has already been shown, in section 1.3, that the probability of a particle having a collision is dependent on the sum of the relevant cross-sections. Therefore, the probability of an inelastic collision can be written as

$$P_{\text{inelastic}} = n_t v \Delta t \sum_j \sigma_j \tag{5.18}$$

where j indexes the inelastic cross-sections. The probability of an inelastic collision occurring can be determined from the sum of all the relevant cross-sections. The sum of the cross-sections is also plotted in figure 5.11.

Once an inelastic collision has been selected the energy loss must still be determined. The relative probabilities of each energy loss can be calculated by looking at the ratios of each cross-section to the sum of all the cross-sections. A surface giving the energy loss in incident energy-probability space can be constructed. The surface for the cross-sections in figure 5.11 can be seen in figure 5.12. Given the energy of the incident electron an appropriate energy loss for an inelastic collision can be selected by choosing a random number.

Not only does the general inelastic cross-section act as an important energy loss mechanism in the system but it can also be used as a diagnostic tool. The energy loss can be used as a marker to determine what excited states are produced through collisions. These excited states will have short life times. Assuming a weakly ionised plasma, where the background neutral species is substantially more abundant than the other species, these excited states will not be involved in any further collisions before they radiatively de-excite. Recording the positions and the energy losses of these inelastic collisions allows an approximation of the photon emission.

Figure 5.13 shows some of the possible radiative transitions with the names of the corresponding spectral system. The wavelengths corresponding to the most important transitions are shown in table 5.3. Details of the molecular nitrogen spectrum are from Lofthus & Krupenie [108].

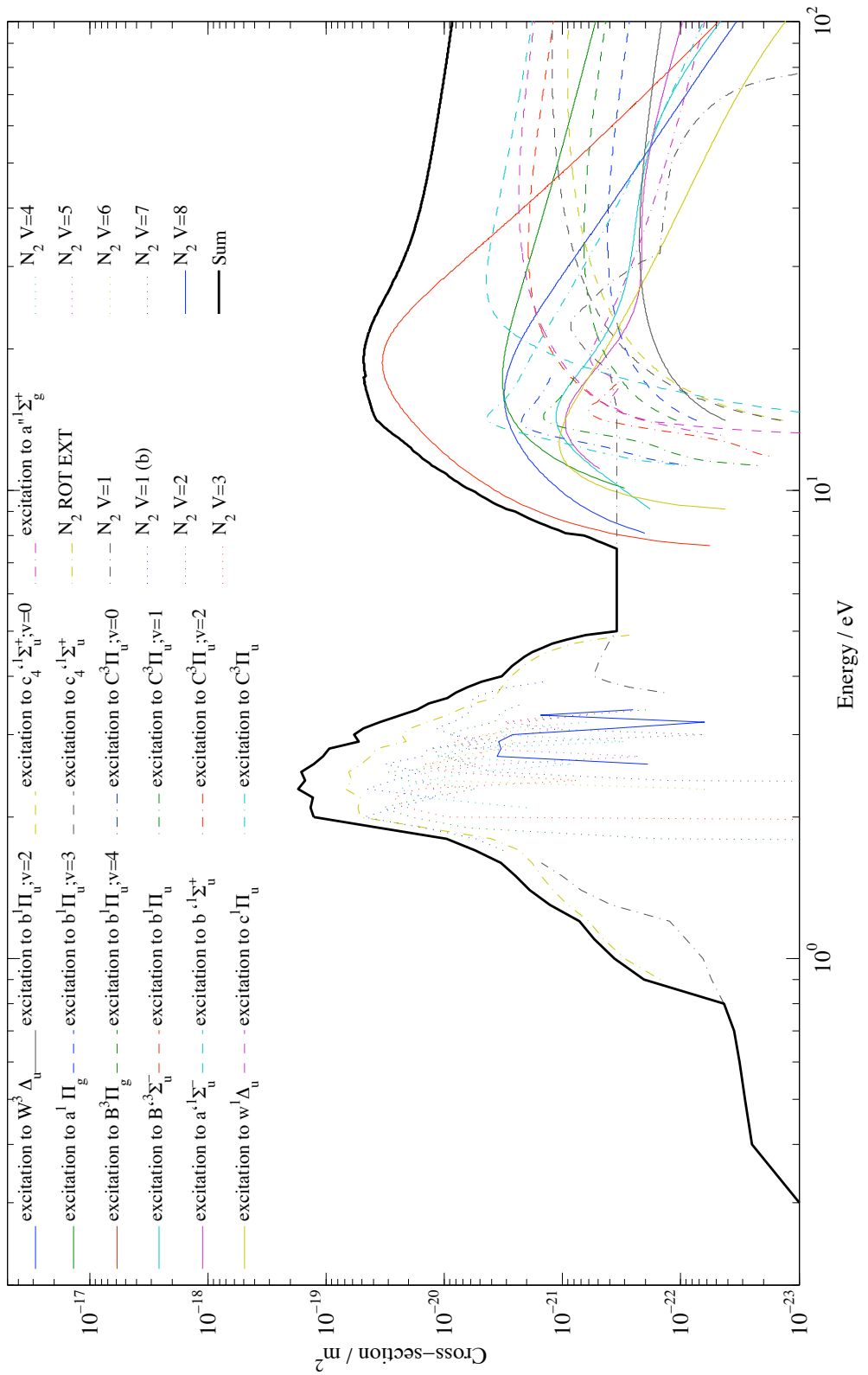

Figure 5.11: Excitation cross-sections for the ground state of molecular Nitrogen and their sum.

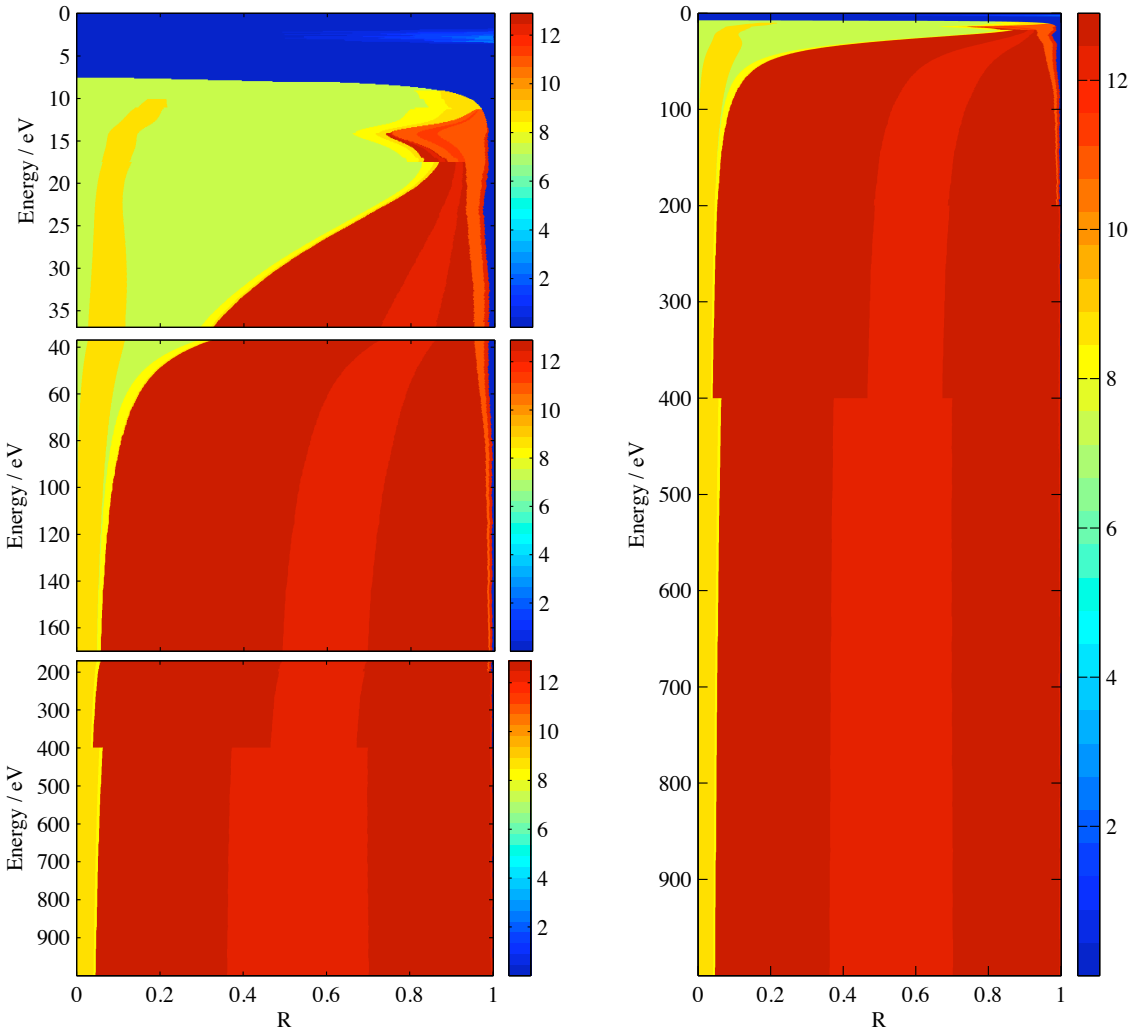

Figure 5.12: Surface used to select the energy loss of the general inelastic cross-section. Given the incident energy and a random number, R in the interval $[0, 1]$ the a relevant energy loss can be determined. The top two panels on the left hand side show a more detailed view of the surface for low energies.

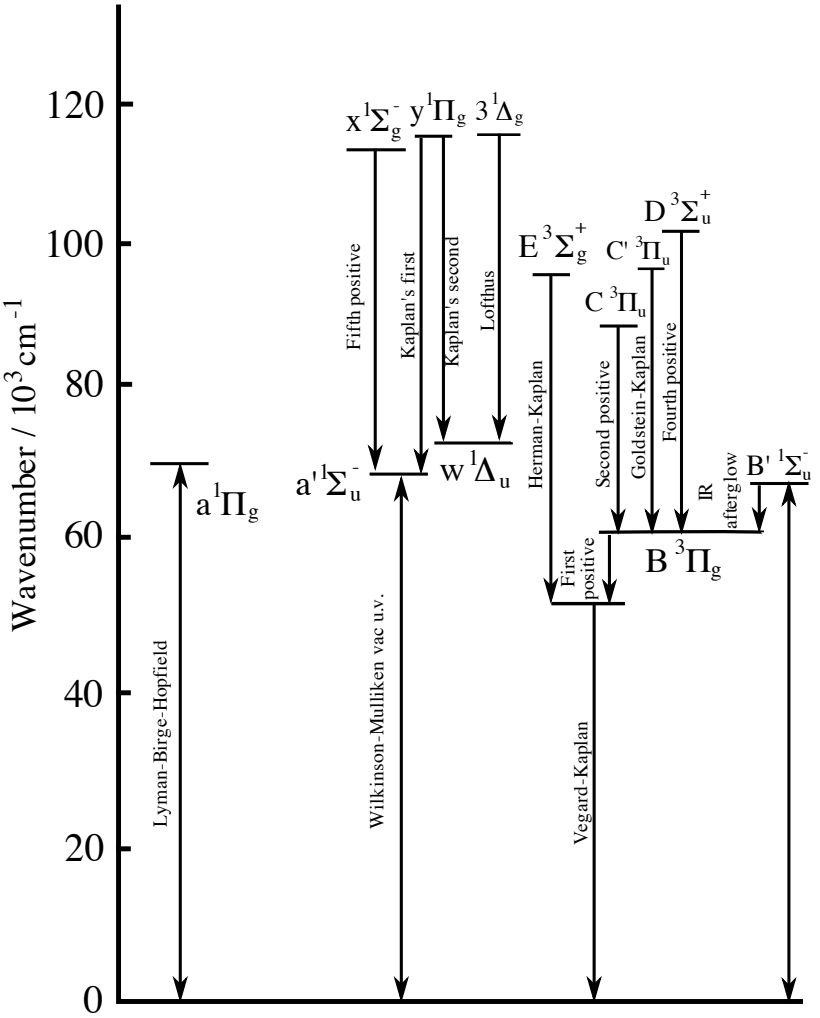

Figure 5.13: Wavenumber diagram showing different emission systems of Nitrogen.[109]

Transition	System name	Wavelength range / nm	Collisional energy loss / eV
$B^3\Pi_g \rightarrow A^3\Sigma_u^+$	First positive	503 - 1051	7.35
$C^3\Pi_u \rightarrow B^3\Pi_g$	Second positive	281 - 498	11.00
$B'^3\Sigma_u^- \rightarrow B^3\Pi_g$	Infra-red Afterglow	674 - 868	8.16
$B'^3\Sigma_u^- \rightarrow X^1\Sigma_g^+$		202 - 223	8.16
$a^1\Pi_g \rightarrow X^1\Sigma_g^+$	Lyman-Birge-Hopfield	200 - 260	8.55
$a'^1\Sigma_u^- \rightarrow X^1\Sigma_g^+$	Wilkinson-Mulliken	108 - 200	8.4

Table 5.3: Table of data for important electronic transitions resulting in photon emission. The collisional energy loss relates the energy lost by an electron to the resulting electronic transition.

5.4 Collision dynamics

In the direct particle model, the collisions between individual particles must be considered. The dynamics must be calculated self-consistently, conserving momentum and energy. The calculation of the post-collision properties are given here for: elastic, inelastic, ionisation and recombination collisions. The following calculations are for the full three-dimensional case. The same steps can be followed for the two-dimensional case.

5.4.1 Electron-neutral elastic scattering

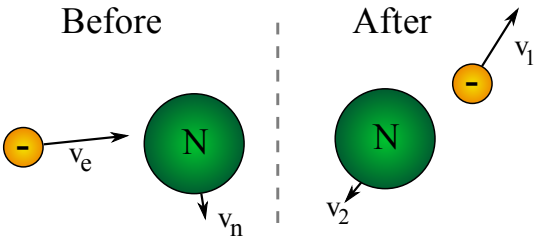

Figure 5.14: Cartoon showing pre- and post-collison properties for an elastic collision between an electron an a neutral.

In elastic collisions both energy and momentum are conserved. The incident electron has an initial speed v_e and the neutral has speed v_n. The post-collision electron and neutral have speeds v_1 and v_2 respectively. The following steps describe the calculation of the post-collision properties.

1. Move into rest frame of neutral.

$$u_e = v_e - v_n \tag{5.19}$$
$$u_n = 0. \tag{5.20}$$

2. Transform into centre of momentum frame where the total linear momentum is zero.

$$u_e = u_e - u_{cm} \tag{5.21}$$
$$u_n = -u_{cm} \tag{5.22}$$
$$u_{cm} = \frac{m_e u_e}{m_e + m_n}. \tag{5.23}$$

3. The post collision velocity of the neutral will be determined by conservation of momentum

$$m_e u_1 + m_n u_2 = 0 \tag{5.24}$$
$$u_2 = -\frac{m_e u_1}{m_n}. \tag{5.25}$$

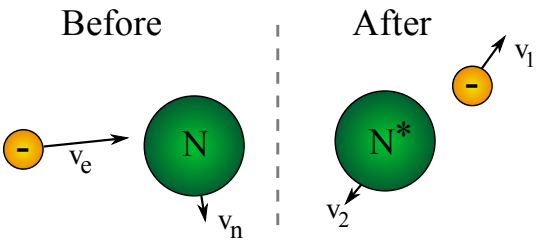

Figure 5.15: Cartoon showing pre- and post-collison properties for an inelastic collision between an electron an a neutral.

4. The trajectory (ϕ_1, θ_1) of the scattered electron is chosen randomly. The electron velocity can be written in terms of the z-component u_{1z}:

$$u_1 = \begin{bmatrix} u_{1z}\tan\phi_1\cos\theta_1 \\ u_{1z}\tan\phi_1\sin\theta_1 \\ u_{1z} \end{bmatrix}. \tag{5.26}$$

The energy available after the collision is described by

$$\varepsilon_{\text{post}} = \varepsilon_e + \varepsilon_n = \frac{1}{2}m_e u_1^2 + \frac{1}{2}m_n u_2^2 \tag{5.27}$$

where ε_e and ε_n are the kinetic energies of the electron and neutral in the centre of momentum frame. From the conservation of energy the velocity of the scattered electron can be calculated

$$\varepsilon_{\text{post}} = \frac{1}{2}m_e u_1^2 + \frac{1}{2}m_n\left(\frac{m_e u_1}{m_n}\right)^2 \tag{5.28}$$

$$u_1^2 = \frac{2\varepsilon_{\text{post}}}{m_e(1+m_e/m_n)} \tag{5.29}$$

$$u_{1z}^2 = \frac{2\varepsilon_{\text{post}}}{m_e(1+m_e/m_n)(\tan^2\phi_1+1)}. \tag{5.30}$$

The remaining components of v_1 and are calculated using (5.38).

5. Each of the electron and neutral velocities must be transformed back to the lab frame by adding the centre of momentum and initial neutral velocities.

5.4.2 Electron-neutral inelastic scattering

The total kinetic energy is not conserved in an inelastic collision. Some of the kinetic energy is transferred to internal excitation of the neutral, denoted by $\varepsilon_{\text{loss}}$. The momentum, however, is conserved. The incident electron has an initial speed v_e and the neutral has speed v_n. The post-collision electron and neutral have speeds v_1 and v_2 respectively. The following steps describe the calculation of the post-collision properties.

1. Move into rest frame of neutral

$$u_e = v_e - v_n \tag{5.31}$$

$$u_n = 0. \tag{5.32}$$

2. Transform into centre of momentum frame where the total linear momentum is zero

$$u_e = u_e - u_{cm} \tag{5.33}$$
$$u_n = -u_{cm} \tag{5.34}$$
$$u_{cm} = \frac{m_e u_e}{m_e + m_n}. \tag{5.35}$$

3. The post collision velocity of the neutral is determined by conservation of momentum

$$m_e u_1 + m_n u_2 = 0 \tag{5.36}$$
$$u_2 = -\frac{m_e u_1}{m_n}. \tag{5.37}$$

4. The trajectory (ϕ_1, θ_1) of the scattered electron is chosen randomly. The electron velocity can be written as

$$u_1 = \begin{bmatrix} u_{1z} \tan\phi_1 \cos\theta_1 \\ u_{1z} \tan\phi_1 \sin\theta_1 \\ u_{1z} \end{bmatrix}. \tag{5.38}$$

The energy after the collision is given by

$$\varepsilon_{\text{post}} = \varepsilon_e + \varepsilon_n - \varepsilon_{\text{loss}} = \frac{1}{2} m_e u_1^2 + \frac{1}{2} m_n u_2^2 \tag{5.39}$$
$$= \frac{1}{2} m_e u_1^2 + \frac{1}{2} m_n \left(\frac{m_e u_1}{m_n} \right)^2. \tag{5.40}$$

This results in the velocity of the scattered electron having total magnetude and z-component given by

$$u_1^2 = \frac{2\varepsilon_{\text{post}}}{m_e(1 + m_e/m_n)} \tag{5.41}$$
$$u_{1z}^2 = \frac{2\varepsilon_{\text{post}}}{m_e(1 + m_e/m_n)(\tan^2\phi_1 + 1)}. \tag{5.42}$$

The remaining components of u_1 can be calculated using (5.38).

5. Each of the electron and neutral velocities must be transformed back to the lab frame by adding the centre of momentum and initial neutral velocities.

5.4.3 Electron impact ionisation of a neutral

The ionising electron has an initial speed v_e and the neutral has speed v_n. The post-collision ion and two electrons have speeds v_n, v_1 and v_2 respectively. The total linear momentum is conserved during the collision. The total energy, *i.e.* the kinetic energy plus the ionisation energy is also conserved. The following steps describe the calculation of the post-collision properties.

1. Move into the rest frame of neutral.

$$u_e = v_e - v_n \tag{5.43}$$
$$u_n = 0. \tag{5.44}$$

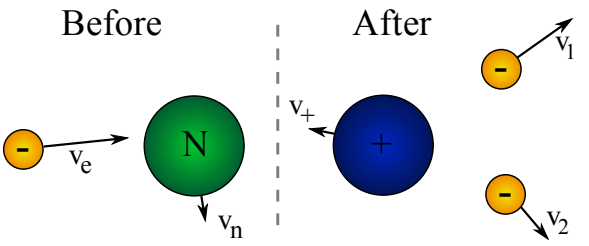

Figure 5.16: Cartoon showing pre- and post-collison properties for an ionisation collision between an electron an a neutral.

2. Transform into centre of momentum frame where the total linear momentum is zero.

$$u_e = u_e - u_{cm} \tag{5.45}$$
$$u_n = -u_{cm} \tag{5.46}$$
$$u_{cm} = \frac{m_e u_e}{m_e + m_n}. \tag{5.47}$$

3. The equation describing the energy during the collision is

$$\varepsilon_e + \varepsilon_n = \varepsilon_1 + \varepsilon_2 + \varepsilon_+ + \varepsilon_{iz}. \tag{5.48}$$

where ε_e is the incident electron energy, ε_n is the neutral energy, ε_+ is the ion energy, ε_{iz} is the ionisation energy, and ε_1 and ε_2 are the energies of the post-collision electrons. The energy available post collision, $\varepsilon_{\text{post}}$, is

$$\varepsilon_{\text{post}} = \varepsilon_e + \varepsilon_n - \varepsilon_{iz}. \tag{5.49}$$

4. The post collision momentum is given by

$$m_e u_1 + m_e u_2 + m_+ u_+ = 0, \tag{5.50}$$

5. The maximum energy the ion can gain through a scattering collision is

$$\max(\varepsilon_+) = \frac{m_e}{m_e + m_+}\varepsilon_{\text{post}}. \tag{5.51}$$

The energy of the positive ion is selected to be a random fraction of this value. The trajectory of the ion is selected at random. The ion velocity is

$$u_+ = \sqrt{\frac{2\varepsilon_+}{m_+}}\,(\sin\phi_+\cos\theta_+, \sin\phi_+\sin\theta_+, \cos\phi_+) \tag{5.52}$$

6. Next the remaining energy must be shared between the electrons. A random trajectory (θ_1, ϕ_1) is calculated for the first electron. Squaring the momentum equation gives

$$(m_e u_2)^2 = (m_e u_1)^2 + (m_+ u_+)^2 - 2|m_e u_1||m_+ u_+|\cos(\pi - \beta) \tag{5.53}$$

where β is the angle between the ion and first electron. Expression (5.53) reduces to

$$\varepsilon_2 = \varepsilon_1 + \frac{m_+}{m_e}\varepsilon_+ + 2\sqrt{\frac{m_+}{m_e}\varepsilon_1\varepsilon_+}\cos\beta \tag{5.54}$$

Substituting

$$\varepsilon_2 = \varepsilon_{\text{post}} - \varepsilon_+ - \varepsilon_1 = \varepsilon_{2e} - \varepsilon_1 \tag{5.55}$$

into (5.54) gives a quadratic equation for $\sqrt{\varepsilon_1}$:

$$2\sqrt{\varepsilon_1}^2 + 2\sqrt{\frac{m_+}{m_e}\varepsilon_+}\cos\beta\sqrt{\varepsilon_1} + \frac{m_+}{m_e}\varepsilon_+ - \varepsilon_{2e}. \tag{5.56}$$

This quadratic equation has the solution

$$2\sqrt{\varepsilon_1} = -\sqrt{\frac{m_+}{m_e}\varepsilon_+}\cos\beta \pm \sqrt{\left(\frac{m_+}{m_e}\varepsilon_+(\cos^2\beta - 2) + 2\varepsilon_{2e}\right)}. \tag{5.57}$$

From this the velocity of the first electron can be computed

$$u_1 = \sqrt{\frac{2\varepsilon_1}{m_e}}\,(\sin\phi_1\cos\theta_1, \sin\phi_1\sin\theta_1, \cos\phi_1) \tag{5.58}$$

7. The velocity of the second electron can be found through conservation of momentum

$$u_2 = -\frac{m_e u_1 + m_+ u_+}{m_e} \tag{5.59}$$

8. Each of the electron and ion velocities must be transformed back to the lab frame by adding the centre of momentum and initial neutral velocities.

5.4.4 Electron-ion recombination

The recombination of particles is a straightforward calculation. The momentum of the post-collision neutral is equal to the total momentum of the recombining electron and ion.

Chapter 6

Electron avalanches

6.1 Introduction

Conventional plasma devices, such as those used in industrial processes, have lifetimes much longer than any intrinsic plasma timescale. When this is the case the plasma has time to relax into an equilibrium or quasi-equilibrium state (*i.e.* non-maxwellian but stable). For these plasmas the initiation of the discharge from a neutral gas is a unimportant fraction of the plasma's lifetime. The breakdown of a gas occurs on the timescale of tens of nanoseconds [110]. However, there are some devices which evolve on timescales where the breakdown is significant. In these early stages, the plasma is far from equilibrium.

A recent development in technological plasmas is to create plasmas on sub-millimetre scales [111]. These microdischarges, or microplasmas, are primarily operated at atmospheric pressure. Large scale plasmas operated at atmospheric pressure are susceptible to instabilities and arcing. This unstable behaviour means they are often unsuitable for use in technological processes. Reducing the scale of the plasma results in a more stable discharge. The scale of the devices used to produce microdischarges is on the order of tens of Debye lengths [112]. This means that complicated charge structures can form across the plasma. The ratio of boundary to plasma is much greater than in macroscale plasmas. Since a large volume of the plasma is exposed to a wall, plasma-surface interactions are very important. These interactions are not well known. These factors: the density, size and surface ratio mean that plasmas on a sub-millimetre scale operate in a different physical regime from conventional discharges.

The conditions present in microdischarges at atmospheric pressure are favourable for the production of some molecular species. Excimers and Ozone are produced in 3-body interactions that occur readily in microdischarges. Several applications have already been identified [111]: destruction of toxins, such as NO_x and SO_x; trace element detection, the light emission from the plasma is sensitive to small impurities; and UV radiation sources, including excimer lamps, flat panel displays and possibly micro-lasers.

A variety of power configurations have been used with microdischarges, *e.g.* DC, RF and nansecond pulses. When a 20ns pulse was applied to a DC microdischarge [113] an

increase in the emission from excimer molecules was observed. The pulsing results in a higher electron number density and mean energy than in the purely DC case.

Pulsed power systems are used a variety of commercial devices: decomposition of harmful gases, ozone generation, treatment of algae bloom, concrete recycling [114]. The rise time and pulse width in these systems can be on the order of nanoseconds. Pulsing the discharge reduces the field strength required to breakdown the gas [115]. Charged particles and metastable states remain in the gas between pulses; this residue makes subsequent breakdowns easier.

It has been found that nanosecond pulses of MVm^{-1} electric fields can be used in cell treatment [116]. The electric field can cause programmed cell death without permanently damaging the outer cell membrane. Manipulation of cellular structures requires pulses short enough to bypass the membrane and deposit the energy inside.

When sub-microsecond pulses are used the initiation of the plasma becomes a significant factor in the evolution of the plasma. Understanding the breakdown of the neutral gas is key to controlling these short pulse plasmas.

Electrical breakdown of gas

There are two main descriptions of breakdown for atmospheric pressure gases [117]: Townsend, or Paschen breakdown; and Streamer breakdown. In the former process, many electron avalanches form in the applied field and the plasma is sustained by secondary emission from the cathode. Streamer breakdown is the name given to the situation where a single avalanche becomes large enough that its self-field becomes equivalent to the applied field. Secondary avalanches intiated by photoionisation evolve towards the main avalanche. This rapidly leads to the formation of a conducting channel between the electrodes.

Consider a DC electric field applied across a plane parallel gap. An electron avalanche can be seeded by a single electron-ion pair created by photoionisation or field emission from irregularities at the electrode surface. The electron is accelerated by the field and once it gains enough energy it can ionise a neutral gas particle, creating another electron-ion pair. Both the electrons are accelerated by the field and will eventually ionise neutral gas particles, doubling the number of electrons (and ions) again. This process is repeated and the population grows exponentially. This process is called an electron avalanche.

Townsend's coefficient (α) relates the ionisation and total scattering mean free paths with the energy gained by the electrons from the electric field and the ionisation threshold. This coefficient gives the probability of ionisation per unit length. It is dependent on the type of gas,

$$\alpha = Ap \exp\left(\frac{-Bp}{E}\right) \tag{6.1}$$

where the constants A and B are properties of the gas, p is the pressure and E is the electric field strength.

The discharge is then sustained by secondary emission of electrons from the negative electrode. Positive ions that impact on the electrode can cause electrons to be ejected from the surface. The rate at which electrons are emitted from the electrode per incident ion is called the secondary electron emission coefficient (γ). For a discharge to be self

sustaining [118] the following condition must be met

$$\alpha d = \log_e \left(1 + \frac{1}{\gamma}\right) \tag{6.2}$$

where d is the electrode separation. Combining (6.1) and (6.2) gives an expression called Paschen's Law. It describes the voltage (V_b) required to breakdown a gas and produce a steady glow discharge. It is a function of pressure (p) and electrode separation (d),

$$V_b = \frac{Bpd}{\log_e(Apd) - \log_e\{\log_e(1 + \gamma^{-1})\}} \tag{6.3}$$

At higher pressure, *i.e.* atmospheric pressure, the Townsend description of breakdown fails [119]. For atmospheric pressures the Streamer mechanism is a better description. The Raether Breakdown Criterion [120] is given by

$$\alpha d = \log_e \left(\frac{4\pi\varepsilon_0 \lambda_{iz} E_{\text{app}}}{e}\right) + \log_e d. \tag{6.4}$$

This expression is derived from the balance of the applied field and the self-field of the avalanche.

The aim of this chapter is to investigate the sub-nanosecond breakdown of a gas by simulating the evolution of an electron avalanche. In section 6.2 the modelling strategy is described. The electron avalanche is initiated between two parallel plates. The initial conditions for the simulations are described in section 6.3. The simulated evolution of the electron avalanches in two-dimensions are shown in section 6.4 and the results from the three-dimensional model are given in section 6.5. Results from the two- and three-dimensional simulations are compared in section 6.6. Finally, the results are discussed in section 6.7.

6.2 Description of physical setup

The particle model described in chapter 3 is used to model an electron avalanche in molecular Nitrogen gas at atmospheric pressure. A simple parallel plate device is considered. An electric field of 12MVm^{-1} is applied to a 1mm gap. The avalanche is initiated from a single electron-ion pair at rest, situated near the cathode.

In the first simulation the electron avalanche is allowed to evolve in a DC electric field. In the second case, the direction of the electric field will be reversed after 1ns. The field reversal is simulated to investigate the production of metastable states in an ultra-fast oscillating electric field. The aim is to maximise the number of metastables without inducing full breakdown and the associated current spike across the device.

The particle model will be used to calculate the trajectories of the electrons, positive ions and one type of metastable (N_2 $A^3\Sigma_u^+$). An isothermal background of neutrals consistent with molecular Nitrogen at atmospheric pressure and a temperature of approximately room temperature (300K) is assumed.

The following collisions are included: elastic scattering [72], inelastic scattering [72; 107], metastable excitation ($A^3\Sigma_u^+$) [72], ionisation [72], metastable ionisation [121] and electron-ion recombination [72]. Figure 6.1 shows the energy dependence of the cross-sections. The

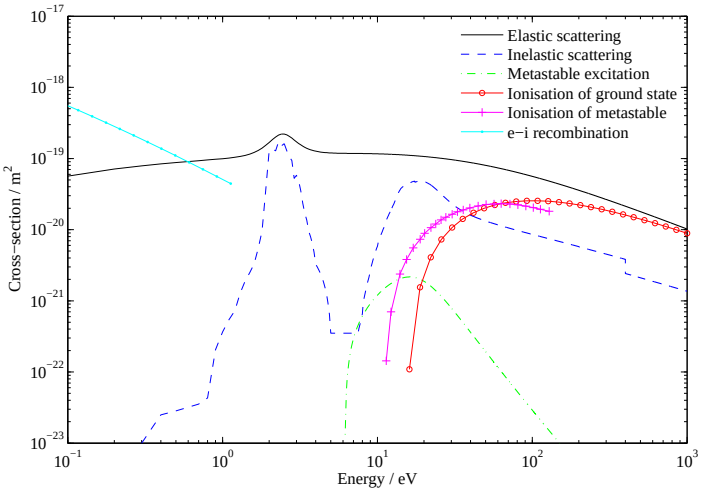

Figure 6.1: Cross-sections for molecular Nitrogen.

ionisation energy threshold of N_2 is 15.58 eV, the excitation threshold for the metastable is 6.17eV and the energy threshold for ionisation of the $A^3\Sigma_u^+$ metastable is 11.4 eV.

Non-dimensionalisation of the governing equations

The equations in the particle model are non-dimensionalised. This means that the particle positions and speeds are measured in units of cell widths and cell widths per time step respectively. The equations required to simulate the evolution of the particles are:

$$m_s \frac{d\boldsymbol{v}}{dt} = q_s \boldsymbol{E}, \tag{6.5}$$

$$\frac{d\boldsymbol{x}}{dt} = \boldsymbol{v}, \tag{6.6}$$

$$\nabla^2 \phi = \frac{e}{\varepsilon_0}(n_+ - n_e), \tag{6.7}$$

$$\boldsymbol{E} = -\nabla\phi \tag{6.8}$$

where m_s is the species dependent particle mass, q_s is the species charge, $\boldsymbol{v}$ is the particle speed, $\boldsymbol{x}$ is the particle position, $\boldsymbol{E}$ is the electric field vector at $\boldsymbol{x}$, ϕ is the electric potential, e is the electron charge, ε_0 is the permitivitty of free space, n_s is the number density of species s, ∇ is the gradient operator and d/dt is the time derivative. These equations are the momentum equation, the rate of change of position, Poisson's equation and the electric

field respectively. The variables are non-dimensionalised as follows:

$$\begin{aligned}
\boldsymbol{v} &\mapsto v_0\hat{\boldsymbol{v}}, && (6.9)\\
t &\mapsto t_0\hat{t}, && (6.10)\\
m_s &\mapsto m_e\hat{m} && (6.11)\\
q_s &\mapsto e\hat{q} && (6.12)\\
\boldsymbol{E} &\mapsto E_0\hat{\boldsymbol{E}}, && (6.13)\\
\boldsymbol{B} &\mapsto B_0\hat{\boldsymbol{B}}, && (6.14)\\
\phi &\mapsto \phi_0\hat{\phi}, && (6.15)\\
n_s &\mapsto n_0\hat{n}_s, && (6.16)\\
\nabla &\mapsto s_0^{-1}\hat{\nabla}, && (6.17)
\end{aligned}$$

where the non-dimensional variables are denoted by the $\hat{}$ notation. Equations (6.5-6.8) become

$$\begin{aligned}
\frac{d\hat{\boldsymbol{v}}}{d\hat{t}} &= \frac{\hat{q}}{\hat{m}}P_E\hat{\boldsymbol{E}} && (6.18)\\
\frac{d\hat{\boldsymbol{x}}}{d\hat{t}} &= P_x\hat{\boldsymbol{v}} && (6.19)\\
\hat{\nabla}^2\hat{\phi} &= P_n(\hat{n}_+ - \hat{n}_e) && (6.20)\\
\hat{\boldsymbol{E}} &= -P_g\hat{\nabla}\hat{\phi}. && (6.21)
\end{aligned}$$

The non-dimensional kinetic energy $\hat{\kappa}$ is defined as,

$$\hat{\kappa} = P_\kappa\hat{m}\hat{\boldsymbol{v}}^2. \quad (6.22)$$

The non-dimensional parameters are:

$$\begin{aligned}
P_E &= \frac{eE_0t_0}{mv_0}, && (6.23)\\
P_x &= \frac{t_0v_0}{x_0}, && (6.24)\\
P_n &= \frac{en_0s_0^2}{\varepsilon_0\phi_0}, && (6.25)\\
P_g &= \frac{\phi_0}{E_0s_0}, && (6.26)\\
P_\kappa &= \frac{mv_0^2}{2e}. && (6.27)
\end{aligned}$$

The kinetic energy has been non-dimensionalised to be in units of electron volts. This is to ensure they are compatible with the cross-sections which are also expressed in terms of electron volts. The numerical simulation is characterised by the characteristic time, length and electric potential. Finally, the substitutions

$$\begin{aligned}
E_0 &= \frac{\phi_0}{s_0} && (6.28)\\
v_0 &= \frac{x_0}{t_0} && (6.29)\\
n_0 &= s_0^{-3} && (6.30)\\
& && (6.31)
\end{aligned}$$

give the non-dimensional parameters:

$$P_E = \frac{e\phi_0 t_0^2}{m_e s_0^2}, \tag{6.32}$$

$$P_x = 1, \tag{6.33}$$

$$P_n = \frac{e}{\varepsilon_0 s_0 \phi_0}, \tag{6.34}$$

$$P_\kappa = \frac{m_e s_0^2}{2e t_0^2}, \tag{6.35}$$

$$P_g = 1. \tag{6.36}$$

6.3 Initial conditions for the simulation

The simulation is carried out in both two- and three-dimensions. In the two dimensional case the computational domain is 1025×513 grid cells. In three-dimensions a $129 \times 65 \times 65$ grid is used. In the early stages of the avalanche, the number of particles is small and evaluating the potential on a grid is not ideal. A particle-particle method would be more suitable for the calculation of the self-field at these early times. However, at this stage of the avalanche the force on the particles is dominated by the applied field and the use of a grid is suitable.

If a particle collides with a boundary then it is deleted. The maximum number of particles that can be stored during the simulation is 17.5 million per type.

The potential at electrode left (x=1) and right (x=N_x) boundaries are fixed at -6kV and +6kV respectively. The non-electrode boundaries are assumed to be far from the computational boundary and so, zero value von Neumann boundaries are used.

In the DC case the electron-ion pair starts the position (15, $N_y/2$, $N_z/2$) and in the case where the field is reversed ($N_x/3$, $N_y/2$, $N_z/2$). The position of the electron is changed in the field reversal case to ensure the avalanche does not encounter the $x = 1$ boundary too early after the field is reversed.

6.4 Results from the two-dimensional model

Each of the following results exhibit similar physical features. When describing the electron avalanches the ionisation front of electrons will be referred to as the 'head' and the trail of ions is termed the 'tail'.

Both collisional and electrostatic effects influence the spatial distribution of the avalanche. In the early stages the diffusion of the avalanche is dominated by the effect of elastic collisions. As the number of electrons grows the diffusion is enhanced by their mutual repulsion.

There is also evidence of instabilities in the electron head. Bifurication of the avalanche can be seen. Once a perturbation in the self-field forms it becomes unrecoverable. Ionisation occurs at the edges of the field perturbations and increases the size of the instability region.

6.4.1 DC electric field

The spatial evolution of the electron avalanche in a DC electric field is shown in figure 6.2. Snapshots of the electron density, ion density, metstable density and the total electric potential are shown for a selection of times. The electron and ion energy distribution functions for the same time selections are shown in figure 6.3. The integrated light emission from the electron avalanche is shown in figure 6.4. The process of estimating the light output was detailed in section 5.3.

6.4.2 Field reversal

The spatial evolution of the electron avalanche when the electric field is reversed is shown in figure 6.15. Snapshots of the electron density, ion density, metstable density and the total electric potential are shown for a selection of times.

After the field reversal the particle densities shown in figure 6.15 have a distinctive dumbbell shape. As the electron avalanche forms in the forward field direction the typical avalanche shape forms. When the field direction reverses the lower energy electrons in the middle and tail are accelerated in the new field direction and reach ionisation energies before the high energy electrons in the avalanche head. The electrons in the tail effectively form a new avalanche and the typical tadpole shape is produced again, this time pointing in the opposite direction. The electron and ion energy distribution functions for the same time selections are shown in figure 6.3. The estimated light emission is shown in figure 6.7.

Instantaneous field reversal

In this case where the direction of the applied electric field is reversed, the reversal occurs during a single timestep. The timestep is fixed by collisional timescales and is 1.70×10^{-14}s. The time for an electric signal to traverse a 1mm gap is 3.35×10^{-12}s. The instantaneous switching is not physical and should be addressed more carefully in future work. This means that the calculation is not strictly self-consistent but it can still be viewed as a guide. The results presented here can be considered as two separate calculations. Including the signal propagation would almost certainly result in an increase in the metastable population when compared to this simple calculation.

The field should change over approximately 147 timesteps. The timestep is based on collision times and so there are a number of collisions that are not accounted for. The instantaneous field reversal will decelerate and accelerate the charged particles more quickly than a gradual change in the electric field. This will result initially in a reduced rate of ionisation and metastable excitation compared to a gradual change. A gradual change of the field will cause the electrons to spend more time at speeds where electron-ion recombination is important thus, the number of recombinations may be underestimated.

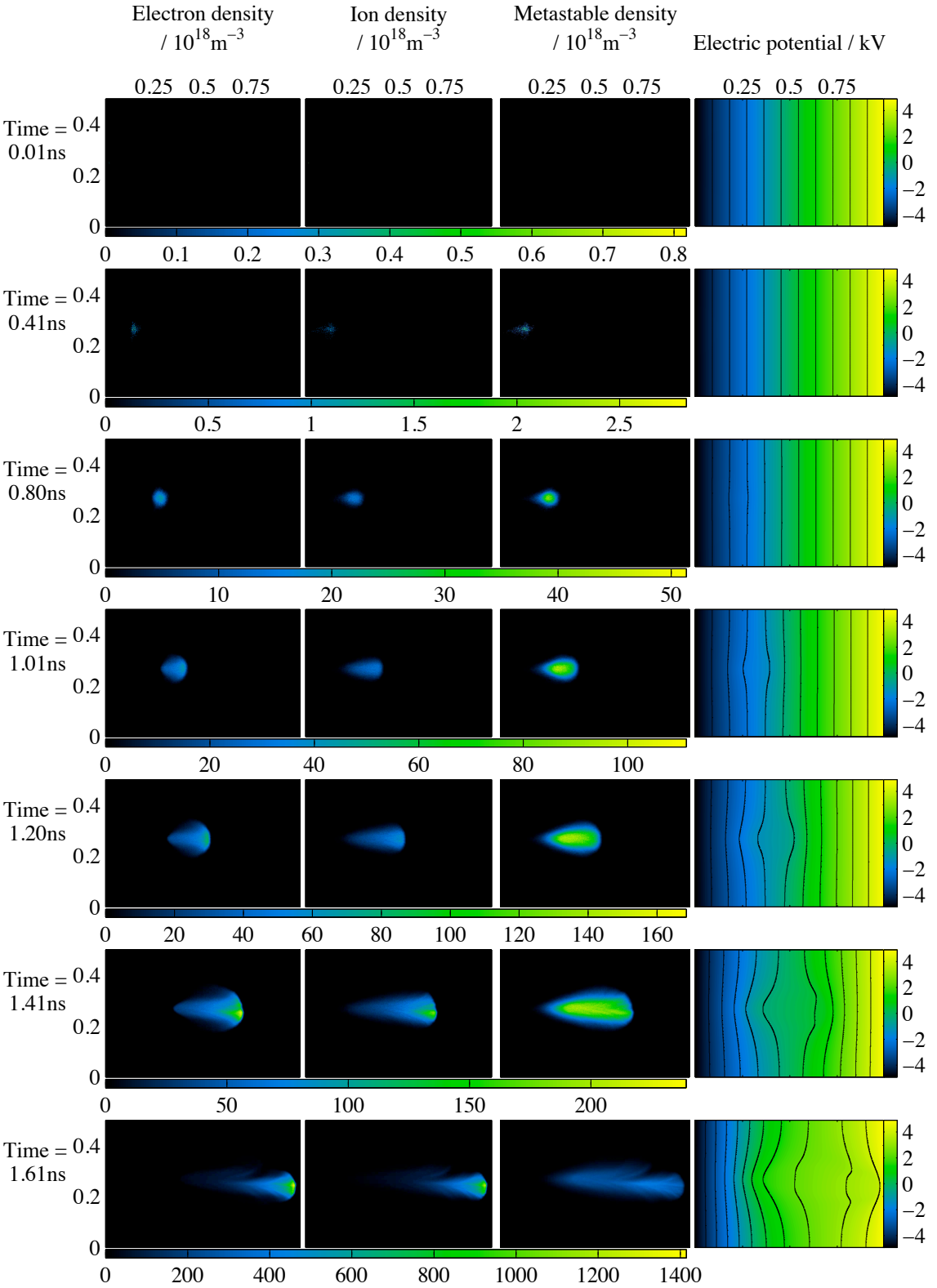

Figure 6.2: Evolution of the electron avalanche in a 1mm gap of atmospheric pressure Nitrogen with an electric field of 12MVm^{-1}. The colour scale for the density plots changes for each series of snapshots. The numerical range of the density scale is shown beneath the density plots. The colour scale for the electric potential is situated to the right of each plot. The x- and y-axes on each plot give the spatial variation in the x and y directions and are expressed in units of mm.

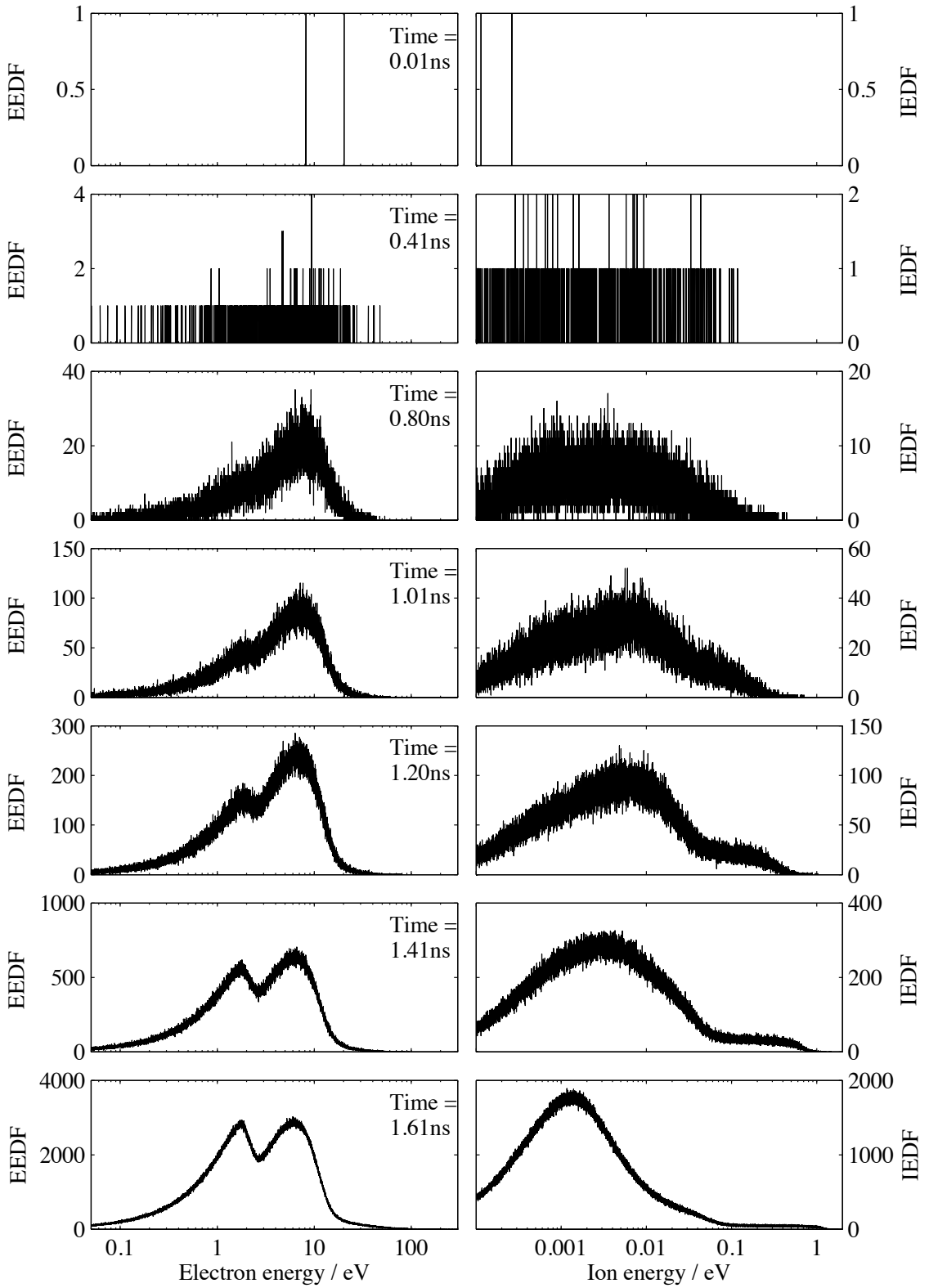

Figure 6.3: Evolution of the electron and ion energy distribution functions. In a DC electric field.

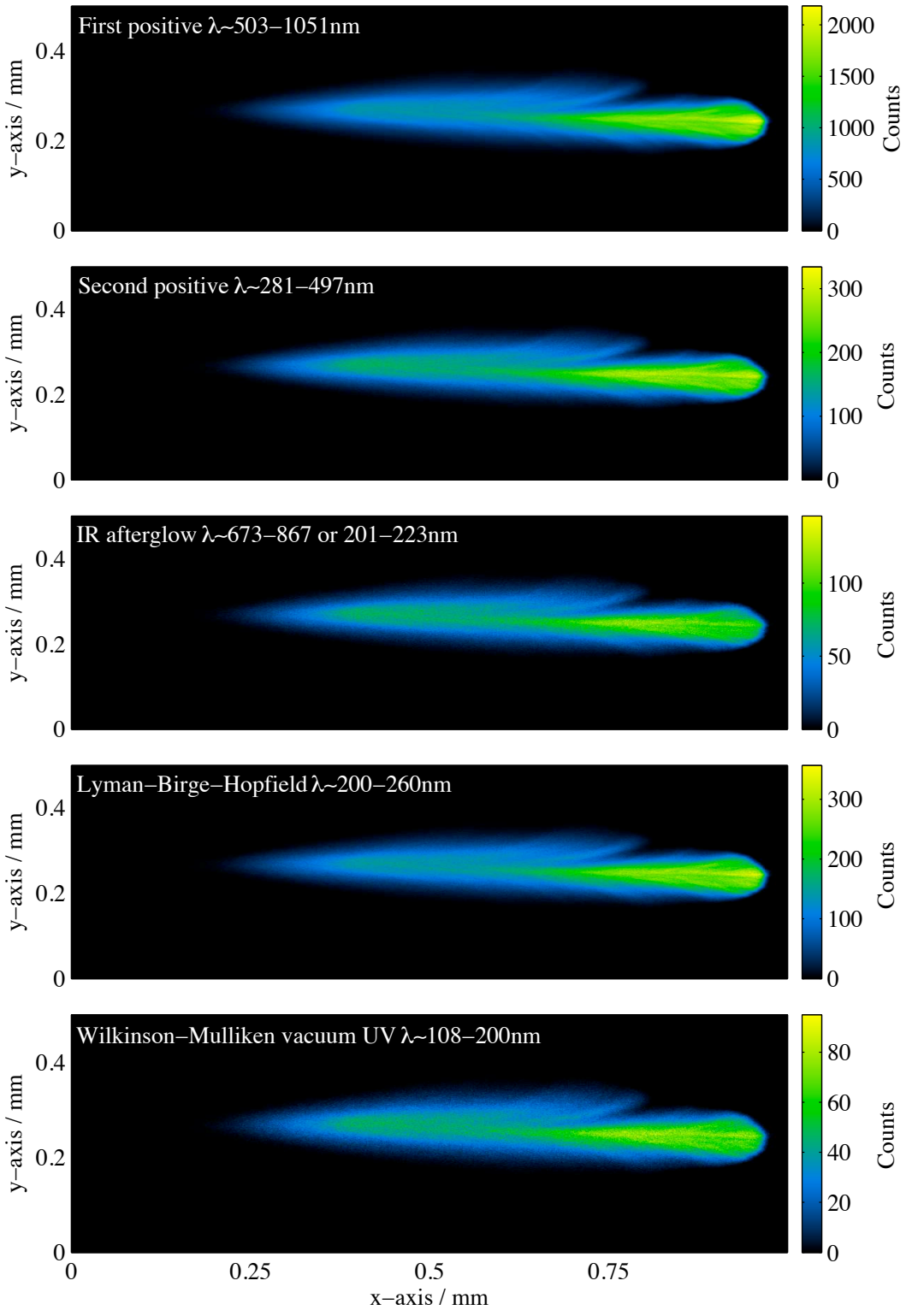

Figure 6.4: The integrated light emission for an electron avalanche in a DC electric field.

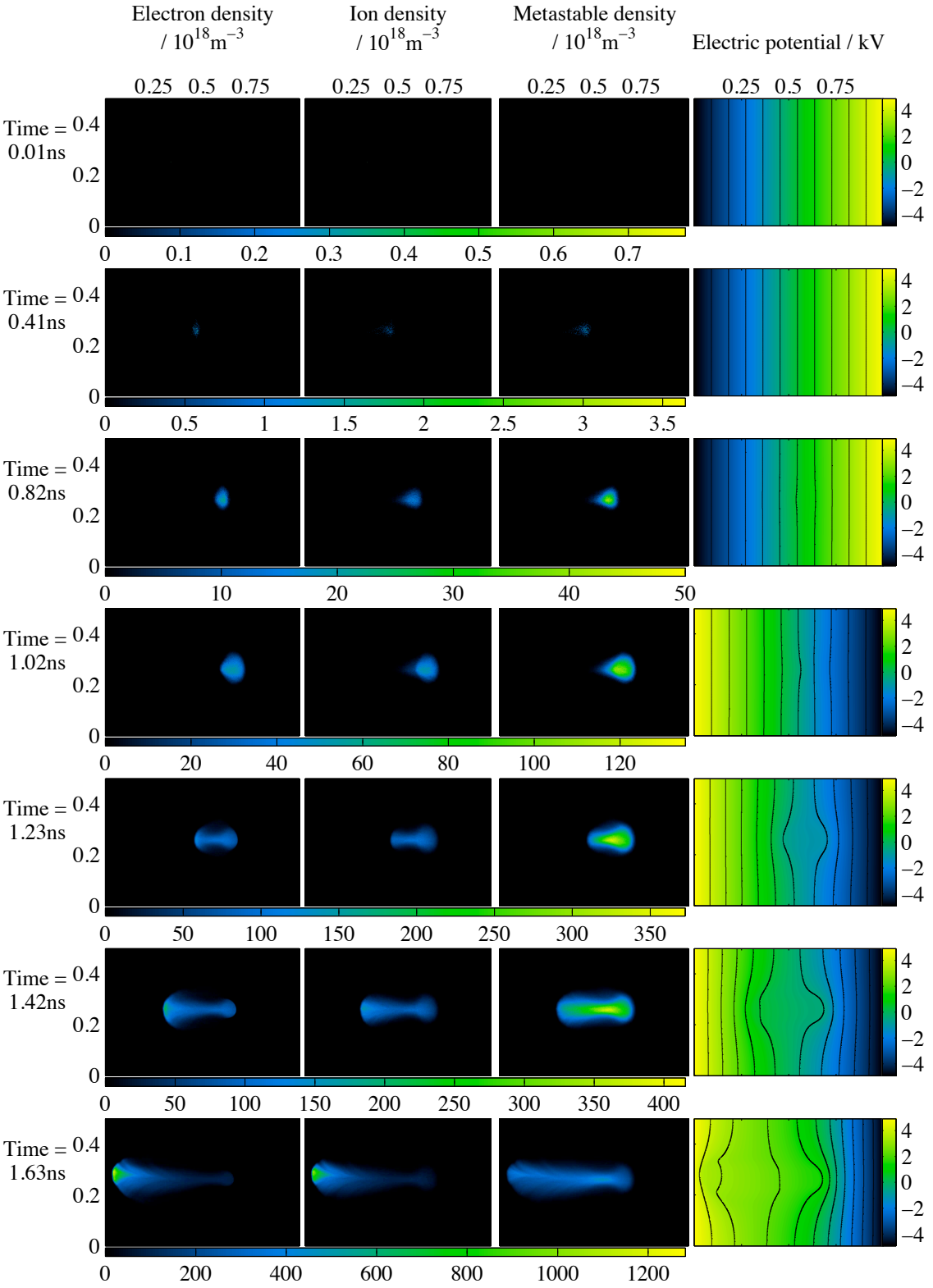

Figure 6.5: Evolution of the electron avalanche in a 1mm gap of atmospheric pressure Nitrogen with an electric field of 12MVm^{-1} reversed at 1ns. The colour scale for the density plots changes for each series of snapshots. The numerical range of the density scale is shown beneath the density plots. The colour scale for the electric potential is situated to the right of each plot. The x- and y-axes on each plot give the spatial variation in the x and y directions and are expressed in units of mm.

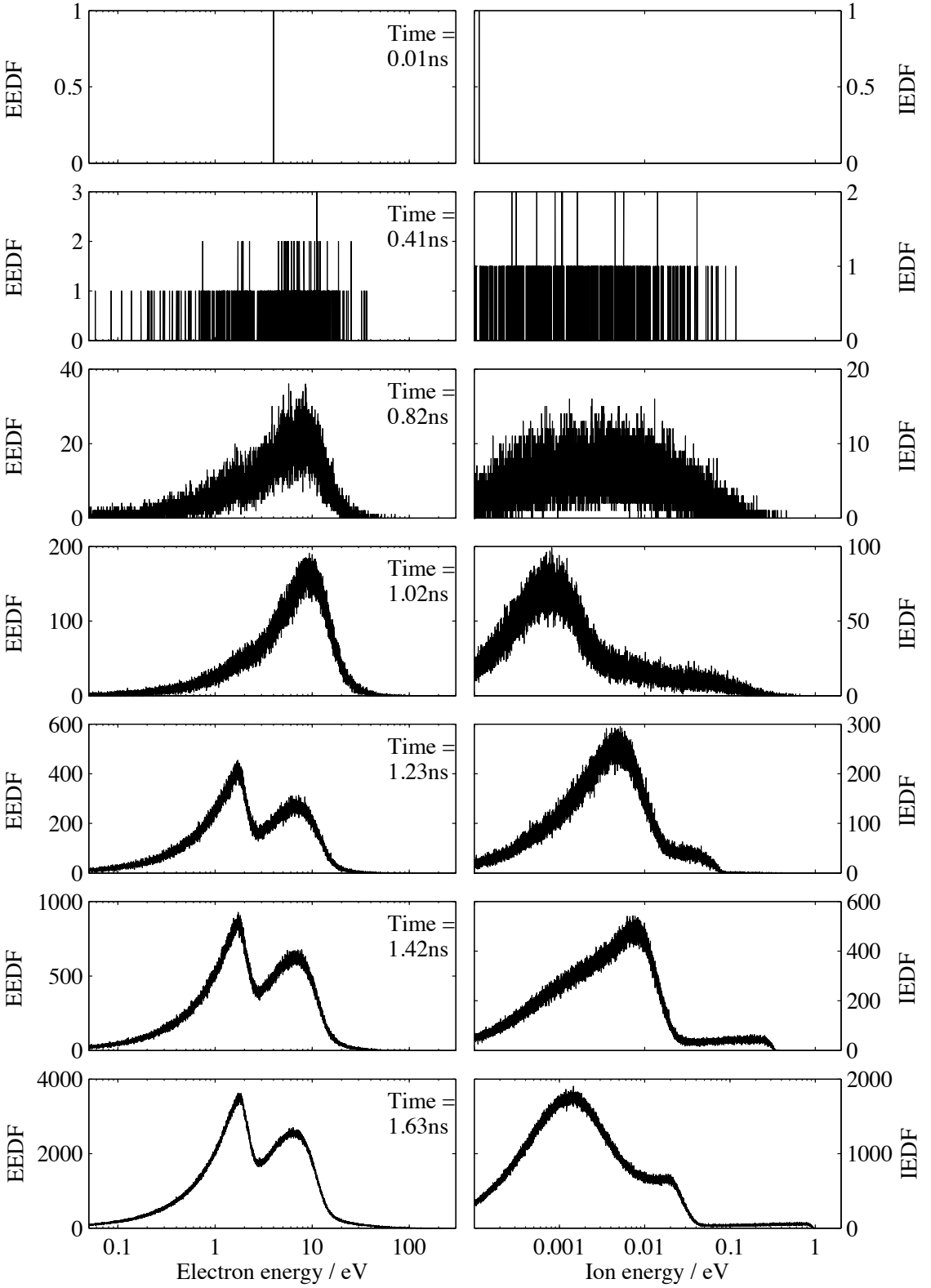

Figure 6.6: Evolution of the electron and ion energy distribution functions. When the electric field is reversed after 1ns.

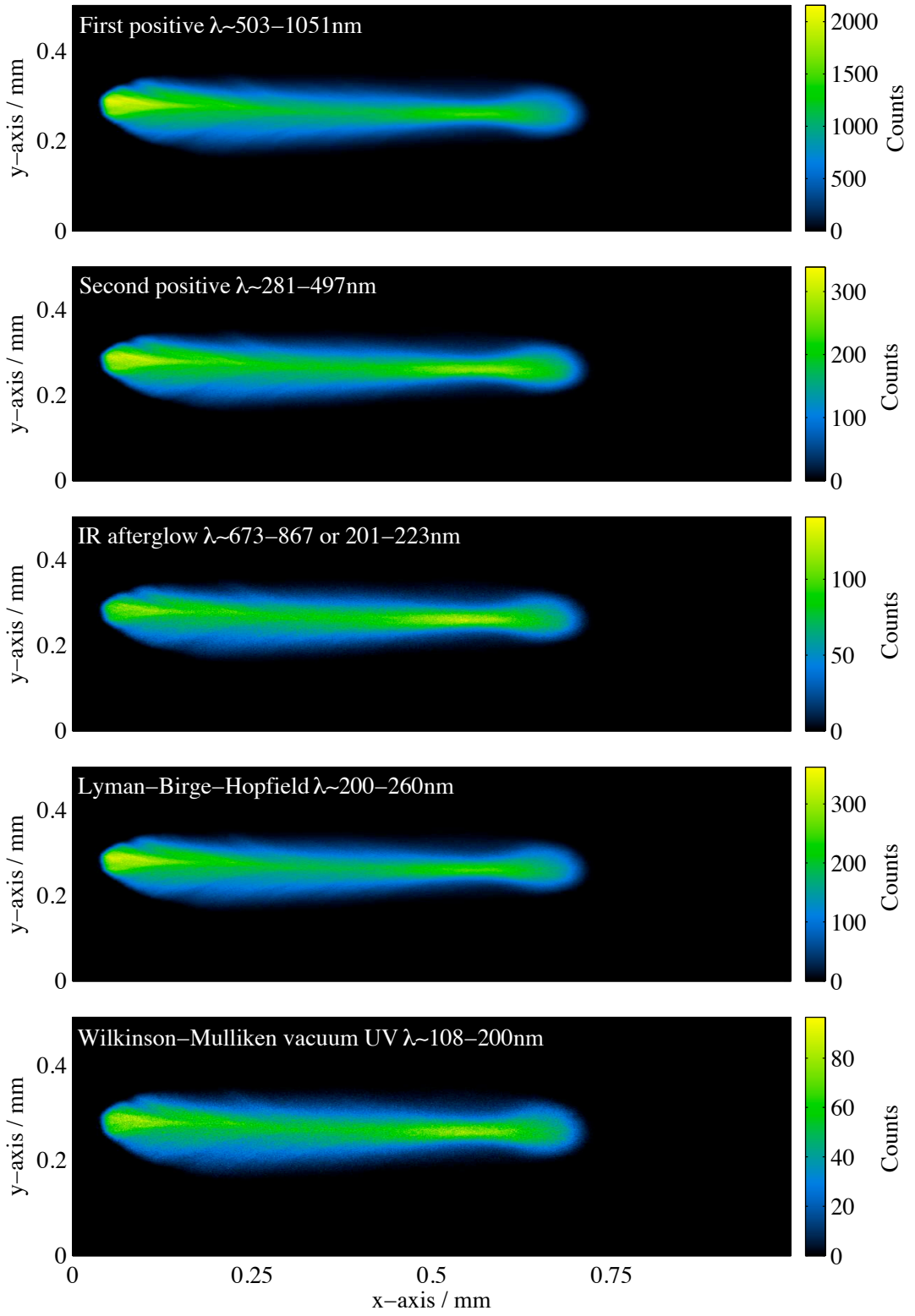

Figure 6.7: The integrated light emission for an electron avalanche with a reversal of the electric field.

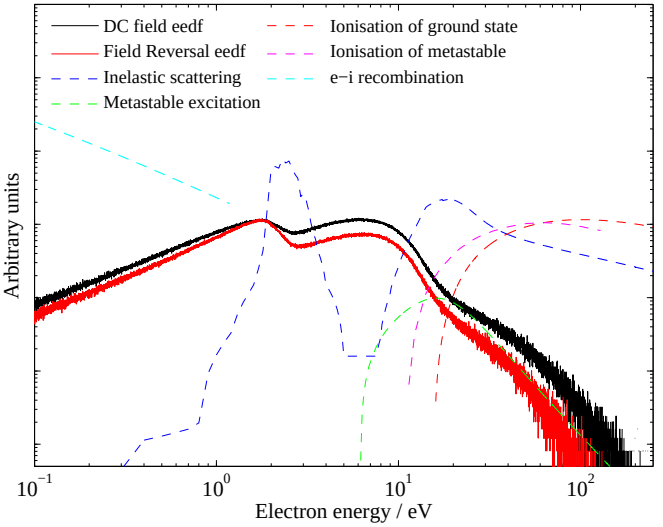

Figure 6.8: Plot showing the normalised energy distributions and the normalised cross-sections. Only the cross-sections that result in an energy loss are shown.

6.4.3 Comparing DC and reversed electric fields

There spatial distribution of the particles in the two cases is obviously different because the fields point in opposite directions during the later stages of the avalanche.

The electron energy distribution functions in both the DC and field reversal cases have quite complicated shapes. Figure 6.8 shows the eedfs at time 1.60ns with the cross-sections of: inelastic scattering, metastable excitation, metastable ionisation, neutral ionisation and recombination superimposed. The inelastic reactions have a noticable effect on the eedfs. At approximately 2eV there is a dip in the electron energy distribution, this absence of electrons corresponds to the peak in the inelastic cross-section. At energies greater than $\sim$ 10eV metastable excitation becomes possible and this results in a drop in the energy distributions. Beyond 16eV the number of electrons falls further due to the ionisation reactions.

The distribution functions decrease at the peaks of the cross-section and there is a peak in the distribution function at 6eV where the inelastic cross-section has a local minima.

The energy distributions show that the populations of both the electrons and ions at lower energies are greater when the field is reversed. This is expected since the direction of the field initially decelerates the charged particles. When the light emission is in both cases have similar structures, particularly the striated patterns towards the head of the avalanche.

Figure 6.18 compares the number of species created in the avalanche for both electric field cases. There is a clear increase in the number of all species when the field is reversed. The increase in the ionisation and metastable excitation rate is caused by the alignment of the self-field and the applied field. When the applied field is reversed it is in the same direction as the self-field created by the electron head and ion tail. This means that the

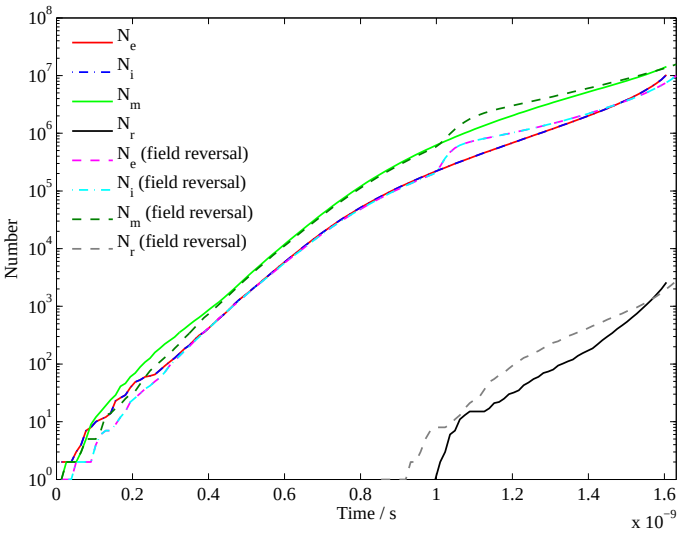

Figure 6.9: Comparison of the numbers of each species for DC and reversed electric fields. The legend entries: N_e, N_i, N_m, N_r correspond to the number of electrons, ions, metastables and total recombinations respectively.

value of the electric field is higher than it would be when there is no field reversal. This results in an boost in the electron acceleration and a boost in the particle production rate. As the avalanche reverses its bulk motion the particle production rate drops and over time the numbers of particles in the DC avalanche catch up.

In figure 6.10 the energy probability functions of the electrons and ions for each of the electric field cases are shown. The plots show that none of the energy distributions can be described fully using Maxwellian or Druyvesteyn distributions. At this stage of the avalanches the energy distributions are non-equilibrium. The electron energy probabilities for the two electric field cases have similar shapes but there is a smaller number of particles in the field reversal case compared to the DC case.

6.5 Results from the three-dimensional model

6.5.1 DC electric field

The spatial evolution of the electron avalanche in a DC electric field is shown in figure 6.11. Snapshots of the electron density, ion density, metstable density and the total electric potential are shown for a selection of times. The plots of the particle densities and electric potential show a slice through through the middle of the z range are shown for each time. The three-dimensional structure of the charge density is shown in figure 6.12. This structure is similar in both field cases.

The electron and ion energy distribution functions for the same time selections as in the density plots (figure 6.11) are shown in figure 6.13. The plots of the integrated light

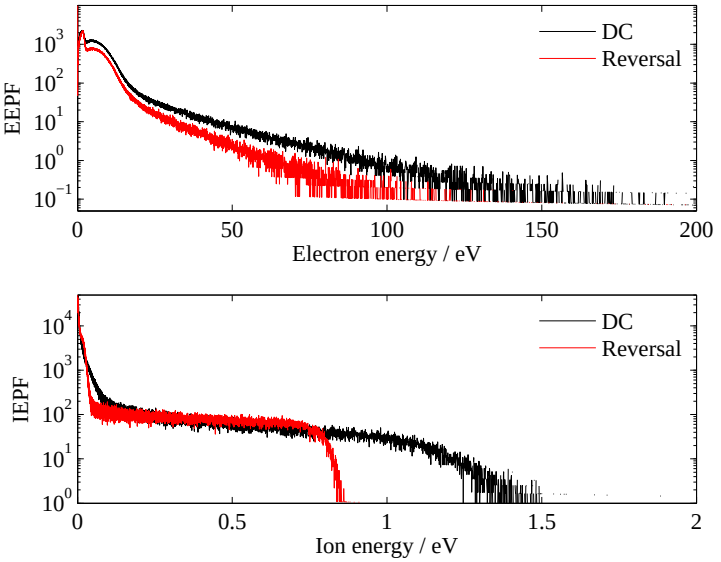

Figure 6.10: Comparison of the electron and ion energy probability functions for DC and reversed electric fields at time 1.61×10^{-9}s.

emission are summed in the z direction and are shown in figure 6.14.

6.5.2 Electric field reversal

The spatial evolution of the electron avalanche when the electric field is reversed is shown in figure 6.15. Snapshots of the electron density, ion density, metstable density and the total electric potential are shown for a selection of times. The plots of the particle densities and the electric potential show a slice through the middle of the z range are shown for each time. The electron and ion energy distribution functions for the same time selections are shown in figure 6.3. The plots of the integrated light emission are also summed in the z direction and are shown in figure 6.17.

6.5.3 Comparing DC and pulsed electric fields

Figure 6.18 compares the number of species created in the avalanche for both electric field cases. In figure 6.19 the energy probability functions of the electrons and ions for each of the electric field cases are shown.

6.6 Comapring two- and three-dimensional simulation results

The main difference between the two situations is the number of particles. There are more particles in the two-dimensional case. There are more particles because the electrons are

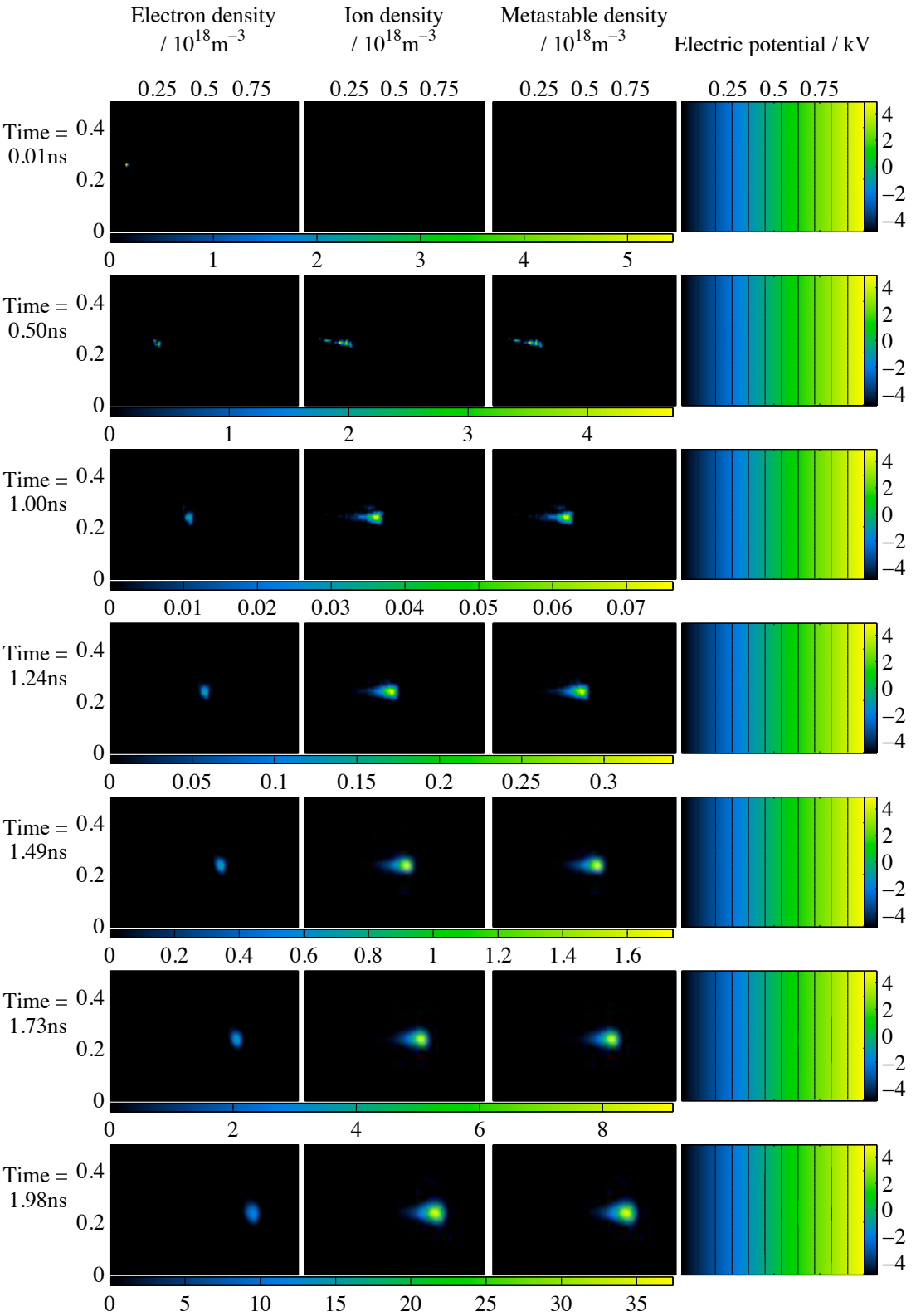

Figure 6.11: Evolution of the electron avalanche in a 1mm gap of atmospheric pressure Nitrogen with an electric field of 12MVm^{-1}.

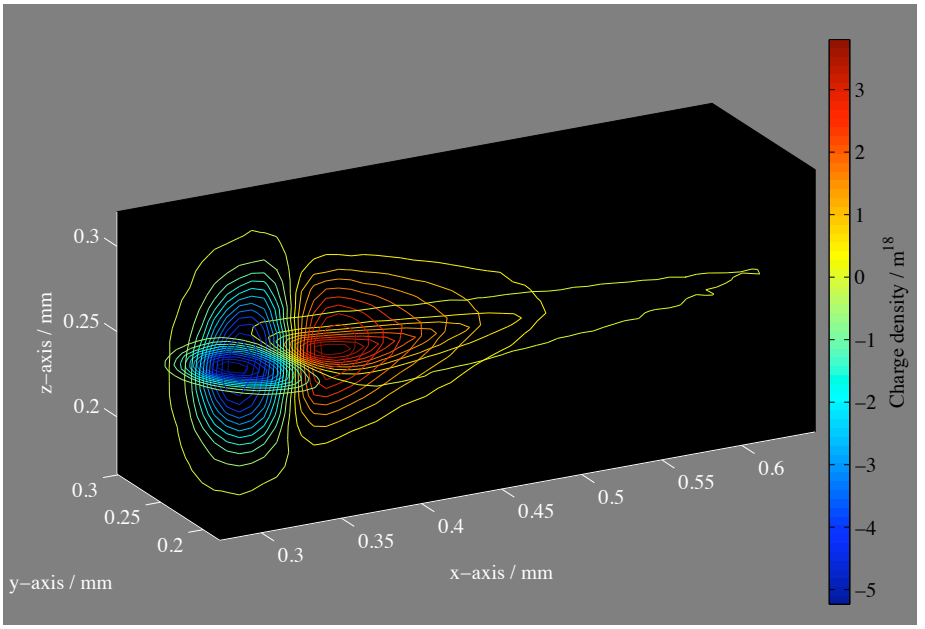

Figure 6.12: Three-dimensional contour plot of charge density showing typical structure of avalanche.

undergo many more inelastic collisions. This can be seen by comparing the counts in the light emission plots (*cf.* figure 6.4 and figure 6.14). In the first positive system the counts in the three-dimensonal cases a factor $\sim$100 greater than in the two-dimensional cases.

In the two dimensional case when the direction of the field is reversed, there is an increase in the particle production rate. This boost is not seen in the three-dimensional case. The rise in the particle production rate is attributed to the alignment of the self-field and the applied field. In the three-dimensional case the self-field is still dominated by the applied field and consequently there is no significant gain from their allignment. The self-field is smaller in the three-dimensional cases because of two factors: the smaller number of particles and the $1/r$ fall off in the potential (see section 3.3).

6.7 Conclusions

A robust particle model has been implemented and used to describe the initial stages of a plasma. Electron avalanches in two- and three-dimensions have been modelled. The population of $A^3\Sigma_u^+$ metastables has been calculated and an estimation of the light emission from short lived excited molecules has been made. The results from the simulations highlight the non-equilibrium nature of the tenuous plasma on a nansecond timescale.

Many existing simulations of breakdown have been carried out with fluid models [122–124]. These models require assumptions about the initial plasma density and it's distribution. The model presented here makes no such assumptions and calculated the breakdown from a single electron-ion pair. The analysis of the energy distributions discussed above cannot be achieved in a fluid context. The distribution function would need to be assumed.

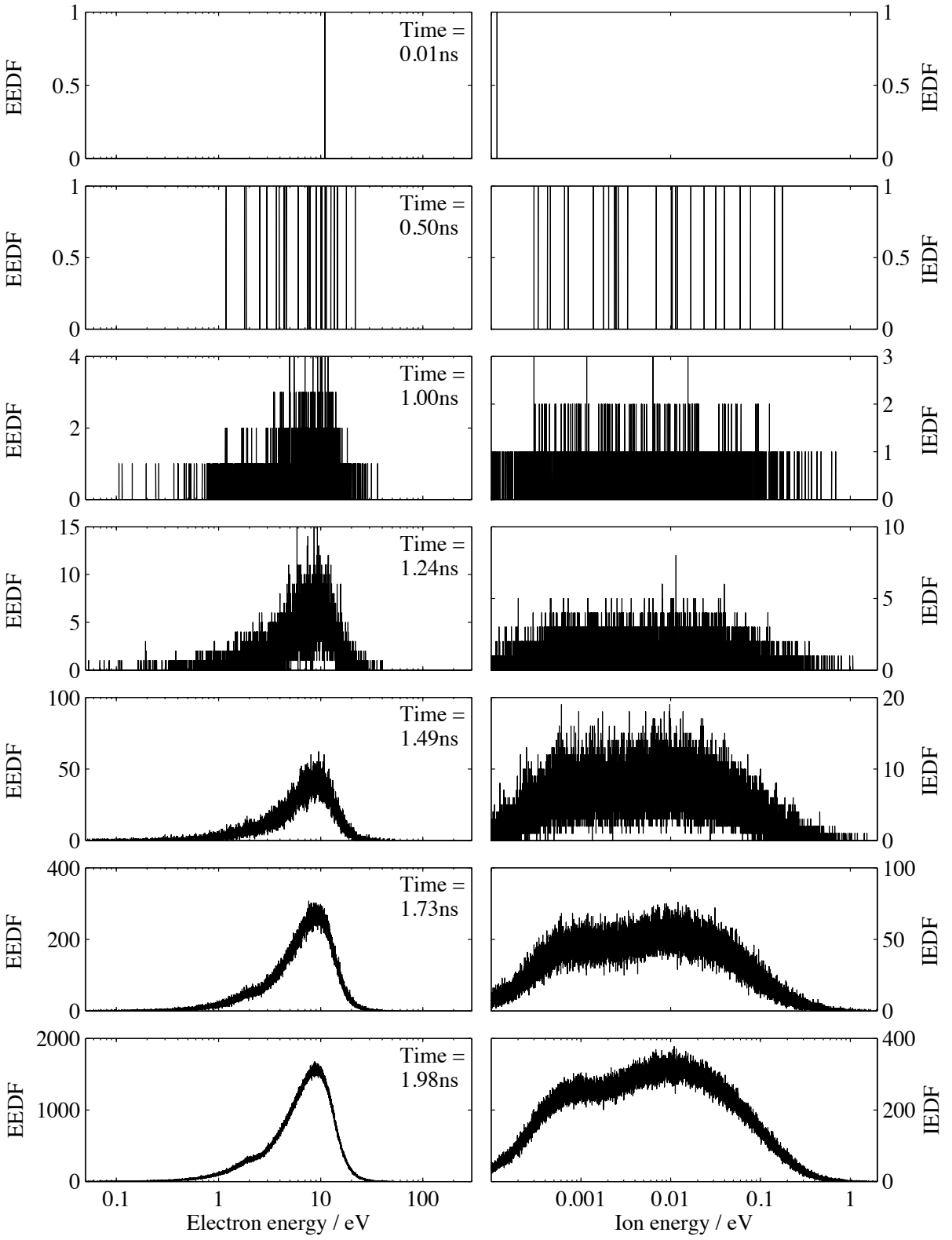

Figure 6.13: Evolution of the electron and ion energy distribution functions. In a DC electric field.

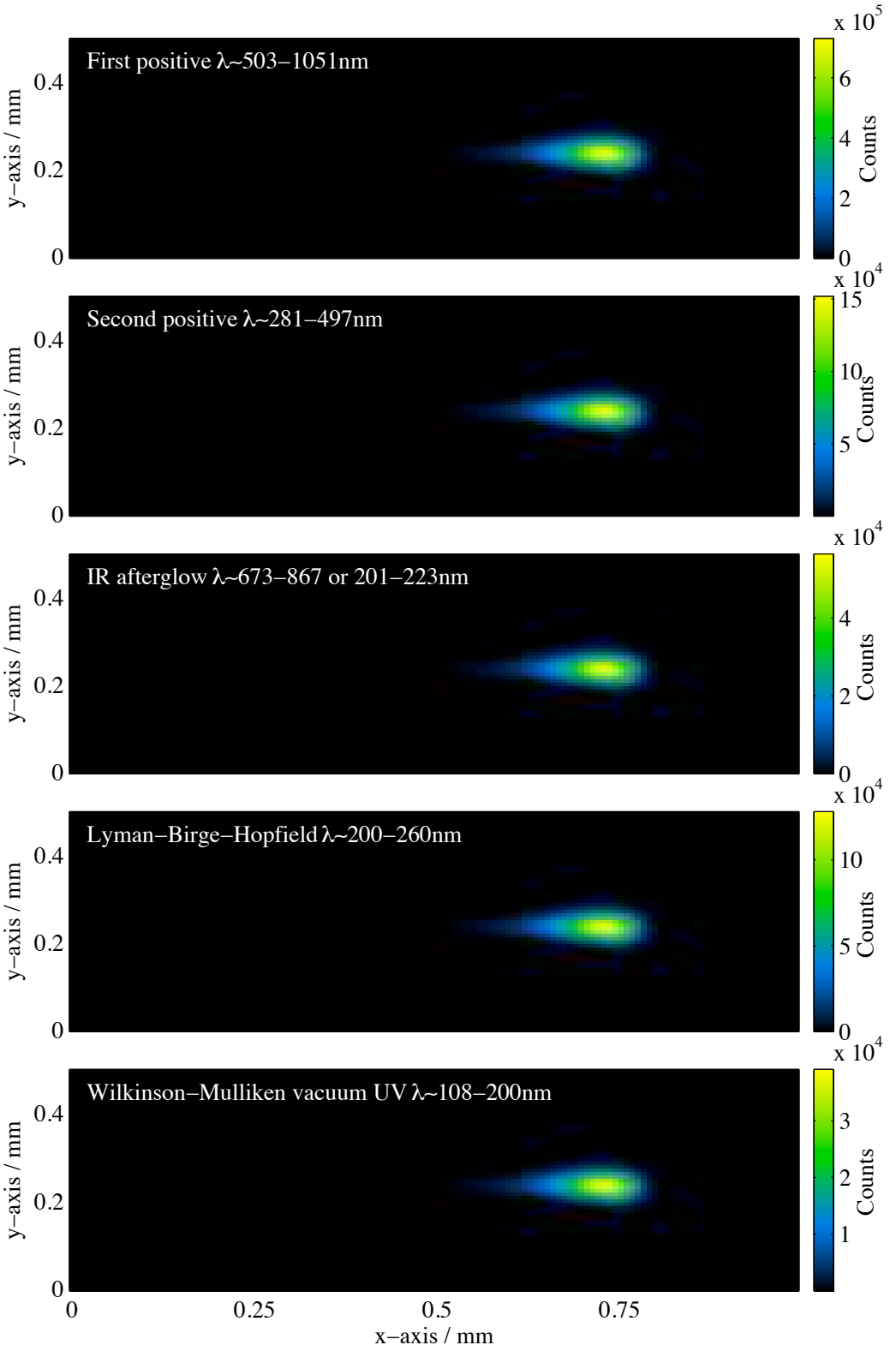

Figure 6.14: The integrated light emission for an electron avalanche in a DC electric field.3d

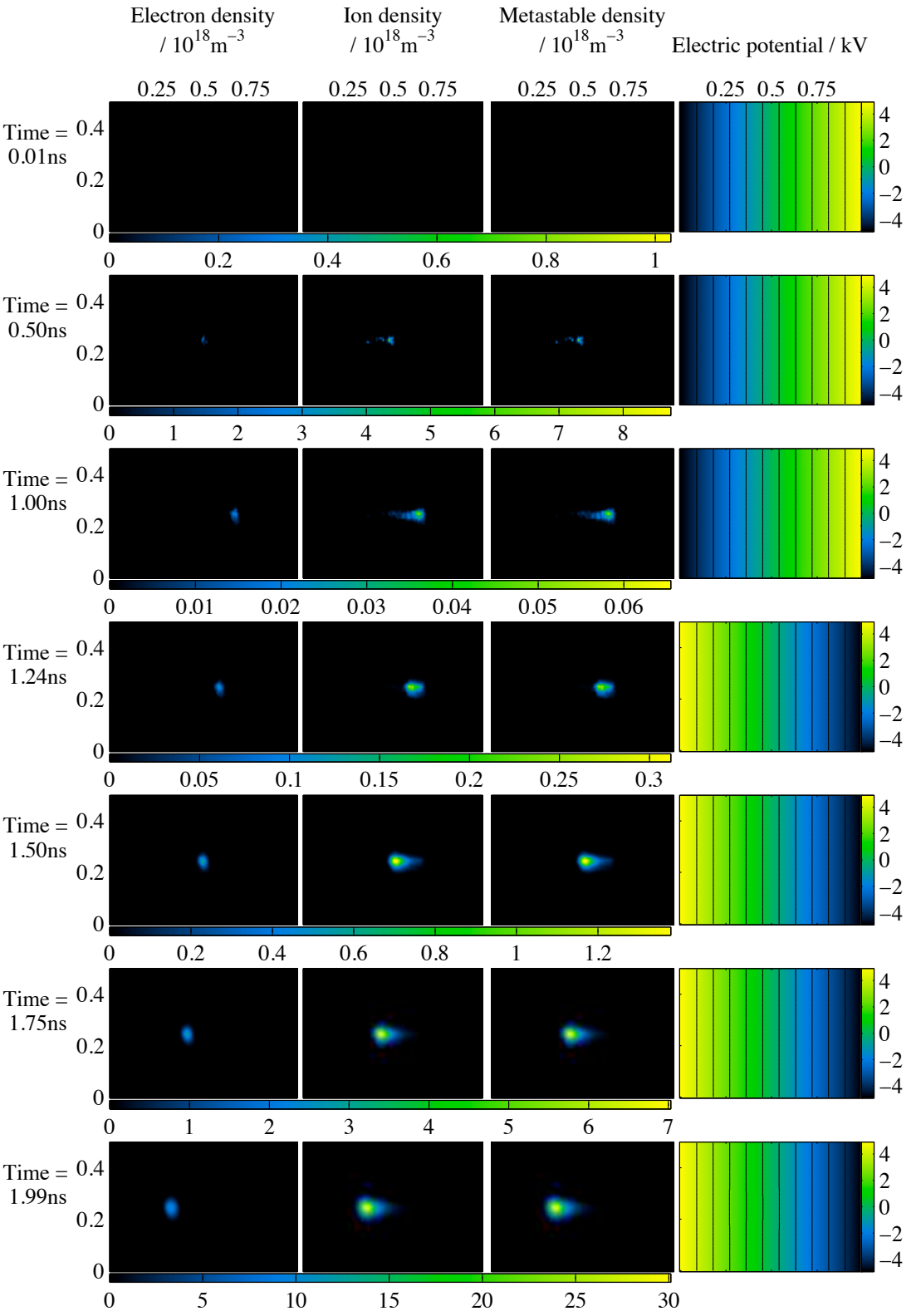

Figure 6.15: Evolution of the electron avalanche in a 1mm gap of atmospheric pressure Nitrogen with an electric field of 12MVm^{-1} reversed at 1ns.

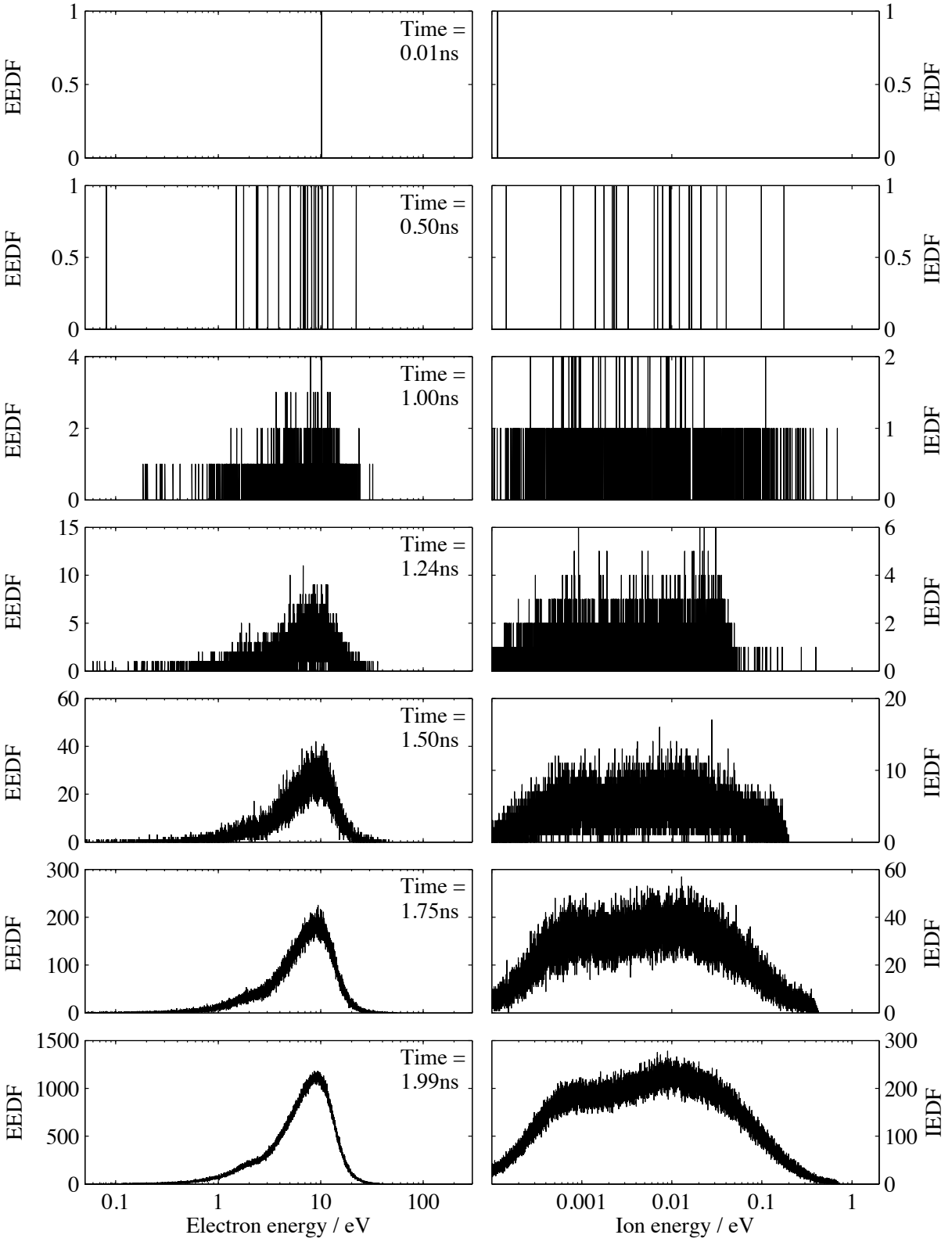

Figure 6.16: Evolution of the electron and ion energy distribution functions. When the electric field is reversed after 1ns.

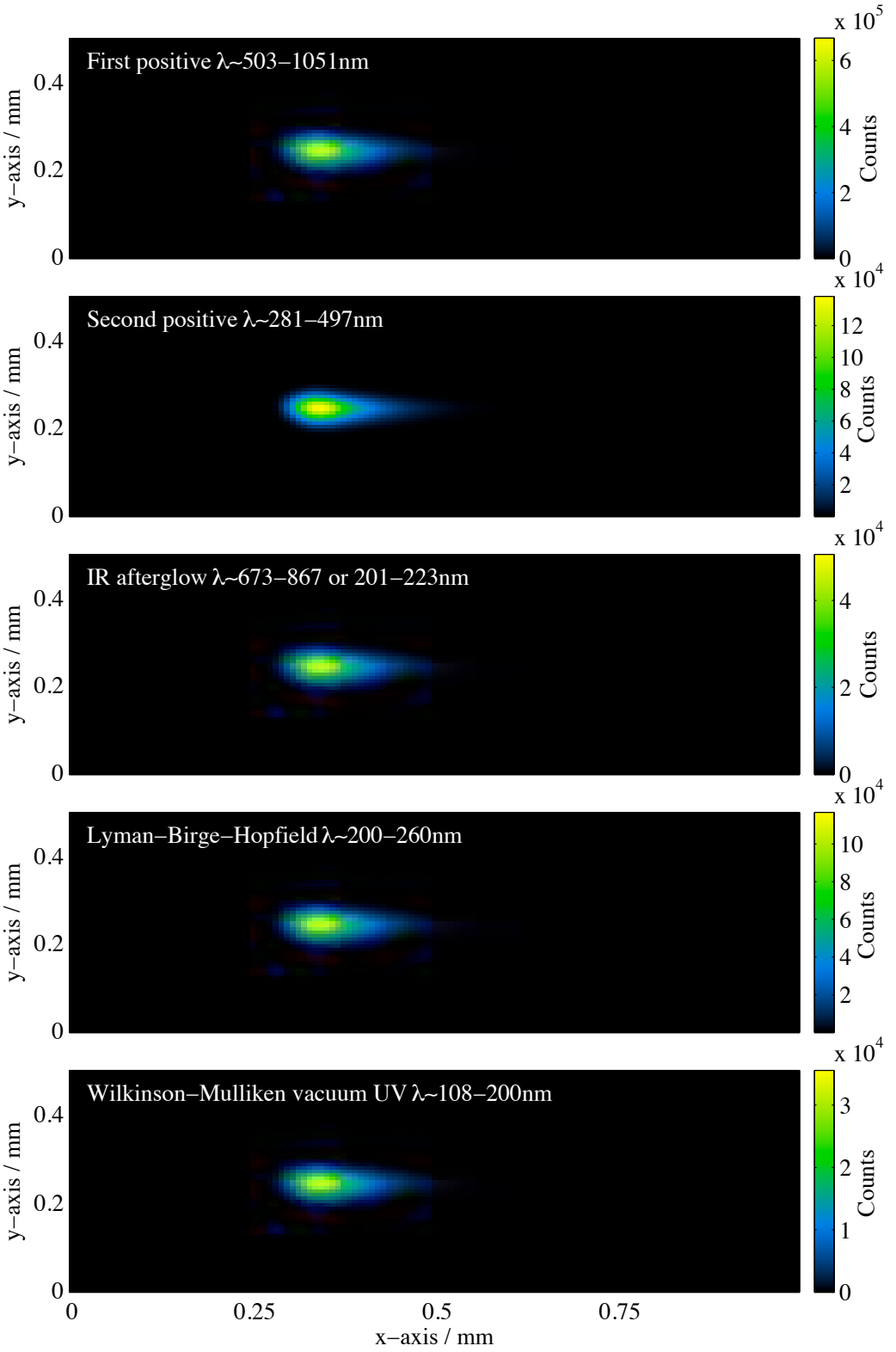

Figure 6.17: The integrated light emission for an electron avalanche with a reversal of the electric field.3d

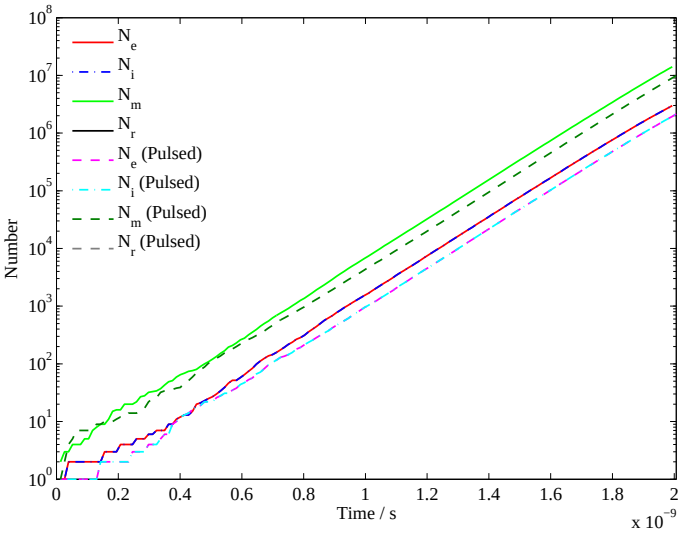

Figure 6.18: Comparison of the numbers of each species for DC and reversed electric fields. The legend entries: N_e, N_i, N_m, N_r correspond to the number of electrons, ions, metastables and total recombinations respectively.

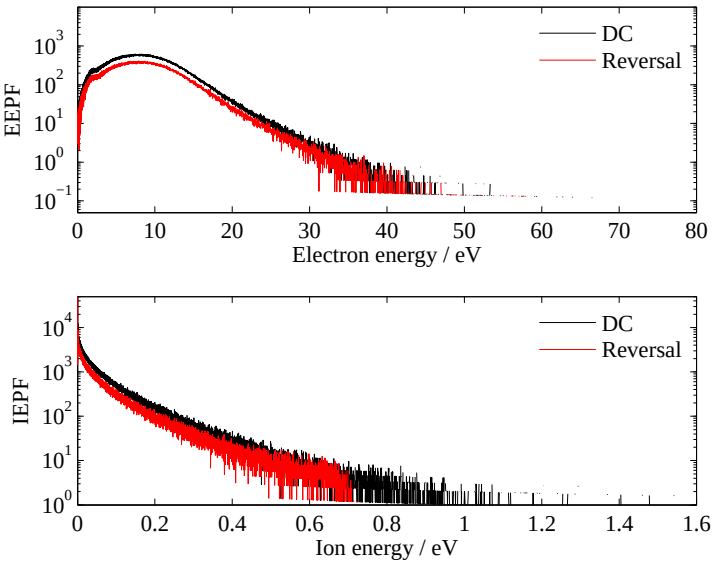

Figure 6.19: Comparison of the electron and ion energy probability functions for DC and reversed electric fields at time 2.00×10^{-9}s.

There have been studies with particle models [96; 125]. This is the first model that has included the creation of metastables and an accurate representation of the inelastic loses.

The metastable population is a key element in determining the required breakdown voltage in pulsed plasmas [115]. The metastables have a long lifetime compared to the pulse length; the N_2 $A^3\Sigma_u^+$ metastable has a lifetime of ~ 2.7s. The metastables can be ionised by lower energy electrons than the ground state neutrals and so, the required field for breakdown is reduced.

The estimation of the photon emission is a valuable diagnostic tool. The main aim of any simulation is to achieve a greater understanding of the physical situation and ultimately, predict the evolution of the plasma. This goal can only be reached if the model represents the physical situation. The output from simulations can only be verified by comparison to experimental data. ICCD cameras with nanosecond resolution are available and would be an effective method to probe an electron avalanche without effecting its evolution. Such experimental measurements could be compared to these simulations.

Chapter 7

Critical Ionisation Velocity interaction

7.1 Introduction

In 1942 Alfvén attempted to explain the positions of the planets in the solar system [126]. He proposed that a neutral gas impinging on a magnetised plasma would cause significant amounts of ionisation when the flow exceeds a threshold velocity, later known as the Critical Ionisation Velocity (CIV). The threshold velocity v_c for the ionisation enhancement is given by

$$v_c = \sqrt{\frac{2e\phi_{iz}}{m_n}}, \tag{7.1}$$

where $e\phi_{iz}$ is the ionisation potential of the neutral species in electron volts and m_n is the mass of the neutral particle.

Neutral gas falling towards the Sun was ionised when it reached the threshold velocity. Since the velocity threshold has a dependence on the mass, different species ionised at different Solar radii. Once ionised, the gas was prevented from falling towards the Sun by its magnetic field and the planets were seeded.

The CIV concept was later confirmed experimentally by Fahleson [127]. A plasma was generated in a gap of 17cm between coaxial cylinders. The inner cylinder was an electrode held a fixed potential and the outer wall was earthed, a diagram can be seen in figure 7.1. An axial magnetic field was applied. The $\boldsymbol{E} \times \boldsymbol{B}$ drift gave the plasma an azimuthal velocity, while the neutral species had no bulk motion. For Hydrogen, speeds of 54kms^{-1} were measured. This is above the critical ionisation velocity and increased ionisation was observed.

Brenning [128] and Lai [129] present extensive reviews of the literature. The CIV phenomena has been implicated in many astrophysical contexts: solar abundances [130], interstellar filaments [131], plasma propulsion [132], comets [133], the Io-Jupiter system [134] and in its first instance, by Alfvén, to explain the seeding of planets in the solar system.

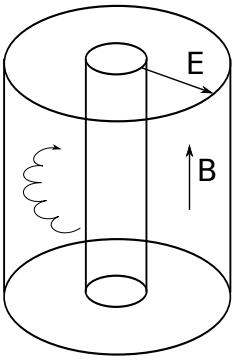

Figure 7.1: Schematic of rotating plasma device.

Many laboratory experiments have successfully confirmed the CIV interaction [127; 135]. A variety of experimental devices have been used. The effect typically exhibited as a period of rapid ionisation and a subsequent slowing of the plasma speed to the critical ionisation velocity. This did not occur for any initial speeds below the critical speed.

There have also been several experiments carried out in space [136]. Shortly after the impact of the Apollo 13 launch vehicle on the moon's surface large ion fluxes were observed [137]. The impact caused a large number of neutrals to enter the atmosphere of the Moon where they interacted with the solar wind. The speed of the solar wind is well above any critical ionisation velocity. It was suggested that a small fraction of the ionisation was the result of the CIV interaction however, the uncertainties in the calculation could easily rule this out [136].

Artificial gas releases into the magnetosphere provided a more effective space test for the CIV interaction but most produced little or no confirmation. Typically the main aim of these experiments was to trace the electric fields by observing the $\boldsymbol{E}\times\boldsymbol{B}$ drift of the particles, not investigate the CIV effect. These tests were done during the day when the released gases are quickly photoionised. The first seconds after the release are most likely to exhibit the CIV effect. These conditions are not optimal for investigating the CIV interaction.

There have been two space experiments designed specifically to investigate CIV effects: Star of Lima [138] and Star of Condor [139]. The former had very good conditions for CIV effect but saw an ionisation efficiency three orders of magnetitude lower than expected. Observations from the star of condor showed no discernible increase in ionisation at all.

The idea is simple: rearranging (7.1) shows the neutral has kinetic energy equal to its ionisation energy threshold. This energy, however, is insufficient for direct electron impact ionisation since ionisation occurs in the centre of momentum frame.

Alfvén explained the CIV phenomena in the following way [140]: neutrals, with kinetic energy $e\phi_{iz}$, streaming across a stationary magnetised plasma, perpendicular to the magnetic field, collide with ions resulting in momentum transfer or charge exchange. The collisions cause a region of unbalanced charge which is not neutralised immediately by the electron population because the magnetic field restricts their transport. Regions of unbalanced negative charge can continue to grow, through the removal of positive charge, until the potential reaches ϕ_{iz}: too great for the ions to escape since the maximum speed the

ions can gain is v_c. The electrons are accelerated by this potential to speeds capable of ionisation.

Figure 7.2 shows a cartoon of the CIV effect: the impinging neutrals transfer momentum to the ions, the new trajectories of the ions move them away from the electrons, whose transport is much more inhibited by the magnetic field, the electrons are heated to higher energies by their self electric field.

More detailed models have been proposed, most depending on the formation of unbalanced charge densities, but details of the structure and electron energisation vary. The lower hybrid instability, also called the modified two-stream instability [141] is most commonly used to explain the electron heating. This instability is caused by ions travelling with the neutrals perpendicular to the magnetic field lines, across the plasma. This seed of positive charge in the neutral beam can be caused by charge exchange, thermal ionisation or photoionisation. The seed ions generate instability waves which energise the electrons. There are problems with this energisation process [129]: the instability has a long wavelength and may not fit in finite experimental dimensions; and secondly, the mechanism requires some resonance between the wave and particle, if an electron does not have an initial speed close to the wave speed then the acceleration is inefficient.

In general any process that creates a negative charge imbalance which heats the electrons to ionising energies can be described as the CIV effect. There is no consensus on a single process responsible for the CIV interaction, several process may be implicated for different conditions.

There have been several simulation studies of the CIV effect [142–144]. These simulations have used particle-in-cell [48] techniques in one and two spatial dimensions to verify the CIV effect. The ionisation enhancement has been recreated in all cases and shown to depend on the type and functional form of the considered cross-sections [143; 144].

A comprehensive investigation of the CIV effect, as a lower-hybrid instability, using simulation was carried out by Machida & Goertz [142]. A mostly neutral beam impinges

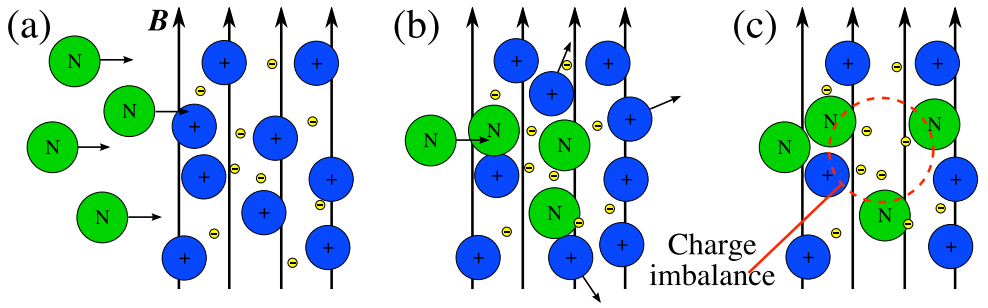

Figure 7.2: A cartoon showing the Alfvén ionisation process. The neutrals impinging on the magnetised plasma are shown in (a). In (b) some of the neutrals have collided with the positive ions transferring momentum. Finally, in (c), a pocket of unbalanced negative charge is created by the absence of positive ions. The electrons are heated by the self-field of this charge imbalance.

on a stationary magnetised plasma. There is some pre-determined level of ionisation in the beam resulting in beam ions. The densities of the beam, stationary and thermal ions (ions resulting from elastic collisions with neutrals or diffused beam ions) are followed, as is the electron density. A uniform beam of neutrals is assumed and so no neutral properties are calculated in the simulation. Three components are used to calculate the electron temperature evolution: resistive heating, due to elastic collisions with neutrals; collective heating, due to plasma waves; and collisional loses resulting from various excitations and ionisation collisions.

Simulation studies thus far have shown the validity of the CIV mechanism but there have been no attempts to describe the dependence of the energy enhancement on the density and magnetic field strength. We aim to investigate the distribution of electron energies resulting from the acceleration under the self-field for different parameters. From this it may be possible not only to determine the optimum conditions for ionisation but also for the creation of specific excited states.

7.2 Model of electron energisation

The CIV interaction can be broken into two problems on separate timescales: the ion-neutral timescale and the electron-electron timescale. On the ion-neutral timescale pockets of unbalanced negative charge are produced through charge exchange and momentum-transfer collisions between the ion and neutral species. The electrons in the pockets of unbalanced negative charge are accelerated by their self field on the electron-electron timescale. The electron transport is restricted in the directions perpendicular to the magnetic field. This restricted transport increases the time the electrons take to neutralise the charge imbalance. The simulation of the electron-electron stage will be discussed here.

This stage is simulated by considering an ensemble of electrons in a magnetic field. Only the unbalanced electrons are simulated; the quasi-neutral background is assumed to be present but is not explicitly included in the calculation. There are two reasons for this choice: firstly the inclusion of the background plasma would add to the computational load; secondly, including the background plasma would require the size of the electron pocket relative to the plasma density to be defined, adding an extra parameter. If the background plasma is strictly quasi-neutral then the contribution to the potential is zero. An initial population of electrons is allowed to evolve using single particle equations. Direct electron-electron collisions are neglected but the electrons still interact through the self-field. The magnetic field remains uniform throughout; any magnetic field induced by the electron current is ignored.

7.2.1 Model equations

The equations required to simulate the evolution of the electrons are:

$$m\frac{d\boldsymbol{v}}{dt} = -e\left(\boldsymbol{E} + \boldsymbol{v} \times \boldsymbol{B}\right), \tag{7.2}$$

$$\nabla^2\phi = \frac{e}{\varepsilon_0}(n_+ - n_e), \tag{7.3}$$

$$\boldsymbol{E} = -\nabla\phi. \tag{7.4}$$

These equations are the momentum equation, Poisson's equation and the electric field respectively. To carry out the numerical simulation the governing equations are non-dimensionalised. The variables are mapped as follows:

$$\begin{aligned} \boldsymbol{v} &\mapsto v_0\hat{\boldsymbol{v}}, & (7.5)\\ t &\mapsto t_0\hat{t}, & (7.6)\\ \boldsymbol{E} &\mapsto E_0\hat{\boldsymbol{E}}, & (7.7)\\ \boldsymbol{B} &\mapsto B_0\hat{\boldsymbol{B}}, & (7.8)\\ \phi &\mapsto \phi_0\hat{\phi}, & (7.9)\\ n_s &\mapsto n_0\hat{n}_s, & (7.10)\\ \nabla &\mapsto s_0^{-1}\hat{\nabla}, & (7.11) \end{aligned}$$

where the zero subscript denotes the scale factor and the non-dimensional variables are denoted by the $\hat{}$ notation. The momentum equation (7.2) becomes

$$\frac{d\hat{\boldsymbol{v}}}{d\hat{t}} = P_E\hat{\boldsymbol{E}} + P_B(\hat{\boldsymbol{v}} \times \hat{\boldsymbol{B}}). \tag{7.12}$$

Poisson's equation (7.3) becomes

$$\hat{\nabla}^2\hat{\phi} = P_n(\hat{n}_+ - \hat{n}_e). \tag{7.13}$$

Equation (7.4) becomes

$$\hat{\boldsymbol{E}} = -P_g\hat{\nabla}\hat{\phi}. \tag{7.14}$$

We also define the non-dimensional kinetic energy $\hat{\kappa}$,

$$\hat{\kappa} = P_\kappa\hat{\boldsymbol{v}}^2. \tag{7.15}$$

The non-dimensional parameters are:

$$\begin{aligned} P_E &= \frac{eE_0t_0}{mv_0}, & (7.16)\\ P_B &= \frac{et_0B_0}{m}, & (7.17)\\ P_n &= \frac{en_0s_0^2}{\varepsilon_0\phi_0}, & (7.18)\\ P_\kappa &= \frac{mv_0^2}{2e\phi_0}, & (7.19)\\ P_g &= \frac{\phi_0}{E_0s_0}. & (7.20) \end{aligned}$$

In an effort to simplify the non-dimensional parameters the following substitutions are made:

$$\begin{aligned} \phi_0 &= E_0s_0, & (7.21)\\ n_0 &= s_0^{-3}, & (7.22)\\ v_0 &= \frac{s_0}{t_0}, & (7.23)\\ E_0 &= \frac{\alpha e}{\varepsilon_0 s_0^2}, & (7.24)\\ t_0 &= \frac{m}{eB_0}. & (7.25) \end{aligned}$$

The variable α is a scaling factor, used to ensure $|\hat{\boldsymbol{E}}| \approx |\hat{\boldsymbol{B}}|$ this makes the meaning of P_E clearer: high P_E means the evolution is electrically dominated, low P_E means the evolution is magnetically dominated. The set of parameters become:

$$P_E = \frac{\alpha m}{\varepsilon_0 s_0^3 B_0^2}, \tag{7.26}$$

$$P_B = 1, \tag{7.27}$$

$$P_n = \alpha^{-1}, \tag{7.28}$$

$$P_\kappa = \frac{1}{2P_E}, \tag{7.29}$$

$$P_g = 1. \tag{7.30}$$

Simplifying the non-dimensional parameters leaves a single free parameter P_E. It may seem that α is also a free parameter, however, it is purely a scaling factor for the non-dimensional values and does not affect the evolution of the electrons. We can see this factor 'cancels' out since

$$E \propto \phi \propto P_n \propto \alpha^{-1} \tag{7.31}$$

and

$$\frac{dv}{dt} \propto P_E E \propto \alpha\alpha^{-1}. \tag{7.32}$$

The parameter P_E can be written as the ratio of the electron plasma frequency (ω_p) and the electron cyclotron frequency (ω_c),

$$P_E = \frac{\alpha m}{\varepsilon_0 s_0^3 B_0^2} = \alpha \frac{n_0 e^2}{\varepsilon_0 m} \cdot \frac{m^2}{e^2 B_0^2} = \alpha \frac{\omega_p^2}{\omega_c^2}. \tag{7.33}$$

7.2.2 Particle motion

The highest energy particles will be those transported parallel to the magnetic field direction. This is intuitive as the transport of electrons perpendicular to the magnetic field is inhibited. This can be mathematically justified by taking the dot product of the velocity and the acceleration (7.12)

$$\hat{\boldsymbol{v}} \cdot \frac{d\hat{\boldsymbol{v}}}{d\hat{t}} = P_E \hat{\boldsymbol{v}} \cdot \hat{\boldsymbol{E}} + P_B \hat{\boldsymbol{v}} \cdot (\hat{\boldsymbol{v}} \times \hat{\boldsymbol{B}}), \tag{7.34}$$

$$= P_E \hat{\boldsymbol{v}} \cdot \hat{\boldsymbol{E}}, \tag{7.35}$$

since $\boldsymbol{a} \cdot (\boldsymbol{a} \times \boldsymbol{b}) = 0$. This shows the dependence of the rate of change of kinetic energy

$$\hat{\boldsymbol{v}} \cdot \frac{d\hat{\boldsymbol{v}}}{d\hat{t}} = \frac{d}{d\hat{t}} \left(\frac{1}{2} \hat{\boldsymbol{v}}^2 \right) \propto \frac{d\hat{\kappa}}{d\hat{t}} \propto \hat{\boldsymbol{v}} \cdot \hat{\boldsymbol{E}}. \tag{7.36}$$

This expression shows that the energy of a particle only changes when $\hat{\boldsymbol{v}} \cdot \hat{\boldsymbol{E}} \neq 0$.

A semi-infinite cylinder of charge is a good example containing both $\hat{\boldsymbol{v}} \cdot \hat{\boldsymbol{E}} \neq 0$ and $\hat{\boldsymbol{v}} \cdot \hat{\boldsymbol{E}} = 0$ conditions. Figure 7.3 shows a diagram of a semi-infinite cylinder of charge annotated with electric field lines. Along the body of the cylinder the electric field is entirely perpendicular to the z axis but at the end of the cylinder there is a fringing field and there are components of the electric field along each axis. The magnetic field is orientated along the z axis. The velocity of a particle gyro-orbiting the body of the cylinder will be perpendicular to the electric field and consequently will no gain energy since $\hat{\boldsymbol{v}} \cdot \hat{\boldsymbol{E}} = 0$. A particle positioned at the end of the cylinder in the fringing field will always have $\hat{\boldsymbol{v}} \cdot \hat{\boldsymbol{E}} \neq 0$ even if it is gyro-orbiting the cylinder.

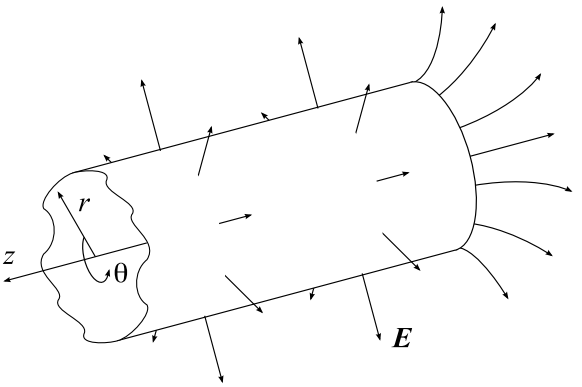

Figure 7.3: Semi-infinite cylinder of charge. The charge cylinder has been annotated with illustrative electric field lines. A cylindrical coordinate system (r, θ, z) is shown.

7.2.3 Numerical model

The 3-dimensional Multigrid solver presented in chapter 4 is used to solve the finite difference representation of Poisson's equation (7.3) on a 129^3 grid.

All calculations have been carried out with zero value Dirichlet boundaries, i.e. the potential at each boundary is fixed at zero. The plasma is assumed to be strictly quasi-neutral outside the computational domain, setting all boundaries to have a fixed potential of zero represents this assumption computationally.

When an electron reaches the boundary of the computational domain the particle is assumed to be absorbed by the quasi-neutral plasma and is removed from the simulation and plays no further part.

The particle trajectories are integrated using a fourth-order Runge-Kutta scheme for the ordinary differential equation of (7.12). The time step is chosen such that the motion of the particles is well resolved: in all cases the time step must resolve the Larmor orbits of the electrons but when the self field dominates ($P_E \gg 1$) a finer time step may be required.

Collisions between electrons and other species have not been included. Clearly inelastic collisions will alter the energy gain of the electron population; this loss factor will be species dependent. By not specifically including such reactions, the calculations provide an initial guide as to where CIV processes may be significant. For example, ionisation of Xenon, from its ground state, requires electrons with energies above 12.12 eV, and so by examining the calculated electron energy distribution, conditions likely to produce enhanced ionisation can be inferred (Xenon also has a metastable state at 8.31 eV and so a two-stage process is possible with two lower energy electrons).

7.2.4 Initial conditions

The magnetic field is fixed to be uniform throughout the computational domain and is orientated solely along the y-axis. The unbalanced electron population consists of 3 mil-

lion electrons, initially at rest, distributed normally in 3 dimensions around the point ($N_x/2$, $N_y/2$, $N_z/2$). The normal distributions in each dimension have a variance of $N_x/3$. Table 7.1 gives a summary of the initial conditions used in the simulations.

Simulation property	Value
Domain dimensions	129^3
x-, y-, z-boundaries	$\phi = 0$
N. of electrons	3×10^6
$\hat{\boldsymbol{B}}$	[0, 1, 0]
dt	$< 0.02t_0$
α	10^3
P_B, P_g	1
P_n	α^{-1}
P_E	$10^{-3} - 10^3$
P_κ	$(2P_E)^{-1}$

Table 7.1: Initial conditions for the electron overdensity simulations.

7.3 Results

The evolution of the electron population was calculated for several values of the parameter P_E, which describes the relative sizes of the electric and magnetic forces. Results from three values of P_E are presented to highlight the behaviour of the electron overdensity in three different regimes, where the system is: magnetically dominated; electrically dominated; and when the forces are similar. Figures 7.4–7.6 show the evolution of the electron overdensity where $P_E = 10^{-2},\ 1,\ 10^2$ respectively. Snapshots were taken at various times through the simulation of the parameters: electron density, electric potential, mean energy and the distribution of kinetic energy. Images of the spatial parameters: electron density, potential and mean energy are slices through the domain in the x-y plane through the centre of the initial spatial distribution in the z-coordinate.

The time slices shown are at four regular intervals between the start and the point when the first electrons reach the boundary. Times are expressed in terms of electron cyclotron periods ($\tau_c = 2\pi t_0$). Non-dimensional units are used for all other quantities. Later, in section 7.3.5, the non-dimensional units are converted to physically meaningful units.

7.3.1 Magnetically dominated: $P_E = 10^{-2}$

In the magnetically dominated regime the transport of the electrons perpendicular to the magnetic field is highly restricted and initial spherical electron distribution evolves towards

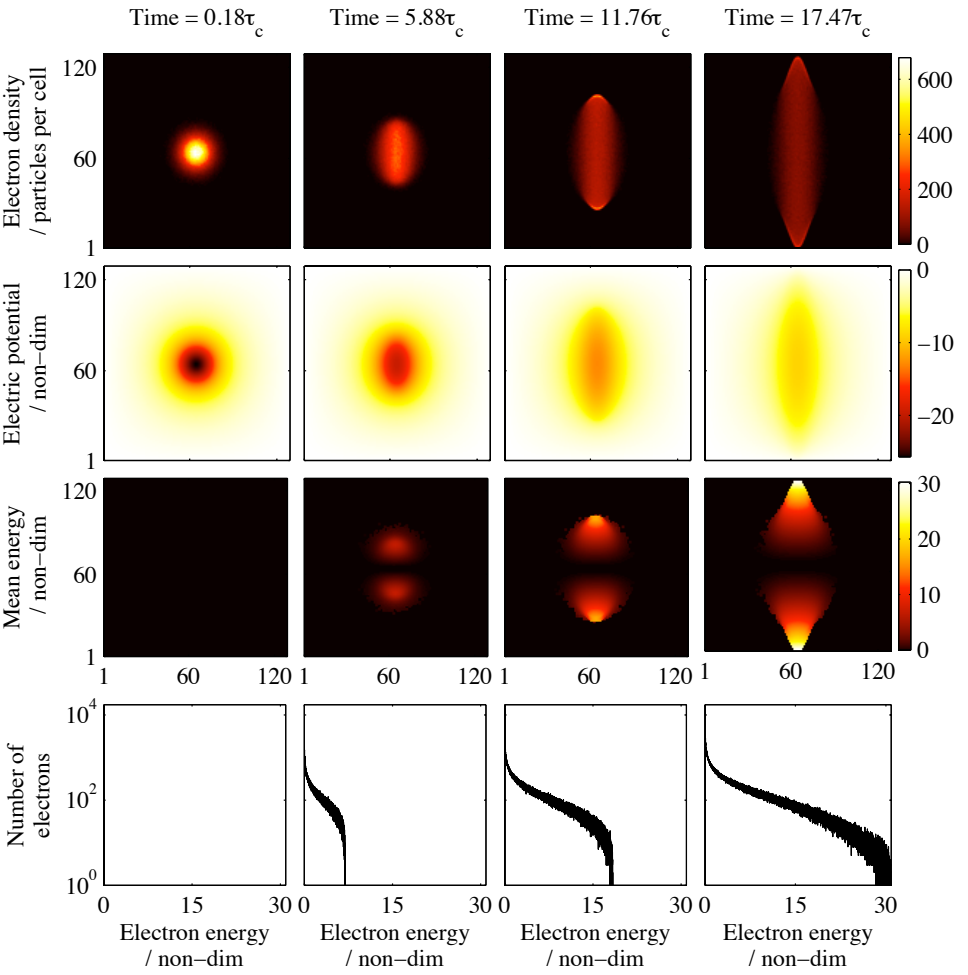

Figure 7.4: Snapshots of the evolution of the electron overdensity where $P_E = 10^{-2}$ (Magnetically dominated). The y-axis lies along the vertical and x-axis along the horizontal. Magnetic field is along the y-axis.

a cylindrical shape. Figure 7.4 shows a series of snapshots from the simulation.

7.3.2 $P_E = 1$

Figure 7.5 shows that the evolution of the electron overdensity for $P_E = 1$ appears to be very similar to the evolution when $P_E = 10^{-2}$. There are some differences most notably the timescale: when $P_E = 1$ the electrons reach the boundary a factor of ten earlier. A peak in the kinetic energy distribution can also be seen.

7.3.3 Self field dominated: $P_E = 10^2$

For the case of $P_E = 10^2$ (figure 7.6) the distribution of electrons evolves much quicker than the previous two cases. The electron density has dropped substantially after a quarter of a

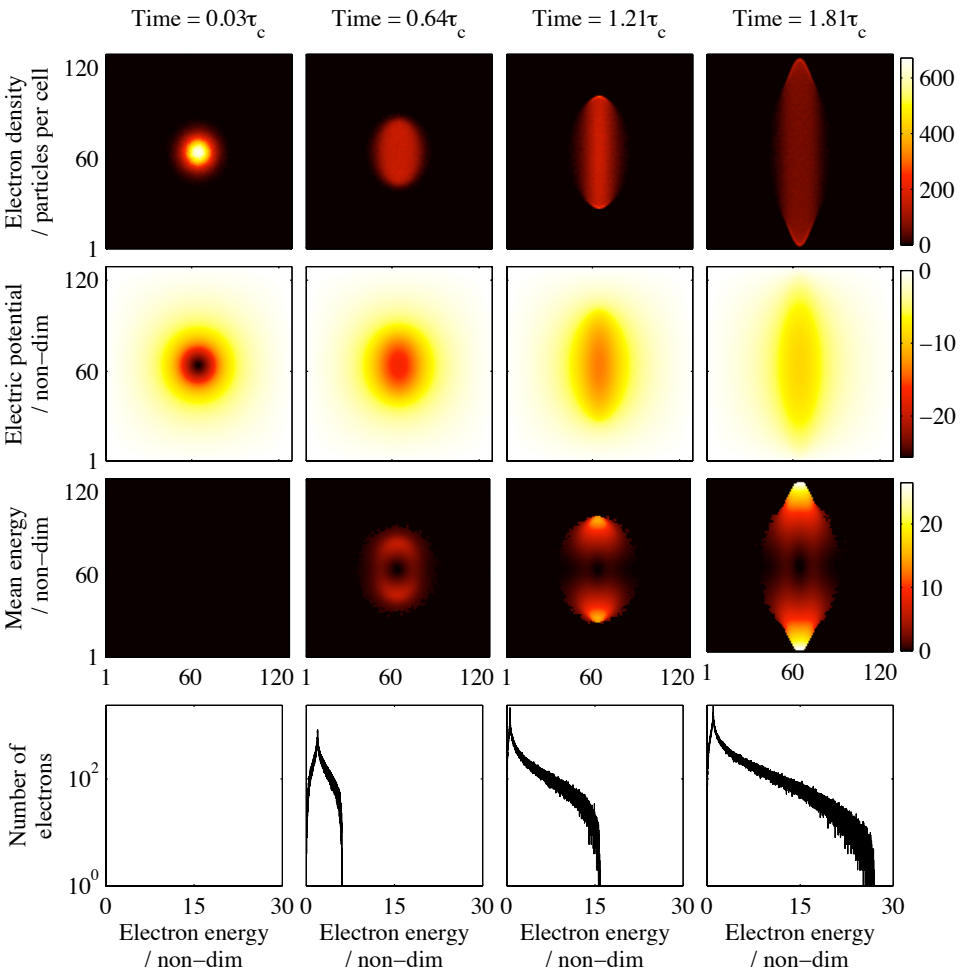

Figure 7.5: Snapshots of the evolution of the electron overdensity where $P_E = 1$.

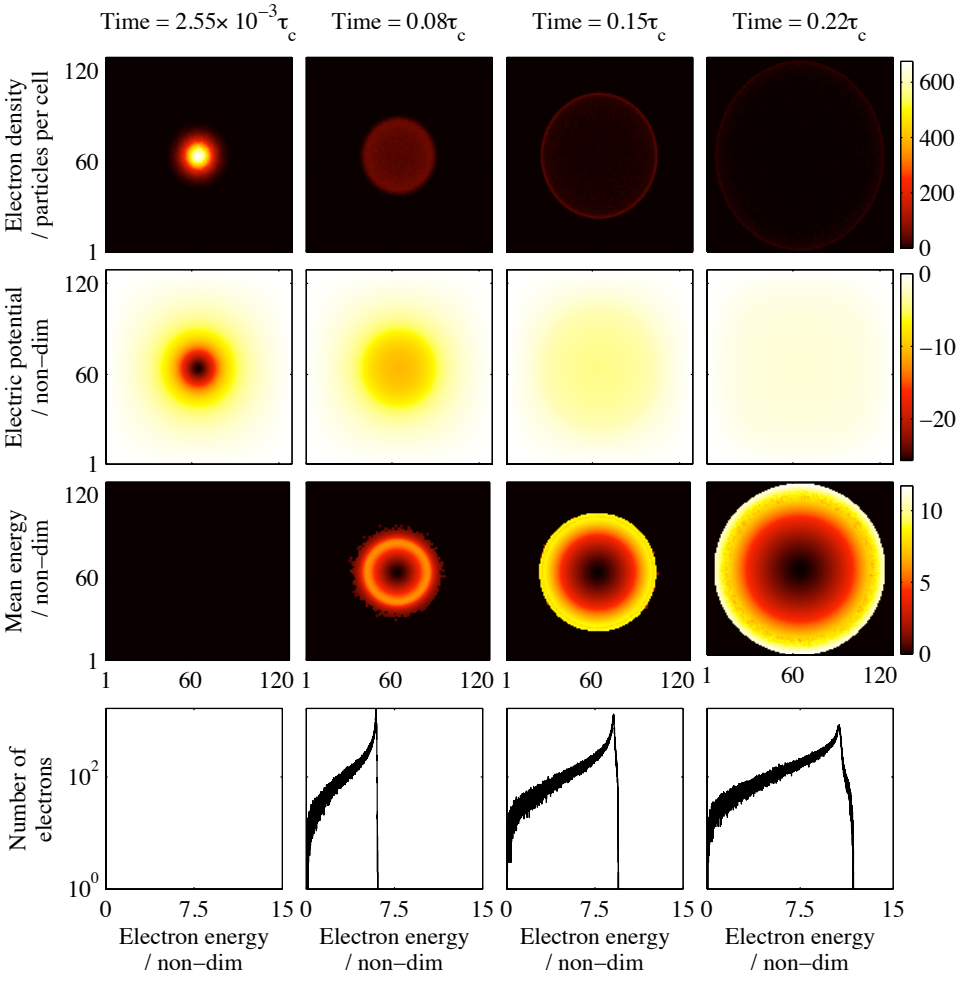

Figure 7.6: Snapshots of the evolution of the electron overdensity where $P_E = 10^2$ (Self-field dominated).

cyclotron period. This drop in density results in a flattening of the potential, in contrast to the previous two cases where the final potential was still relatively high when the electrons reached the boundaries.

7.3.4 Comparing results

The ions that are displaced to form the initial charge imbalance will enter gyro-orbits and return approximately to their initial positions, neutralising the charge imbalance after a gyroperiod. Once the charge imbalance is negated the acceleration of the electrons would end. In each case here the energisation of the electrons occurs on a timescale much less than the ion gyroperiod.

The kinetic energy distributions for a range of values of P_E are shown in figure 7.7. The distributions show the kinetic energy of the electrons as the first electrons reach the computational boundary. The maximum magnitude of the initial potential is denoted by

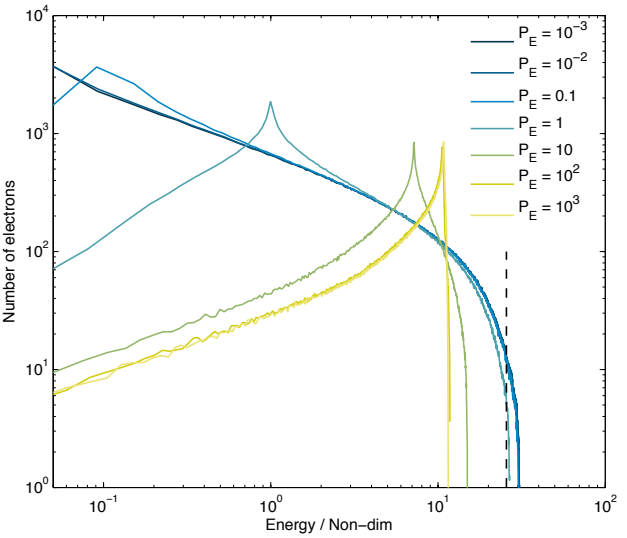

Figure 7.7: Final energy distributions. Dashed black line shows the magnitude of the initial potential. The times for increasing values of P_E shown in the plot are 54.98, 17.47, 5.53, 1.81, 0.68, 0.22, $0.07\tau_c$ respectively.

a dashed, black line. In the simulations where $P_E > 1$ the kinetic energies of the electrons do not exceed the maximum initial potential. Clearly the magnetic field plays a key role in the energy enhancement.

The fraction of the electron population exceeding the maximum initial potential is shown in figure 7.8. When the self field dominates ($P_E > 1$) there are many high energy particles but this maximum energy does not exceed the initial potential. When the magnetic field dominates the distribution is peaked at a lower energy but has a high energy tail which exceeds the initial potential. The fraction of particles exceeding 50%, 75% and 110% of the maximum initial potential are also plotted. To put this in context, if an overdensity with twice the potential of the ionisation energy is created then for $P_E < 1$ up to 13% of the electron population could exceed the ionisation threshold.

An efficiency factor, η can also be defined as the ratio of maximum electron energy to the maximum of the modulus of the initial potential,

$$\eta = \frac{\max(\hat{\kappa})}{\max(|\hat{\phi}_{t=0}|)}. \tag{7.37}$$

Figure 7.9 shows the variation of the efficiency for different values of P_E. The efficiency factor is clearly dependent on the relative strength of the magnetic field; when the magnetic field dominates the maximum achievable energies are greater than the maximum initial potential.

7.3.5 Translating results into dimensioned qualtities

The maximum energy achieved, in eV, for various values of electron density and magnetic field strength is shown in figure 7.10. A logarithmic scaling is used for the maximum

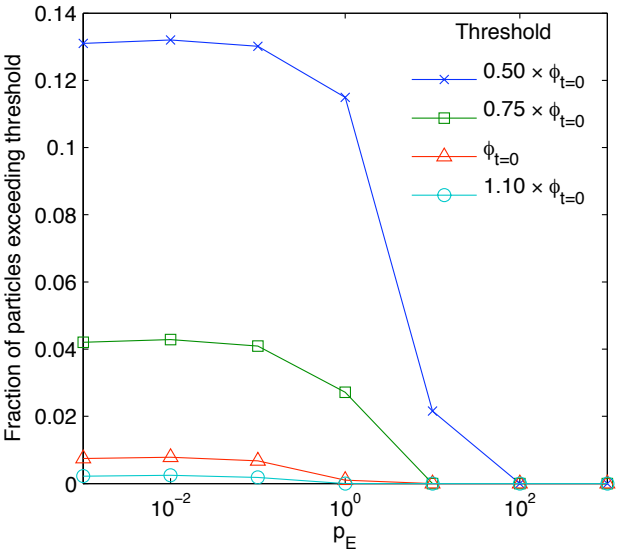

Figure 7.8: Fraction of electron population reaching energies in excess of the initial potential $\phi_{t=0}$. Fraction of electrons exceeding 50%, 75% and 110% of the initial potential are also shown. For $P_E = 1$: 12% of the electrons exceed half of the initial potential, 3% exceed three-quarters of the initial potential and approximately 0.5% gain energies greater than or equal to the maximum initial potential.

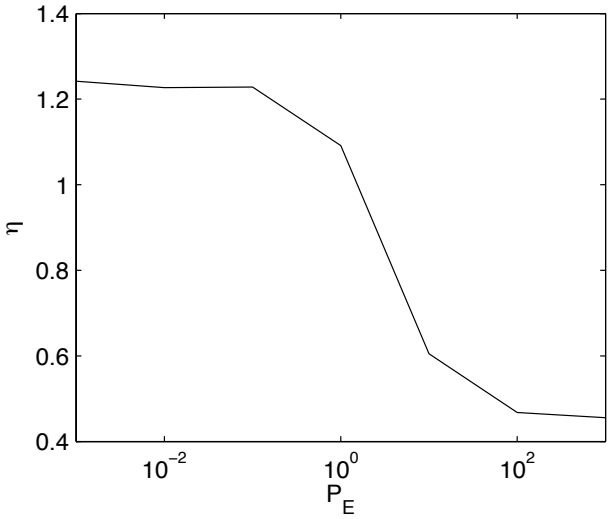

Figure 7.9: Variation of efficiency with P_E. The efficiency is the ratio of maximum kinetic energy to magnitude of initial potential. The plot shows that greater maximum energies are achieved when the magnetic field is dominant.

energy colour scale. Higher number densities result in higher maximum energies since the potential is related directly to the number density. For a given number density increasing the magnetic field strength gives a greater maximum energy.

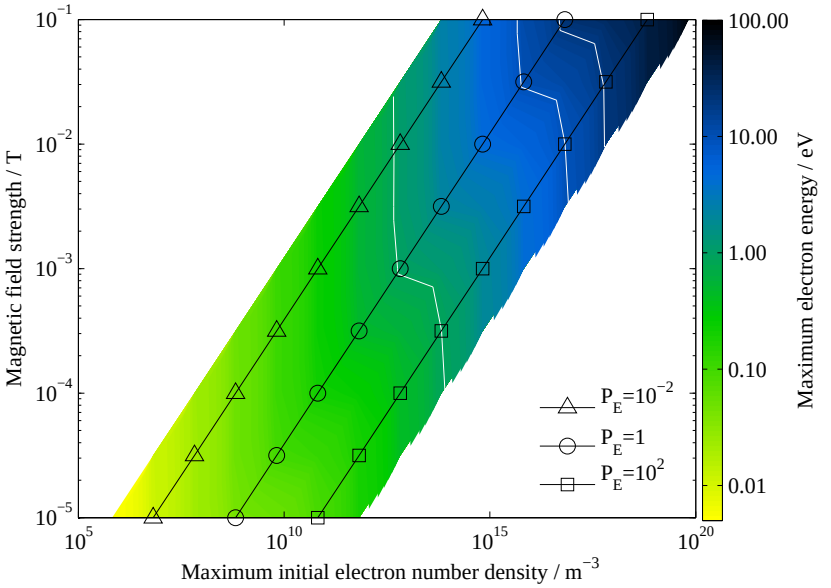

Figure 7.10: Plot showing the maximum particle energy achieved for a range of magnetic field strengths and electron densities. White lines show contours of maximum energy at 1, 10 and 20 eV.

7.3.6 Estimating the induced magnetic field

In the cases where the magnetic field dominates the evolution of the electrons there is a preferred direction of motion along the magnetic field axis. This bulk motion of electrons could induce a non-negligible magnetic field in an azimuthal direction around the direction of motion. Beginning with Ampere's Law:

$$\oint_C \boldsymbol{B} \cdot \mathrm{d}\boldsymbol{l} = \mu_0 I \tag{7.38}$$

where $\oint_C$ is the closed line integral around the closed curve C, $\boldsymbol{B}$ is the magnetic field, $\mathrm{d}\boldsymbol{l}$ is a line element of curve C, μ_0 is the absolute permeability of free space and I is the enclosed current.

If the charge distribution is is assumed to be an infinite cylinder Ampere's Law reduces to:

$$B = \frac{\mu_0 I}{2\pi r} \tag{7.39}$$

where r is the distance from the charge cylinder. The current I can be expressed as:

$$I = envA \tag{7.40}$$

where e is the electron charge, n is the number density, v is the electron speed and A is the cross-sectional area ($A = \pi r^2$).

Non-dimensionalising (7.39) gives:

$$\hat{B} = P_i \hat{n}\hat{v}\hat{r} \tag{7.41}$$

where

$$P_i = \frac{\mu_0 e n_0 v_0 s_0}{2B_0} \tag{7.42}$$

The following definitions from section 7.2.1 are used to re-express P_i:

$$n_0 = s_0^{-3}, \tag{7.43}$$
$$s_0 = v_0 t_0, \tag{7.44}$$
$$B_0 = \frac{m_e}{e t_0}, \tag{7.45}$$
$$P_E = \frac{\alpha m_e}{\varepsilon_0 s_0^3 B_0^2}. \tag{7.46}$$

Factoring out P_E gives,

$$P_i = \frac{\mu_0 n_0 v_0 e s_0}{2B_0} \frac{\varepsilon_0 s_0^3 B_0^2}{\alpha m_e P_E} \tag{7.47}$$

Substituting expressions (7.43–7.45) into (7.47):

$$P_i = \frac{\mu_0 \varepsilon_0 v_0^2}{2\alpha P_E} \tag{7.48}$$
$$= \frac{1}{2\alpha P_E} \frac{v_0^2}{c^2} \tag{7.49}$$

where c is the speed of light in a vacuum.

Table 7.2 shows that numerical values of each of the non-dimesnional values ($\hat{n}$, $\hat{v}$, $\hat{r}$); these are the maximum values. The non-dimensional speed is calculated from the energy, it is not a component of the velocity in any single direction. Re-arranging (7.41) to give an expression for v_0^2 gives

$$v_0^2 = \frac{2\alpha P_E c^2 \hat{B}}{\hat{n}\hat{v}\hat{r}}. \tag{7.50}$$

The induced magnetic field can be neglected if it is less than 1% of the applied magnetic field. Using (7.50) an energy limit for the validity of neglecting the induced magnetic field can be calculated. The maximum allowable energy is given in table 7.2. There is also some symmetry in the electron motion. There are groups of electrons which move along the magnetic field lines in opposite directions. This will lead to the cancellation of the induced magnetic field in some places.

This shows that the results given in figure 7.10 are valid.

7.4 Discussion

In this section some features of the electron overdensity evolution are discussed and in section 7.4.2 an explanation for these observations is offered.

P_E	10^{-3}	10^{-2}	10^{-1}	1	10	10^2	10^3
$\hat{n}$ / electrons per cell	~ 250	~ 230	~ 250	~ 190	~ 60	~ 21	~ 19
$\hat{v}$ / cell widths per timestep	~ 0.25	~ 0.8	~ 0.25	~ 7.4	~ 17	~ 48	~ 150
$\hat{r}$ / cell widths	20	12	14	18	37	100	120
Max. allowable energy / eV	4	23	584	202	1350	5000	15000

Table 7.2: Numerical values from the simulations. In each case $\alpha = 10^3$ and $\hat{B} = 0.01$.

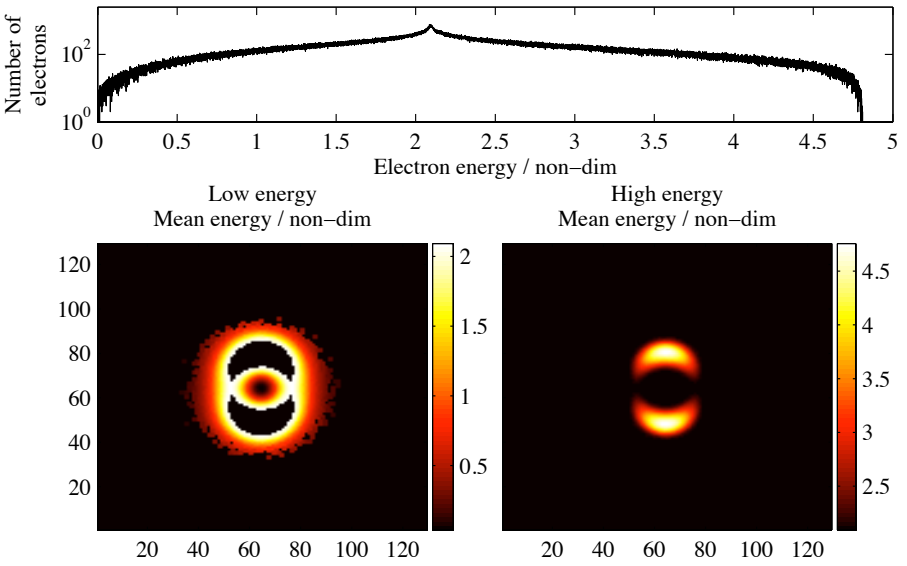

Figure 7.11: Energy density plots of the high and low energy wings with the kinetic energy distribution in the top panel. This is a snapshot where $P_E = 1$ after approximately $0.5\tau_c$.

7.4.1 Features of the overdensity evolution

One of the most interesting features of the simulation results are the shapes of the electron kinetic energy distributions. The distributions all show similar morphologies: a peaked distribution with wings at higher or lower energies, or both (see figure 7.7). To investigate the origin of the distribution shape it is separated into high and low energy parts, using the peak of the distribution as the dividing point. Slices of the mean energy showing the high energy and low energy parts are shown in the bottom panels of figure 7.11, the kinetic energy distribution is shown in the top panel.

In regimes where the magnetic field plays a significant role, such that the distribution evolves over several cyclotron periods, the energy of the peak of the distribution can be seen to oscillate with a frequency approximately equal to the electron gyrofrequency. The temporal evolution of the distribution of kinetic energies can be seen in figure 7.12.

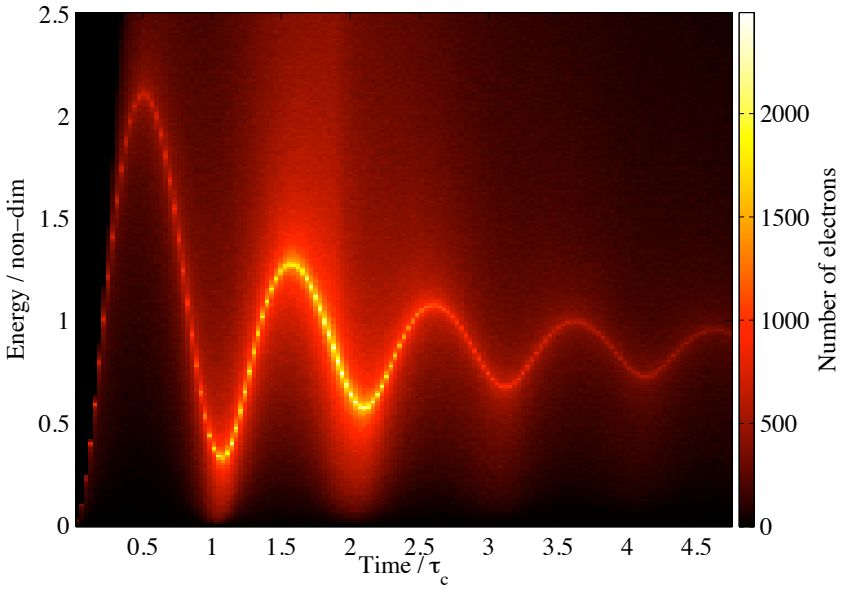

Figure 7.12: Surface showing a section of the energy distribution evolving with time where $P_E = 1$. The colour scale gives the number of electrons at any particular energy. At approximately two cyclotron periods electrons begin to reach the computational boundary reducing the total number of electrons in the system.

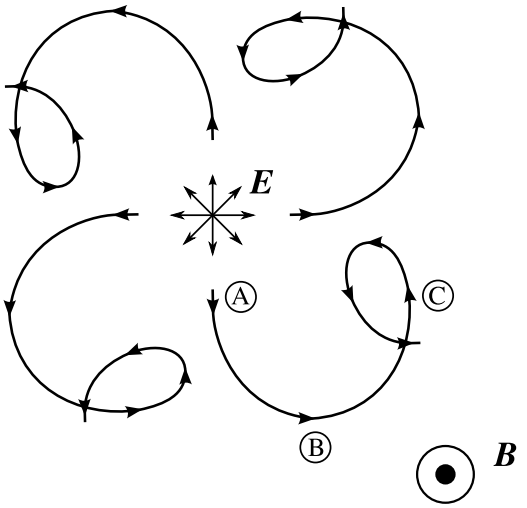

Figure 7.13: Sketch of projected electron trajectories in the plane perpendicular to uniform magnetic field $\boldsymbol{B}$. The curved arrow lines show the paths of electrons perpendicular to a magnetic field when there is a radial electric field. Points A, B and C correspond to the motion at time zero, quarter of a cyclotron period and half of a cyclotron period, respectively.

7.4.2 Explanation of the observed features

Figures 7.4, 7.5 and 7.11 show that there is a preferred direction for the highest energies as expected in section 7.2.2. The points made in section 7.2.2 can be used to understand the evolution of the electron distribution. Figure 7.13 is a sketch showing the electron gyromotion perpendicular to the magnetic field direction. The ensemble of electrons are initially in a spherical distribution. The electrons are accelerated by the self-field. The electrons located in the highest electric field positions gain a similar maximum energy and there is a sharp fall off in the kinetic energy distribution above the maximum energy. Electrons in other positions of the distribution gain lower amounts of energy filling out a low energy wing in the distribution. All electrons are travelling parallel to the electric field, i.e. $\hat{\boldsymbol{v}} \cdot \hat{\boldsymbol{E}} \neq 0$ and all electrons are gaining energy (figure 7.13, point A).

After a quarter of a cyclotron period (figure 7.13, point B) the electrons initially travelling at an angle to the magnetic field will be moving perpendicular to the electric field and the amount of energy being acquired by these electrons will be reduced since $\hat{\boldsymbol{v}} \cdot \hat{\boldsymbol{E}} \approx 0$. This reduction in the gain of energy will effect a large proportion of the electrons including those represented by the peak in the kinetic energy distribution. The energy value of the peak will stop increasing. Some electrons will be moving parallel to the magnetic field; their transport will not be hindered by the magnetic field and they will continue to accelerate, creating a high energy wing.

For the next half of the gyroperiod (figure 7.13, point C), those particles undergoing gyromotion will be travelling back across the magnetic field axis. This will most likely be travelling against the electric field and they will be decelerated. This reduction in acceleration can be seen in the oscillation of the peak in the kinetic energy distribution.

7.5 Conclusions

The numerical simulation demonstrates that electrons can be accelerated to energies capable of impact ionisation by the self field of a charge imbalance. The physical processes involved in the CIV interaction can be grouped into two timescales: an ion-neutral stage and an electron energisation stage. The work presented here focuses on the short timescale energisation part. The ion-neutral stage is responsible for the formation of regions in plasma where ions have been displaced leaving a negative charge imbalance. Calculating the evolution of these pockets of unbalanced electrons gives an estimation of the energy that can be obtained. Figure 7.10 shows that for certain charge imbalance densities and magnetic field strength values that ionisation energies (typically $\phi_{iz} > 10\text{eV}$) can be exceeded.

A single pocket of unbalanced charge consisting of 3 million electrons is simulated and the trajectory of each electron is calculated. The distribution of energies is important for determining the enhancement of the ionisation rate. Figure 7.8 shows that when the magnetic field dominates the self field of the overdensity then approximately 1% of the electrons exceed the potential of the pocket. Under similar conditions more than 10% of the electron population exceed half the maximum initial potential. The value of the initial potential depends on the speed of the neutrals, so if the neutrals are travelling at twice the critical velocity then the maximum initial potential should be twice the ionisation potential and consequently, when the magnetic field is dominant, 10% of the electrons would exceed the ionisation threshold.

The importance of the magnetic field was investigated by varying the parameter P_E. The distribution of kinetic energies was found to be different in magnetically and electrically dominated regimes. Figure 7.7 shows the distributions for various values of P_E. When the self field dominates the distribution is peaked and drops sharply at higher energy, consequently there is a large fraction of electrons in the high energy part of the distribution but the energies do not exceed the maximum initial potential. The magnetically dominated cases ($P_E < 1$) have wide high energy tails reaching energies greater than the maximum initial energy. In this regime the transport of electrons perpendicular to the magnetic field is restricted this means that the density structure evolves on a slower timescale and some electrons can gain energies in excess of the initial electrostatic potential.

Parameter	Space Experiments	Homopolar Devices
B field strength / T	3×10^{-5}	10^{-2} - 1
electron density / m^{-3}	10^{9} - 10^{11}	10^{18} - 10^{21}
ion density / m^{-3}	10^{11} - 10^{15}	10^{19} - 10^{22}

Table 7.3: Experimental CIV conditions from Lai [129].

The CIV phenomena has been easily reproduced in laboratory experiments but space experiments have mostly failed to show any ionisation enhancement. Comparing the experimental parameters [129], shown in table 7.3, with the results in figure 7.10 may explain the experimental discrepancy. The electron pocket densities in the simulation results and the absolute electron density values given in table 7.3 cannot be directly compared but some

basic understanding can be gained. The electron densities in the simulation are reflect the size of the charge imbalance they are not the total electron density of the plasma.

The conditions for space experiment lie roughly in the bottom left corner in figure 7.10. Here the energy enhancement is less than 0.1eV, substantially less than any ionisation threshold. Homopolar devices operate in the density and magnetic field strength regime located near the top right of figure 7.10. In this region the electron energies exceed ionisation thresholds. The reason for the occurrence of the CIV effect in the laboratory and not the space experiments is the density; without a sufficiently high plasma density pockets of unbalanced charge with potential equal to the ionisation potential cannot be created.

Chapter 8

Conclusions & Future work

The principle motivation of this thesis was to investigate basic physical processes in low temperature plasmas using various numerical techniques. Three main situations have been investigated: instabilities in electronegative plasmas (chapter 2); electron avalanches (chapter 6); and the Critical Ionisation Velocity effect (chapter 7). Numerical methods have been introduced and implemented to examine these physical processes. Where possible, the veracity of the results has been examined by comparing numerical and experimental results.

Electronegative instabilities

The numerical and analytic models in chapter 2 show that simple numerical models, that isolate the key physical processes, can reproduce the essential aspects of a electronegative plasma instability.

The results from the zero-dimensional model are compared to experimental measurements and there is good agreement between the experimental and numerical frequencies. There is some disagreement between the neutral densities. The simulation requires a neutral density a factor ~ 30 smaller. This discrepancy may arise from the spatial difference between the experimental measurement in the centre and the simulation prediction at the plasma edge.

The system of equations used in the zero-dimensional model are simplified to give an analytic expression for the period of the instability. Evaluating the expression for experimental data from a molecular Oxygen discharge shows very good agreement between the analytic expression and the experimental observations. The analytic expression requires data from the experiment to calculate the instability period and it affirms the relevance of the physical process.

There is disagreement between the neutral number densities measured in the experiment and the values required by the zero-dimensional model. There are two possible strategies to reconcile this discrepancy: change the model or change the experiment.

Introducing the spatial variation present in the discharge system by constructing a one- or two-dimensional model would have two main benefits. Firstly, spatial variation in the

model of the plasma would show the effect of the instability, located at the plasma edge, on the bulk plasma. Including the bulk plasma in the simulation would allow direct comparison between the existing experimental measurements and the simulation.

The fluctuation of the position of the plasma edge could be used as a diagnostic. Measurements of the spatial expansion in the experiment could be compared to the simulated variation. The numerical model could predict the parameter regimes where the greatest or least size change occurs. Elimination of the spatial variation is desirable for a uniform plasma process. If the instability could be controlled, this would provide an environment similar to a pulsed plasma which could be beneficial for some plasma processes.

Alternatively, the simplicity of the numerical model could be maintained by conducting a new experiment. Measurements taken at the plasma edge would allow direct comparison between the simulation and experiment. The electronegative instability has been observed in experiments in gases other than Oxygen. The model could be applied to these gases. The most important chemical reactions for each of the gas mixtures would have to be determined.

Poisson solver

The Poisson solver presented in chapter 4 can solve the potential in complex systems on two and three dimensional Cartesian grids. The solver is fast, efficient and accurate.

The potential in most plasma simulations is calculated on a grid. This is a well established practice and the techniques are robust. Some technological plasma devices have very complex electrode geometries which would be poorly represented on any type of grid. There will always be errors associated with representing continuous properties on a discrete grid. Other options for solving the potential field that do not rely on grids do exist. Gridless potential solvers will eventually replace mesh-based Poisson solvers as the technique of choice.

There is an existing gridless technique used mainly in the field of cosmology, called a tree-code [97; 145]. In gravitational simulations the force on a particle is calculated directly from the positions of the other particles. A hierarchical addressing system is used to assign each particle to a separate box. The problem is simplified by assuming that masses at a certain distance can be treated as a single continuous mass. When evaluating the gravitational force on a particle the particle's nearest neighbours can be considered at the finest address level and particles further away can be considered as centres of mass at coarser address levels. Constructing an efficient tree code is a very difficult task and their execution is still very computationally intensive but billions of particles can be simulated[146]. This technique has been applied to the simulation of plasmas [147–149] but not extensively.

Collisions

A Monte-Carlo collision routine is introduced in chapter 5 and several modifications to improve the efficiency of the algorithm are suggested. Various implementations of the routine are examined to determine the most efficient combination. The accumulated selection errors are investigated for a standard and an extended time step. For fifty iterations of the collision selection with the standard time step the errors are less than 10%.

The inclusion of the general inelastic cross-section gives two benefits: it provides an accurate description of the energy loss from the electrons and it provides a useful diagnostic. The summation of many cross-sections allows many reactions to be included efficiently. The photon emission from short lived excited states could be compared to experimental measurements. The simulated emission in different wavelengths can be constructed from the model output.

Electron avalanches

In chapter 6 electron avalanches in two and three dimensions using the particle model discussed in chapters 3, 4 and 5. The evolution of the avalanche when the electric field is reversed is also investigated. The aim of the field reversal cases was to investigate if the metastable excitation rate could be maximised without allowing full breakdown of the gas. The inclusion of the field reversal does need a more careful treatment but the results are still instructive. There is a boost in the metastable production when the field is reversed.

The importance of the inelastic cross-sections is seen in the electron energy distributions. Features in the energy distributions can be related to the cross-sections. Photon emission from the electron avalanche could allow a valuable comparison to experiment.

The particle model used in the simulation of electron avalanches could be enhanced in two ways. The evolution of an electron avalanche is limited by the number of particles that can be stored. A function that agglomerates the individual particles into super-particles would allow the simulation to carry on indefinitely. This would allow the simulation of the initiation of a discharge from a single electron-ion pair to a dense plasma. The agglomeration of particles would have to be done carefully to maintain spatial, momentum and energy distributions.

The simulation presented here provides the foundation for further investigation into a novel pulsed plasma device. Short pulses of the electric field could result in efficient production of excited states without the current spike that follows full breakdown.

CIV interaction

In chapter 7 the CIV effect is investigate using the particle model discussed in this thesis. This effects manifests as a rapid increase in the ionisation rate. It occurs when a neutral gas impinges on a stationary magnetised plasma and the neutrals exceed a threshold velocity. This process occurs on two main timescales: an ion-neutral collision time and electron acceleration time.

The later timescale is investigated by considering an ensemble of electrons in a uniform magnetic field that are accelerated by their self-field. A numerical simulation is used to calculate the energy gain of the electrons. Under some conditions electrons can be accelerated to speeds capable of electron impact ionisation of neutrals. The results from the simulation may explain why the CIV interaction is readily produced in laboratory devices but not in space experiments.

The simulation of electron overdensities is instructive for determining some of the parameters which are important for the CIV interaction. This is only part of the story. Including

the interaction between the ions and neutrals would give a more complete description of the CIV effect. This may be achieved through a two-stage model or a brute force approach.

A of model of the interaction between the ions and neutrals, which ignored the electrons, could be used to determine the size and structure of the overdensities. In a separate model the energy gain and ionisation rate could be calculated, this would be based on the modelling of the electron overdensities.

In the brute force approach all the species would be simulated in the same model. The main problem with this approach is the disparity in timescales. The charge imbalances must form on a timescale shorter than the ion gyroperiod, or the neutrality will be re-established by the returning ions. Chapter 7 shows that the pockets of electrons evolve over a few electron gyroperiods, a factor of a thousand shorter.

There is an obvious aim for the work: determining the mechanism, or mechanisms, causing the ionisation enhancement. It would also be interesting to investigate if other reactions can be favoured instead of ionisation. The CIV effect could be used to produce particular species, such as negative ions, or excited molecular states. Most technological plasma processes rely on specific molecules or states, producing these efficiently would increase the effectiveness of the processes.

References

[1] I Langmuir. Oscillations in ionized gases. *Proceedings Of The National Academy Of Sciences Of The United States Of America*, 14:627–637, 1928.

[2] OED online, June 2008.

[3] C R Stark. *Plasma processes in pulsar environments.* PhD thesis, University of Glasgow, 2008.

[4] G E Morfill, H M Thomas, U Konopka, and M Zuzic. The plasma condensation: Liquid and crystalline plasmas. *The 40th annual meeting of the division of plasma physics of the american physical society*, 6(5):1769–1780, 1999.

[5] P K Shukla. A survey of dusty plasma physics. *Physics of Plasmas*, 8(5):1791–1803, 2001.

[6] J Winter. Dust: A new challenge in nuclear fusion research? *Physics of Plasmas*, 7(10):3862–3866, 2000.

[7] J D Huba. *NRL Plasma Formulary.* Naval Research Laboratory, 2004 rev. edition, 2004.

[8] R G Poulsen. Plasma etching in integrated circuit manufacture—a review. *Journal of Vacuum Science and Technology*, 14(1):266–274, 1977.

[9] H Abe, M Yoneda, and N Fujiwara. Developments of plasma etching technology for fabricating semiconductor devices. *Japanese Journal of Applied Physics*, 47(3):1435–1455, 2008.

[10] L Martinu and D Poitras. Plasma deposition of optical films and coatings: A review. *Journal of Vacuum Science & Technology A: Vacuum, Surfaces, and Films*, 18(6):2619–2645, 2000.

[11] C M Chan, T M Ko, and H Hiraoka. Polymer surface modification by plasmas and photons. *Surface Science Reports*, 24(1-2):1 – 54, 1996.

[12] G G Lister, J E Lawler, W P Lapatovich, and V A Godyak. The physics of discharge lamps. *Reviews of Modern Physics*, 76(2):541–598, Jun 2004.

[13] U Kogelschatz. Dielectric-barrier discharges: Their history, discharge physics, and industrial applications. *Plasma Chemistry and Plasma Processing*, 23(1):1–46, March 2003.

[14] G Fridman, M Peddinghaus, M Balasubramanian, H Ayan, A Fridman, A Gutsol, and A Brooks. Blood coagulation and living tissue sterilization by floating-electrode dielectric barrier discharge in air. *Plasma Chemistry and Plasma Processing*, 26(4):425–442, Aug 2006.

[15] R E J Sladek, E Stoffels, R Walraven, P J A Tielbeek, and R A Koolhoven. Plasma treatment of dental cavities: a feasibility study. *Plasma Science, IEEE Transactions on*, 32(4):1540–1543, Aug. 2004.

[16] J L Glover, P J Bendick, and W J Link. The use of thermal knives in surgery: Electrosurgery, lasers, plasma scalpel. *Current Problems in Surgery*, 15(1):1 – 78, 1978.

[17] G Fridman, G Friedman, A Gutsol, A B Shekhter, V N Vasilets, and A Fridman. Applied plasma medicine. *Plasma Processes and Polymers*, 5(6):503–533, 2008.

[18] T Nozaki and K Okazaki. Carbon nanotube synthesis in atmospheric pressure glow discharge: A review. *Plasma Processes and Polymers*, 5(4):300–321, 2008.

[19] D A Diver. Kinetic theory. Plasma Technology Training School lecture notes, 2005.

[20] D D Monahan and M M Turner. Global models of electronegative discharges: critical evaluation and practical recommendations. *Plasma Sources Science and Technology*, 17(4):045003 (10pp), 2008.

[21] M A Lieberman and A J Lichtenberg. Principles of plasma discharges and materials processing. *Wiley-Interscience*, 2005.

[22] D A Diver. *A Plasma Formulary for Physics, Technology, and Astrophysics*. Wiley-VCH, Berlin, Germany, 2001.

[23] D A Diver, L F A Teodoro, C S MacLachlan, and H E Potts. The influence of gas-kinetic evolution on plasma reactions. *In preperation*, 2009.

[24] K Nanbu. Probability theory of electron-molecule, ion-molecule, molecule-molecule, and coulomb collisions for particle modeling of materials processing plasmas and cases. *Plasma Science, IEEE Transactions on*, 28(3):971–990, Jun 2000.

[25] W N G Hitchon, D J Koch J B, and Adams. An efficient scheme for convection-dominated transport. *Journal of Computational Physics*, 83(1):79–95, 1989.

[26] T J Sommerer, W N G Hitchon, and J E Lawler. Self-consistent kinetic model of the cathode fall of a glow discharge. *Physical Review A*, 39(12):6356–6366, Jun 1989.

[27] D A Fixel and W N G Hitchon. Convective scheme solution of the boltzmann transport equation for nanoscale semiconductor devices. *Journal of Computational Physics*, 227(2):1387–1410, 2007.

[28] J B Adams and W N G Hitchon. Solution of master and fokker–planck equations by propagator methods, applied to au/nacl thin film nucleation. *Journal of Computational Physics*, 76(1):159–175, 1988.

[29] G J M Hagelaar and L C Pitchford. Solving the boltzmann equation to obtain electron transport coefficients and rate coefficients for fluid models. *Plasma Sources Science and Technology*, 14(4):722–733, 2005.

[30] R E Robson, R D White, and Z L Petrovic. Colloquium: Physically based fluid modeling of collisionally dominated low-temperature plasmas. *Reviews of Modern Physics*, 77(4):1303–1320, OCT 2005.

[31] S S Yang, J K Lee, S W Ko, H C Kim, and J W Shon. Two-dimensional kinetic and three-dimensional fluid-radiation transport simulations of plasma display panel. *Contributions to Plasma Physics*, 44(5-6):536–541, 2004.

[32] J Meunier, Ph Belenguer, and J P Boeuf. Numerical model of an ac plasma display panel cell in neon-xenon mixtures. *Journal of Applied Physics*, 78(2):731–745, 1995.

[33] W J M Brok, M F Gendre, and J J A M van der Mullen. Model study of dc ignition of fluorescent tubes. *Journal of Physics D: Applied Physics*, 40(1):156–162, 2007.

[34] J D Bukowski, D B Graves, and P Vitello. Two-dimensional fluid model of an inductively coupled plasma with comparison to experimental spatial profiles. *Journal of Applied Physics*, 80(5):2614–2623, 1996.

[35] G Chen and L L Raja. Fluid modeling of electron heating in low-pressure, high-frequency capacitively coupled plasma discharges. *Journal of Applied Physics*, 96(11):6073–6081, 2004.

[36] J W Coburn Cheng-Che Hsu, M A Nierode and D B Graves. Comparison of model and experiment for ar, ar/o 2 and ar/o 2 /cl 2 inductively coupled plasmas. *Journal of Physics D: Applied Physics*, 39(15), 2006.

[37] E Meeks and J W Shon. Modeling of plasma-etch processes using well stirred reactor approximations and including complex gas-phase and surface reactions. *Plasma Science, IEEE Transactions on*, 23(4):539–549, Aug 1995.

[38] C Lee and M A Lieberman. Global model of ar, o[sub 2], cl[sub 2], and ar/o[sub 2] high-density plasma discharges. *Journal of Vacuum Science & Technology A: Vacuum, Surfaces, and Films*, 13(2):368–380, 1995.

[39] C Lee, D B Graves, M A Lieberman, and D W Hess. Global model of plasma chemistry in a high density oxygen discharge. *Journal of The Electrochemical Society*, 141(6):1546–1555, 1994.

[40] T Kimura and K Ohe. Probe measurements and global model of inductively coupled ar/cf4 discharges. *Plasma Sources Science and Technology*, 8(4):553–560, 1999.

[41] I G Kouznetsov, A J Lichtenberg, and M A Lieberman. Modelling electronegative discharges at low pressure. *Plasma Sources Science and Technology*, 5(4):662–676, 1996.

[42] Sungjin Kim, M A Lieberman, A J Lichtenberg, and J T Gudmundsson. Improved volume-averaged model for steady and pulsed-power electronegative discharges. *Journal of Vacuum Science & Technology A: Vacuum, Surfaces, and Films*, 24(6):2025–2040, 2006.

[43] P Chabert, A J Lichtenberg, M A Lieberman, and A M Marakhtanov. Instabilities in low-pressure electronegative inductive discharges. *Plasma Sources Science and Technology*, 10:478–489, 2001.

[44] G Roberson, M Roberto, J Verboncoeur, and P Verdonck. Global model simulations of low-pressure oxygen discharges. *Brazilian Journal of Physics*, 37:457–465, 2007.

[45] C K Birdsall. Particle-in-cell charged-particle simulations, plus monte carlo collisions with neutral atoms, pic-mcc. *Plasma Science, IEEE Transactions on*, 19(2):65–85, Apr 1991.

[46] P K Tien and J Moshman. Monte carlo calculation of noise near the potential minimum of a high-frequency diode. *Journal of Applied Physics*, 27(9):1067–1078, 1956.

[47] J Dawson. One-dimensional plasma model. *Physics of Fluids*, 5(4):445–459, 1962.

[48] C K Birdsall and A B Langdon. *Plasma Physics Via Computer Simulation.* IOP Publishing, 1991.

[49] R W Hockney and J W Eastwood. *Computer Simulation Using Particles.* Adam Hilger, 1988.

[50] H C Kim, F Iza, S S Yang, M Radmilovic-Radjenovic, and J K Lee. Particle and fluid simulations of low-temperature plasma discharges: benchmarks and kinetic effects. *Journal of Physics D: Applied Physics*, 38(19):R283–R301, 2005.

[51] C H Shon and J K Lee. Striation phenomenon in the plasma display panel. *Physics of Plasmas*, 8(3):1070–1080, 2001.

[52] V A Godyak and R B Piejak. Abnormally low electron energy and heating-mode transition in a low-pressure argon rf discharge at 13.56 mhz. *Physical Review Letters*, 65(8):996–999, Aug 1990.

[53] V Vahedi, C K Birdsall, M A Lieberman, G DiPeso, and T D Ronhlien. Capacitive rf discharges modelled by particle-in-cell monte carlo simulation. ii. comparisons with laboratory measurements of electron energy distribution functions. *Plasma Sources Science and Technology*, 2(4):273–278, 1993.

[54] D O'Connell, R Zorat, A R Ellingboe, and M M Turner. Comparison of measurements and particle-in-cell simulations of ion energy distribution functions in a capacitively coupled radio-frequency discharge. *Physics of Plasmas*, 14(10):103510, 2007.

[55] K Matyash, R Schneider, F Taccogna, A Hatayama, S Longo, M Capitelli, D Tskhakaya, and F X Bronold. Particle in cell simulation of low temperature laboratory plasmas. *Contributions to Plasma Physics*, 47(8-9):595–634, 2007.

[56] A L Alexandrov and I V Schweigert. Two-dimensional pic-mcc simulations of a capacitively coupled radio frequency discharge in methane. *Plasma Sources Science and Technology*, 14(2):209–218, 2005.

[57] H C Kim, O Manuilenko, and J K Lee. Particle-in-cell monte-carlo simulation of capacitive rf discharges: Comparison with experimental data. *Japanese Journal of Applied Physics*, 44:1957–1958, 2005.

[58] H Takekida and K Nanbu. Effect of driving frequency on the electron energy probability function of capacitively coupled argon plasmas comparison between simulation and experiment. *Japanese Journal of Applied Physics*, 43(6A):3590–3591, 2004.

[59] T J Sommerer and M J Kushner. Numerical investigation of the kinetics and chemistry of rf glow discharge plasmas sustained in he, n[sub 2], o[sub 2], he/n[sub 2]/o[sub 2], he/cf[sub 4]/o[sub 2], and sih[sub 4]/nh[sub 3] using a monte carlo-fluid hybrid model. *Journal of Applied Physics*, 71(4):1654–1673, 1992.

[60] M Shimada, G R Tynan, and R Cattolica. Neutral depletion in inductively coupled plasmas using hybrid-type direct simulation monte carlo. *Journal of Applied Physics*, 103(3):033304, 2008.

[61] M Surendra, D B Graves, and G M Jellum. Self-consistent model of a direct-current glow discharge: Treatment of fast electrons. *Physical Review A*, 41(2):1112–1125, Jan 1990.

[62] N Sato and H Tagashira. A hybrid monte carlo/fluid model of rf plasmas in a sih4/h2 mixture. *Plasma Science, IEEE Transactions on*, 19(2):102–112, Apr 1991.

[63] A V Vasenkov and M J Kushner. Electron energy distributions and anomalous skin depth effects in high-plasma-density inductively coupled discharges. *Physical Review E*, 66(6):066411, Dec 2002.

[64] R K Porteous and D B Graves. Modeling and simulation of magnetically confined low-pressure plasmas in two dimensions. *Plasma Science, IEEE Transactions on*, 19(2):204–213, Apr 1991.

[65] Han-Ming Wu. Two-dimensional hybrid model simulation and validation for radio frequency inductively coupled oxygen plasma. *Plasma Sources Science and Technology*, 9(3):347–352, 2000.

[66] J K Lee and C K Birdsall. Velocity space ring-plasma instability, magnetized, part ii: Simulation. *Physics of Fluids*, 22(7):1315–1322, 1979.

[67] P Belenguer and J P Boeuf. Transition between different regimes of rf glow discharges. *Physical Review A*, 41(8):4447–4459, Apr 1990.

[68] Z Donkó, P Hartmann, and K Kutasi. On the reliability of low-pressure dc glow discharge modelling. *Plasma Sources Science and Technology*, 15(2):178–186, 2006.

[69] Xiao-Song Li, Zhen-Hua Bi, Da-Lei Chang, Zhi-Cheng Li, Shuai Wang, Xiang Xu, Yong Xu, Wen-Qi Lu, Ai-Min Zhu, and You-Nian Wang. Modulating effects of the low-frequency source on ion energy distributions in a dual frequency capacitively coupled plasma. *Applied Physics Letters*, 93(3):031504, 2008.

[70] M Rondanini, C Cavallotti, D Ricci, D Chrastina, G Isella, T Moiseev, and H von Kanel. An experimental and theoretical investigation of a magnetically confined dc plasma discharge. *Journal of Applied Physics*, 104(1):013304, 2008.

[71] M Surendra. Radiofrequency discharge benchmark model comparison. *Plasma Sources Science and Technology*, 4(1):56–73, 1995.

[72] T Tabata, T Shirai, M Sataka, and H Kubo. Analytic cross sections for electron impact collisions with nitrogen molecules. *Atomic Data and Nuclear Data Tables*, 92(3):375–406, 2006.

[73] M B Hopkins. Langmuir probe measurements in the gaseous electronics conference rf reference cell. *Journal of Research of the National Institute of Standards and Technology*, 100(4):415–425, July 1995.

[74] A Descoeudres, L Sansonnens, and Ch Hollenstein. Attachment-induced ionization instability in electronegative capacitive rf discharges. *Plasma Sources Science and Technology*, 12(2):152–157, 2003.

[75] C S Corr, P G Steen, and W G Graham. Instabilities in an inductively coupled oxygen plasma. *Plasma Sources Science and Technology*, 12:265–272, 2003.

[76] C S Corr, P G Steen, and W G Graham. Temporal phenomena in inductively coupled chlorine and argon–chlorine discharges. *Applied Physics Letters*, 86(14):141503, 2005.

[77] D L Goodman and N M P Benjamin. Active control of instabilities for plasma processing with electronegative gases. *Journal of Physics D: Applied Physics*, 36(22):2845–2852, 2003.

[78] M Tuszewski. An electronegative inductive discharge instability. *Journal of Applied Physics*, 79:8967–8975, 1996.

[79] F Soberón, F G Marro, W G Graham, A R Ellingboe, and V J Law. Chlorine plasma system instabilities within an icp tool driven at a frequency of 13.56 mhz. *Plasma Sources Science and Technology*, 15(2):193–203, 2006.

[80] M Tuszewski and S P Gary. Downstream instabilities of electronegative plasma discharges. *Physics Of Plasmas*, 10(2):539–545, Feb 2003.

[81] M Tuszewski and R R White. Instabilities of ar/sf6 inductive plasma discharges. *Journal of Applied Physics*, 94(5):2858–2863, Sep 2003.

[82] M A Lieberman, A J Lichtenberg, and A M Marakhtanov. Instabilities in low-pressure inductive discharges with attaching gases. *Applied Physics Letters*, 75(23):3617–3619, 1999.

[83] A M Marakhtanov, M Tuszewski, M A Lieberman, A J Lichtenberg, and P Chabert. Stable and unstable behavior of inductively coupled electronegative discharges. *Journal of Vacuum Science & Technology A: Vacuum, Surfaces, and Films*, 21(6):1849–1864, 2003.

[84] M Tuszewski, R R White, and G A Wurden. Relaxation oscillations of low-frequency ar/sf6 inductive plasma discharges. *Plasma Sources Science and Technology*, 12(3):396–402, June 2003.

[85] N Plihon, C S Corr, P Chabert, and J-L Raimbault. Periodic formation and propagation of double layers in the expanding chamber of an inductive discharge operating in ar/sf[sub 6] mixtures. *Journal of Applied Physics*, 98(2):023306, 2005.

[86] C S Corr. *A study of instabilities in electronegative RF-driven discharges*. PhD thesis, Queen's University Belfast, 2003.

[87] S A Lawton and A V Phelps. Excitation of thr b [sup1] sigma [sup +]sub g state of o[sub 2] by low energy electrons. *Journal of Chemical Physics*, 69(3):1055–1068, 1978. Phelps JILA website data.

[88] W Hwang, Y K Kim, and M E Rudd. New model for electron-impact ionisation cross sections of molecules. *Journal of Chemical Physics*, 104(4):2956–2966, 1996. This is the source for the NIST data.

[89] L Vejby-Christensen, D Kella, D Mathur, H B Pedersen, H T Schmidt, and L H Andersen. Electron-impact detachment from negative ions. *Physical Review A*, 53(4):23712378, 1996.

[90] T Jaffke, M Meinke, R Hashemi, L G Christophorou, and E Illenberger. Dissociative electron attachment to singlet oxygen. *Chemical Physics Letters*, 193:62–68, 1992.

[91] P M Mul and J Wm McGowan. Merged electron-ion beam experiments iii. temperature dependence of dissociative recombination for atmospheric ions no^+, o_2^+ and n_2^+. *Journal of Physics B: Atomic and Molecular Physics*, 12(9):1591–1601, 1979.

[92] J T Gudmundsson. Science institute report rh-17-2004. Technical report, University of Iceland, 2004.

[93] S Gomez. *Laser induced fluorescence measurements in inductively coupled RF processed*. PhD thesis, Queen's University Belfast, 2001.

[94] M Shimada, G R Tynan, and R Cattolica. Neutral gas density depletion due to neutral gas heating and pressure balance in an inductively coupled plasma. *Plasma Sources Science and Technology*, 16(1):193–199, 2007.

[95] R N Franklin. A critique of models of electronegative plasmas. *Plasma Sources Science and Technology*, 10:162–167, 2001.

[96] B J P Dowds, R K Barrett, and D A Diver. Streamer initiation in atmospheric pressure gas discharges by direct particle simulation. *Physical Review E*, 68(2):026412, 2003.

[97] J E Barnes and P Hut. A hierarchical o(n log n) force-calculation algorithm. *Nature*, 324:446 – 449, 1986.

[98] W H Press, S A Teukolsky, W T Vetterling, and B P Flannery. *Numerical Recipes in Fortran 77, Second Edition*. Cambridge University Press, 1992.

[99] R L Coren. *Basic Engineering Electromagnetics: An Applied Approach*. Prentice-Hall International Edition, 1989.

[100] U Trottenberg, C W Oosterlee, and A Schüller. *Multigrid*. Elsevier Academic Press, 2001.

[101] W L Briggs, V E Henson, and S F McCormick. *A multigrid tutorial (2nd ed.)*. Society for Industrial and Applied Mathematics, Philadelphia, PA, USA, 2000.

[102] M J Berger and J Oliger. Adaptive mesh refinement for hyperbolic partial differential equations. *Journal of Computational Physics*, 53(3):484 – 512, 1984.

[103] K Nanbu. Simple method to determine collisional event in monte carlo simulation of electron-molecule collision. *Japanese Journal of Applied Physics*, 33:4752–4753, 1994.

[104] H Sugawara, N Mori, Y Sakai, and Y Suda. Timesaving techniques for decision of electron-molecule collisions in monte carlo simulation of electrical discharges. *Journal of Computational Physics*, 223(1):298–304, 2007.

[105] J T Gudmundsson and E G Thorsteinsson. Oxygen discharges diluted with argon: dissociation processes. *Plasma Sources Science and Technology*, 16(2):399–412, 2007.

[106] M L Boas. *Mathematical methods in the physical sciences*. John Wiley and Sons, 1983.

[107] A V Phelps and L C Pitchford. Anisotropic scattering of electrons by $n2$ and its effect on electron transport. *Physical Review A*, 31(5):2932–2949, May 1985.

[108] A Lofthus and P H Krupenie. The spectrum of molecular nitrogen. *Journal of Physical and Chemical Reference Data*, 6(1):113–307, 1977.

[109] R W B Pearse and A G Gaydon. *The identification of molecular spectra*. Wiley, 1976.

[110] R. C. Fletcher. Impulse breakdown in the $10 - 9$-sec. range of air at atmospheric pressure. *Phys. Rev.*, 76(10):1501–1511, Nov 1949.

[111] K H Becker, K H Schoenbach, and J G Eden. Microplasmas and applications. *Journal of Physics D: Applied Physics*, 39(3):R55–R70, 2006.

[112] J G Eden and S-J Park. Microcavity plasma devices and arrays: a new realm of plasma physics and photonic applications. *Plasma Physics and Controlled Fusion*, 47(12B), 2005.

[113] Klaus Frank Mohamed Moselhy, Isfried Petzenhauser and Karl H Schoenbach. Excimer emission from microhollow cathode argon discharges. *Journal of Physics D: Applied Physics*, 36(23), 2003.

[114] H Akiyama, S Sakai, T Sakugawa, and T Namihira. Invited paper - environmental applications of repetitive pulsed power. *Dielectrics and Electrical Insulation, IEEE Transactions on*, 14(4):825–833, Aug. 2007.

[115] T Shao, G Sun, P Yan, and S Zhang. Breakdown phenomena in nitrogen due to repetitive nanosecond-pulses. *Dielectrics and Electrical Insulation, IEEE Transactions on*, 14(4):813–819, Aug. 2007.

[116] P Krishnaswamy, A Kuthi, P T Vernier, and M A Gundersen. Compact subnanosecond pulse generator using avalanche transistors for cell electroperturbation studies. *Dielectrics and Electrical Insulation, IEEE Transactions on*, 14(4):873–877, Aug. 2007.

[117] A J Palmer. A physical model on the initiation of atmospheric-pressure glow discharges. *Applied Physics Letters*, 25(3):138–140, 1974.

[118] N St J Braithwaite. Introduction to gas discharges. *Plasma Sources Science and Technology*, 9:517–527, 2000.

[119] Leonard B. Loeb and John M. Meek. The mechanism of spark discharge in air at atmospheric pressure. i. *Journal of Applied Physics*, 11(6):438–447, 1940.

[120] B J P Dowds. *Particle-in-Cell simulations of streamer initiation and plasma generation*. PhD thesis, University of Glasgow, 2003.

[121] D Ton-That and M R Flannery. Cross sections for ionization of metastable rare-gas atoms (ne*, ar*, kr*, xe*) and of metastable $n2^*$, co* molecules by electron impact. *Physical Review A*, 15(2):517–526, Feb 1977.

[122] P A Vitello, B M Penetrante, and J N Bardsley. Simulation of negative-streamer dynamics in nitrogen. *Phys. Rev. E*, 49(6):5574–5598, Jun 1994.

[123] S K Dhali and P F Williams. Two-dimensional studies of streamers in gases. *Journal of Applied Physics*, 62(12):4696–4707, 1987.

[124] M Arrayás, U Ebert, and W Hundsdorfer. Spontaneous branching of anode-directed streamers between planar electrodes. *Phys. Rev. Lett.*, 88(17):174502, Apr 2002.

[125] Chao Li, U. Ebert, and W. Brok. Avalanche-to-streamer transition in particle simulations. *Plasma Science, IEEE Transactions on*, 36(4):910–911, Aug. 2008.

[126] H Alfvén. On the cosmogony of the solar system. *Stockholms Observatoriums Annaler*, 14(2), 1942.

[127] U V Fahleson. Experiments with plasma moving through neutral gas. *Physics of Fluids*, 4(1):123–127, 1961.

[128] N Brenning. Review of the civ phenomenon. *Space Science Reviews*, 59(3-4):209–314, Feb 1992.

[129] S T Lai. A review of critical ionization velocity. *Reviews of Geophysics*, 39(4):471–506, November 2001.

[130] D A Diver, L Fletcher, and H E Potts. Fip enhancement by alfvén ionization. *Solar Physics*, 227(2):207 – 215, 2005.

[131] A L Peratt and G L Verschuur. Observation of the civ effect in interstellar clouds: a speculation on the physical mechanism for their existence. *Plasma Science, IEEE Transactions on*, 28(6):2122–2127, Dec 2000.

[132] K F Schoenberg, R A Gerwin, Jr. R W Moses, J T Scheuer, and H P Wagner. Magnetohydrodynamic flow physics of magnetically nozzled plasma accelerators with applications to advanced manufacturing. *Physics of Plasmas*, 5(5):2090–2104, 1998.

[133] V Formisano, A A Galeev, and R Z Sagdeev. The role of the critical ionization velocity phenomena in the production of inner coma cometary plasma. *Planetary and Space Science*, 30(5):491–497, 1982.

[134] P A Cloutier, R E Daniell, A J Dessler, and T W Hill. A cometary ionosphere model for io. *Astrophysics and Space Science*, 55(1):93–112, May 1978.

[135] L Danielsson. Review of the critical velocity of gas-plasma interaction. *Astrophysics and Space Science*, 24(2):459–485, October 1973.

[136] P T Newell. Review of the critical ionization velocity effect in space. *Reviews of Geophysics*, 123(1):93–104, 1985.

[137] R A Lindeman, R R Vondrak, J W Freeman, and C W Snyder. The interaction between an impact-produced neutral gas cloud and the solar wind at the lunar surface. *J. Geophys. Res.*, 79, 1974.

[138] E M Wescott, H C Stenbaek-Nielsen, T Hallinan, H Föppl, and A Valenzuela. Star of lima: Overview and optical diagnostics of a barium alfvén critical velocity experiment. *Journal of Geophysical Research-Space Physics*, 91:9923, 1985.

[139] E M Wescott, H C Stenbaek-Nielsen, T Tallinan, H Föppl, and A Valenzuela. Star of condor: A strontium critical velocity experiment, peru, 1983. *Journal of Geophysical Research-Space Physics*, 91:9933–9938, 1985.

[140] H Alfvén. Collision between a nonionized gas and a magnetized plasma. *Reviews of Modern Physics*, 32(4):710–713, Oct 1960.

[141] J B McBride, E Ott, J P Boris, and J H Orens. Theory and simulation of turbulent heating by the modified two-stream instability. *Physics of Fluids*, 15(12):2367–2383, 1972.

[142] S Machida and C K Goertz. A simulation study of the critical ionization velocity process. *Journal of Geophysical Research-Space Physics*, 91(A11):11965–11976, Nov 1986.

[143] J C Person, D Resendes, H Petschek, and D E Hastings. Effects of collisional processes on the critical velocity hypothesis. *Journal of Geophysical Research-Space Physics*, 95(A4):4039–4055, April 1990.

[144] W J McNeil, S T Lai, and E Murad. Interplay between collective and collisional processes in critical velocity ionization. *Journal of Geophysical Research-Space Physics*, 95(A7):10345–10356, July 1990.

[145] J E Barnes and P Hut. Error analysis of a tree code. *Astrophysical Journal Supplement Series*, 70(2):389–417, 1989.

[146] U Becciani, V Antonuccio-Delogu, and M Gambera. A modified parallel tree code for n-body simulation of the large-scale structure of the universe. *Journal of Computational Physics*, 163(1):118–132, 2000.

[147] P Gibbon. A 3d hierarchical tree code for dense plasma simulation. *Computer Physics Communications*, 79(1):24–38, 1994.

[148] K Qiao and T W Hyde. Numerical simulation and analysis of thermally excited waves in plasma crystals. *Scientific Exploration, Planetary Protection, Active Experiments And Dusty Plasmas*, 34, 2004.

[149] P Gibbon, F N Beg, E L Clark, R G Evans, and M Zepf. Tree-code simulations of proton acceleration from laser-irradiated wire targets. *Physics Of Plasmas*, 11(8):4032–4040, 2004.